Ollscoil na hÉireann, Corcaigh

National University of Ireland, Cork

University College Cork, Ireland
Coláiste na hOllscoile Corcaigh

The Application of Object-Based Image Analysis to Geomorphological Seabed Mapping

Thesis presented by:

Gerard Summers, BSc (Hons), MSc

[ORCID iD: 0000-0002-5964-4746]

for the degree of

Doctor of Philosophy

University College Cork

School of Biological Earth and Environmental Sciences

Head of School/Department: Prof Astrid Wingler

Supervisor(s): Prof. Andy Wheeler & Dr. Aaron Lim

February, 2023

Table of Contents

List of Figures

List of Tables

List of Abbreviations

*.shp	Shapefile
°C	degrees Celsius (temperature)
ADCP	acoustic Doppler current profiler
BMP	Belgica Mound Province
CBD	Convention on Biological Diversity
cm	centimetres
CWC	cold water coral
EU	European Union
kHz	kilo Hertz
m	metres
MBES	multibeam echosounder
ML	machine learning
MOW	Mediterranean outflow water
MPA	Marine Protected Area
NMCI	National Maritime College of Ireland
NN	neural network
OBIA	object-based image analysis
PBIA	pixel-based image analysis
RF	random forest
ROV	remotely operated vehicle
SAC	Special Area of Conservation

SBES	singlebeam echosounder
SSS	side scan sonar
SSB	seabed sedimentary bedform
SSD	sinuous sediment dune
SVM	support vector machine
SW	sediment wave
UCC	University College Cork
UN	United Nations

Declaration

This is to certify that the work I am submitting is my own and has not been submitted for another degree, either at University College Cork or elsewhere. All external references and sources are clearly acknowledged and identified within the contents. I have read and understood the regulations of University College Cork concerning plagiarism and intellectual property.

Signed 

Gerard Summers, author.

Signed 

Prof. Andy Wheeler, supervisor of research.

Signed 

Dr. Aaron Lim, co-supervisor of research.

Acknowledgements

Concluding this degree and writing up my progression throughout its entirety has left me with no short measure of melancholy, knowing that I that I will leave a group of marvellous friends and colleagues. Naturally, the completion of this work was impossible without the input, support, empathy, and sympathy of many brilliant people. Therefore, I would like to earnestly thank each one of you, you made this possible and you made this a truly remarkable and unique experience.

Firstly, to my mother Sheila, the very fact that you brought me into this world would be sufficient to top this list. However, you have exceeded beyond every possible expectation of you as parent, you spent endless hours burning the midnight oil, patiently teaching me to read and write, to understand arithmetic as well as imbuing me with every bit of support that you could muster. I could never even begin to pay back this debt of gratitude nor could I accurately portray the exact magnitude of effort that you put down; I can only say thank you with all the love in my heart. To my brother Jake, you were the greatest companion to have during the outbreak of the COVID 19 pandemic. I doubt I would have had the will to continue my studies without your continued reassurance. Your IT expertise has profoundly enhanced the work that I was able to execute, thank you. To my grandmother Nora, one of my very first memories was seeing you break steel wire with your bare hands was the first time I saw the capacity of knowledge and the power it bestowed upon its bearer, you were my earliest inspiration for a career in academia.

To my partner Saoirse, you have provided me with encouragement, sage council, and most importantly a smile on my face at my greatest times of need. Thank you for being my rock during the most turbulent months of the thesis. Thank you to your family Joe, Ana, Róisín, and Homer for opening their home up to me during the early months of the pandemic. Thank you to Shane and Mateo for providing us with some of the most inspirational experiences and thought-provoking conversations.

To Luke O'Reilly, you were there at the start of my incursion into research. You have been a fast friend since, providing great banter and advice at key points throughout this expedition. Please never change. You are a gem, I am certain Ronnie and Caroline are proud as punch to call you their son, thank you for everything. To Evan O'Mahoney, the advice on exercise and fitness kept the remaining elements of my sanity intact throughout the entirety of the pandemic lockdown, I will be forever thankful for your patient guidance of me through the initial DOMS. To Larissa Macedo de Oliveira, you have been a great friend and colleague over the last few years. Your strength in the face of an extreme workload is something to behold. Thank you for tolerating my long ranting sessions in the office. To Ruaihri (Rasher) Strachan, your intense passion for all things marine, whether it be diving, cartography, or offshore wrecks always motivated me to be better, thank you. To John Appah, the positive attitude that you always brought to the office was infectious, your humility and work ethic are benchmarks that I try (and often fail) to achieve. Thank you for the wise words over the years. To David Price, you were meant to be a visiting member of the marine geosciences research group, but you have taken up permanent residence in my heart. Thank you for the many pints that we shared after weeks of intensive work.

To the remaining members and former members of the group: Felix Butschek, Alicia Cardenas, Riccardo Arosio, Audrey Recouvrer, Guillaume Michel, Jared Peters, Kimberley Harris, thank you for all your advice and encouragement. Thank you to Odhrán McCarthy for your assistance in the early days, listening to me rant about coding. and for the stimulating conversations at lunch time. I have had the privilege of sharing the cave with many different characters over the years including in no particular order: Daniel Falk, Juergen Lang, Tiffany Slater, Valentina Rossi, Eileen McCarthy, Darren Daly, Hannah Binner, Siobhán Burke, Obaid Alharbi, Aisling Scully, and Luisa Andrade, a big thank you for sharing the woes, trial and tribulations throughout each stage of the experience. Thank you to the UCC Geology teaching staff, in particular Ed Jarvis, Pat Meere, and John Reavy for granting me with an excellent background in geoscience. Thank you to Bettie Higgs for guiding me through my final year project, the lessons that you gave me during this process have stuck with me and I will never forget that experience. Thank you to all of the administrative team, Christine

Dennehy, Phil Fogarty, Mary McSweeney, and Elaine Kelly for logistical assistance. Thank you to the Heads of School Astrid Wengler and Andy Wheeler for their steadfast dedication to improving the already great workplace on offer at BEES. Thank you to Agust Magnusson for keeping a steady ship during the COVID 19 lockdown and providing me with great insight into the best mapping practices. Thank you to the ship technicians Mark O'Connor and Anthony English, your depth of knowledge and tolerance for answering inane questions, often asked by yours truly, are something to behold. Thank you to John Boyd for teaching me the true art of scepticism. Thank you to Tim Le Bas, our time together in Southampton was brief but illuminating, it was great to meet a kindred coding spirit.

To Andy Wheeler, 4 years and 4 months ago you had a bunch of candidates all vying for this very Ph. D. programme. The profound privilege I felt when you chose me to fill this position has left an indelible mark on me. I will be forever thankful for the punt that you took on me. Thank you for being a great supervisor.

To Aaron Lim, you have provided steadfast expertise, experience, and friendship during the entire Ph. D. I met you properly for the first time 6 years ago and you have maintained the same modesty and work ethic since then, it is honestly inspirational. I have cherished the time that you have spent with me, I can say with all clarity that without this I would not have finished this project. Lucy and Zoe are lucky to have you in their lives. Thank you for everything.

Finally, I would like to thank the crew and scientific team of the CE15009 and CV18027 research cruises. Without their contributions I would not have the data to complete this Ph. D.

Sincerely thank you to everyone,

Gerard.

Abstract

Increasing anthropogenic pressures on marine ecosystems due to the reliance on marine resources and the intense development of the marine realm within the last 10 years has threatened the effective functioning of many unique and fragile marine habitats. These environmental stresses warrant effective monitoring and management practices to ensure the preservation of good environmental status. *In situ* monitoring of marine environmental processes, such as current flow analysis through Acoustic Doppler Current Profilers, provide data with a high temporal resolution at distinct points on the seafloor. However, extensive spatial coverage of seafloor environmental requires a more efficient strategy to quantify these processes. Seabed mapping has long been established as an essential implement in the effective administration of marine ecosystems. Furthermore, in recognition of the significance of seabed mapping in the successful governance of the marine realm, several international seabed mapping initiatives and national seabed mapping programmes have been established with the goal to achieve complete mapping coverage of the seafloor by 2030. Such a significant volume of data evokes the necessity for an objective and repeatable approach to extract meaningful information from the seabed. Geomorphological seafloor features, including current induced seabed sedimentary bedforms (SSBs), are important indicators of habitat, and are readily apparent in seabed mapping data. Moreover, SSBs are common to many marine habitats and spatial scales and are the physical expression of seafloor hydrodynamics, thus these features are appropriate for a standardised approach designed to ascertain objective information on seabed hydrodynamics. This thesis develops a scale robust object-based image analysis (OBIA) approach that is created to classify SSBs as depicted in multibeam echosounder (MBES) bathymetry and derive hydrodynamic information from their morphometrics. This OBIA approach was applied to SSBs occurring in two spatial resolutions of MBES data. Here, four machine learning classifiers support vector machines, two multi-layer perceptrons, and voting ensemble were assessed on their ability to classify SSBs in these two resolutions of data. The results show that the voting ensemble classifier provided the most accurate results for both datasets. The OBIA framework was applied to SSBs depicted in MBES data acquired in a cold-water coral (CWC) habitat in the "downslope Moira Mounds" in the Porcupine Seabight. The SSB attributes of wave height and wavelength were derived from the SSBs classified in these data were used as an input to a multiple linear regression that predicted the seabed current velocity. These predictions

illustrated the variable influence of topographic steering occurring at regional-, local-, and micro-spatial scales on regional hydrodynamics. This workflow presented the first estimation of current flow velocity and direction from SSBs in MBES data. Finally, this OBIA approach was used to assess SSBs occurring in multiple resolutions of data within the same region, altering the resolution of observation to evaluate the effect of spatial resolution on the temporal resolution of seabed current hydrodynamics. Moreover, this study determined that the coarse spatial resolution MBES data prevented the assessment of short-term variations in seabed benthic habitat hydrodynamics.

Chapter 1. Advances in Seabed Mapping, Habitats and the Characterisation of Seabed Sedimentary Bedforms

Habitats are locations where the arrangement of environmental variables provide conditions that are key for the presence and diversity of specific biological assemblages (Greene et al., 2007). Marine benthic habitats are host to many significant ecosystems, with numerous environments forming hotspots of biodiversity that provide a wide range of ecosystem services to a plethora of marine species, many of which are economically valuable (Baillon et al., 2012; Roberts and Cairns, 2014; Bargain et al., 2017). Furthermore, biodiversity has been identified to support a wide range of ecological functions and ecosystem services (Corbane et al., 2015). Numerous Irish marine habitats have been described as biodiversity hotspots and offer a wide range of ecosystem services that have contributed to the most biologically prolific yet delicate environments in the EU (Casal et al., 2022). Many marine species contained within these hotspots are vulnerable to external pressures as they have a low fecundity and productivity and a greater longevity and age of first maturity (Zacharias and Gregr, 2005; Fabri et al., 2014). Moreover, anthropogenic demands placed on these vulnerable biodiversity hotspots is increasing due to the rapid growth of the world's coastal population, with >50% of the global population living within 100 km of the coast (Brown and Blondel, 2009). Consequently, several legislative devices such as Marine Protected Areas (MPAs) have been created to conserve and protect these species and their associated environments (Kachelriess et al., 2014). Thus, habitats that are associated with rich species assemblages are used as surrogates for biodiversity to avoid the exorbitant toll on time and money associated with the physical sampling schemes required to determine the distribution of each individual species (Costello, 2009). MPAs are zones of protection that impose restraints on the use of the marine resources through a variety of methods including regulating fishing equipment and imposing no take zones (Kachelriess et al., 2014). Assigning vulnerable biodiversity hotspots MPA status is regarded as one of the most effective conservation instruments available to policy makers (da Silveira et al., 2021). However, successful implementation of these MPAs necessitates the selection of ecologically pertinent regions and thorough maintenance of the integrity and abundance of their associated biological assemblages (Schéré et al., 2020; da Silveira et al., 2021). Designation of these zones of conservation is propelled by several international policies, the most significant of which was the Convention on Biological Diversity (CBD) Aichi Target 11 which dictated the conservation of 10% of the marine and coastal realm by 2020 (CBD, 2010). More contemporary research indicates that 30% of marine habitats should be protected to provide the most effectual implementation of MPAs (O'Leary et al., 2016). The High Seas Treaty is the latest international policy and is a commitment from the United Nations Convention on the Law of the Sea to protect 30% of the world's oceans by 2030 (United Nations Convention on the Law of the Sea, 2023). In Europe, these international policies are enacted through EU legislation including the Marine Strategy Framework Directive, this directive obligates member states to supply a representative and interconnected system of MPAs (Langton et al., 2020). However, despite these collaborative international efforts, 2.4% of global oceans have been designated and managed as MPAs (MPAtlas, 2022). Furthermore, information on environmental processes and the distribution of marine species is often scarce; consequently, many MPAs are designated due to socio-economic factors (da Silveira et al., 2021). Therefore, efficient methods of extracting such information from vulnerable marine ecosystems need to be developed to underpin the efficacious designation, management, and monitoring of MPAs (Copeland et al., 2013; Huvenne et al., 2016; Pergent et al., 2017).

1.1. Habitats

Habitats are regions whose abiotic and biotic components are bespoke to an individual species therefore, many habitats may be defined from the same area (Brown et al., 2011). Benthic habitats are often populated by biological communities or assemblages that are associated with each other and abiotic environmental attributes (Pillay et al., 2021). This implies the connection of a series of environmental attributes to both biotic and abiotic processes that are essential for the presence of specific biological assemblages (Kostylev, 2012). Moreover, many environmental processes are scale dependent (de Knegt et al., 2010). Therefore, establishing a standardised method for describing habitat requires the definition of a scale of observation to frame the environment and the processes that govern it and how they interact with the organisms therein (Brown et al., 2011; Lamarche et al., 2016). Furthermore, the scale of analysis influences the quantification of the affiliation of these processes with the target species or assemblage (Costello, 2009). Contemporary research has identified three categories of scale when evaluating a habitat: temporal, thematic, and spatial (Lecours et al., 2015). Once these domains of scale have been established, the effective assessment of the faunal relationship with the environment can be effectively drawn (Strong and Elliott, 2017). Creating snapshots of ecological activity speckled over space and time (Kostylev and Hannah, 2007). Thus, different habitats can be evaluated at the same scale to compare processes, or the complexity of the same ecosystem can be appraised at multiple scales (Lecours et al., 2015; Buhl-Mortensen et al., 2015). Enabling the interpretation of the drivers of the composition of marine benthic assemblages that occur between environments or drivers that function within the same environment over local and global scales (Porskamp et al., 2018). Typically, terrestrial habitats are organised by the complex 3D frameworks imposed by autogenic engineers including humans and vegetation (Zajac, 2008). However, the influence of vegetation in the marine realm is restricted to the shallow water habitats of the photic zone (Brown and Blondel, 2009). Therefore, benthic seabed habitats are often defined by physical environmental characteristics (Harris and Baker, 2020). Consequently, producing reliable maps of benthic habitats requires thorough descriptions of the topography, substrate type and composition, and geomorphology of the seabed (Pierdomenico et al., 2015).

1.1.1. Geomorphology

Geomorphology of the seafloor pertains to the bedforms that are present on the seafloor surface and how they relate to the subsurface geology (Dove et al., 2020). Their physical attributes can provide information on the processes responsible for their formation (Dove et al., 2020). For instance, seabed habitats that are composed of unconsolidated sediments are often organised by the overlying hydrodynamic regime (Barnard et al., 2013; Lebrec et al., 2022). Current-induced processes such as sediment winnowing, remobilisation, and erosion can shape the seafloor through an extensive range of scales (Miramontes et al., 2019). Consequently, these currents are imprinted on the sedimentary environment, producing erosional and depositional seabed sedimentary bedforms (SSBs) (Knaapen et al., 2005; Duţu et al., 2018). Therefore, careful measurement of these SSBs can help deduce the nature of the properties of the currents responsible for their formation (Stow et al., 2009; Lefebvre et al., 2022). SSBs can be divided by their morphology into erosion- and deposition-dominated features (Symons et al., 2016). With erosion-dominated SSBs forming depressions in the seafloor that are termed scours, whereas deposition dominated SSBs create positive topographical features with crests that are aligned perpendicular to flow (transverse, i.e., sediment waves) or parallel to flow (linear, i.e., sand ridges) (Stow et al., 2009). SSBs can be classified as moribund, relict, or active dependent on their morphodynamic activity, with the original morphology of moribund SSBs becoming altered during present sedimentary processes (Simarro et al., 2015). Relict SSB morphologies do not present any interaction with present day sedimentary processes (Simarro et al., 2015). The crests of active SSBs migrate across space when monitored over time, with the direction of the migration demonstrating the nature of the current flow responsible for their formation (Symons et al., 2016). Therefore, plan- and cross-sectional assessment of sediment ridges and sediment waves are employed to determine the inherent nature of the bedload transport (Creane et al., 2022).

1.1.1.1. Sediment Waves

Sediment waves are deposition-dominated SSBs that are composed of a crest that is bounded by two troughs at either side, the asymmetry of the sediment wave profile in cross section determines the direction of migration for the bedform (Van Landeghem et al., 2009b). The longer flank, or stoss side, is orientated in the direction of the current whereas the shorter flank of the sediment wave, or lee side, is orientated towards the direction of sediment wave migration (Figure 1) (Koop et al., 2019).

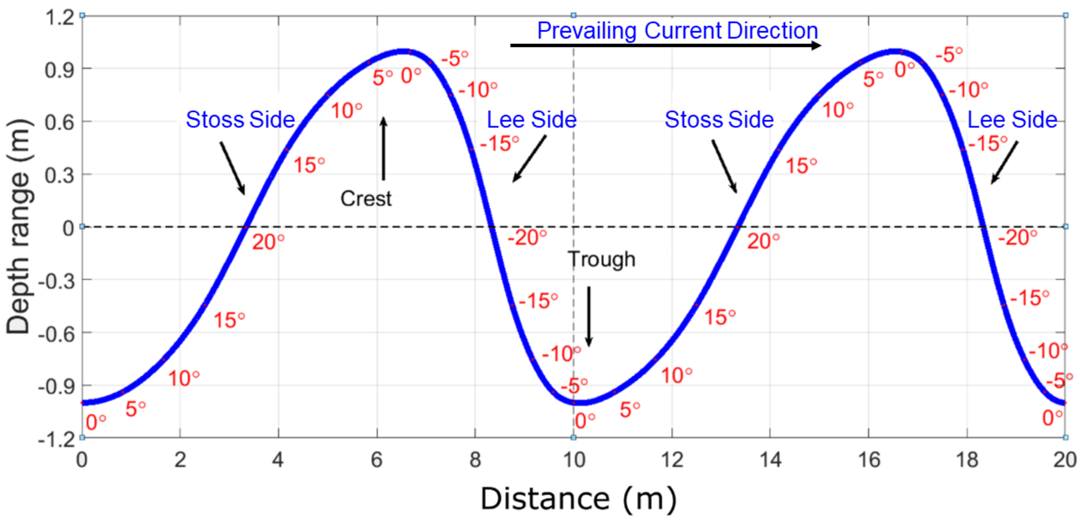

Figure 1. Adapted from Koop et al. (2019), schematic structure of a sediment wave; wavelength is 10 m and depth variation is ~1 m. Also indicated are crest vs trough area and lee vs stoss sides.

Moreover, these features can be distinguished by their sediment composition, for instance fine grained sediment waves occurring in regions that contain currents with flow velocities between 0.09–0.30 m·s^{-1} (Wynn and Masson, 2008). While coarse grained sediment waves such as sand waves occur where current flow velocities exceed 0.4 m·s^{-1} (Wynn and Masson, 2008; Ashley, 1990). Furthermore, current flow velocity influences the morphology of sediment waves, with linear to sinuous crested sediment waves forming due to lower current velocities than crescent shaped sediment waves, i.e. barchan dunes (Stow et al., 2009). A barchan dune consists of two horns and a slip face on the lee side, and a more gradually sloped stoss side and occurs on hard substrate with a limited supply of sand (Figure 2) (Khosronejad and Sotiropoulos, 2017; Allen, 1984).

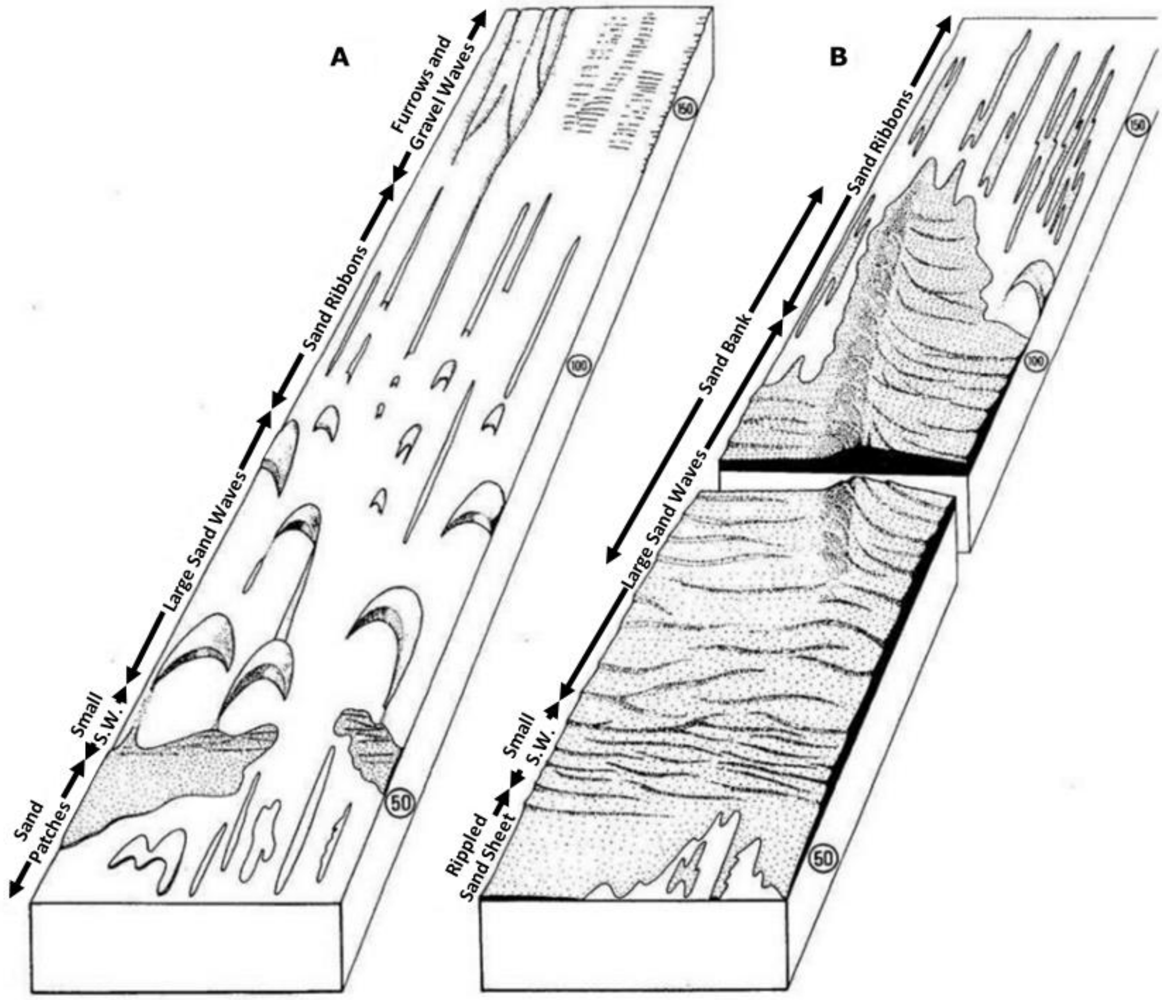

Figure 2. Adapted from Belderson et al. (1982) ,block diagrams of bedforms made by tidal currents on the continental shelf with low supply (**A**) or abundant supply (**B**) of sand, respectively.

Sediment transport is considered to be continuous across the entire length of a linear sediment wave. However, sediment transport for a barchan dune begins at the toe of the stoss side and ends at the horns at the lee side (Couldrey et al., 2020). Additionally, sediment waves can be separated by scale and can range from sediment waves with heights of 10 m and wavelengths of 100–1000 m that migrate several metres per year, to sediment ripples with wavelengths of several centimetres that migrate several metres per day (Damveld et al., 2018). Therefore, the temporal resolution of the hydrodynamic processes expressed through these seabed features is controlled by the spatial scale at which they occur, with smaller sediment waves altering with short term variations in current flow (Knaapen et al., 2005). Whereas larger sediment waves reflect the properties of long-term seabed benthic current processes (Lobo et al., 2010; Li and King, 2007).

Moreover, nested multiscale structures formed due to the superimposition of different SSBs may indicate intricate bottom current flow with significant temporal variation (Li and King, 2007; Mestdagh et al., 2020). Smaller scale SSBs superimposed on larger scale SSBs have been observed, with the smaller scale SSBs orientated oblique or sometimes perpendicular to their larger scale counterparts indicating short term interruption in long term current flow regimes (Barnard et al., 2011). Hence, understanding the geomorphology of the seabed over time and space will provide an insight into the processes that direct sediment transport over a variety of temporal scales (Tecchiato et al., 2015). Comprehending the nature of the sediment transport within the region is significant for to offshore infrastructure projects as regions of constant sedimentary flux are unstable and are not conducive to offshore development (Greene et al., 2021).

Information on sediment mobility and benthic currents can provide a valuable understanding of habitat distribution in regions lacking detailed ecological data, where seabed physical properties are employed as proxies for the estimation of species distribution (Ryan et al., 2007; Meijer et al., 2022). Additionally, the substrate stability inferred by the geomorphology of the seafloor offers a significant physical control on biodiversity, oceanographic flow path estimations or sedimentation processes (Freeman and Rogers, 2003; Jerosch et al., 2016). Moreover, SSBs provide refuge and winter feeding grounds for species that are crucial to marine food webs (Greene et al., 2017; 2020). Meijer et al. (2022) show that bedforms characterised to help predict seafloor stability were good indicators of distribution for macrozoobenthic species in shallow sea environments. Geomorphological heterogeneity has been found to be a significant indicator of biodiversity, with regions of high geomorphological heterogeneity being recommended to be prioritised as regions of conservation (Lucatelli et al., 2020).

1.1.2. Cold-Water Coral Habitats

Cold water corals (CWCs) are autogenic filter feeding organisms that can produce complex 3D frameworks that form reefs and potentially mounds through repeated accumulation of sediment and biological material over time (Wheeler et al., 2008). These mounds can form significant topographic structures that range from several of metres to several of kilometres across forming giant carbonate mounds (Kenyon et al., 2003; van Weering et al., 2003; Wheeler et al., 2005; Dorschel et al., 2010). These mounds are often described as biodiversity hotspots and offer a wide range of ecosystem services to a plethora of marine species, many of which are economically valuable (Baillon et al., 2012; Roberts and Cairns, 2014). Consequently these organisms have been protected under the European Union Habitats Directive (92/43/EEC) (Jackson et al., 2014). Local scale distribution of CWCs is associated with the provision of fresh labile organic matter and hard grounds for larval settlement (Kiriakoulakis et al., 2007; Huvenne et al., 2011). Recent research estimating biomass in CWC habitats showed that 5–9% of all primary production required to sustain CWC mounds percolates down through the water column from the sea surface (De Clippele et al., 2021). Therefore, it has been postulated that another mechanism must be responsible for supplying these organisms with nutrients. SSBs have frequently been described to occur proximal to CWCs, indicating a relationship between the CWCs and enhanced bottom currents (Dorschel et al., 2009; Lim et al., 2018a). Moreover, *in situ* current measurements taken from canyon environments show that CWC bearing habitats occur in regions with higher current velocities than non-CWC bearing habitats (Mienis et al., 2007; Wagner et al., 2011; Lim et al., 2020). Contemporary research postulates that increased current velocities deliver a greater volume of food for the corals (De Clippele et al., 2017). However, a greater proportion of CWCs have been found to occur on slopes facing away from the prevailing current direction thus, they are sheltered from the erosive impact from the higher current velocities (Lim et al., 2020). These observations are congruent with those found in aquaria studies, whereby CWC polyps have a higher mortality when exposed to higher current speeds (Buhl-Mortensen et al., 2001). The intricate relationship that these organisms have with their surrounding hydrodynamic environment underlines the importance of developing techniques that can analyse their distribution while maintaining a contextual view of the local and regional hydrodynamics (Howell et al., 2011).

Despite efforts to conserve these environments, significant changes in the species assemblage composition has been observed over relatively short timeframes (Boolukos et al., 2019). Furthermore, high resolution monitoring efforts focused on CWC mounds within MPAs reported that colonies that had previously been impacted due to human activities exhibit low levels of re-growth (Huvenne et al., 2016). Thus, the slow growth rate of these organisms makes them vulnerable to environmental pressures and emphasises the need to understand the environmental processes that drive their success (Montseny et al., 2021). Traditionally, the mapping of seabed habitat was centred on the data acquired from physical sampling and the observations made by diving personnel (Micallef et al., 2012). However, such methods are costly and offer small windows of inspection for the seafloor (Harper et al., 2010). Moreover, the precision of such physical sampling methods is difficult to ascertain as they are subjective, preventing effective comparison between surveys (Zlinszky et al., 2015). Therefore, more efficient workflows that provide accurate high resolution environmental data that can be assessed at a variety of scales from these habitats are required to ensure their effective conservation (Savini et al., 2014).

1.2. Remote Sensing and Habitat Mapping

High resolution data is essential in determining organism behaviours that are fundamental to discerning larger ecological patterns (Prada et al., 2008). Remote sensing has been established as a foundational approach for the establishment, management, and monitoring of MPAs (Kachelriess et al., 2014). These data provide the means to extrapolate local scale observations developed from field sampling techniques to encompass larger scale environments (Tong et al., 2004). Many of the procedures and techniques involved in marine remote sensing were inspired or adapted from satellite remote sensing of terrestrial environments (Diesing et al., 2016). As terrestrial ecosystems are often defined by the vegetation contained within them, remote sensing efforts in this realm have focused on developing specific sensors that record the spectral nature of the electromagnetic radiation (EMR) reflected by these habitats (Patino and Duque, 2013). This EMR can provide direct information on the organisms, species, or ecological communities present in the habitats, or provide indirect information on biodiversity through environmental proxies (Corbane et al., 2015). High resolution and high-volume data collection can be achieved by mounting these sensors on a wide range of platforms including airplanes, unmanned aerial vehicles, and satellites (Patino and Duque, 2013; Easterday et al., 2019). This vast quantity of high resolution data has led to significant advances in the understanding of reflected spectral signatures, resulting in the production of extensive spectral indices (SIs) that have been used as surrogate values for terrestrial habitats (Klimetzek et al., 2021). Additionally, these SIs have been correlated with other habitat attributes including richness, abundance, and biomass, allowing for the estimation of these properties from the remote sensing data (Michaud et al., 2012; Fern et al., 2018). In the marine realm, traditional remote sensing techniques are restricted to shallow water environments, as EMR attenuates quickly in the water column, resulting in limited penetrative capabilities (Ruddick et al., 2014; Reshitnyk et al., 2014; DeSanto et al., 2016). Furthermore, due to the limited penetrative capacity of photosynthetically active EMR in water, marine vegetation is limited to the euphotic zone, with deep benthic seabed habitats being defined by the sessile organisms and underlying geology (Beisiegel et al., 2017). Therefore, benthic seabed habitat mapping requires other technological avenues to acquire remote sensing data from these ecosystems (Anderson et al., 2008).

1.3. Acoustic Seabed Habitat Mapping

Similar to satellite remote sensing, the acoustic data recorded by underwater echosounders offer the ability to measure the benthic seabed habitat (Kostylev et al., 2001). These data are used in combination with *in situ* sampling and observations to provide groundtruthed predictions of the physical seabed environment, significantly reducing survey time and costs (Schimel et al., 2010; Amiri-Simkooei et al., 2011). Moreover, underwater echosounders are viewed as the most effective method for the mapping and monitoring of the seabed substrata over extensive areas (Anderson et al., 2008). Early acoustic research employed single beam echosounders (SBESs) that measure the return time and the strength of a single broad sonar beam to determine the depth and acoustic impedance of the seabed (Hutin et al., 2005). Furthermore, the area ensonified by an SBES beam is circular in shape at vertical incidence and thus, is dependent on the beam width and pulse width of the sonar signal and the relative depth of the seafloor (Marks and Smith, 2008). The returned acoustic signal is represented as a single datapoint for the entire area ensonified by the SBES beam (Maleika, 2013). Signal processing software, such as RoxAnn, can exploit specific properties of the returned acoustic signal to provide information on the roughness and hardness of the seafloor (Collier and Brown, 2005; Serpetti et al., 2011). SBES systems offer a cheaper alternative to multibeam echosounder (MBES) equipment and are often used in shallow waters where the swath width of an MBES system is limited (Amiri-Simkooei et al., 2011; Arseni et al., 2019). However, SBES data are dense along track with no corresponding across track coverage therefore, full mapping coverage with SBES data requires close survey line spacing combined with interpolation between adjacent survey points (Kenny et al., 2003; Hutin et al., 2005; McGonigle et al., 2010a; Mayer, 2006; Schimel et al., 2010; Landero Figueroa et al., 2021). Consequently, a significant proportion of the final map is a result of a prediction, introducing uncertainty into the data (Schimel et al., 2010). Furthermore, the most effective interpolation approach for SBES data is still under debate, with interpolation of sparse SBES data resulting in track line artefacts (Landero Figueroa et al., 2021). The uncertainty introduced by interpolation can be reduced by decreasing the distance between adjacent survey lines, however this proposes increasing the time required to survey the same area (Parnum et al., 2009).

1.3.1. Side Scan Sonar (SSS)

Side scan sonars (SSSs) were first developed in the 1940s (Kaeser et al., 2013). This equipment can be deployed as part of a pole mounted configuration attached to the hull of the vessel, or hauled as part of a hydrodynamically stable towfish behind the vessel (Pearce and Bird, 2013). Typically, SSSs transmit two acoustic beams at an angle from either side of the sonar, these beams are narrow along track and broad across track, providing continuous 2D data on seafloor reflected energy (backscatter intensity) (Buscombe, 2017; Pearce and Bird, 2013). Traditional benthic habitat mapping studies that employed SSSs integrated the full coverage backscatter data acquired with bottom samples collected from the mapped seafloor (Shumchenia and King, 2010; Isachenko et al., 2014). Furthermore, these samples are then extrapolated from to predict the seafloor properties for the entire SSS mosaic (Isachenko et al., 2014). Several SSS systems allow for the comparison of the phase between pairs of receiver arrays, this comparison enables the production of depth measurements from the acoustic data, these systems are known as interferometric SSS (Mayer, 2006). Difficulties occur when quantitatively analysing SSS data as swathe acoustic systems provide a more complicated sound scattering regime than for single beam sonars (Brown and Collier, 2008). The scattering regime is regulated by the relative geometry of the sensors that make up the SSS array, angle of incidence of the beam, the physical characteristics and composition of the seafloor (Degraer et al., 2008). A slight change in any of these factors can preclude the interpretation of the backscatter image, impediments encountered during acquisition can include water column noise, changes in the attributes of the water column and an unstable towfish (Lathrop et al., 2006). Additionally, SSS systems require the use of ultra-short base line or short base line position systems to provide accurate positioning for the towfish configuration, the use of both is prohibitive due to their high costs (Shang et al., 2019). Moreover, the absence of secondary information including bathymetry and angular dependence from non-interferometric SSSs prevents the effective correction of radiometric and geometric artifacts for the backscatter data (Fakiris et al., 2012). Bathymetry produced through interferometric SSS is sensitive to ambient noise in the water column and deteriorates in quality with increasing proximity to the nadir (Fezzani et al., 2019). These corrections are readily implemented in MBES backscatter workflows (Fakiris et al., 2012).

1.3.2. Multibeam Echosounders (MBES)

MBESs were invented in the 1960s and were initially developed to provide bathymetric measurements from 11 to 22 adjacent sonar beams across a swath of 55° with acquisition settings adjusted to prioritise the quality of the bathymetry over the backscatter intensity (White, 1971; McGonigle et al., 2010a). Thus, providing multiple soundings across the swath for every individual sonar ping (Held and Schneider von Deimling, 2019). Over time, the number of beams, precision, and swath width of these echosounders increased (Le Bas and Huvenne, 2009). Today, MBESs deliver high quality backscatter and bathymetry measurements with typical modern systems providing 1024 to 1700 beams across their swath (Snellen et al., 2011; Czechowska et al., 2020; Held and Schneider von Deimling, 2019). The quality and resolution of these measurements are highly dependent on the depth of the seafloor, as the beam footprint on the seafloor increases with increasing depth (Costa et al., 2009).Thus, MBESs can generate data at sub-metre resolutions in ideal, shallow water conditions, offering a dense array of soundings that do not require the same interpolation protocols as SBES systems (Lacharité et al., 2018; Lamarche et al., 2016). Moreover, these data provide the ability to depict the seafloor at a resolution akin to that terrestrial remote sensing, enabling the production of high quality habitat maps for benthic ecosystems (Zhao et al., 2021). Most MBES transmit and receive arrays consist of a Mills cross design; here, the transmit array creates a signal with a narrow band around the central frequency, creating a single frequency backscatter dataset (Lurton, 2002). The beams emitted are usually broad in the athwartship direction and narrow in the alongship direction, the receiver array mirrors the transmit array except that it is orientated orthogonally to the transmit array (Hughes Clarke et al., 2006). Therefore, objects ensonified by the transmitter can be detected by angular discrimination through beamforming (Hughes Clarke et al., 2006). Single head MBES systems can achieve coverages of up to 130° with dual head systems offering coverages up to 170° (da Silva Pereira and Clarke, 2015). Although, the attenuation of the signal strength with increasing distance travelled, refraction effects, and the low signal to noise ratio present at low grazing angles creates uncertainties within the data consequently precluding accurate data collection above 120° (da Silva Pereira and Clarke, 2015). Additionally, SSSs provide accurate data collection at higher grazing angles than MBESs and are more useful in shallow water surveys as a result (Fakiris et al., 2019).

The relationship between the sediment characteristics and the reflected acoustic energy from the seabed is dependent on the frequency of the sonar and the angle of incidence of the sonar signal (Masetti et al., 2011; Feldens et al., 2018). For instance, lower frequency sonar (30−90 kHz) can penetrate further through finer seabed substrate, generating increased backscatter intensity responses when subsurface heterogeneities are encountered relative to higher frequency sonars (>100 kHz) (Lurton et al., 2015; Fezzani et al., 2021). Moreover, lower frequency MBESs have been found to have greater correlation with grain size in coarser grained sands and gravels, whereas higher frequency sonar exhibits a greater correlation with finer grained sands, silts and muds (Runya et al., 2021; Snellen et al., 2019). Therefore, many contemporary studies are now focused on deploying multifrequency MBES to better determine the attributes of the seabed (Brown et al., 2019). Furthermore, this research has described an enhanced discriminative capability between distinct seafloor classes (Gaida et al., 2018; Costa, 2019).

Currently, there are few commercially available MBES systems that provide the ability to simultaneously collect multifrequency MBES data whereas many modern SSSs offer simultaneous collection of multifrequency datasets (Gaida et al., 2018; Tamsett et al., 2016). Consequently, many multifrequency MBES studies are limited to repeat mapping of the same section of seabed at different frequencies thereby increasing the required survey time (Hughes Clarke, 2015; Janowski et al., 2018b; Feldens et al., 2018). Moreover, the grazing angle of each beam has a significant impact on the backscatter response precise colocation of ensonification geometries is problematic and introduces inconsistency into the analysis

(McGonigle et al., 2010a; Brown et al., 2019). This is significant considering that separate scattering mechanisms operate at different incident angles on the seafloor, causing a significant difference in the degree of penetration, and backscatter intensity of the seafloor (Huang et al., 2018; Hillman et al., 2018). Much of the uncertainty surrounding MBES backscatter data has yet to be resolved and this strongly contrasts with the meticulously defined error models available for MBES bathymetry data that impart significant data quality assurances (Eleftherakis et al., 2018). This is further compounded by the lack of widespread calibration of MBES backscatter data (Lurton et al., 2015). Furthermore, MBES surveys are typically designed to prioritise the collection of the bathymetry, as backscatter dedicated surveys require greater overlap between survey lines to achieve an adequate density of soundings (Alevizos and Greinert, 2018).

MBES backscatter intensity data production requires the subtraction of the backscatter angular response to ensure that the variations in intensity are due to geographical changes in seafloor composition (Hasan et al., 2014). However, removing this angular response also erases crucial information pertaining to the physical seafloor substrate characteristics (Hamilton and Parnum, 2011). Fonseca and Mayer (2007) have exploited this information by relating the angular response of an area of seafloor to a mathematical model in a technique called angular range analysis (ARA) that provides quantitative data on seabed characteristics including grain size. This approach groups together 20–30 consecutive acoustic pings over half or a full swath width (Fonseca et al., 2009). Grouping these data together reduces the impact of noise innate to MBES backscatter data; however, this limits the spatial resolution of the data to a half or full swath width (Fonseca and Mayer, 2007; Hasan et al., 2012a; Rzhanov et al., 2012; McGonigle and Collier, 2014). Thus, seabed substrates that are relatively heterogeneous over this spatial resolution may not be effectively resolved within this approach (Rzhanov et al., 2012). ARA derived attributes have been integrated with traditional MBES backscatter intensity data to ameliorate this spatial resolution deficiency (Fonseca et al., 2009; Hasan et al., 2012b). Furthermore, the combination of these ARA data with MBES backscatter intensity in seabed classifications has improved the accuracy of results, providing a near perfect discrimination between hard and soft seabed (Zhi et al., 2014; Hasan et al., 2014). Santos et al. (2018) showed that effective estimations of seafloor characteristics through ARA of MBES backscatter can be derived from regions of high heterogeneity of seabed sedimentary coverage.

As of 2018, 18% of the seafloor has been mapped by underwater echosounders thus, several international mapping initiative and national mapping programmes have been established to amend this data deficit (Mayer et al., 2018; Guinan et al., 2021; Thorsnes, 2009). This proposition requires the collection of vast volumes of MBES data which raises the issue of deriving objective, consistent, ecosystem information from these data (Diesing et al., 2014). Additionally, new methods have been developed to reconcile adjacent MBES coverage and classify MBES data acquired from multiple sources, improving comparison between MBES data derived from distinct regions (Misiuk et al., 2020; Proudfoot et al., 2020; Lacharité et al., 2018; Prampolini et al., 2021). Traditionally, expert interpreters would delineate regions of similar acoustic response and apply classes that are relevant to the perceived environment and processes therein (Rzhanov et al., 2012). However, the production of such expansive high resolution datasets would thwart manual interpretation, particularly when considering the increased dimensionality introduced through the ARA and collection of multifrequency MBES data (Menandro et al., 2022). Moreover, subtle variations in the backscatter intensity remain undetected in studies that deploy manual digitisation over large scale mapping extents (Montereale Gavazzi et al., 2016). Therefore, automated classification approaches need to be developed to effectively reduce the subjectivity introduced during human appraisals of MBES data (Menandro et al., 2020).

1.4. Automated Classification

Classification of seabed habitats reduces the spatial variability observed over large spatial scales by applying labels to seabed facies depicted in data acquired from seafloor; thus, simplifying noisy seabed mapping data into an inventory of seabed substrates across a biogeographic region (Cooper et al., 2019). Automated seabed classification approaches have been applied to provide information on the substrata of the seabed from acoustic mapping data (Ierodiaconou et al., 2011). Typically, these techniques consist of two groups: unsupervised and supervised classification (Li et al., 2017). Unsupervised, or automated, classifications exploit the regularities within the data by applying a clustering technique that determines the classification, with user control limited to the number of clusters (Zhi et al., 2014; Ismail et al., 2015). Furthermore, these approaches seek to define boundaries between classes where the data density is low and the variance is high (Lucieer and Lamarche, 2011). Association of the classes with the environmental processes and parameters is completed after the clustering by comparing groundtruth samples with the resultant categories (Calvert et al., 2014). Several automated classification techniques have been utilised in the marine setting; however, an academic consensus on a ubiquitous automated classification workflow has yet to be achieved (Diesing and Stephens, 2015). Moreover, determining the appropriate number of clusters required to attain the most representative classification for these workflows is the most subjective component in these approaches (Hogg et al., 2016). For instance, a smaller number of clusters may produce categories with a lot of intra class heterogeneity, whereas a high number of clusters may produce specialised classes with minimal extra class heterogeneity (Omo-Irabor, 2016). Therefore, unsupervised classification schemes are beneficial when groundtruthing data are limited; however, where groundtruthing data are abundant a supervised classification is preferred (Diesing et al., 2016). Additionally, the accuracy and replicability of unsupervised classification schemes is not maintained when applied to separate datasets acquired over consecutive days, particularly in comparison with supervised classification schemes (Zelada Leon et al., 2020).

Supervised, or semi-automated, classifications identify features through the direction of an expert interpreter (Linklater et al., 2019). Machine learning (ML) is an example of supervised classification, here an algorithm absorbs the configuration of features depicted by sample data that were categorised into classes that were predefined by an expert analyst from groundtruth observations (Linklater et al., 2019). The success of this type of classification is determined by deploying this algorithm on a withheld portion of the training data, the proportion of correctly predicted labels, or accuracy, is obtained (Hasan et al., 2012a; Hillman et al., 2018). Thus, determining the degree of influence that the noise within the data imposed on the classification output (Mohamed et al., 2020). ML is considered to offer a more valid replication of expert interpretation than unsupervised classification schemes (Herkül et al., 2017). Typically, these ML workflows will extract secondary features from bathymetry and backscatter data to enhance the classification efficacy including slope, curvature, and bathymetric position index (BPI) (Diesing et al., 2016). Several ML algorithms pervade seabed habitat mapping research including support vector machines (SVMs), random forest (RF), and neural network (NN) classifiers (Hasan et al., 2012b; Marsh and Brown, 2009). SVMs determine the optimal configuration of class boundaries in multi-dimensional feature space that remains robust despite limited training data, high feature dimension space, and non-linear distributions (Wicaksono et al., 2019; Cui et al., 2021). RF is an ensemble classifier that comprises multiple binary decision tree classifiers, combining their predictions and producing a classification that is resilient to noise (Liu et al., 2019a; Misiuk et al., 2019). RF classifiers exhibit robust classification outputs despite the inclusion of large numbers of image features (Ierodiaconou et al., 2018). NNs consist of an input layer, one or more hidden layers, and an output layer, each consisting of a series of adjustable weights referred to as nodes or edges (also known collectively as neurons) (Conti et al., 2019). Initial studies employed NNs with a single hidden layer, these nascent classifiers combined with RF and SVM classifiers are termed shallow ML classifiers (Hopkinson et al., 2020). Ensemble classifiers that integrate the resultant classification of multiple accurate shallow models that each have a distinctive architecture, providing uncorrelated errors (Diesing and Stephens, 2015).

More recent research has examined the use of NNs with multiple hidden layers, increasing the model complexity and thus the capacity of the model to assimilate the nuances of the pattern exhibited by the features depicted in the sample data (Conti et al., 2019). Such ML algorithms are further categorised as “deep” learning algorithms (Wan et al., 2022). The increased complexity of these ML algorithms also increases the likelihood that the classifier will overfit to the data and increase the variance in the output of the classification (Feldens et al., 2018). Furthermore, the inclusion of insignificant bathymetric and backscatter derivatives due to the increased dimensionality of modern MBES classification workflows will compound this issue (Zhu et al., 2021). Therefore, extensive feature selection protocols must be employed to ensure the success of the outcome classification for all ML classification schemes (Nemani et al., 2022). These protocols often identify image features that are correlated and either remove the correlated feature that explains the least variance within the training data, or transforming the features into a lower dimension feature space that remove the variation in the data (Boswarva et al., 2018; Nemani et al., 2022). Typically, the correlation between features is determined and a threshold is applied to remove highly correlated features, then a feature selection algorithm is applied to the remaining features to ensure that those included are relevant to the classification (Janowski et al., 2021). Spatial autocorrelation occurs between neighbouring groundtruthing samples, where observations proximal in location have proximal feature values (Brandt et al., 2016). Thus, spatial cross-validation techniques and equidistant sampling strategies have been developed to ensure that more robust training schemes are in place (Brandt et al., 2016; Gazis et al., 2018; Gazis and Greinert, 2021). Moreover, effective implementation of "deep learning" algorithms requires a large training dataset that is representative of each seafloor class (Yasir et al., 2021). This requirement exacerbates the already prevalent issue of manual annotation of training data necessary for the successful deployment of ML classifications (Schoening et al., 2014).

1.4.1. Pixel-Based Image Analysis and Object-Based Image Analysis

Supervised and unsupervised classification schemes are deployed in two main approaches; through pixel-based image analysis (PBIA), or object-based image analysis (OBIA) (Ierodiaconou et al., 2018). Initial habitat mapping data generally had a coarse spatial resolution; consequently, the spectral response of the feature of interest was often represented by a single pixel (Hossain and Chen, 2019). PBIA classification workflows were prevalent early during the automated classification of this coarse spatial resolution remote sensing data (Ma et al., 2017). During PBIA, the image feature values for each individual pixel are assessed and a classification is applied; therefore, the features of interest within an image are determined to be separable solely through their spectral properties (Drăguţ et al., 2010). However, this prevents the consideration of the contextual relationship between neighbouring pixels (Yang et al., 2020). Moreover, a pixel does not reflect the direct physical extent of a seabed cover class (Costa et al., 2017). Today, MBES sensors can depict seabed features at fine spatial resolutions of data; therefore, seabed features are often represented across multiple pixels (Lucieer, 2008). This increases the noise depicted for image features and increases their spectral variance and hence, producing erroneous classifications when incorporated into a PBIA (Viala et al., 2021). These misclassifications manifest as a "salt and pepper effect" and capture minor inconsistencies within larger image features (Lucieer, 2008; Ierodiaconou et al., 2018; Zhang et al., 2020). Furthermore, the maps produced by this workflow depict seabed features occurring at a single scale (Costa and Battista, 2013). Conversely, a strong emphasis is placed on mapping seabed habitats at multiple scales to effectively capture all the features that are evident in each environment therefore, pixel-based classifications are insufficient to fulfil this requirement (Shang et al., 2021). Consequently, PBIA is considered when the spatial resolution of the data is similar or greater than the extent of the feature of interest (Gao and Mas, 2008; Cassol et al., 2021). Therefore, in mapping scenarios that contain fine resolution MBES data, PBIA has been superseded by

OBIA approaches as they allow multiple spatial scales of analysis and are robust to noise found in these fine spatial resolution data (Blaschke et al., 2014).

Object-based image analysis operates over two separate stages, the first being segmentation, the second is classification (Diesing and Thorsnes, 2018). Objects are defined in OBIA as distinct portions of the image that are internally homogeneous (Cassol et al., 2021). Segmentation seeks to separate images into image objects by amalgamating adjacent homogeneous image pixels, this internal homogeneity is maintained relative to the intra object homogeneity criterion (Blaschke, 2010). Furthermore, this homogeneity criterion also ensures that maximum heterogeneity between neighbouring image objects is attained (Hussain et al., 2013; Janowski et al., 2020). Therefore, this process is a direct reflection of the spatial and contextual relationship of the pixels (Gao et al., 2011). Summary statistics such as mean and median pixel values can be derived from these image objects, effectively reducing the variance within each image object and the noise included in the resultant classification (Diesing et al., 2016). Geometrical attributes of these image objects including size, shape, texture and relative position can provide a further dimension for classification of seabed features (Phiri and Morgenroth, 2017). Thus, the image objects become the basic unit for the classification rather than the individual pixels, creating a more intuitive methodology as it is similar to how people interpret images (Hay and Castilla, 2006). Moreover, using image objects as the minimum mapping unit reduces the computational requirements for an automated classification (Mitchell et al., 2018).

The multiresolution segmentation (MRS) algorithm provided by eCognition Developer is the most commonly used segmentation method (Ma et al., 2017). Image objects are formed in a bottom up approach where adjacent pixels with similar values are merged into image objects (Lucieer and Lamarche, 2011). These image objects are then iteratively merged until the intra-object homogeneity indicated by the scale parameter is met (Koop et al., 2021). Increasing the scale parameter increases the average size of the image objects and thus, the intra-object heterogeneity (Drăguţ and Blaschke, 2006). Precise segmentations construct image objects with borders that match the outlines of the target features (Kavzoglu and Tonbul, 2018). However, selection of an appropriate value for the scale parameter lacks a ubiquitous procedure therefore, segmentation can be a heuristic process and difficult to duplicate (Grippa et al., 2017). Furthermore, the scale parameter chosen during segmentation has a significant impact on the classification output (Wicaksono et al., 2019).

A method has been proposed to standardise the selection of an appropriate scale parameter for the MRS algorithm (Drăguţ et al., 2010). However, the use of singular metrics to describe the variation exhibited in complex seabed mapping data is not adequate (Kucharczyk et al., 2020). Furthermore, successful performance of a segmentation is heavily dependent on the resolution of the data, higher spatial resolution data produces better quality segmentations and thus, better quality seafloor classifications (Rende et al., 2020). Therefore, OBIA is implemented in scenarios where a disparity in size between the features of interest and the spatial resolution of the image exists, where the features are depicted across multiple pixels of data (Blaschke et al., 2014; Lacharité et al., 2015; Zhang et al., 2020). Additionally, seafloor habitats with small and large features that are interwoven together further obstruct effective segmentation of the area using a single scale parameter, requiring the implementation of several scale parameters optimised for each feature (Anders et al., 2011).

Several OBIA approaches have been developed to the production of seabed habitat maps that are separable by spatial hierarchies (Phinn et al., 2012; Janowski et al., 2020). Hence, seabed features such as seabed sedimentary bedforms that occur across a variety of spatial scales can be effectively represented in large scale OBIA mapping efforts (Greene et al., 1999; Koop et al., 2021). Additionally, OBIA has been utilised to effectively map habitats generated by autogenic engineers including CWC mounds within MBES and underwater video data (Conti et al., 2019; Diesing and Thorsnes, 2018; de Oliveira et al., 2021). Thus, indicating the enhanced capacity of this technique to integrate vastly different seabed facies cover types.

1.5. Aims and Objectives of this Research

The aim of this research is to establish a scale robust OBIA framework for the assessment of the seafloor hydrodynamics expressed through SSB evident in MBES data. Specifically, it aims to derive meaningful environmental interpretations from the identification and measurement of SSBs within MBES bathymetric data that have been acquired across a wide range of environmental conditions and gridded across a wide range of spatial resolutions. The research is divided into 3 specific areas of concentrated investigation that are outlined below as chapters. Each of these chapters has been developed as a paper that is *“published”* or is “ under review” with an international peer reviewed scientific journal. Moreover, this research project is aimed to build progressively on each consecutive chapter.

Chapter 2 (**A Scalable, Supervised Classification of Seabed Sediment Waves Using an Object-Based Image Analysis Approach**) develops an OBIA that appraises the ability of four separate machine learning classifiers to characterise seabed sediment waves occurring as high-resolution image features within in two separate spatial resolutions of MBES bathymetry data. As such this chapter answers 3 main research questions:

1. Which classifier provided the most stable classification results for high resolution MBES bathymetry?
2. Which classifier provided the highest accuracy score for the low resolution MBES bathymetry?
3. What implications do these findings have for the suitability of each classifier for a scale standardised object-based technique?

To answer these questions an OBIA was deployed on high-resolution data acquired in Cork Harbour, and low-resolution bathymetry acquired from Hemptons Turbot Bank SAC and offshore South Wexford Ireland. A k-folds cross-validation approach was used to train and assess the accuracy of these classifiers on the higher resolution data. The training and test accuracy metrics for each classifier were compared. The low-resolution data were kept separate from this k-folds cross-validation and a separate set of accuracy metrics were derived from this dataset to determine the precision of each classifier with the coarser resolution data.

Building on the scale-robust OBIA approach to seabed sediment wave characterisation developed in Chapter 2, Chapter 3 (**Characterisation of Benthic Currents from Seabed Bathymetry: An Object-Based Image Analysis of Cold-Water Coral Mounds**) adapted this framework to derive hydrodynamic information from SSBs classified in ROV borne MBES data collected from CWCs habitat in the downslope Moira Mounds. Lim et al. (2018a) successfully deployed the bedform velocity matrix outlined by Stow et al. (2009) on manually acquired wavelengths and wave heights derived from MBES bathymetry data. As such, Chapter 3 aims to answer the following research questions:

1. Can a semi-automated methodology be developed to identify SSBs and separate them based on their inherent morphological features?
2. Can this method be further developed to estimate current speed from bathymetric profiles extracted from MBES data?

3. What do the classified SSB morphologies in combination with the current speed estimates infer about the regional, local, and, micro-hydrodynamics?
4. Does CWC mound proximity influence the velocity of the currents?

To address these research questions, a multiple linear regression was constructed to automate this process and derive current speed estimates from the wavelengths and wave heights derived from the SSBs as part of the OBIA. This workflow was combined with a k-means classification of the morphology of the SSBs to provide information on the current flow velocity and consistency.

Chapter 4 (**Multi-Resolution Appraisal of Cork Harbour Estuary: An Object-Based Image Analysis Approach**) investigated the influence of increasing the resolution of the bathymetry data on the current velocity estimated influence the representation of the tidal regime within Cork Harbour. As such, Chapter 4 aims to answer the following research questions:

1. Can the tidal regime at each sub-site of Cork Harbour be determined?
2. What is the optimum resolution to reconstruct the tidal regime?
3. Do the ARA-derived grain-size measurements help to evaluate the consistency of sediment disturbance due to the influence of the change in tide?

To address these questions the bathymetry acquired in Cork Harbour was resampled to 0.5, 1.0, 1.5, 2.0, and 2.5 m resolutions and current speeds estimations were derived from each resolution of data. ARA of 400 kHz backscatter was derived to determine sediment grain size, and this was used to deduce the degree of sediment disturbance within different sections of the harbour.

Preface to Chapter 2

Chapter 2 seeks to define the optimal OBIA workflow required to classify SSBs This workflow will be flexible to the physical extent of the SSBs. This workflow is further assessed by deploying a series of ML classifiers, to determine the effective representation of these seafloor features.

This chapter was published on the 04/06/2021 in the MDPI journal *Remote Sensing*. *Remote Sensing* has an impact factor of 5.349. To date this publication has received 7 citations according to the Web of Science website.

Summers, G., Lim, A. & Wheeler, A.J. (2021). A scalable, supervised classification of seabed sediment waves using an object-based image analysis approach. *Remote Sensing,* **13***,* 2317. doi: 10.2290/rs13122317

Author Contributions

Gerard Summers and Aaron Lim were responsible for the concept of this study. Gerard Summers and Aaron Lim were responsible for the development of the methodology used within this study. Gerard Summers was responsible for the development of the Python code used in this paper. Validation techniques for this paper were established by Gerard Summers and Aaron Lim. Formal Analysis was completed by Gerard Summers. Investigation of the results was conducted by Gerard Summers. The resources and data curation were organised by Gerard Summers. Writing and preparation of the original draft of the original manuscript was completed by Gerard Summers. The manuscript underwent a single round of corrections from three separate anonymous reviewers. The editing and review of the manuscript were coordinated by Gerard Summers, Aaron Lim, and Andrew James Wheeler. All data visualisation was completed by Gerard Summers. Supervision of the development of this manuscript was completed by Aaron Lim and Andrew James Wheeler. Administration of the project was conducted by Andrew James Wheeler. The funding for this research was acquired by Andrew James Wheeler. All authors have read and agreed to the published version of the manuscript.

Chapter 2. A Scalable, Supervised Classification of Seabed Sediment Waves Using an Object-Based Image Analysis Approach

(Current Status: Published, Remote Sensing, https://doi.org/10.3390/rs13122317)

. **Gerard Summers [1,*], Aaron Lim [2] and Andrew J. Wheeler [1,3]**

1. *School of Biological, Earth and Environmental Sciences/Environmental Research Institute, University College Cork, Distillery Fields, North Mall, T23 N73K Cork, Ireland*
2. *Green Rebel Group, Crosshaven Boatyard, Crosshaven, Co., P43 EV21 Cork, Ireland*
3. *Irish Centre for Applied Geosciences (ICRAG), Marine & Renewable Energy Institute (MaREI), University College Cork, T12 K8AF Cork, Ireland**

Abstract:

National mapping programs (e.g., INFOMAR and MAREANO) and global efforts (Seabed 2030) acquire large volumes of multibeam echosounder data to map large areas of the seafloor. Developing an objective, automated and repeatable approach to extract meaningful information from such vast quantities of data is now essential. Many automated or semi-automated approaches have been defined to achieve this goal. However, such efforts have resulted in classification schemes that are isolated or bespoke, and therefore it is necessary to form a standardised classification method. Sediment wave fields are the ideal platform for this as they maintain consistent morphologies across various spatial scales and influence the distribution of biological assemblages. Here, we apply an object-based image analysis (OBIA) workflow to multibeam bathymetry to compare the accuracy of four classifiers (two multilayer perceptrons, support vector machine, and voting ensemble) in identifying seabed sediment waves across three separate study sites. The classifiers are trained on high-spatial-resolution (0.5 m) multibeam bathymetric data from Cork Harbour, Ireland and are then applied to lower-spatial-resolution EMODnet data (25 m) from the Hemptons Turbot Bank SAC and offshore of County Wexford, Ireland. A stratified 10-fold cross-validation was enacted to assess overfitting to the sample data. Samples were taken from the lower-resolution sites and examined separately to determine the efficacy of

classification. Results showed that the voting ensemble classifier achieved the most consistent accuracy scores across the high-resolution and low-resolution sites. This is the first object-based image analysis classification of bathymetric data able to cope with significant disparity in spatial resolution. Applications for this approach include benthic current speed assessments, a geomorphological classification framework for benthic biota, and a baseline for monitoring of marine protected areas.

2.1. Introduction

Vast amounts of high-resolution multibeam echosounder (MBES) data have been acquired and further are proposed in support of national (e.g., Ireland's INFOMAR (Guinan et al., 2021) and Norway's MAREANO (Thorsnes, 2009) projects) and global mapping efforts (e.g., the Nippon Foundation-GEBCO Project Seabed 2030 (Mayer et al., 2018)). Thus, the need for a standardised classification system to extract meaningful seabed, habitat-relevant geomorphological information from these vast datasets is critical for marine spatial management (Diesing et al., 2014). Seabed habitats are not defined by the traditional frameworks evident in terrestrial habitats, and as such are characterised in terms of seabed geomorphology and sediment composition (Zajac, 2008). As a result, there is a growing interest in establishing the nature of the interaction between seabed geomorphology and biological assemblages (Damveld et al., 2019; Greene et al., 2017). Seabed sediment waves are geomorphological features that affect the distribution of marine biological communities (Damveld et al., 2018). These features have a consistent morphology across a variety of spatial scales and are consequently, depicted across several scales of spatial resolution of data (Brown et al., 2011). As such, they offer an ideal platform for the development of a scalable automated classification scheme (Goodchild, 2011; Brown et al., 2012; Kucharczyk et al., 2020). Object based image analysis (OBIA) provides a method complementary to this goal (Goodchild, 2011), with the pixels aggregated together to create image objects that relate to the physical extent of the target features diametrically to their respective environment (Blaschke, 2010; Phinn et al., 2012; Blaschke et al., 2014; Janowski et al., 2018a; Kucharczyk et al., 2020; Diesing et al., 2016; Ierodiaconou et al., 2018).

Previous seabed habitat mapping efforts have focused on OBIA utilising MBES bathymetric derivatives, or a combination of bathymetric derivatives and backscatter, forming isolated studies that are focused on extracting regional information at a single scale (Lucieer and

Lamarche, 2011; Diesing et al., 2016; Lacharité et al., 2018; Diesing and Thorsnes, 2018; Ierodiaconou et al., 2018). Recent research is looking to incorporate multispectral backscatter information into these classification systems which can help to derive additional information regarding seafloor texture and composition (Janowski et al., 2018b; Brown et al., 2019; Fakiris et al., 2019; Ierodiaconou et al., 2018). Incorporation of multi-source, nonoverlapping MBES backscatter from separate regions in classification schemes is limited as calibration of MBES equipment is not yet widespread (Lurton et al., 2015). This can be further compounded with *ad hoc* data acquisition parameters prioritising the collection of bathymetric data over backscatter data, inhibiting the use of backscatter data in quantitative research (McGonigle et al., 2010a; McGonigle et al., 2010b; Lurton et al., 2015; Hughes Clarke, 2015; Malik et al., 2018; Lacharité et al., 2018). Moreover, the method used to measure backscatter intensity differs between manufacturers, and even between older models from the same manufacturers, and this information is proprietary and is not disclosed to the community (Lamarche and Lurton, 2018). Lacharité et al. (2018) created a classification scheme derived from non-overlapping data derived from uncalibrated surveys, conducted at different frequencies to create a seamless habitat map. However, this research does not account for the effect of backscatter in frequency dependent variable acoustic penetration due to insufficient ground truthing data (Hughes Clarke, 2015). Standardisation of data acquisition is a key component of automated and semi-automated classification techniques and the equivocacy that MBES backscatter affords to any classification system impedes the replication of such schemes elsewhere (Diesing et al., 2016). Furthermore, a consolidated backscatter data infrastructure congruent with the coverage and framework of bathymetric data has not been implemented (Lamarche and Lurton, 2018; Schimel et al., 2018; Koop et al., 2021). Hence, pending solutions to overcome backscatter ambiguity issues, the focus must be maintained on classifying accessible benthic terrain data that remains consistent between separate regions (Koop et al., 2021).

MBES bathymetry is regionally congruous with the accuracy and precision of the data often being maintained to international hydrographic standards (International Hydrographic Organisation, 2020; McGonigle et al., 2010a; Lurton et al., 2015; Eleftherakis et al., 2018). Carefully constructed automated models for the correction of MBES bathymetric errors have been well developed and incorporated into commercial processing software (McGonigle et al., 2010b; Lurton et al., 2015). Therefore, a more uniform classification approach would integrate OBIA with MBES bathymetry to provide a classification system that targets geographic features that occur as high-resolution features across a range of spatial resolutions. Until now, the main constraint preventing this avenue of investigation was the consistency of backscatter data across regions, and a lack of exploration on the effects of spatial resolution on geomorphometric variables (Calvert et al., 2014; Koop et al., 2021). Moreover, contemporary research shows that the spatial resolution of the data employed within these schemes must remain the same, with increases in spatial resolution having a detrimental impact on the accuracy of OBIA classifications (Chen et al., 2018; Kucharczyk et al., 2020). Such studies are conducted on the same remote sensing data, applying image filters to the data at increasing scale intervals to mimic the coarsening of spatial resolution (Powers et al., 2012; Momeni et al., 2016; Liu et al., 2020). This does not account for geomorphological features that can occur across a variety of scales whose relative spatial resolution is dependent on the interplay between the size of the feature and the resolution of the image (Chen et al., 2018; Kucharczyk et al., 2020).

Here, we present a study designed to categorise seabed sediment waves occurring as positive topographic features within MBES bathymetry with bathymetric derivatives only, occurring in two separate spatial resolutions, using a semi-automated OBIA approach. Four separate classifiers were trained on sample objects derived from high resolution (0.5 m pixel size) MBES data acquired in Cork Harbour, Ireland. A k-fold cross validation was used to assess their ability to classify this high-resolution data. These classifiers were then applied to image objects procured from coarser resolution (25 m pixel size) bathymetric data recorded at Hemptons Turbot Bank Special Area of Conservation (HTB SAC) and offshore South Wexford (OSW). This represents a magnitude resolution change of 50 times between the Cork Harbour bathymetry and the bathymetric data acquired from the HTB SAC and OSW. This study is the first to classify geographic features as high-resolution objects across multiple spatial resolutions of data.

2.1.1. Study Sites

The location of the three study sites is shown in Figure 3. Each site was chosen as they present seabed sediment waves occurring at different spatial scales. Site A, Cork Harbour, is a macrotidal harbour, with a maximum tidal range of 4.2 m. It is the second largest estuary in Ireland and one of the largest natural harbours in the world (Nash et al., 2011; Bartlett and Celliers, 2016). A strong tidal current driven by the channelised high tidal range in the harbour induces bedload sediment transport and produces migratory mega-scale bedforms such as sediment waves (Figure 3 A(ii)). Sinuous, bifurcating crests are visible in these asymmetric bedforms throughout the area. The lee side of the sediment waves in this region are orientated to the north–west suggesting that they migrate predominantly with the ebb tide entering the harbour. Sediment waves in this locality range from 0.5–1 m in height with an average wavelength of 10 m, (Figure 3 A (iii)). The sediment at this locality has been cleared of sediment deposits through dredging with a thin veneer of fine to medium sands occurring over the bedrock (O'Toole et al., 2012).

Site B, Hempton’s Turbot Bank Special Area of Conservation (HTB SAC), contains a sediment wave covered sand bank a tidal range of 1.4 m and is located to the north of Ireland, (Figure 3B) (Verfaillie et al., 2007; Wolf et al., 2009). This SAC is designated as a sandbank that is constantly covered by seawater under the EU Habitats (93/43/EEC) in Annex I (National Parks & Wildlife Service, 2015).The offshore sediment waves range from 5–20 m in height (Wallis, 2005), with wavelengths that average 400 m (Figure 3 B(ii)). In the north and west of the area, the sediment waves display asymmetry with the sediment waves facing southeast (Wallis, 2005). The sediment waves change in shape becoming symmetrical in the centre of the region and again are asymmetric in the east of the site, where the lee side of the sediment waves face northwest, bifurcations are more prevalent in the eastern portion of the site (Wallis, 2005). The mobile sediments within these sediment waves generates an active environment apposite for marines species acclimatised to change (National Parks & Wildlife Service, 2014). Sediment grain size at this region is dominated by coarse and medium sand, the biological assemblages found at this location are typical of coarse sediment and include polychaete worms, crustaceans, amphipods, nematodes, and echinoderms (National Parks & Wildlife Service, 2014).

Site C, the offshore South Wexford (OSW) study site can be subdivided into 2 separate regions, the north and south OSW. In the northern portion of the site, the lee sides of the sediment waves are orientated to the south. This is aligned with flood tide of the dominant tidal regime leaving the Irish Sea moving North–South (Van Landeghem et al., 2012), the dominant sediment grain size is a mixture of medium-grained and coarse-grained sands, and can range from fine sands to gravel (Ward et al., 2015). This region contains the Long Bank SAC and a portion of the Blackwater Bank SAC (Figure 3C). Both are designated as sandbanks that are constantly covered by seawater under the EU Habitats (93/43/EEC) in Annex I. High velocity tidal currents occur within the Blackwater Bank SAC, reaching 2 $m \cdot s^{-1}$ (Atalah et al., 2013). The southern portion of the OSW is affected by strong currents that round Carnsore Point as they exit the Celtic Sea and enter the Irish Sea. This region is microtidal with ranges reaching 1.75 m at Carnsore Point and decreases northwards towards a degenerate tidal amphidrome occurring between Wicklow and Cahore Point (Van Landeghem et al., 2009a; Wolf et al., 2009). This contributes to a bimodal distribution of sediment wave asymmetry direction. The sediment waves in the south OSW range in height from 1–12 m and have an average wavelength of 600 m (Figure 3 C(iii)). This wavelength and wave height changes throughout this study area, reducing to an average of 200 m wavelength and 3m wave height to the north–east of line F–F’ (Figure 3 C(ii)). The south–eastern portion of the OSW site contains sediment waves with lee sides inclined to the south. In the South–West OSW, they alter direction. with the lee side of the sediment waves inclined to the north–east. Sediment wave height decreases to the south–west until they cease entirely. Sediment waves in the South OSW have rounded crests and bifurcations throughout the region (Van Landeghem et al., 2009a). Sediment composition to the north of the South OSW are coarse grained sands that grade into fine sands to the south–west of the OSW (Ward et al., 2015).

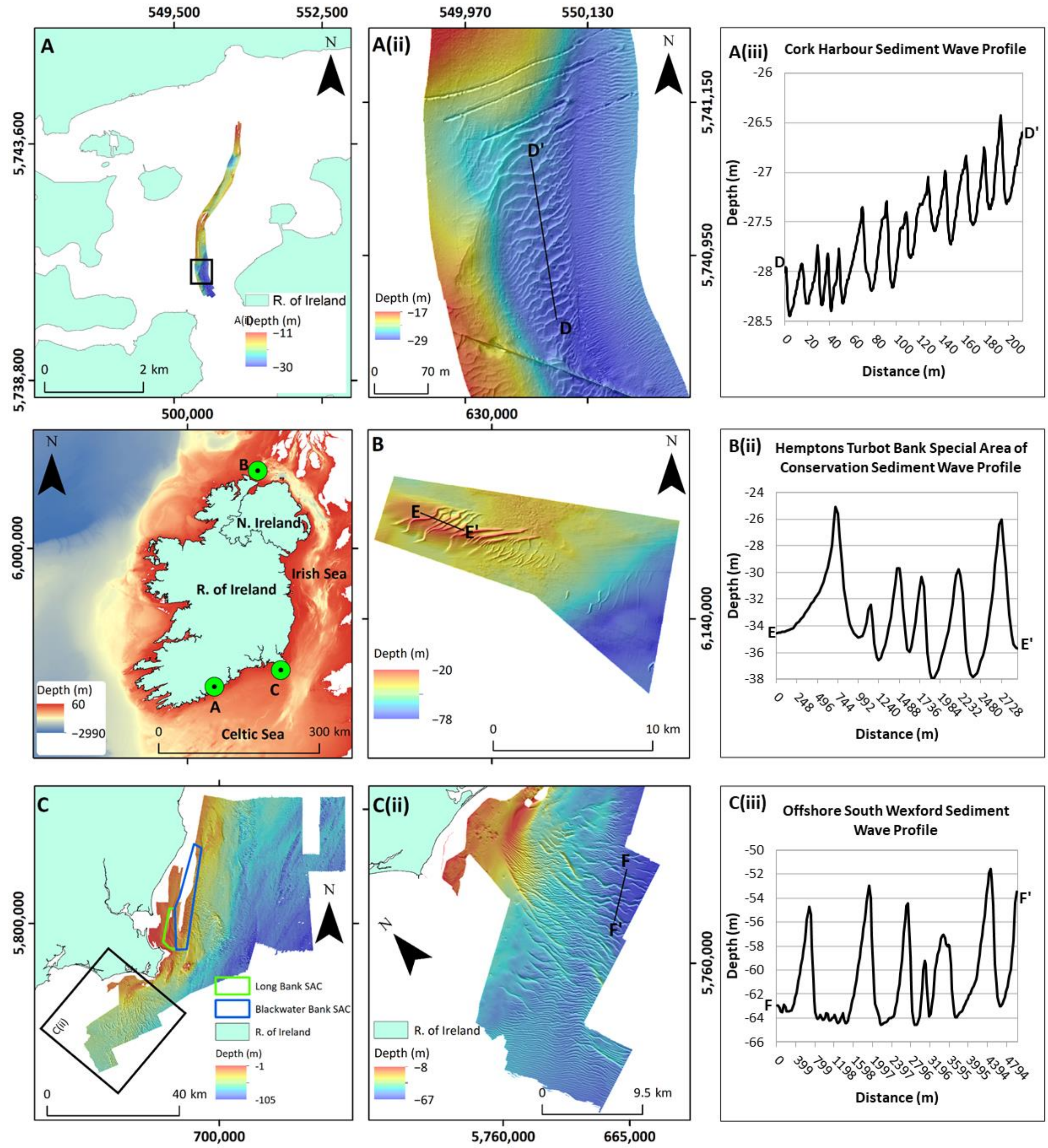

Figure 3: Map showing the location of the three study sites with details of sediment waves imaged with MBES bathymetric data. (**A**) Cork Harbour high resolution bathymetry displaying extent of **A(ii)**; **A**(**ii**)) South Cork Harbour with the line D–D′ for the sediment wave profile in **A(iii)**) (**B**) Hemptons Turbot Bank SAC low resolution bathymetry (acquired from EMODnet) with the line E–E′ for the sediment wave profile in **B(ii)**; (**C**) Offshore South Wexford (OSW) low resolution bathymetry (acquired from EMODnet) displaying extent of **C(ii)** (in black) and the extent of the Blackwater Bank SAC and the Long Bank SAC, (**C(ii)**) South–West OSW with the line F–F′ for the sediment wave profile in **C(iii)**.

2.2. Materials and Methods

2.2.1. Multibeam Echosounder Data and Processing

In Cork Harbour, data were collected in 2018 with a Kongsberg EM2040 MBES operating at a frequency of 400 kHz on board the RV Celtic Voyager in a series of slope-parallel lines. The along-track beam width used was 2° and the across-track beam width was set at 1.5°. The beam mode was set to short continuous wave. The swath was maintained at an equal angle of 65° either side of the sonar head. Sound velocity profiles were recorded and applied to the raw data during acquisition. A speed of four knots was maintained throughout the survey and data were managed and monitored using Seafloor Information Systems (SIS). Raw data were stored in *.all file format and imported into Qimera where tidal corrections were applied from the tide gauge at Ringaskiddy. This tidal gauge occurs 4 km upstream from the study site. The swath editor in QPS's bathymetric processing suite Qimera was used to remove data anomalous data spikes via operator supervision(QPS, 2019b). The cleaned data were gridded at a 0.5 m resolution and then exported in an ArcGRID *.asc file format.

High resolution bathymetric datasets were acquired from the EMODnet bathymetric data portal for the OSW and HTB SAC sites as *.emo files and were uploaded into Qimera and gridded at a 25 m resolution(EMODnet Bathymetry Consortium, 2020; QPS, 2019b). These data were exported in an ArcGRID *.asc file format. The datasets downloaded from EMODnet for each region are specified in Table 1.

Table 1: Datasets acquired from the EMODnet bathymetry data portal, including the original name of each file as designated on the EMODnet bathymetry data portal (EMODnet Bathymetry Consortium, 2020).

EMODnet Dataset Name	Corresponding Region	Resolution (m)
CV16 CelticSeaIreland 14m	South–West Offshore South Wexford (OSW)	25
HRDTM IrishSeaWexford 14m	North–East OSW	25
366_NorthAtlanticOceanDonegal	Hemptons Turbot Bank Special Area of Conservation (HTB SAC)	25

All bathymetric datasets were imported into ArcGIS 10.6 to extract image derivatives recommended by Diesing et al. (2016) and Diesing and Thorsnes (2018). The bathymetric position index (BPI)(Wilson et al., 2007), zeromean, and relative topographic position (RTP) layers were created using Equations 1–3 below:

$$BPI = Zgrid - focalmean(Zgrid, circle, r) \quad (1)$$

$$Zeromean = Zgrid - focalmean(Zgrid, square, r) \quad (2)$$

$$RTP = \frac{Zgrid - focalmean(Zgrid, square)}{focalmax(Zgrid, square, r) - focalmin(Zgrid, square, r)} \quad (3)$$

where *Zgrid* is the bathymetric data (Wilson et al., 2007). The *focalmean*, *focalmax*, and *focalmin* calculate the mean, maximum, and minimum respectively of the bathymetric data within a circle of radius *r*, or a square with sides of length *r*. These image derivatives were generated using the focal statistics tool in the neighbourhood toolset in combination the raster calculator tool in the map algebra toolset in the spatial analyst toolbox in ArcGIS 10.6.

The remaining derivatives, or image layers, were generated using the benthic terrain modeler 3.0 toolbox in ArcGIS 10.6 (Walbridge et al., 2018). The scale indicated for the BPI layers in Table 2 represents the radius of the circle used to determine the pixel neighbourhood in the focal statistics tool. The remaining layers were derived using a square pixel neighbourhood, with the scale indicating the height and the width of the square used.

Table 2: Bathymetric derivatives extracted at each site. * Variable directly used in segmentation process.

Bathymetric Derivatives	**Scale (pixels)**
Aspect	3
Bathymetric Position Index (BPI)*	3, 5*, 9, 25
CosAspect (Northness)*	3
Curvature	3
Planiform Curvature	3
Profile Curvature	3
Relative Topographic Position (RTP)	3
SinAspect (Eastness)*	3
Slope*	3
Vector terrain Ruggedness (VRM)*	3, 5*, 9, 25
Zeromean	3, 9

2.2.2. Object Based Image Analysis

2.2.2.1. Segmentation

Segmentation is an important component in OBIA and is often the first step in OBIA workflows (Kucharczyk et al., 2020). During this process, the image is separated into distinct regions of consistent image values forming segments or image objects (Lang, 2008). The multiresolution segmentation algorithm — in Trimble's image processing suite eCognition Developer v10.0 — generates image objects by aggregating adjacent pixels together until they reach a homogeneity threshold (Lacharité et al., 2018). Thus, maximum permitted heterogeneity has been achieved, as defined by the scale parameter (Diesing and Thorsnes, 2018). Furthermore, the influence of object shape and the pixel value is constrained by the shape parameter (Trimble, 2014), and the smoothness of the segments produced by the algorithm is controlled by the compactness factor (Trimble, 2014). An ideal scenario is where a single segment directly corresponds to the physical extent of the geographical feature of interest (Gao et al., 2011; Johnson and Xie, 2011; Hossain and Chen, 2019). During the initial segmentation, this is often not the case, resulting in over- or under-segmentation (Marpu et al., 2010; Johnson and Xie, 2011). Several algorithms in the eCognition Developer suite are used to refine segments produced during the early stages of OBIA either through separation or amalgamation. The spectral difference algorithm combines image objects if the difference between the mean image layer intensities is below a user-defined value (Trimble, 2014). A class can be assigned to segments whose criteria meet a set of conditions via the assign class algorithm. This classification can be used within eCognition to target specific image objects during the refinement of the segmentation (Trimble, 2014). The boundaries for the preliminary image objects can be expanded or contracted to create a more appropriate representation of the feature of interest (Wu et al., 2014). eCognition offers algorithms that can extend the coverage of a classified object until an image layer threshold is met, or until a specific object geometry is achieved (Johansen et al., 2011).

A series of image layers may display a relationship that can highlight features of interest when they are arranged in the 3 bands available to digital imagery (red, green, blue or RGB). Performing a colour transformation such as a hue-saturation-intensity (HSI) transformation separates the intensity from the colour information, the hue and saturation (Jensen, 2005). Hue represents the wavelength of the dominant colour; saturation is the purity of this dominant colour. The shapefiles representing the HTB SAC and OSW datasets were clipped to focus on the sites of interest (see supplementary information). The layers included within the segmentation process were sinaspect (Eastness), cosaspect (Northness), BPI5, slope, and VRM5.In this study, the segmentation process was applied over a series of phases at each study site (Figure 4).

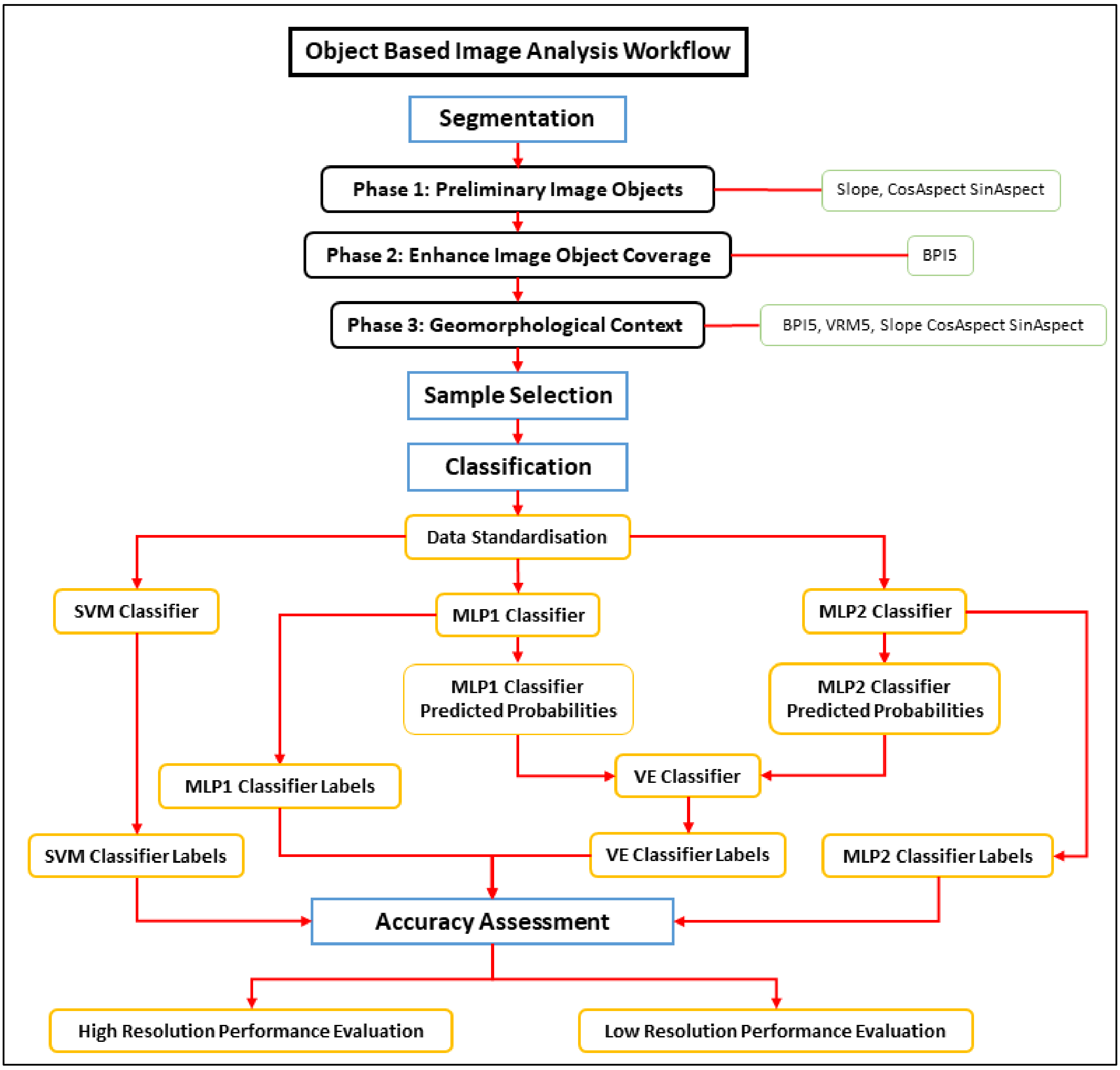

Figure 4: Workflow chart for the object-based image analysis (OBIA), with the image layers used in each phase of segmentation outlined in green.

The parameters for each algorithm applied at each phase were determined through trial and error. Each image layer listed in Table 2 was imported into eCognition Developer working environment, excluding the VRM9 and VRM25 image layers as the inclusion of these layers resulted in the creation of square artifacts during segmentation.

Phase 1 of the segmentation was designed to target regions that potentially represented sediment waves. In this instance, they are defined as truncated objects with a high slope value, that are delineable by a common slope direction. To complete this phase, 3 separate algorithms were required; the multiresolution segmentation, spectral difference segmentation, and assign class algorithms. The multiresolution segmentation algorithm was deployed on the sinaspect and cosaspect image layers. A scale parameter of 3, a compactness of 0.1, and a shape of 0.1 were chosen. The segments produced were refined using the spectral difference algorithm on the mean sinaspect and cosaspect value stored within the image objects, the maximum spectral difference was 0.3. These 2 algorithms were designed to delineate truncated objects in the sinaspect and cosaspect image layers with a common slope direction. A "sediment waves" class was assigned to potential sediment wave image objects using the assign class algorithm. A HSI colour transformation was applied as part of this classification, where the slope, sinaspect and cosaspect were arranged as a red, green, and blue (RGB) 3-band composite band image (Figure 5A). The mean hue for each image object was derived from this 3-band composite image and any segment with a hue of ≥0.9 and a border length/area ≥0.35 were assigned to sediment waves. This hue value represents regions where the dominant colour is red, thus providing image objects with a high slope value and a common slope direction. Sediment waves are bathymetric features with a high border length relative to the area that they encompass when analysed in plan view. Therefore, the border length/area selected prevents the inclusion of objects that have a high area value relative to their border length. This process was repeated with the RGB colour arrangement was set at slope as red, cosaspect as green, and sinaspect as blue. All image objects with a hue of ≥0.9 and a border length/area of to ≥0.5 were assigned to the "sediment waves" class. The final part of the first phase classified any objects with a border length/Area of ≥0.5 pixels and a length/width of ≥6.5 to the sediment waves class. This was to ensure that geographically isolated sediment waves that occur apart from the main wavefields at each locality were captured (Figure 5B).

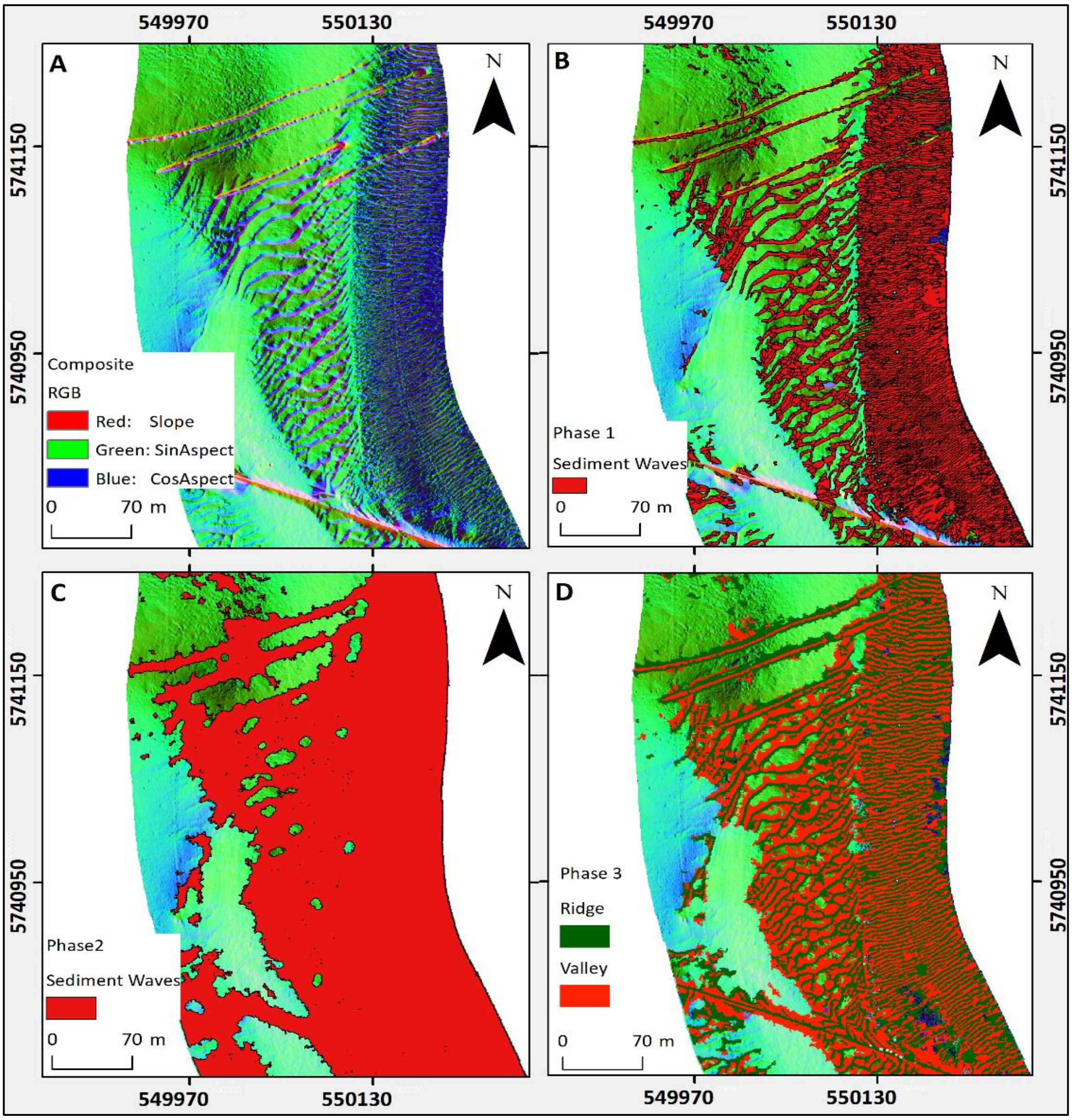

Figure 5: An example of (**A**) A red, green, blue (RGB) 3 band composite image of slope (R), sinaspect (G), and cosaspect (B) derived from the bathymetry at Cork Harbour; (**B**) the product of the first phase of segmentation; (**C**) the product of the second phase of segmentation and (**D**) the product of the third phase of segmentation.

The second phase of the segmentation ensured that the "sediment waves" image objects encompassed the full extent of the lee and stoss side of each sediment wave. Each image object in this class was first merged with all neighbouring "sediment waves" image objects using the merge object algorithm. The BPI5 image layer was determined to be the variable that provided the most accurate extent of the sediment waves at each study site (Wilson et al., 2007; Diesing and Thorsnes, 2018). This image layer depicts positive bathymetric features with a positive value and negative bathymetric features with a negative value, flat bathymetric features have a value of ~0 m. Therefore, this was the image layer used in combination with the pixel-based object resizing algorithm to enhance the coverage of the "sediment waves" image objects (Johansen et al., 2011). A proportion of the standard deviation of the BPI5 image layer in each instance was used to define the boundary threshold for the "sediment waves" troughs and crests; thus, providing a standardised value that is not bespoke to one dataset. The pixel-based object resizing algorithm was implemented to grow all "sediment waves" image objects until a threshold of >37.5% of one standard deviation of the BPI5 image layer was reached (Johansen et al., 2011). This corresponds to the boundary threshold for the crests as positive bathymetric features. This algorithm was deployed a second time to grow all "sediment waves" class objects until a threshold of <-37.5% of one standard deviation of the BPI5 image layer was attained. This corresponds to the boundary threshold for the troughs as negative bathymetric features. The third application of the algorithm shrank any "unclassified" inset image objects that occurred within the "sediment waves" image object (Wu et al., 2014). This was done using the candidate surface tension parameter, which uses a square defined in image pixels by the user, to delineate the relative area of classified objects (Trimble, 2020). Once the relative area of the "unclassified" object was greater than 40% of the area contained within the square, then it would remain unchanged (Trimble, 2020). However, if the area was less than 40%, the "unclassified" image object would shrink and any pixels removed would be reclassified to a new "flat" class (Johansen et al., 2011). The objects within this new class would be assessed to determine if they shared a significant portion of their border with the "waves" class object and if they have a lower border length to area ratio. If the proportion of the inset image object border shared with "sediment waves" image objects is ≥65% and the border length/area for this inset image object is ≥ 0.35 then it will be classified as a "sediment waves" image object. Any image objects that are classified as "flat" are redesignated as "unclassified". It is important to note that the pixel-based object resizing algorithm grows or shrinks the image objects by one row of pixels at a time (Johansen et al., 2011). The growth/contraction of each image object will cease once the specified threshold has been met. To ensure that the thresholds are met for each image object, this algorithm is repeated for 200 iterations. The standard deviations for the BPI5 image layer for each study site were generated individually in Python 3.7. These figures were not standardised and are unique to each study site (Figure 5C).

Phase 3 of the segmentation process used the multi-threshold algorithm to further segment the regions contained within the image objects classified as "sediment waves". This algorithm uses the pixel values from a given image layer — in this case the BPI5 image layer— and thresholds the data into segments (Witharana and Lynch, 2016). A classification can simultaneously be applied to image objects produced by this algorithm (Witharana and Lynch, 2016). The algorithm was deployed with a series of thresholds and segmented the pixel values of the regions contained within the “sediment waves” image objects (Witharana and Lynch, 2016). Damveld et al. (2018) reported that biological assemblages were more abundant in sediment wave troughs than they were at sediment wave crests. Hence, obtaining this geomorphological context within each “sediment waves “image object is vital to delineating biological assemblage occurrence in seabed sediment waves. BPI provides an opportunity to apply geomorphological context to the “sediment waves” image objects. Positive BPI values indicate relative bathymetric highs where the pixel is greater than the mean of the neighbouring pixels within a circle of radius r, Equation 1 (Wilson et al., 2007; Secomandia et al., 2017). Whereas negative BPI values indicate bathymetric lows where the pixel value is lower than the mean of the neighbouring pixels within a circle with radius r, Equation 1 (Wilson et al., 2007; Secomandia et al., 2017). In this study, we define all bathymetric highs or “ridges” as any region occurring within an image object classified as “sediment waves” with a BPI5 value of >25% of a standard deviation of the BPI5 image layer. Any area within an image object classified as “sediment waves” and has a BPI5 value of <-25% of a standard deviation of the BPI5 image layer is described as a topographic low or “valley”. Additionally, regions with a BPI5 value of <25% or >-25% of a standard deviation of the BPI5 image layer are described as “Unclassified”. The thresholds employed in this algorithm were derived using technique as outlined in phase 2. −

A minimum object size can be defined in the multi-threshold algorithm to prevent over-segmentation, this was set at 50 pixels. Any “ridge” or “valley” image objects with a mean VRM5 value of ≥12.5% or ≤-12.5% of a standard deviation of VRM5 were redesignated as “unclassified”. For the low-resolution data, this threshold was altered to ≥25% or ≤-25% of a standard deviation of VRM5 to eliminate image objects that included bedrock. The “ridge” and “valley” class objects were reassigned to the “sediment waves” class. The pixel-based object resizing algorithm was applied to shrink any image objects designated as “unclassified” that were inset to the image objects classified as “sediment waves”. Once this had been completed the multi-threshold algorithm was reapplied to the “sediment waves” image objects, thus, recreating the “ridge” and “valley” class objects using the same thresholds for the BPI5 image layer as outlined at the beginning of phase 3. Any regions that occurred within the “sediment waves” image objects that did not occur within the range of values to be designated as either “ridge” or “valley” were classified as “flat”. The remaining “unclassified” image objects were redesignated as “flat”. The multiresolution segmentation algorithm was then applied separately to the “ridge” image objects and the “valley” image objects. In both iterations the algorithm was applied to the cosaspect and sinaspect image layers, with a scale parameter of 4, a shape factor of 0.1, and a compactness factor of 0.1. The spectral difference algorithm was applied separately to the “ridge” class objects and the “valley” class objects. The algorithm was maintained to the sinaspect and cosaspect image layers. The maximum spectral difference was maintained at 0.3 (Figure 5D). This value ensures that neighbouring image objects representing slopes with a common slope direction are merged, excluding image objects representing slopes with a significantly different orientation.

2.2.2.2. Sample Selection

Once segmentation was completed, 4 new classes were created to describe the 2 sides of sediment waves within the geomorphological context developed in the segmentation process. The classes created were “Upper Lee”, “Lower Lee”, “Upper Stoss”, and “Lower Stoss”. The “Upper Lee” and “Upper Stoss” classes reflect the opposing sides within the image objects previously classified as “ridge”. The “Lower Lee” and “Lower Stoss” classes reflect the opposing sides of the image objects previously classified as “valley”. Samples were evaluated on the relationship of each object to the neighbouring “ridge” and “valley” objects to determine whether the object occurred on the steeper lee side of a sediment wave, or if it was part of the more gradual stoss side of a sediment wave. The criteria used to make this decision were the mean values of slope, aspect of each object. If a “ridge” image object had an adjoining “ridge” image object that had a lower mean slope value, and the mean aspect of this adjoining “ridge” image object indicated that it was facing in a different direction. Then the first “ridge” image object would be deemed to occur on the steeper lee side of the sediment wave and classified as “Upper Lee”. It would then be deduced that the second “ridge image object occurred on the stoss side of the sediment wave and would be classified as “Upper Stoss”. The classification of the “valley” objects would be determined by the neighbouring “ridge” image object.

Six hundred samples were chosen at the Cork Harbour study site (150 per class). At the OSW site 1444 samples were obtained (361 per class), class samples were kept at an equal number at each study site to ensure that any resultant accuracy metrics were balanced. One thousand and eighty samples were selected for the southern portion of the OSW site (270 per class). As the southern portion of the OSW site displayed a bimodal distribution of sediment wave direction the data was separated once more using mean aspect. Any object with a mean aspect in the range of 0–160° was partitioned into the South–West OSW dataset. Any object with a mean aspect in the range of 161–330° was placed into the South–East OSW dataset. The samples for each class were not equally distributed within either dataset, so each set of samples were subset to balance the class distribution. The SW OSW dataset had 628 samples, and the SE OSW dataset had 428 samples. 364 samples were selected in the Northern section of the site (91 per class). 56 samples were attained at the HTB SAC (14 per class). Upon completion of the selection process the image objects were exported as a shapefile. 16 image derivative variables were derived by acquiring the mean for each variable — outlined in Table 2 — in eCognition Developer. Object geometries values asymmetry, length/width, and border length/area were included in this export. The shapefile was imported into ArcGIS 10.6 to add the mean values for the VRM9 and VRM25 image layers for each image object.

2.2.2.3. Classification

On completion of segmentation, selection processes and extraction of the appropriate image object attributes, the data were imported into Jupyter Notebook through the GeoPandas library (Jordahl, 2014). Any image objects that were classified as “flat” were excluded from the machine learning workflow. Image objects that were classified as either “ridge” or “valley” were reclassified in the machine learning workflow to one of the new classes outlined in Section 2.2.2.1. All data were standardised through the preprocessing module of sklearn (Pedregosa et al., 2011). The samples selected from the training data from Cork Harbour were used as the reference range for the data standardization. The data derived from the OSW and HTB SAC sites were standardized with reference to the range of data found within the Cork Harbour sample data.

Each classifier deployed has a series of settings, or hyper parameters, most of which are unique to each classifier. These hyper parameters are adjustable and provide the opportunity to improve accuracy results and prevent overfitting to the training data. A hyper parameter tuning workflow was established within python to iteratively adjust a single hyper parameter for a single classifier, the accuracy results for this adjusted classifier were then attained. The configuration of hyper parameters that yielded the highest aggregated accuracy result was the final configuration chosen for deployment across all sites. This process was repeated for each classifier included in this study. The Ray module was implemented in this workflow to enable parallel processing across multiple cores on the same processor (Moritz et al., 2018), in this case an Intel i7-8750H. The number of hyperparameter changes enacted during this process vary between each classifier. This is due in part to the bespoke settings and to the contrasting complexities of each classifier.

2.2.2.3.1. Classifiers

The 4 classifiers employed were LinearSVC (SVM), two Multilayer Perceptrons (MLP and MLP2), and Voting Ensemble (VE) algorithms, all found within the scikit-learn library in Python 3.7 (Pedregosa et al., 2011). Each are listed in increasing order of model complexity.

The LinearSVC is a support vector machine (SVM) classifier and is frequently used in the machine learning community (Jozdani et al., 2019; Kucharczyk et al., 2020). SVMs classify data by defining the optimal separation for hyperplanes for each feature included in the classification (Cortes and Vapnik, 1995). Classifications utilising SVMs generalize well to new data, including in studies where the training data is limited (Dixon and Candade, 2008; Wicaksono et al., 2019; Liu et al., 2019b). However, SVMs are not suitable when data are noisy and highly dimensional (Mountrakis et al., 2011). The main hyper parameters reviewed for this classifier were the normalization used in the penalty, the optimization process enacted optimization (dual), the margin of tolerance (tol), the regularization parameter (C), and the loss function (loss). The randomly generated seed value (random state) was set to ensure repeatable results. In this study, the penalty was set at L1, the dual was set at False, the tol was set at 0.1, the C was set at 100, the loss was set at squared hinge, the random state was set at 57. The remaining hyper parameters were maintained at the default setting.

The Multilayer Perceptron (MLP) classifiers are artificial neural networks (ANN), each network is composed of a series of layers: an input layer, one or more hidden layers, and an output layer (Jozdani et al., 2019). Each hidden layer is made up of a series of neurons interconnected by weights (Zhong et al., 2019; Conti et al., 2019; Jozdani et al., 2019). These neural layers were inspired by the neural mechanisms present in biological nervous systems

(Mas and Flores, 2008; Conti et al., 2019) These weights are altered via an automated optimization process during the training of the classifier (Jozdani et al., 2019). The complexity of the MLP classifier is determined by the number of layers and the number of neurons contained within these layers (Zhong et al., 2019). Altering the neuron configuration within these hidden layers can have a significant effect on the performance of this algorithm (Sheela and Deepa, 2013). For example, increasing the complexity of the MLP classifier by increasing the neurons in each layer or increasing the number of hidden layers can lead to the increasing probability of overfitting to the training data (Jozdani et al., 2019). Several hyper parameters may be adjusted to prevent overfitting and increase the efficacy of the classifier (Zhang, 2019). The hyper parameters adjusted during this study were the number of hidden layers and the number of neurons contained within each layer, the learning rate initiation value, and the regularization penalty (alpha). The remaining hyper parameters were maintained at their default settings with the seed point (random state) being set to provide repeatable outputs. The first MLP classifier used within this study (MLP1) contained 4 hidden layers containing the following configuration of neurons; 22, 20, 16, 8. The alpha for this classifier was set at 0.001 and the learning rate initiation was set at 0.01, with a seed point set at 396. The second MLP classifier (MLP2) also had 4 hidden layers with a neuron configuration of; 20, 22, 22, 20. The alpha was set at 0.1, the learning rate initiation was set at 0.001 with a seed point of 173.

Voting ensemble (VE) classifier combines multiple classifiers to create a single classifier, where each classifier has a weighted vote for an unknown input object whilst disregarding the performance of the original classifier (Jony et al., 2018; Zhang, 2019). The class of the output object is determined by a majority vote, which can be achieved either through a soft vote or a hard vote. Hard votes use the class label output from each classifier and the class with the majority across all classifiers is used (Jony et al., 2018). Soft votes occur where each classifier inputs a probability for each candidate class for each image object (Saqlain et al., 2019). The candidate class with the greatest amalgamated probability is the resultant label for that image object (Saqlain et al., 2019). The VE algorithm employed in this study consisted of the MLP1 and MLP2 classifiers. The voting scheme employed within this model was the soft voting scheme and the weights for the input classifiers were 1:1. All python code used to implement this classification is uploaded to a public GitHub repository titled ScaleRobustClassifier.

2.2.2.4. Accuracy Assessment

The accuracy of each classifier was determined by assessing their ability 1) to assimilate the pattern within the data and classify new information at the same resolution as the training data, 2) to categorise data at lower spatial resolution acquired at separate study sites. Samples were selected in the Cork Harbour dataset to train the classifiers. A k-fold cross validation was deployed on these training samples to assess ability 1. A second set of samples were derived from the OSW and HTB SAC study sites to assess ability 2.

2.2.2.4.1. K-Fold Cross Validation

K-fold cross validation permits the assessment of each algorithm's aptitude in extracting the pattern from subsets of the sample data. This technique resamples the reference data into a training subset and a test subset (Zhang, 2019). The classifier is fitted to the training subset and is then deployed on the test subset. The resultant classes for the training and test subsets are compared with the user defined labels and an accuracy score is acquired for both subsets. Resampling of the reference data is repeated k times, and the train and test accuracy is noted each time. The proportion for training and test subsets is maintained across all folds at 90% train data and 10% test data. Once completed, a mean of the accuracy scores can be drawn and the classifier with the lowest variance between train and test accuracy scores is deemed to have the most stable output. Retaining the desired pattern at each iteration of the reference data and reducing the impact of overfitting (Jozdani et al., 2019).

The trained model is then applied separately to the training and test subsets. For each algorithm, the mean training Cohen's kappa coefficient (K-score), mean training accuracy score, mean test accuracy score, and mean test K-score across the k-folds were derived. The mean difference between the training and test K-scores, and the mean difference between training and test accuracies were then used to determine the algorithm with the greatest classification stability. Sklearn's StratifiedKFold tool (Pedregosa et al., 2011) from the model_selection module was used to provide a stratified 10-fold cross validation of the Cork Harbour data. StratifiedKFold ensures that the samples included in each training and test fold unique from each previous iteration of the validation and that sample numbers between classes are kept equal. A full copy of the code used to create the classification and the accuracy assessment is included within the GitHub repository ScaleRobustClassifier.

2.2.2.4.2. Hemptons Turbot Bank Special Area of Conservation (SAC) and Offshore South Wexford Test Data

Samples derived from the HTB SAC and OSW study sites were used to measure the proficiency of each classifier at identifying the classes in 25 m spatial resolution data. This validation was conducted to appraise the stability of accuracy of each classifier to categorise data at coarser spatial resolutions and to classify sediment waves occurring at different orientations. All 600 samples selected in Cork Harbour were used to train the model for each classifier.

2.3. Results

2.3.1. Segmentation

The segmentation derived 24426, 1353, and 47740 objects in the Cork Harbour, HTB SAC, and OSW study sites, respectively. Average image object size for the Cork Harbour study site was 29 m^2, 55,000 m^2 for the OSW study site, and 88,000 m^2 for the HTB SAC study site.

2.3.2. High Resolution Performance Evaluation

The SVM classifier had the lowest difference between the mean training and test kappa score and the training and test accuracy, followed by the MLP2 model and then the MLP1 model (Figure 6).

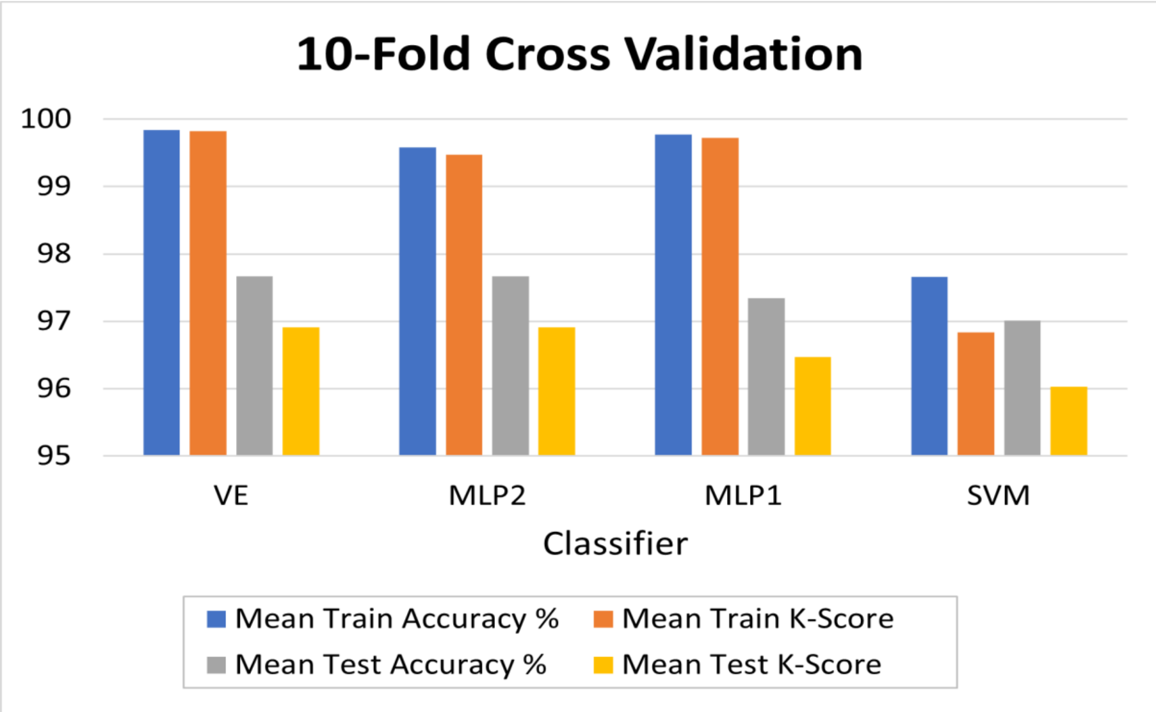

Figure 6: K-Fold Cross validation mean train and test, accuracy, and K-scores for the VE, MLP2, MLP1 and SVM classifiers.

Therefore, the SVM has the least variance between the training and test accuracy scores. The model with the highest mean test accuracy and K-score was achieved by the VE and MLP2 classifiers, followed by the MLP1 algorithm. The VE classifier sustained the highest mean train accuracy and K-scores and the SVM model the lowest for the cross validation. The SVM model also had the lowest mean training accuracy at 97.66% of each model and the lowest mean train K-score at 96.84. This classifier displayed the highest standard deviation between folds for the train and test accuracy score, K-score, and mean train and mean test accuracy difference and K-score difference (Table 3).

Table 3: Cross validation train accuracy (Train Acc), test accuracy (Test Acc), train and test accuracy difference (Acc Score Diff), train K-score, test K-score, and train and test K-score difference summarised across all 10 folds.

Model	Statistic	Train Acc Score	Test Acc Score	Acc Score Diff	Train K-score	Test K-score	K-score Diff
SVM	Mean	97.66	97.01	1.57	96.84	96.03	2.10
	St Dev	0.25	2.18	1.59	0.31	2.92	2.15
MLP2	Mean	99.58	97.67	2.23	99.47	96.91	2.98
	St Dev	0.23	1.60	1.34	0.33	2.14	1.78
VE	Mean	99.84	97.67	2.27	99.82	96.91	3.00
	St Dev	0.21	1.60	1.50	0.24	2.14	2.03
MLP1	Mean	99.77	97.34	2.48	99.72	96.47	3.29
	St Dev	0.34	1.39	1.37	0.43	1.87	1.84

The MLP1 classifier exhibited the lowest standard deviation in test accuracy and K-scores between folds at 1.39 percentage points and 1.87 percentage points, respectively. The VE and MLP2 classifiers had the second lowest standard deviations for test accuracy and K-scores. The VE classifier had the lowest standard deviation in training accuracy and K-scores between folds at 0.21 and 0.24, respectively. The variation in mean test and train accuracy scores between classifiers is low with the greatest difference occurring between the SVM and VE classifiers at 2.11 percentage points. A difference of 0.66 percentage points was observed in the mean test accuracy between the SVM and VE classifiers. This is the largest discrepancy between the mean test accuracies between classifiers in this study.

2.3.3. Low Resolution Performance Evaluation

For the data acquired in the overall OSW study site, the VE algorithm achieved the highest figures for the accuracy and K-score (Figure 7). Attaining an accuracy of 71.75% and a K-score of 62.33 for the 1444 samples. The lowest accuracy and K-scores for this classifier was found at the northern portion of the study site at 66.48% and 55.31, respectively. Similar decreases in accuracy and K-score were seen in the MLP1, MLP2, and SVM classifiers in this region. The SVM classifier achieved the highest accuracy score at the HTB study site with an accuracy of 75% and a K-score of 66.67. However, the SVM classifier achieved the lowest accuracy score and K-score for the overall OSW study site at 68.28% and 57.71, respectively.

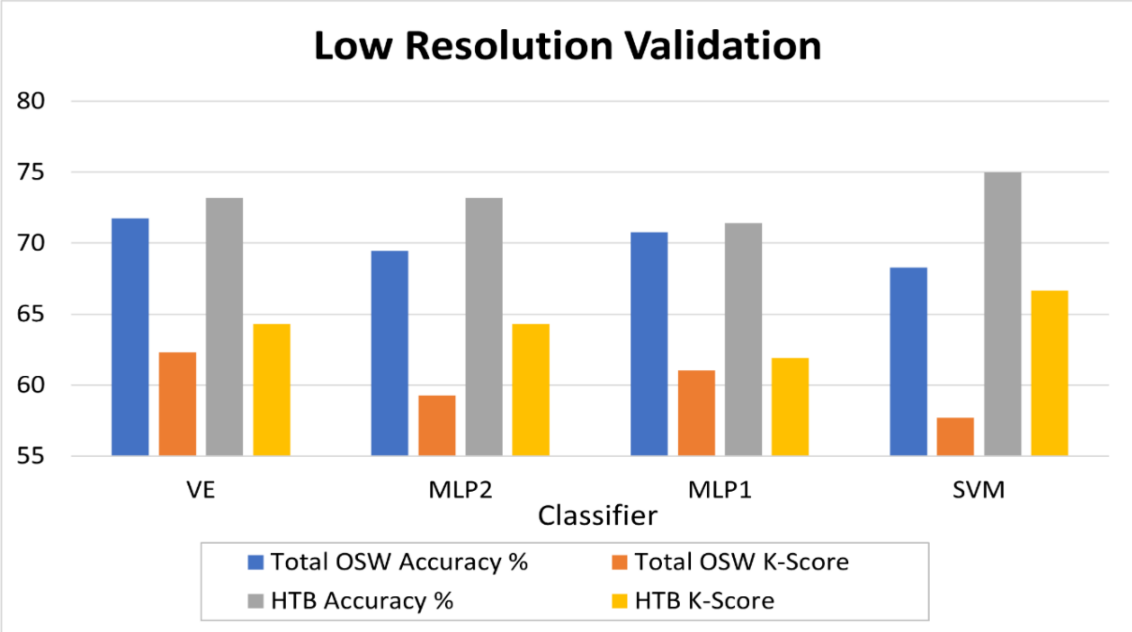

Figure 7: Accuracy and K-scores for each classifier for the OSW and HTB sites.

When examining the confusion matrices of the VE algorithm at each site (Figure 8 and Figure 9), the largest misclassification occurs when differentiating the “Lower Lee” class and “Lower Stoss” class. The “Upper Stoss” and “Upper Lee” classes exhibited a consistently lower misclassification score than that of the “Lower Lee” and the “Lower Stoss” classes. Considering the figures for the “Upper Lee” and the “Upper Stoss” classes, the average accuracy for the VE classifier at the overall OSW site increases to 73.27%, for the HTB SAC site the VE classifier’s accuracy would increase to 75.00%. Most of this accuracy increase is seen in the sites that achieved the lowest accuracy scores, such as the N OSW and SE OSW site, with improved accuracy scores of 70.33%. and 72.43% respectively (Table 4).

Table 4: The accuracy and K-scores for each of the North OSW (N OSW), the South–East OSW (SE OSW), and the South–West OSW (SW OSW) subset sites.

Model	North-OSW	South-East OSW	South-West OSW
SVM Accuracy (%)	62.36	65.89	73.28
SVM K-score	0.50	0.55	0.64
MLP2 Accuracy (%)	65.11	62.62	75.48
MLP2 K-score	0.53	0.50	0.67
VE Accuracy (%)	66.48	67.06	76.43
VE K-score	0.55	0.56	0.69
MLP1 Accuracy (%)	65.66	67.99	74.52
MLP1 K-score	0.54	0.57	0.66

The lowest accuracy score for the VE classifier occurred within the northern section of OSW. This algorithm attained the highest accuracy in the south–western portion of the OSW site where the accuracy is 76.43%. A slight increase in accuracy can also be observed here when the results for the Lower Stoss and Lower Lee classes are removed, bringing the score up to 76.75%. Comparable improvements in accuracy can be observed in the other classifiers, for instance in the northern OSW site the MLP2 classifier increases in accuracy to 72.53% when excluding the results from the Lower Stoss and Lower Lee classes. However, the increases for this algorithm are not consistent at each location, for example in the south–west portion of the OSW site the accuracy decrease to 71.66%. The MLP2 classifier is also the only algorithm to misclassify a Lower Stoss or Lower Lee class object Upper Stoss, as seen in the HTB SAC confusion matrix for this classifier in Figure 9.

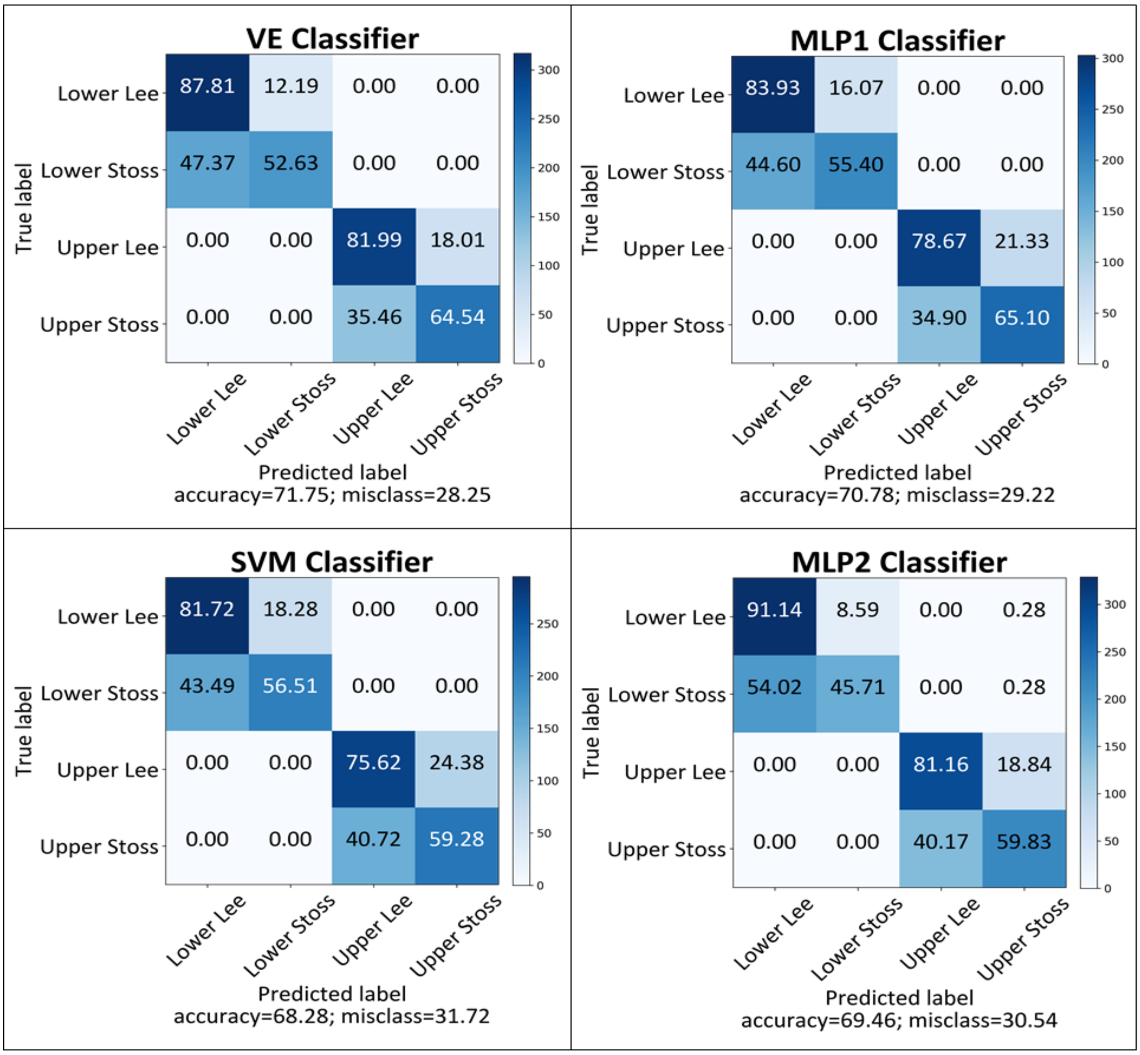

Figure 8: Confusion matrices for the VE, MLP1, SVM, and MLP2 classifiers derived from the overall OSW site.

The MLP1 classifier displayed a similar pattern at each site to the VE and MLP2 algorithms, with an increase in accuracy once the results for the “Lower Stoss” and “Lower Lee” were excluded. This increase is not equal to the increase in accuracy seen in the VE classifier at each low-resolution location. For example, when applying this technique in the northern section of the OSW the accuracy increase is 0.82 percent points, in comparison with the 3.85 percentage points and the 5.34 percentage points augmentation in the VE and MLP2 algorithms, respectively.

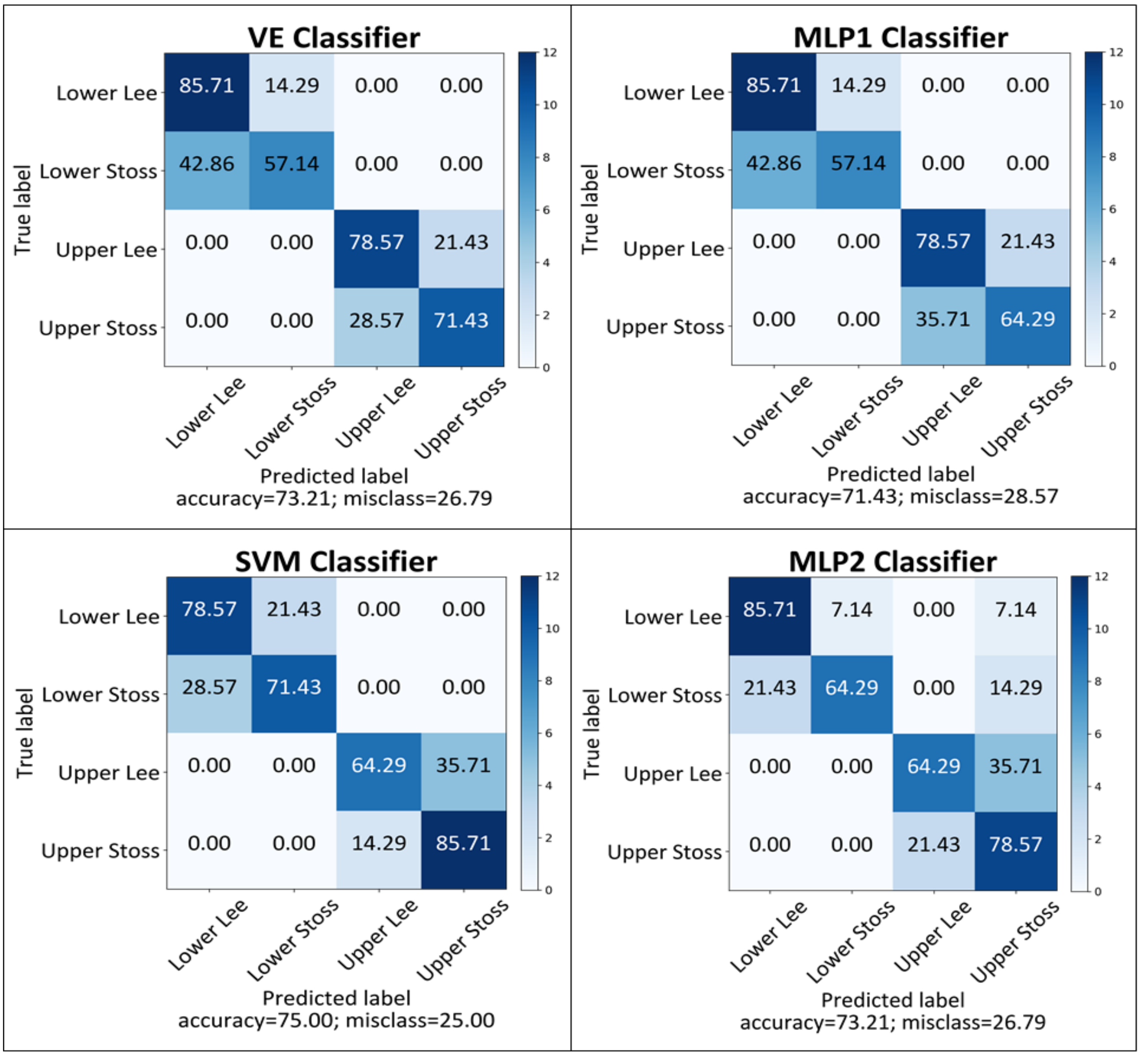

Figure 9: Confusion matrices for the VE, MLP1, SVM, and MLP2 classifiers derived from the HTB SAC study site.

Classified maps for each site can be seen in Figure 10A–C. The misclassifications produced by the VE classifier are not equally distributed across the OSW study site. The north–eastern portion of the southern OSW site contains a significant portion of the false positives for the "Upper Lee" and the "Lower Lee" classes (Figure 10C). This misclassification occurs on the boundary between the south–eastern and south–western OSW subset sites (Figure 11A–C). Here the direction of the lee side of the mean aspect of the sediment waves in this site changes direction. These misclassification clusters are observed within the northern portion of the OSW site. One hundred and forty-four image objects misclassified as either "Upper Lee" or "Lower Lee" by the VE classifier (68.2%) are also misclassified by the SVM, MLP1, and MLP2 classifiers.

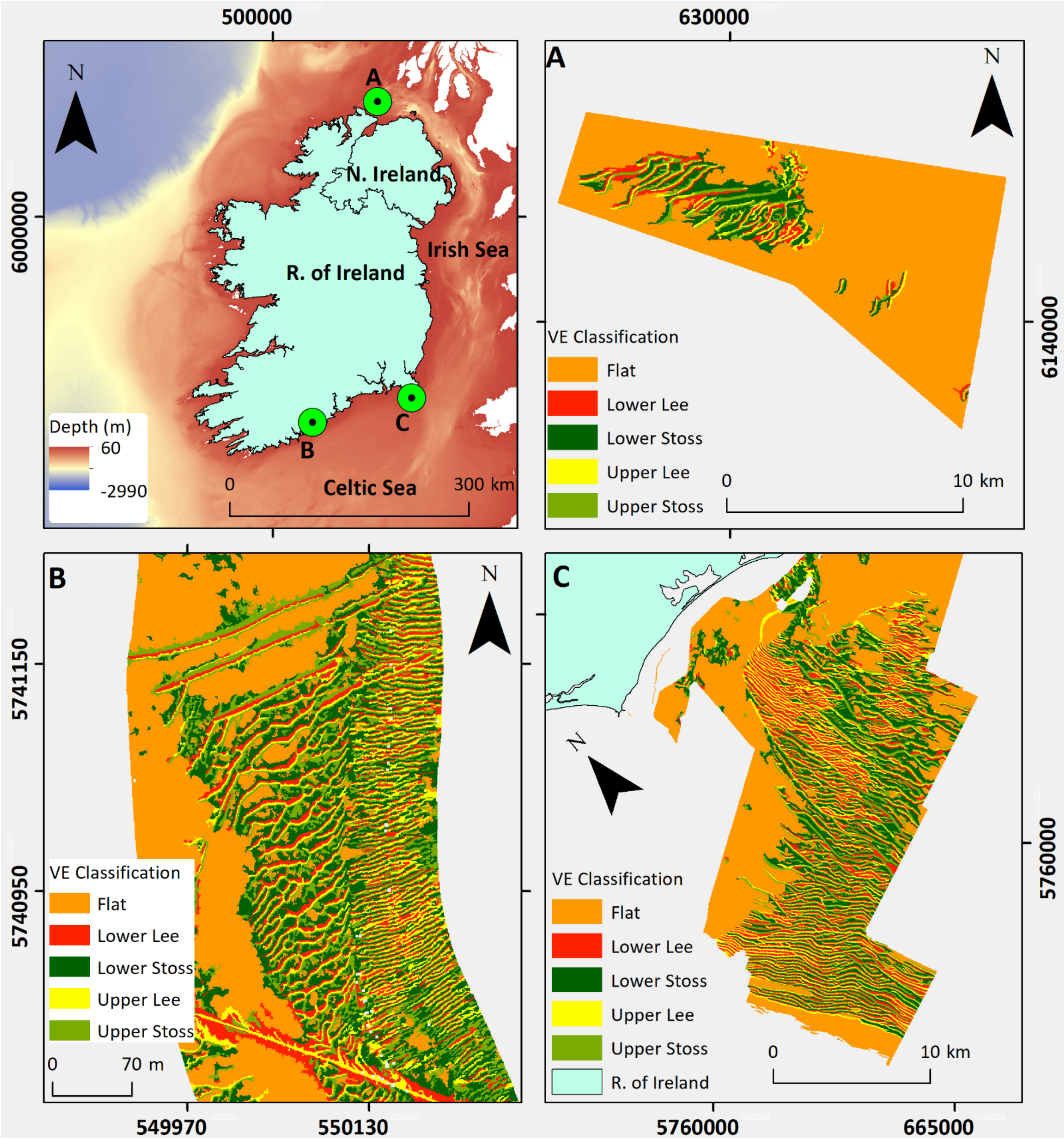

Figure 10: VE classification maps for the; (**A**) HTB SAC, (**B**) Cork Harbour, and (**C**) South OSW sites.

Eighty of these common misclassifications occur in the convergence region between the SW OSW and SE OSW subset sites (Figure 11A–C). When calculating the mean for the features extracted from these misclassified objects the mean values for slope and BPI5 are more compatible with the means derived for these features for the "Lower Lee" and "Upper Lee" sample objects in the South OSW. Furthermore, the average sediment wavelength in this region reduce to 200 m, the wave height reduces to an average of 5 m (Figure 11D−F).

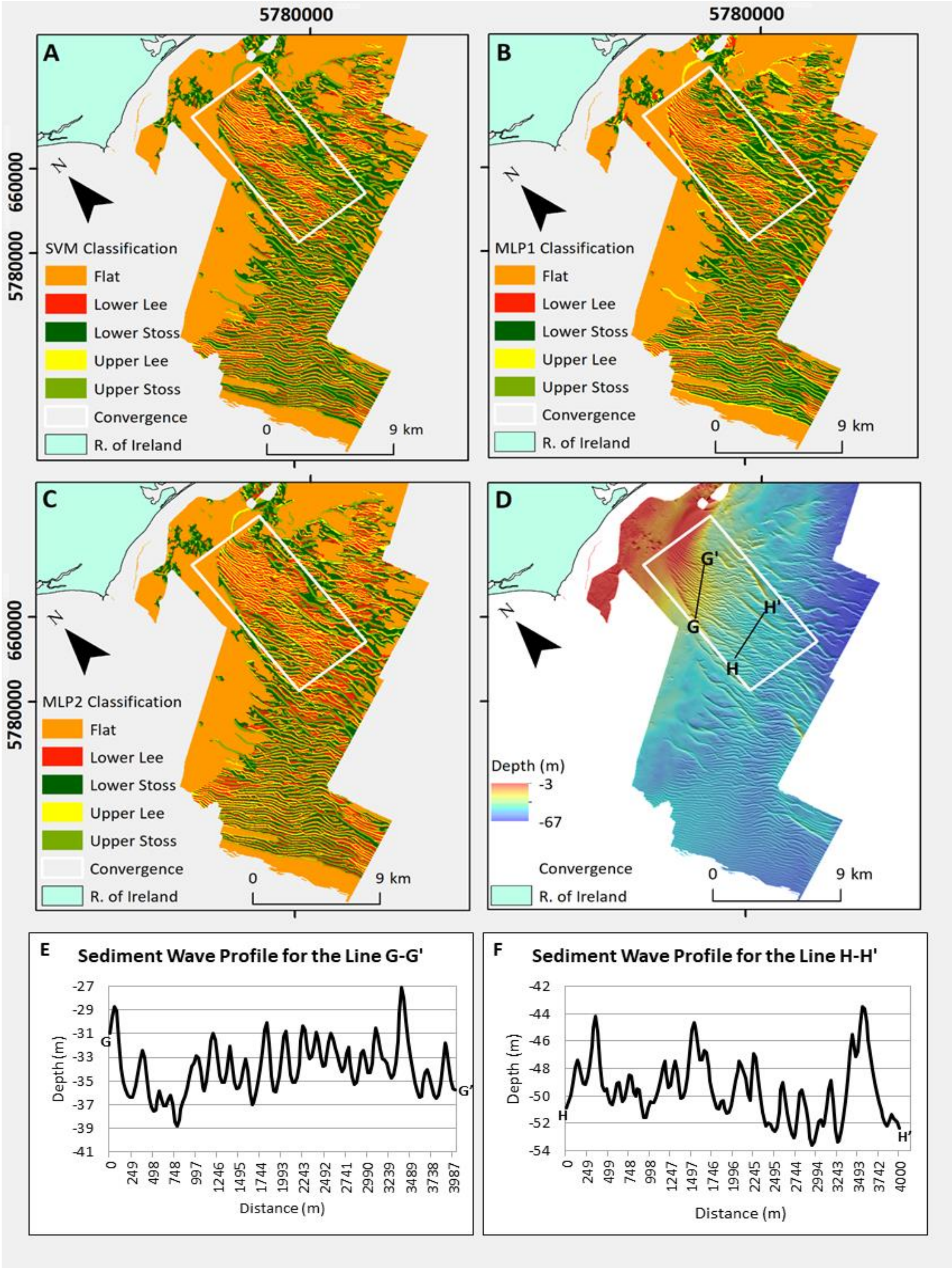

Figure 11: Classification maps for the southern section of the OSW including an outline for the convergence zone between the SW and SW OSW. (**A**) SVM classifier, (**B**) MLP1 classifier, (**C**) MLP2

classifier (**D**) bathymetry for the corresponding region including th e line for the sediment wave profile for line G-G’ and line H-H’ displayed in (**E**) and (**F**) respectively.

The performances of each algorithm on the HTB SAC site were comparable to the accuracies attained in the SW OSW survey site. Each classifier maintained an accuracy score of above 71% (Figure 12A–C).

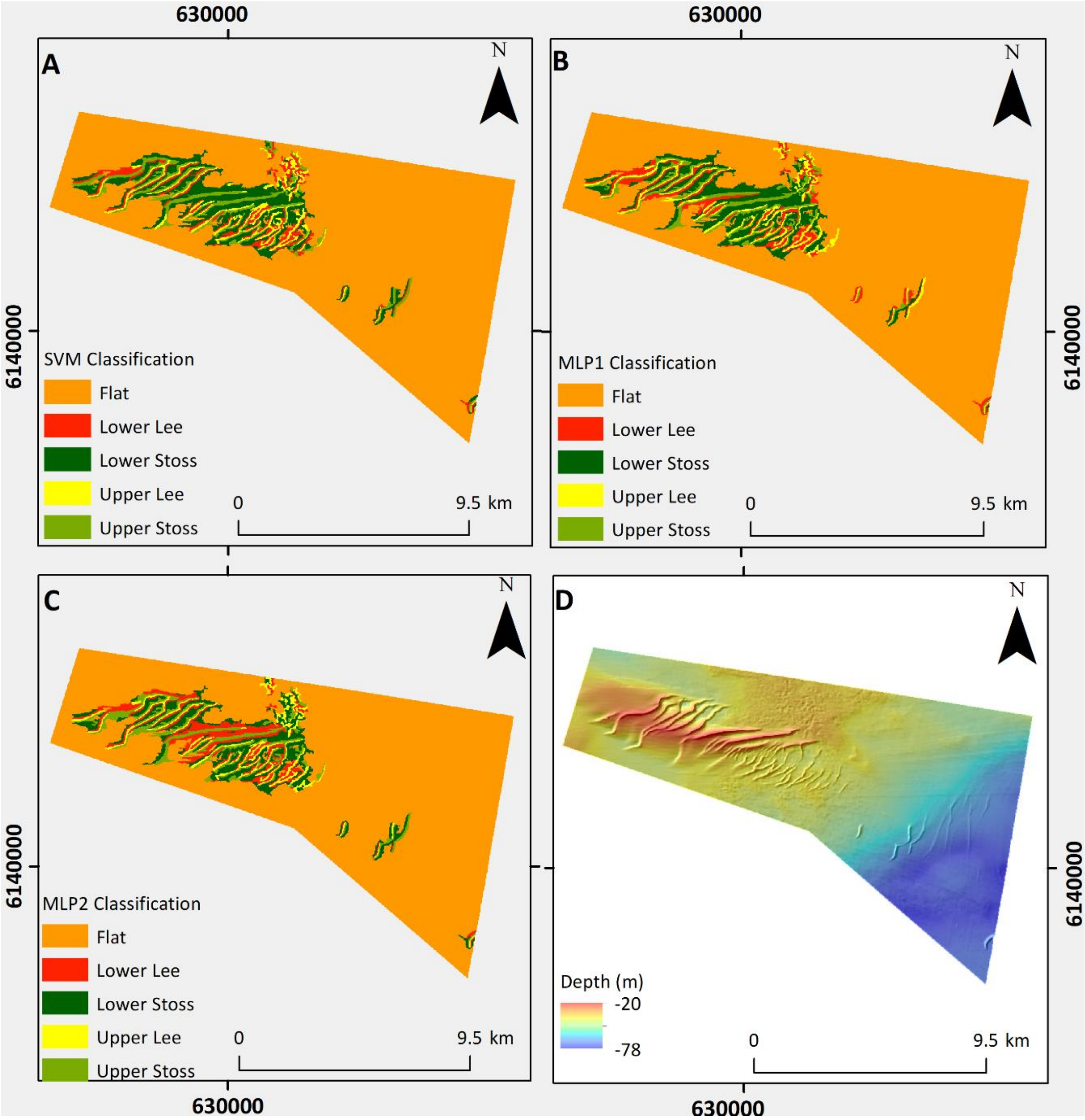

Figure 12: Classification maps for the (A) SVM, (B) MLP1, (C) MLP2 classifiers and (**D**) the bathymetry for the HTB SAC site.

2.4. Discussion

2.4.1. Accuracy of each classifier on high spatial resolution data

The variations in accuracy produced for all classifiers in the cross-validation study are minor, with each classifier exhibiting a train-test accuracy difference of <3%. Coupled with mean test accuracy scores of >97% imparts a high fidelity of classification to each algorithm when presented with unseen high-resolution data. This low variation between the training and test datasets bestows each classifier with a high level of classification stability. Overall, the VE and MLP2 classifiers displayed the best test accuracy and K-scores while displaying low variances between folds. Therefore, these classifiers are the most suitable for the classification of high-resolution bathymetric data. Although the SVM classifier produced the lowest difference between train and test classification scores, the classifier produced the lowest test accuracy and K-scores. This, combined with the high standard deviation for these scores across folds, shows that this classifier has the least stable classification results.

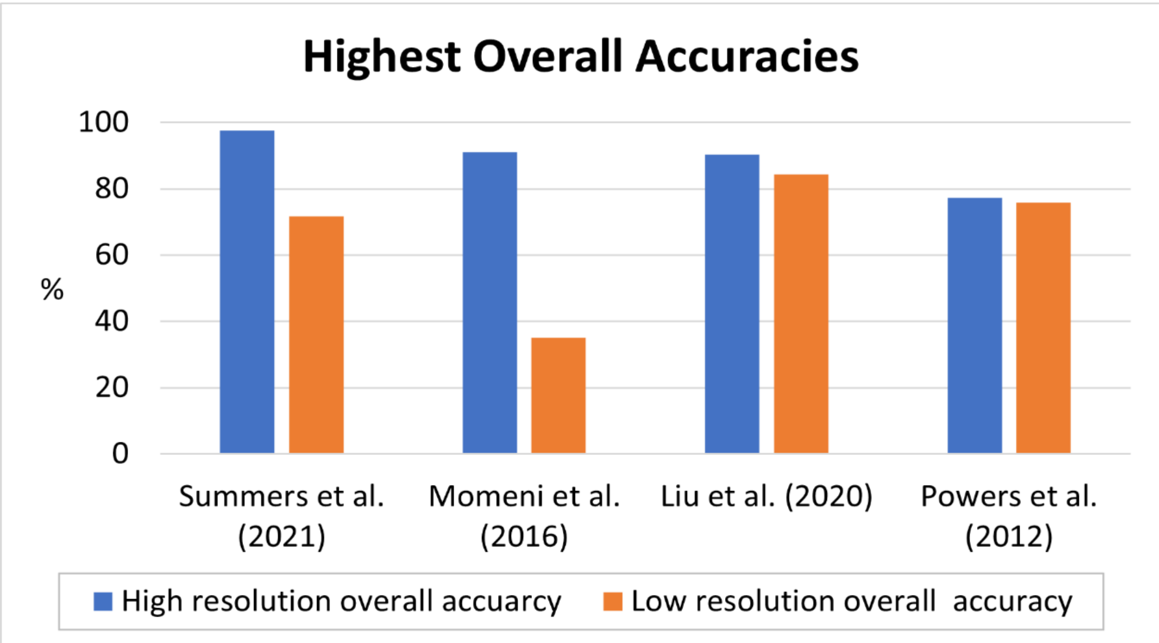

Figure 13: The highest overall accuracy for finest spatial resolution data from this study and other studies within the literature employing multiple spatial resolutions within classification.

Consequently, the SVM classifier would be the least suited for categorising high-resolution data. This represents an improved classification accuracy for high spatial resolution data relative to previous findings with comparable spatial resolution variation (Figure 13) (Powers et al., 2012; Momeni et al., 2016; Liu et al., 2020). This is significant considering the classification schemes deployed within these studies were supported by the inclusion of calibrated spectral information and well-defined feature spectral indices (Powers et al., 2012; Momeni et al., 2016; Liu et al., 2020). The ability to use standardised spectral data and spectral indices in marine classification schemes is hindered by ambiguity of MBES backscatter data (Koop et al., 2021). Consequently, these schemes may not achieve the same success in a marine setting.

2.4.2. Accuracy of each classifier on low spatial resolution data

Each classifier produces a reduction in accuracy of ~27% when comparing the mean test accuracy from the K-Fold classification and the test accuracy score for the OSW and HTB SAC sites. The performance of each classifier is affected by the orientation of the sediment waves in these low-resolution sites (Figure 14).

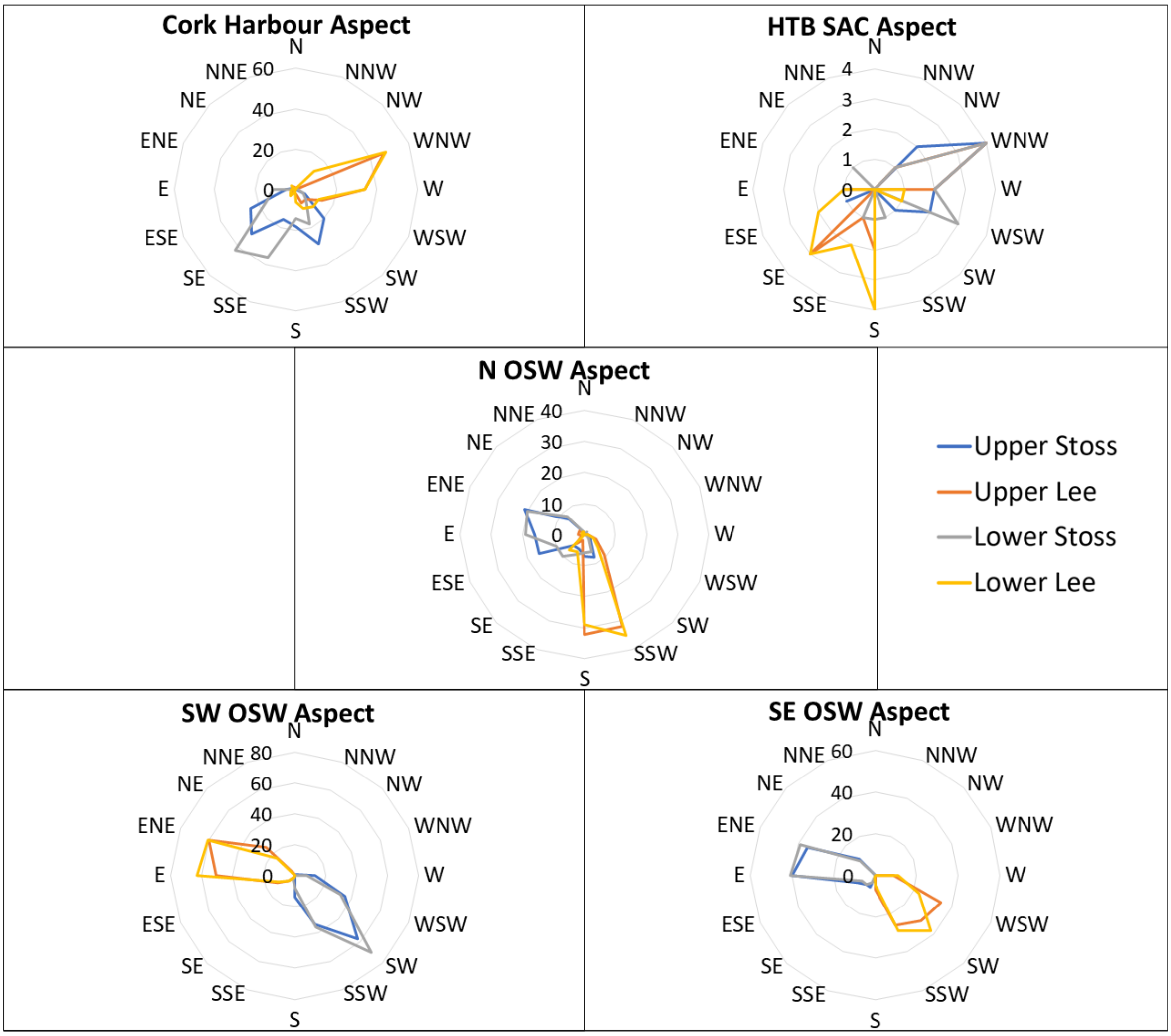

Figure 14: Mean aspect by class for the samples taken at each study site.

For example, the classifiers achieve a decrease in accuracy scores of ~10% in the N and SE OSW subset sites when compared to the SW OSW subset site (Figure S1–S3). Consequently, we assert that the classifiers are overfitting to a feature within the training data that is common to the data acquired at the SW OSW site. Upon closer inspection of the training data, the cosaspect (Northness) feature shows a similar pattern between the Cork Harbour site and the SW OSW site (Figure 15).

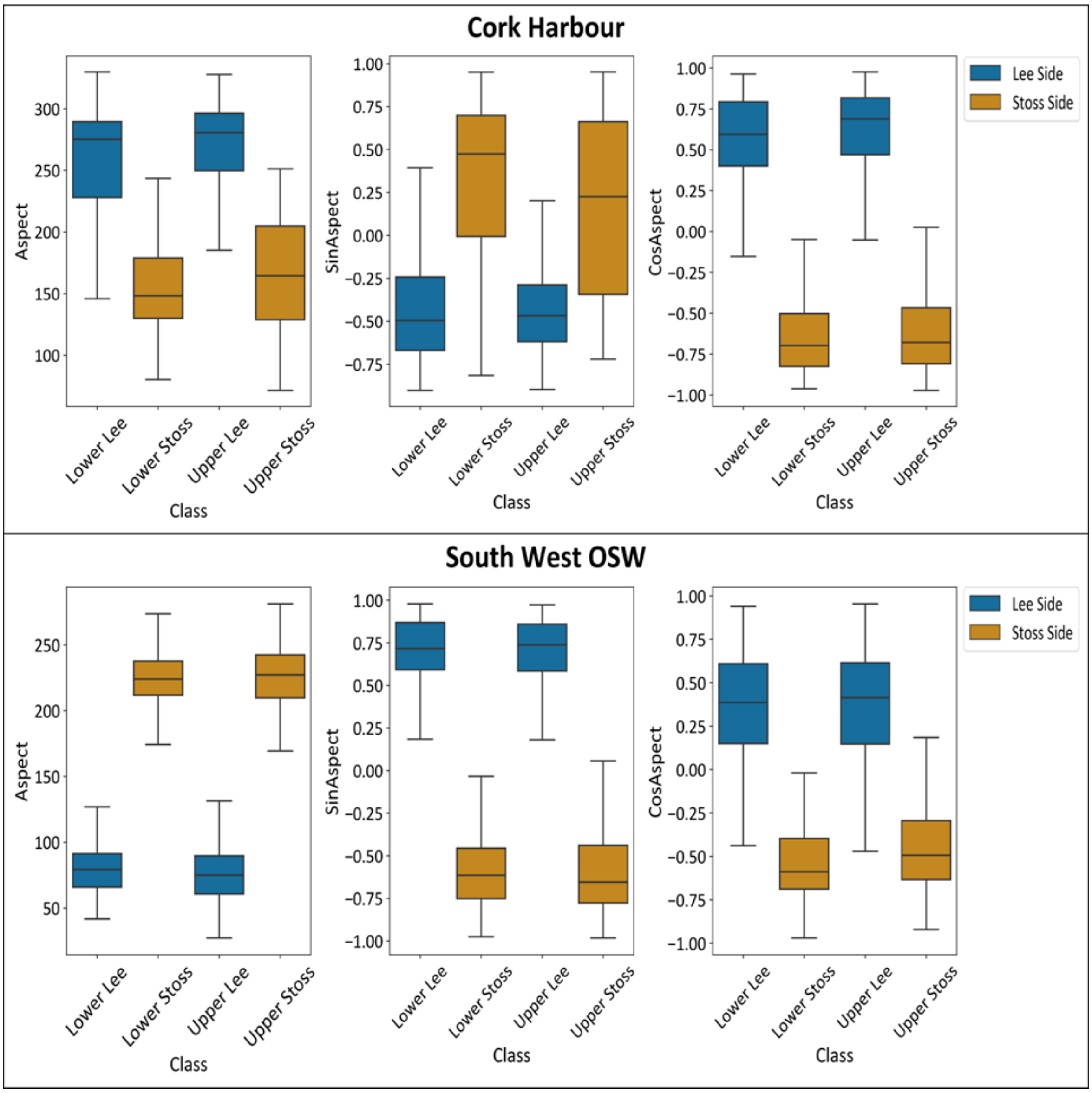

Figure 15: Mean aspect, sinaspect, and cosaspect for the 4 separate classes for both the Cork study site and the South-West OSW site.

Thus, a potential improvement to the classification workflow would ensure that sample objects are obtained from sediment waves of various orientations (Shorten and Khoshgoftaar, 2019; Rey-Area et al., 2020). One such method would be to apply an image rotation to align the training data with each cardinal direction. The OBIA workflow would be applied to these new images and an equal number of samples from each class would be acquired from each of these datasets. This would allow each classifier to assimilate the geomorphological context of the classes, rather than overfitting to a particular mean aspect

(Rey-Area et al., 2020). A greater accuracy score for these regions could be generated as a result. Accuracy scores for the VE classifier can be enhanced at each low-resolution site by classifying the “valley” image objects by referencing the classification given to the adjoining “ridge” object. As the classifier was consistently more accurate at classifying the lee and stoss side of the “ridge” image objects. Therefore, if a “ridge” image object were classified as “Upper Lee”, any neighbouring “valley” image object would be classified as “Lower Lee”. A similar deduction could be made if a “ridge” image object were classified as “Upper Stoss”.

If the accuracy scores for the “Upper Stoss” and “Upper Lee” classes can be taken as a guide, this would afford the VE classifier with the highest accuracy scores at each low-resolution subset site. A significant proportion of misclassified objects were shared between classifiers within the low-resolution data. These misclassified objects occurred within clusters, where the “Lower Lee” and the “Upper Lee” classes were over-represented. The largest cluster of shared misclassified objects was observed in the convergence region between the SW and SE OSW subset sites (Figure 11). This convergence may be causing confusion within each classifier as the variables derived from these sediment waves are influenced by the changing sediment wave migration direction. Such influence could contribute to the decrease in accuracy scores when examining the high-resolution and low-resolution outputs. Furthermore, the significant reduction in the sediment wave wavelength and wave height at this location may also have affected the ability of the classifiers ability to discern between the classes. As the sediment waves in this region are more spatially compact and the image objects derived here display a mean area that is more comparable with the “Lower Lee and Upper Lee” in the S OSW. A similar relationship is found when examining the mean for each classification variable within the sample image objects. The ratio between the average sediment wave wavelength and the spatial resolution of the data in this region is 8:1. In the Cork Harbour site, the ratio between the sediment wave wavelength and the spatial resolution of the bathymetry is 20:1, a similar figure is seen in the HTB SAC site (16:1). Shorter wavelengths would suggest that the image objects created in this region would be smaller relative to the spatial resolution of the data. Potentially increasing the within-class heterogeneity and, with it, the influence of noise on the classification (Blaschke et al., 2014). This may have exacerbated the drop in performance of the classifiers at this location, especially with respect to the “Lower Stoss” image objects. As they occurred on the longer, more gradual stoss side of the sediment wave they were more distinguishable by the area that they encompassed. However, in the convergence zone, the disparity in area between the stoss side and lee side of the troughs of the sediment waves in this area decreased. Thus, it was more difficult for the classifiers to distinguish between the image objects representing “Lower Stoss” and “Lower Lee” classes in this region. The improvements suggested for the VE classifier would not amend the misclassification of these objects, as the increase in the within-class heterogeneity is an inherent limitation of OBIA. The image transform solution may allow the classifiers to better separate to the subtle differences between class features in the lower resolution data overall. However, it may not resolve the misclassification introduced due to the increase in within-class heterogeneity observed in the convergence zone.

2.4.3. Implications for Suitability for a Scale Standardised Object-Based Technique

Remote sensing research seldom investigates the stability of OBIA classification accuracy when spatial resolution of the data changes. The few studies that have explored this developed algorithms that ran over the same region on the same data where image blurring techniques are applied to imitate the coarsening of spatial resolution (Powers et al., 2012; Momeni et al., 2016; Liu et al., 2020). Furthermore, attempts have been made to increase the relative altitude of the sensor to decrease spatial resolution of the data (Yuba et al., 2021). Such methods do not effectively capture the relationship between a feature’s spatial resolution and the scale of measurement. Another issue shared by this research is the inconsistency of the segmentation parameters used between resolutions (Momeni et al., 2016; Liu et al., 2020). These studies use different scale parameters for the multiresolution segmentation algorithm at separate resolutions (Momeni et al., 2016; Liu et al., 2020). This alters the nature of the objects that are put into the classification and raises questions about the validity of the classification (Ming et al., 2018). Increasing scale parameter with increasing spatial resolution may decrease within class spectral variation, reducing the influence of noise and leading to improved discrimination during classification (Gao et al., 2011; Mishra and Crews, 2014; Ming et al., 2018). Powers et al. (2012) demonstrated consistent segmentation at both coarse and fine spatial resolutions, however the range of spatial resolutions is the lowest found in the literature. To date, no research has been conducted to assess classification rigour when examining features that occur as high-resolution objects through multiple spatial resolutions of data, which remains a simple task for an expert interpreter. Therefore, to augment the authenticity and consistency of the replication of human interpretation through machine learning, we must produce segmentation and classification methods that are robust to changes in spatial resolution. Seabed habitats lack the traditional environmental framework present in terrestrial habitats (i.e., vegetation) and thus, are defined by seabed geomorphology and composition (Zajac, 2008). The ability to produce classification systems that reflect seabed habitat geomorphological features common to many scales of environment and avoid schemes that are Isolated and specific is therefore imperative to this objective. OBIA grants the infrastructure to build a classification workflow that is resilient to change in spatial resolution. Commitments to map the entire seafloor by 2030 warrant the establishment of a standardised classification approach that can be applied to large datasets and can be replicated with relative simplicity on multiple regions with comparative results (Mayer et al., 2018).

This study presents the first OBIA classification workflow to be implemented across separate resolutions, at separate study sites, whilst maintaining a high fidelity of accuracy. We accomplished this while maintaining a consistent set of parameters throughout the segmentation and classification stages. This classification system offers a geomorphological framework to help define benthic seabed and terrestrial habitats. Providing a valuable input for species distribution modelling and a seamless classification map from the terrestrial to the marine realm (Damveld et al., 2018). Given that sediment wave and dune asymmetry are linked with sediment transport direction, sediment wave/dune migration rates, and bed shear stress (Van Landeghem et al., 2012), a quantitative analysis could be derived from this model to provide regional estimates for these properties. Assessment of sediment wave migration is crucial for the effective management of equipment deployed on the seabed (Van Landeghem et al., 2012). Multi-temporal investigations utilising the outputs of such models could feed into infrastructural marine spatial planning initiatives for marine renewable energy, i.e., offshore windfarms. This classification scheme is not restricted to seabed sediment waves and has the capacity to identify additional or alternative features with supplementary image layers designed to target those features. The inclusion of the ray module within the hyperparameter tuning workflow will aid in expediting the training of classification algorithms to identify these features.

2.5. Conclusions

This paper establishes an open-source OBIA workflow that operates on high-resolution sediment wave objects from MBES bathymetry data at 2 separate spatial scales, with a magnitude of spatial difference of 50 times. Although a small decrease in accuracy was observed in the coarser resolution data, this is the first classification scheme to maintain consistent segmentation and classification parameters and preserving a high fidelity of accuracy to date. This success exhibits the resilience of an OBIA workflow when applied to high-resolution objects occurring across various spatial resolutions of MBES bathymetric data. Thus, achieving a more veracious duplication of expert MBES bathymetric data analysis. Improvements made within the final classification for all locations have been suggested in depth and will inform future work on the classification of seafloor features. Once the equivocacy of MBES backscatter data has been amended, backscatter data could be included to supplement the classification with seabed textural information. This workflow can be adapted to target other ecologically significant seabed morphological features occurring within MBES bathymetry.

Supplementary Materials

The following are available online at https://www.mdpi.com/article/10.3390/rs13122317/s1, Figure S1: Confusion Matrices for the N OSW, Figure S2: Confusion Matrices for the SE OSW, Figure S3: Confusion Matrices for the SW OSW, Shapefile S1: HTB SAC Outline, Shapefile S2: OSW Outline.

Author Contributions: Conceptualisation, G.S. and A.L.; Methodology, G.S. and A.L.; Software, G.S.; Validation, G.S and A.L.; Formal Analysis, G.S.; Investigation, G.S.; Resources, G.S.; Data Curation, G.S.; Writing – Original Draft Preparation – G.S.; Writing – Review & Editing, G.S., A.L., and A.J.W.; Visualisation, G.S.; Supervision, A.L. and A.J.W.; Project Administration, A.J.W.; Funding Acquisition, A.J.W. All authors have read and agreed to the published version of the manuscript.

Funding: This research was developed under the Marine Protected Area Management and Monitoring (MarPAMM) (Project IVA5059) supported by the European Union's INTERREG VA Programme, managed by the Special EU Programmes Body (SEUPB). Bathymetric data were supplied by the Geological Survey Ireland and Marine Institute INFOMAR programme. The data processing workflow was developed by Gerard Summers and Aaron Lim is funded by the EU INTERREG V through the Special EU Programmes Body (SEUPB) and the Irish Research Council, respectively.

Data Availability Statement: The low-resolution EMODnet data is available for public download at the link https://www.emodnet-bathymetry.eu. The high-resolution Cork Harbour MBES data are available on request from the institution of the corresponding author. The data are not publicly available as they are part of ongoing research.

Preface to Chapter 3

Chapter 3 seeks to define a current velocity estimation workflow. This workflow will utilise the SSB classification capabilities of Chapter 2 to identify these features in MBES data and measure their physical extent. This physical extent will be used to estimate the current velocities responsible for their formation. Additionally, this will be used to determine the different influences affecting these currents including regional, local, and micro scale impacts.

This chapter was published on the 21/09/2022 in the MDPI journal *Remote Sensing*. *Remote Sensing* has an impact factor of 5.349. This publication has yet to receive a citation.

Summers, G., Lim, A., & Wheeler, A.J. (2022). A characterization of benthic currents from seabed bathymetry: an object-based image analysis of cold-water coral mounds, *Remote Sensing,* **14***,* 4731. https://doi.org/10.3390/rs14194731

Author Contributions

Gerard Summers and Aaron Lim were responsible for the concept of this study. Gerard Summers and Aaron Lim were responsible for the development of the methodology used within this study. Gerard Summers was responsible for the software used in this paper. Validation techniques for this paper were established by Aaron Lim. Formal Analysis was completed by Gerard Summers. Investigation of the results was conducted by Gerard Summers. The resources were organised by Gerard Summers and the data curation was organised by Gerard Summers and Aaron Lim. Writing and preparation of the original draft of the original manuscript was completed by Gerard Summers. The manuscript underwent a single round of corrections from two separate anonymous reviewers. The editing and review of the manuscript were coordinated by Gerard Summers, Aaron Lim, and Andrew James Wheeler. All data visualisation was completed by Gerard Summers. Supervision of the development of this manuscript was completed by Aaron Lim and Andrew James Wheeler. Administration of the project was conducted by Andrew James Wheeler. The funding for this research was acquired by Andrew James Wheeler. All authors have read and agreed to the published version of the manuscript.

Chapter 3. Characterisation of Benthic Currents from Seabed Bathymetry: An Object-Based Image Analysis of Cold-Water Coral Mounds

(Current Status: Published, Remote Sensing, https://doi.org/10.3390/rs14194731)

Gerard Summers [1,*], Aaron Lim [2] and Andrew J. Wheeler [1,3]

1. *School of Biological, Earth and Environmental Sciences, Environmental Research Institute, University College Cork, Distillery Fields, North Mall, T23 TK30 Cork, Ireland*
2. *Department of Geography, University College Cork (UCC), T12 K8AF Cork, Ireland*
3. *Irish Centre for Applied Geosciences (ICRAG), Marine & Renewable Energy Institute (MaREI), University College Cork, P43 C573 Cork, Ireland*

* *Corresponding author*

Abstract:

Seabed sedimentary bedforms (SSBs) are strong indicators of current flow (direction and velocity) and can be mapped in high resolution using multibeam echosounders. Many approaches have been designed to automate the classification of such SSBs imaged in multibeam echosounder data. However, these classification systems only apply a geomorphological contextualisation to the data without making direct assertions on the velocities of benthic currents that form these SSBs. Here, we apply an object-based image analysis (OBIA) workflow to derive a geomorphological classification of SSBs in the Moira Mounds area of the Belgica Mound Province, NE Atlantic through k-means clustering. Cold-water corals are sessile filter-feeders that benefit from strong currents; consequently, they are often found in close association with sediment wave fields. This OBIA provided the framework to derive SSB wavelength and wave height. These SSB attributes were used as predictor variables for a multiple linear regression to estimate current velocities. Results show a bimodal distribution of current flow directions and current speed. Furthermore, a 5 k-means classification of the SSB geomorphology exhibited an imprinting of current flow consistency which altered throughout the study site due to the interaction of regional, local, and micro-scale topographic steering forces. This is a proof-of-concept study for an assessment tool applied to vulnerable marine ecosystems but has wider applications for

seabed appraisals and can inform management and monitoring practice across a variety of spatial and temporal scales. Deriving spatial patterns of hydrodynamic processes from widely available multibeam echosounder maps is pertinent to many avenues of research, including scour predictions for offshore structures such as wind turbines, sediment transport modelling, benthic fisheries, e.g., scallops, cable route and pipeline risk assessment and habitat mapping.

3.1. Introduction

Understanding the current regime affecting seabed environments and habitats therein is a recurrent research requirement. Not only are currents an important influence on habitat for various organisms, especially filter feeders, but currents also have a direct control on seabed sediment grain-size and composition through selective sedimentation processes. In areas where current-controlled sediment transport produces mobile bedforms such as sediment waves, these may offer a hazard to cables and pipelines which may become excavated and exposed (Carter et al., 2014). Likewise, structures may also become buried over time. Interpreting benthic current speeds from bedform morphologies also enables appropriate infrastructure design and assists sediment transport modelling, which are important for coastal erosion management or to predict recovery from marine aggregate extraction (Guo et al., 2021; Prasad and Kumar, 2014; Degrendele et al., 2010). Cold-water corals (CWCs) are sessile organisms that can generate complex three-dimensional frameworks that form reefs and coral mounds over time by the accumulation of biological remains, including coral rubble and the trapping of sediments (Wheeler et al., 2008; Roberts et al., 2006). Over hundreds of thousands to millions of years, such reefs may eventually form giant carbonate mounds through successive periods of growth (Kenyon et al., 2003; Thierens et al., 2013). Habitats constructed by framework building scleractinian CWCs support other marine species, including commercial fish species, and provide refuge, feeding grounds, and nurseries creating biodiversity hotspots (Baillon et al., 2012; Roberts and Cairns, 2014; Chapron et al., 2018; Boolukos et al., 2019). Seabed sedimentary bedforms (SSBs) have been observed in many CWC habitats implicating an inherent connection between CWCs and strong benthic currents (Wheeler et al., 2008; Dorschel et al., 2009; Lim et al., 2018a; Lim et al., 2020). Moreover, studies developing palaeoenvironmental reconstructions of CWC habitat conditions indicate that periods of CWC habitat decline have been linked to weakened current regimes (Matos et al., 2017; Wienberg et al., 2020). This is not surprising as CWCs are filter feeders ensnaring and consuming suspended food particles thus, enhanced current speeds can increase the encounter rate of these suspended food particles with coral feeding apparatuses (De Clippele et al., 2017; van der Kaaden et al., 2020). Although the significance of CWC habitats to marine biodiversity has widely been acknowledged, anthropogenic activities and environmental changes in the deep sea continue to adversely impact these environments (Burgos et al., 2020; de Oliveira et al., 2021). Furthermore, the slow recuperation rates for these habitats from such impacts underlines the need to elucidate the processes that govern the success of these vulnerable marine ecosystems and proactively assign protective status (Huvenne et al., 2016). Effective conservation and management of these vulnerable marine ecosystems requires detailed and accurate spatial information to be acquired of CWCs and their surrounding environments (Coiras et al., 2011; Diesing and Thorsnes, 2018). Providing an accurate portrayal of seabed environmental conditions requires the production of seabed habitat maps that are applicable at multiple scales (Savini et al., 2014; Conti et al., 2019).

Multibeam echosounders (MBES) provide bathymetry and backscatter data that readily portray the geomorphological context of the seafloor (Calvert et al., 2014; Janowski et al., 2018b) offering an efficient input for seabed habitat maps, depicting the spatial distribution of CWCs and their relationships with adjacent seabed environments (Lim et al., 2018a; Huvenne et al., 2011; Robert et al., 2017). Despite the availability of this technology, only 18% of the world's oceans are mapped at a resolution akin to terrestrial datasets (Mayer et al., 2018). Consequently, several national and international initiatives have been established to ameliorate this data deficit (Mayer et al., 2018; Thorsnes, 2009; Guinan et al., 2021). Executing this goal necessitates the acquisition of significant volumes of data, which require processing to create seabed habitat maps (Diesing et al., 2014). Additionally, these seabed habitat maps need to be objective and replicable to ensure the consistency of the analysis when appraising these conditions over repeated surveys (Zelada Leon et al., 2020). Manually interpreting such volumes of data is laborious, dependent on the expertise of the analyst, vulnerable to bias, and introduces variability to the production of seabed habitat maps (Diesing et al., 2016; Durden et al., 2016; Lim et al., 2021). Several approaches have been developed to automate the production of seabed habitat maps in CWC environments (de Oliveira et al., 2021; Diesing and Thorsnes, 2018; Conti et al., 2019). Object-based image analysis (OBIA) offers the ability to characterise groups of pixels into distinct image objects that relate directly to physical seabed features (Blaschke, 2010; Ierodiaconou et al., 2018). Spectral features acquired from SSBs enable frequency analysis to be incorporated into OBIA workflows (Trzcinska et al., 2020). Stow et al. (2009) generated a bedform velocity matrix to offer estimations of current speed, current direction, and variability using similar spectral characteristics derived from the seafloor geomorphology. Moreover, this technique has been applied and proven effective in obtaining current speeds in CWC environments (Lim et al., 2018a). Despite the demonstrated advantages of spectral features as part of an OBIA workflow and the importance of hydrodynamic regimes to CWCs, these features have yet to be exploited to provide automated appraisals of current speed.

Here, we provide a semi-automated OBIA workflow designed to categorise CWC mounds and SSBs present within MBES bathymetric data using a geomorphological classification that depicts the consistency of the hydrodynamic regime and provides the framework for current velocity estimations. A fast Fourier transform (FFT) was applied to bathymetric profiles derived from image objects associated with SSBs crests. Wavelength and wave height were calculated as part of this analysis and a current velocity estimate was obtained using a multiple linear regression generated from parameters outlined in Stow et al. (2009) Geomorphological characterisation of the SSB crest image objects was achieved using a k-means classification deployed on the morphological attributes associated with the crests including wavelength and wave height. This is the first study to provide a semi-automated OBIA characterisation of seabed hydrodynamics solely using MBES bathymetry. As expressed above, this has rich application but is applied here to better understand current speed controls on cold-water coral reefs.

3.1.1. Study Site

The Belgica Mound Province (BMP) is found at the eastern flank of a north–south trending embayment occurring along the Irish continental margin called the Porcupine Seabight in the NE Atlantic (Huvenne et al., 2002; Foubert et al., 2005; Wheeler et al., 2005). The BMP consists of two chains of CWC giant carbonate mounds orientated north–south occurring at 650 m depth and 950 m, respectively (Wheeler et al., 2005; Beyer et al., 2003; Wheeler et al., 2011). A portion of the BMP is encompassed by a Special Area of Conservation (SAC) designated under the EU Habitats Directive (Lim et al., 2017). The BMP hosts several examples of active and buried mounds with sizes varying from giant carbonate mounds approaching 150m in height to smaller structures that are approximately 10 m in height, these mounds occur at a depth range of 550 m to 1030 m (White, 2007; Fentimen et al., 2018). Salinity profiles for this region show that the Mediterranean Outflow Water (MOW) occurs between 800 m and 1100 m water depth forming a water mass that flows from the Gulf of Cadiz along the continental margin and creates a cyclonic flow in the Porcupine Seabight (White, 2007; Dorschel et al., 2007). The Moira Mounds (MMs) are a series of small-scale coral mounds, with diameters of 20 m to 50 m, heights of up to 11 m, that occur throughout the BMP (Wheeler et al., 2011). One such MM has shown considerable temporal variability where erosion by strong currents has likely exhumed dead coral framework on the mound over 4 years (Boolukos et al., 2019; Lim et al., 2018b). Spatial arrangement of these mounds forms 4 distinct groups: the upslope area, the midslope area, the northern area, and the downslope area (Lim et al., 2018b). The downslope MMs are found within a north-north-east trending blind channel and have the highest density ever recorded at 22.9 mounds per km^2 (Lim et al., 2018a). Mean current flow is directed poleward and has an estimated speed of between 0.36 $m{\cdot}s^{-1}$ and 0.40 $m{\cdot}s^{-1}$ (Lim et al., 2018a; White, 2007). Transverse, sinuous, bifurcating SSBs formed due to these currents are prevalent throughout the site (Foubert et al., 2011). The location of the MMs study site is shown in Figure 16.

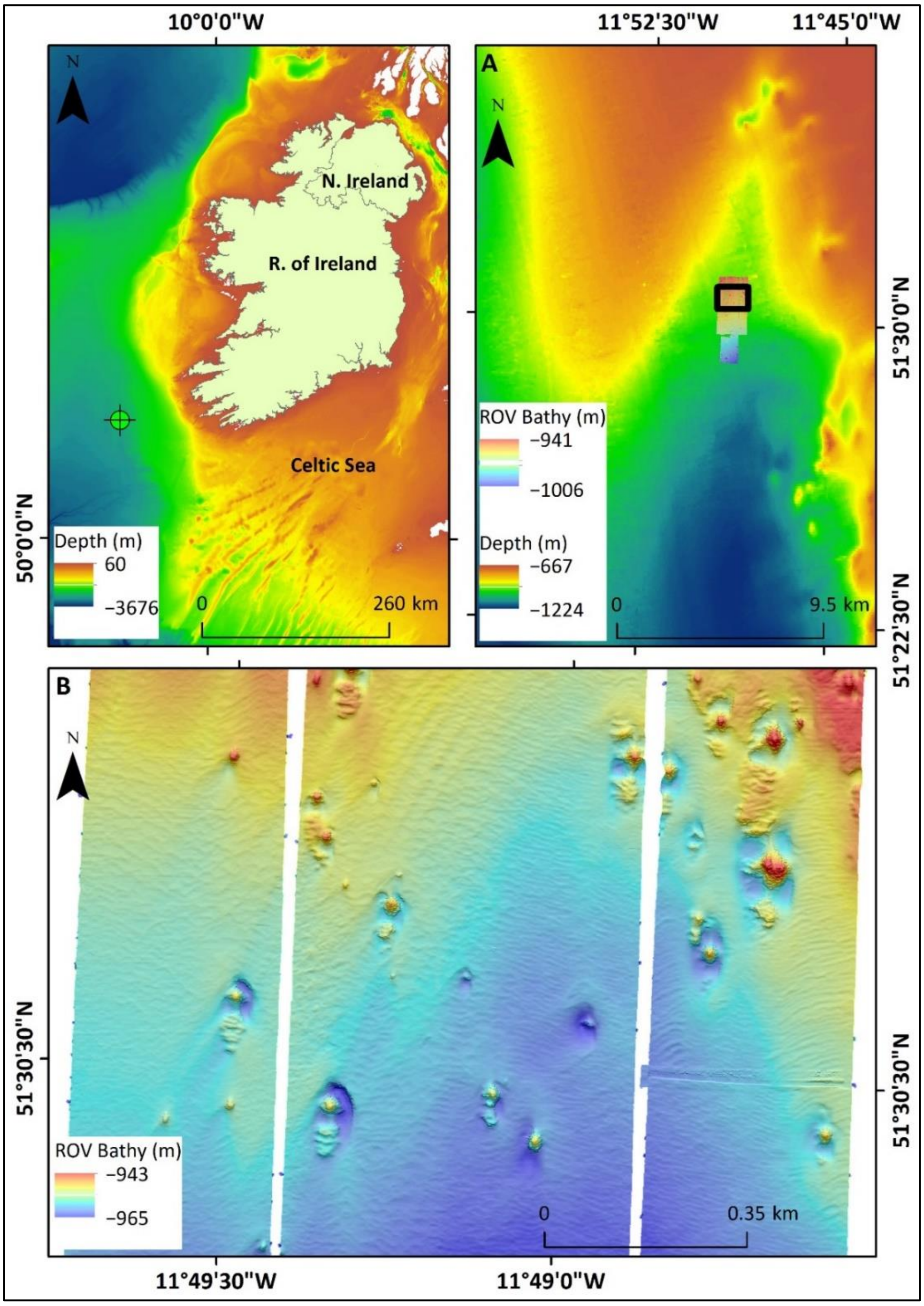

Figure 16: (**A**) Study site area. The bathymetry acquired in the downslope Moira Mounds region derived from remotely operated vehicle (ROV) based multibeam echosounder (MBES) data displaying the extent of (**B**) outlined in black, (**B**) moated cold-water coral mounds surrounded by mobile sediment worked into sediment waves. Coral ridges appear immediately south of the larger mounds.

3.2. Materials and Methods

3.2.1. Multibeam Echosounder Data Acquisition and Processing

The MBES data were collected using a Kongsberg EM2040 mounted to the Holland 1 ROV operating at a frequency of 300 kHz as part of the QuERCI survey in 2015 aboard the RV Celtic Explorer (Wheeler et al., 2015). The survey altitude was maintained at 150 m and was recorded using the ROV altimeter. The navigation and positioning were acquired using a Sonardyne USBL and a 1200 kHz RDI workhorse DVL beacon and were corrected using a Kongsberg HAINS (INS) system. Raw MBES data were sorted as *.all file formats and imported into Qimera processing software to manually remove any erroneous data using the swath editor tool (QPS, 2019b). Horizontal and vertical offsets within the data were removed using the horizontal shift tool and the varying vertical shift tool in Qimera (QPS, 2019b). A cross check analysis was applied to these data to determine the accuracy of the bathymetric data processing against the processing standards set by the International Hydrographic Organisation (IHO) (International Hydrographic Organisation, 2020). These data were gridded at 1 m resolution and exported into an ArcGRID *.asc file format. All bathymetric data were imported into ArcGIS 10.6 to derive bathymetric derivatives (Table 5). The slope, aspect, sinaspect, cosaspect, and variance were calculated using the benthic terrain modeler 3.0 toolbox in ArcGIS 10.6 (Walbridge et al., 2018). The bathymetric position index (BPI) was generated at 2 separate scales using the equation outlined below:

$$BPI = Zgrid - focalmean(Zgrid, circle, r) \qquad (1)$$

where Zgrid is the bathymetric data (Wilson et al., 2007). The focalmean derives the mean of the bathymetric data within a circle shaped kernel of radius r, this was completed in the focal statistics tool in the neighbourhood toolset in ArcGIS 10.6. The radius of the kernel determines the scale of the BPI. The BPI layer was then created by subtracting the mean bathymetric layer from the Zgrid, this was completed in the raster calculator tool in the map algebra toolset in ArcGIS 10.6.

Table 5: Image layers used for segmentation in eCognition Developer.

Image Layers	Scale (Pixel)
Aspect	3
Bathymetric Position Index (BPI)	5, 25
CosAspect (Northness)	3
SinAspect (Eastness)	3
Slope	3
Variance	3

3.2.2. Object-Based Image Analysis

3.2.2.1. Morphological Characterisation

Segmentation is a semi-automated process by which an image is separated into discrete image objects and is the first step in object-based image analysis (OBIA) (Lang, 2008; Blaschke, 2010). The effectiveness of object based image analysis is predicated on the efficacy of the segmentation in demarcating the features of interest (Hossain and Chen, 2019). In this paper, the segmentation was deployed in a hierarchal process, to distinguish between features, such as CWC mounds and SSBs, that exhibit a significant disparity in scale and characterise their morphology. This morphological characterisation was performed over a series of four phases that were adapted from Summers et al. (2021) (Figure 17). These phases utilise the multiresolution segmentation algorithm (MRS), the spectral difference algorithm, and the pixel-based object resizing algorithm, which are all found within the eCognition Developer processing suite (Trimble, 2014). The MRS algorithm groups pixels together into image objects using a predefined homogeneity value that ceases the amalgamation of pixels once this value is met, this homogeneity value is defined as the scale parameter (Lacharité et al., 2018; Trimble, 2014). Moreover, the influence of image object shape on the segmentation is controlled by the shape parameter, the smoothness of the image object outline created by the segmentation is regulated by the compactness factor (Trimble, 2020). An ideal segmentation presents an accurate reflection of the outline of the targets of interest (Gao et al., 2011; Johnson and Xie, 2011; Hossain and Chen, 2019). However, this is seldom the case, with many features of heterogeneous classes occurring within the same image object (under segmentation), or one feature being demarcated by multiple image objects (over segmentation) (Marpu et al., 2010). Amalgamation of neighbouring image objects can be completed using the spectral difference algorithm, where image objects are merged if the difference between mean layer intensities is below a user-defined value (Trimble, 2014). The pixel-based object resizing algorithm can contract or expand image object boundaries until a specific geometry has been achieved or image layer value has been met (Johansen et al., 2011).

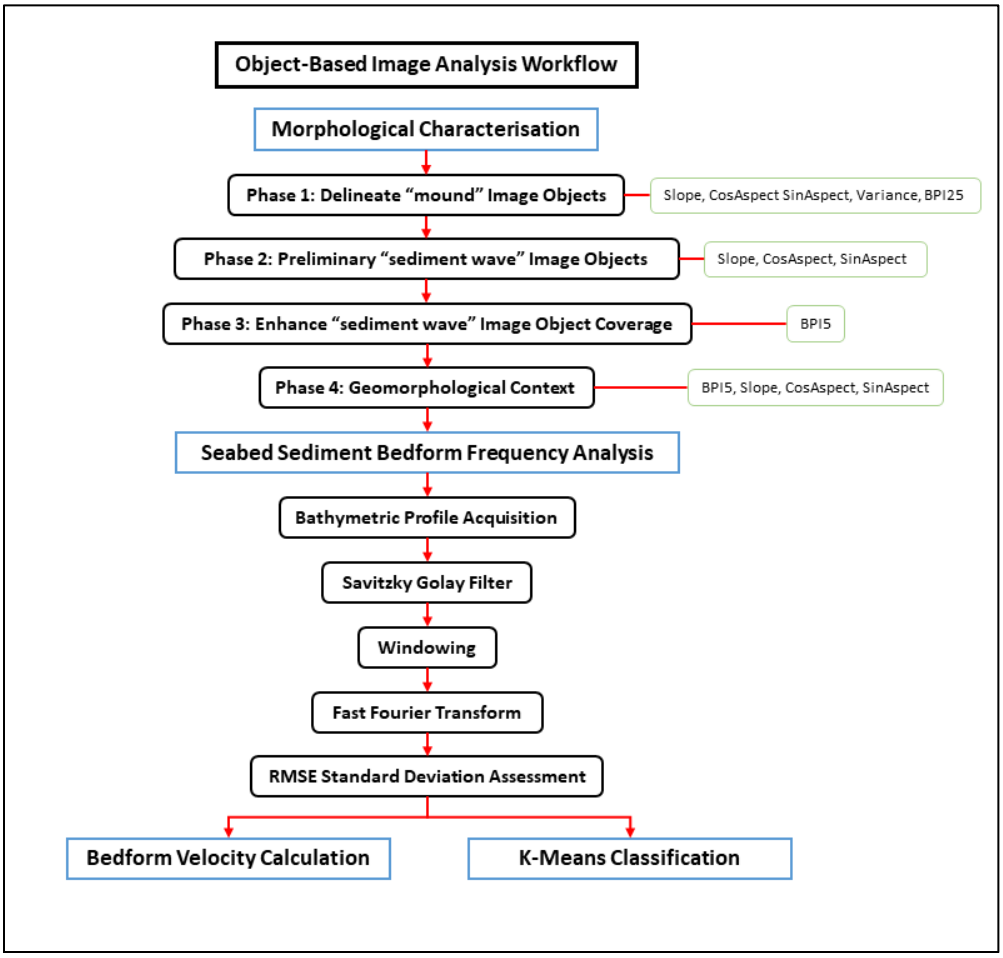

Figure 17: Workflow chart detailing the separate phases for the morphological characterisation, outlined in black and the image layers deployed during this section, outlined in green. The steps required for the seabed sediment bedform frequency analysis are also mapped out, with the outputs of this analysis feeding into the bedform velocity calculation and the k-means classification.

In the first phase, the MRS algorithm was deployed on the cosaspect, sinaspect, slope, and variance image layers with a scale parameter of 10, a shape factor of 0.1, and a compactness factor of 0.1. Any image object with a mean BPI25 of ≥100 standard of a deviation of BPI25 were merged using the spectral difference algorithm. This algorithm merges adjacent image objects if the difference in mean image layer values be-tween the image objects is below a defined threshold (Trimble, 2014). Slope, sinaspect, and cosaspect were the image layers included in this process and a maximum spectral threshold value of 12 was chosen. A second iteration of the spectral difference algorithm was applied to image objects with a mean

BPI25 value of <100% of a standard deviation of BPI25. This combination of algorithms provided preliminary outlines of large-scale features such as the coral mounds and their surrounding moats. Thus, a classification was developed to add geomorphological context for these two larger scale features. “Mound” image objects—hereafter described as “mounds”—were identified as positive topographical features depicted in the BPI25 image layer. “Moat” image objects—hereafter described as “moats”—were identified as negative topographical features depicted by the BPI25 image layer. Any image object with a mean BPI25 value of >50% of a standard deviation of BPI25 was classified as a “mound”. The pixel-based image object resizing algorithm was deployed to improve the accuracy of the “mounds” by expanding their borders until a threshold of >12.5% of a standard deviation of BPI25 was met. Any image object with a mean BPI25 value of <−50% of a standard deviation of BPI25 was classified as a “moat”. The pixel-based image object resizing algorithm was deployed to improve the accuracy of the “moats” by expanding their borders until a threshold of <−12.5% of a standard deviation of BPI25 was met.

Phase two of the morphological characterisation process was deployed on the remaining “unclassified” image objects to delineate regions that potentially represented SSBs. The MRS algorithm was used to segment the sinaspect and cosaspect layers with a scale parameter of 3, a shape parameter of 0.1, and a compactness factor of 0.1. These initial image objects were merged using the spectral difference algorithm on the cosaspect and sinaspect layers with a maximum spectral difference threshold value of 0.3. A “sediment waves” class was assigned to image objects that represented SSBs. To execute this classification, a hue-saturation-value (HSV) colour transformation was employed to help capture truncated image objects with a common slope direction. This colour transformation was applied twice, once with an image layer configuration of slope as red, cosaspect as green, and sinaspect as blue, and a second time with slope as red, sinaspect as green, and cosaspect as blue. Any Image objects with a HSV value derived from the first image layer configuration of ≥0.9 and a high border length/area of ≥0.32 were classified as “sediment waves”. Thus, capturing truncated image objects that represent slopes with a common orientation. Any image object with a HSV value derived from the second image layer configuration of ≥0.9 and a border length/area of 0.32 were classified as “sediment waves”.

During phase three, “sediment waves” image object boundaries were adjusted over several iterations to provide a more accurate representation of these. Summers et al. (2021)

identified BPI5 as the most appropriate image layer for accurately identifying the extent of SSBs. Accordingly, the BPI5 image layer was used here with the pixel-based object resizing algorithm to improve the coverage of SSBs by “sediment waves”. All “sediment waves” were grown until a threshold of >12.5% of one standard deviation of BPI5 had been met. A second implementation of this algorithm grew the “sediment waves” until a threshold of <−12.5% of a standard deviation of BPI5 was met. Any inset “unclassified” image objects found within the “sediment waves” were removed by shrinking the “unclassified” image objects using the pixel-based object resizing algorithm. The candidate surface tension parameter was used as the criterion for this contraction. This parameter creates a square that is defined in image pixels by the user and determines the relative proportion of the classified pixels within this square. Any portion of an inset image object that had <40% labelled as “unclassified”, the resulting portion of that inset image object would be shrunk. The shrunken inset object is replaced with an “intermediate” class, if this “intermediate” image object shared ≥65% of its border with “sediment waves” and if the border length/area was ≥0.35, then it would be classified as a “sediment wave”. Any remaining “intermediate” image objects were redesignated as “unclassified” image objects.

Phase four of the morphological characterisation is similar to the third phase detailed in Summers et al. (2021). However, this phase deviates from the previous workflow by using the MRS algorithm to demarcate the individual sediment wave crests and their corresponding troughs. To complete this action the MRS algorithm is deployed separately to segment the “ridge” image objects—hereafter described as “crests”—and the “valley” image objects—hereafter described as “troughs”—by using the cosaspect and sinaspect bathymetric derivatives. The scale parameter, shape parameter, and the compactness factor were set to 12, 0.1, and 0.1, respectively.

3.2.2.2. Seabed Sediment Bedform (SSB) Frequency Analysis

Upon conclusion of the morphological characterisation, the data were exported as a line shapefile. Any line object that was classified as “crest” was selected for processing. The mean trend for each “crest” line object was acquired using the linear directional mean tool from the spatial statistics toolbox in ArcGIS 10.6 (Figure 18A). The mean compass bearing derived as part of this analysis was integrated with the “crest” line objects to bestow them with the trend direction. A perpendicular line was generated extending 50 m from either side of each line object to avoid geometrical distortions introduced by measurements taken at oblique cross sections (Figure 18B) (Lebrec et al., 2022). This length was chosen as it exceeded the maximum perceived wavelength of all SSBs within the area (Lebrec et al., 2022). The bathymetric profile was extracted at every metre along the perpendicular line, corresponding with the minimum horizontal spatial resolution achievable with these data. As two separate principal SSB orientations were observed in the region, the data were separated by the orientation values after classification.

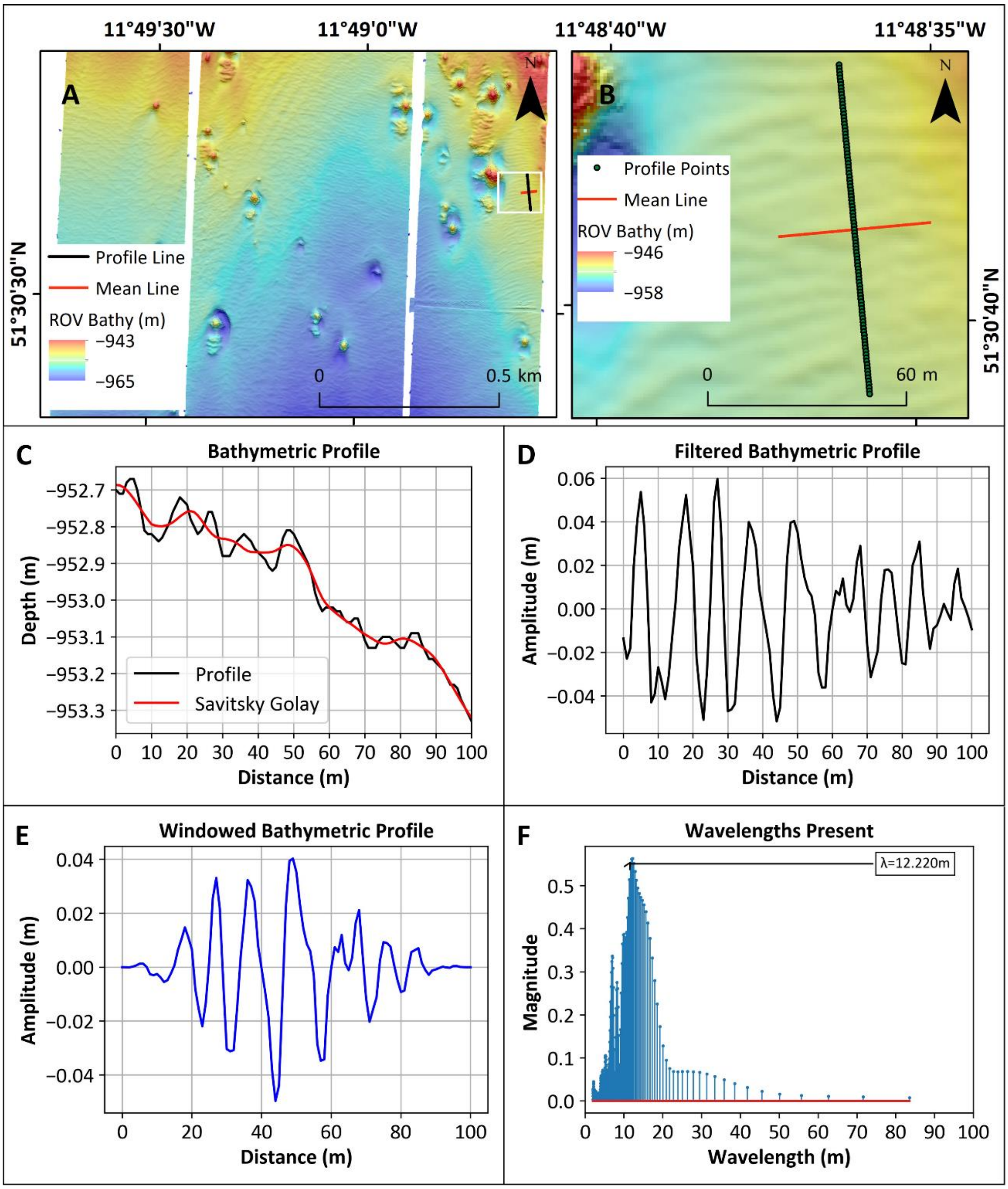

Figure 18: Displaying (**A**) an example of a mean line, its corresponding perpendicular profile line and the extent of (**B**) outlined in white, (**B**) the points generated along the perpendicular line (**C**) the bathymetric profile extracted from the bathymetry with an averaged line generated by a Savitzky

Golay filter with a chosen window of 21 and a polynomial value of 3, (**D**) the bathymetric profile after the subtraction of the Savitzky Golay filter profile, (**E**) the filtered bathymetric profile with a window function applied, and (**F**) a Fast Fourier Transform of the windowed profile providing a spectral view of the wavelengths present in the profile after the removal of the Savitzky Golay filter.

Contemporary research has deployed fast Fourier transformations (FFTs) to deliver spatial series information on profiles derived from SSBs (Trzcinska et al., 2020; Cazenave et al., 2013; Tegowski et al., 2016; Tęgowski et al., 2018). This technique provides the capacity to derive the number of SSBs over a defined interval of space, represented as wavenumber, and the space between each individual SSB, defined as wavelength (Levey et al., 1980). Therefore, after acquisition of the bathymetric profile data had been achieved, they were imported into a pythonic coding environment to apply a FFT to extract the wavelength and wave height of each sediment wave. This workflow was executed using the numpy library in Python 3.7 (Harris et al., 2020). An effective FFT approach requires the data to meet certain prerequisites including stationarity (Perron et al., 2008). Stationarity is a property of the data that asserts that a superimposed trend is not present, and that the wavenumber content remains constant along the length of the appraised profile (Perron et al., 2008; Kuai and Tsai, 2012). Here, this stationarity was assessed using an augmented Dickey–Fuller (ADF) unit root test (Harris, 1992). As many of the SSBs were found to occur on larger scale slope features, detrending techniques were deployed to ensure stationarity was achieved (Spagnolo et al., 2017; Wang et al., 2020). Thus, preventing these regional low frequency slopes from dominating the analysis and obfuscating the local wavenumber value (Kuai and Tsai, 2012). The Savitsky Golay filter was deployed to achieve this, which fits data points contained within a moving window to a polynomial (Savitzky and Golay, 1964; Chen et al., 2004; Azami et al., 2012). Several values for moving window size were assessed in each instance, with the window size set at 10-step intervals ranging from 21 to 101. The window size chosen was the one that achieved stationarity and the lowest combined root mean square and standard deviation values and was subtracted from the bathymetric profile (Figure 18C & D). Another assumption of FFT is the presence of an integral number of SSBs within the analysis (Perron et al., 2008). Data that fail to fulfil this condition can introduce spectral leakage into the analysis, where many additional wavenumbers occur adjacent to the high amplitude peaks (Spagnolo et al., 2017). The solution was to window the SSB profile, which ensures that the edges of the sample taper to 0 m and an integral value of wavelength is achieved (Figure 18E) (Cazenave et al., 2013; Spagnolo et al., 2017). After windowing, the data were then zero padded to ensure that the associated wavenumber is more resolvable in the spectral profile. FFT was applied to the data after zero padding had been completed. Once achieved, the wavenumbers that were derived were limited to below 0.01 m^{-1} to further exclude any large profiles. The wavenumber with the highest spectrum value from this subset was converted to wavelength in each instance (Figure 18F). Any SSB profile that failed to achieve stationarity after the initial processing were filtered at a moving average of 11 to capture regional slopes with a higher wavenumber. If this failed to achieve stationarity, then the SSB was designated a wavelength and wave height value of 0. The Nyquist interval is the minimum measurable wavelength discernible within a dataset, this was obtained by doubling the sampling resolution of the data (Cazenave et al., 2013).

3.2.2.3. K-Means Classification

K-means classification separates the objects into a group or cluster with a similar data profile while ensuring that the object is sufficiently distinct from other groups in the analysis (Heil et al., 2019). The number of clusters employed is user defined by determining the cluster with the lowest Euclidean distance from its cluster centre to the object within the multi variant data space (Javadi et al., 2017). Initially these cluster centres are randomly distributed. Data are categorised by bestowing the class of the closest cluster centre (Ismail et al., 2015). The positions of these cluster centres are optimised by discerning the centre configuration with the lowest aggregated squared error in n-dimensional space, with n corresponding to the number of variables included (Javadi et al., 2017; Ismail et al., 2015; Orhan et al., 2011). K-means clustering is the most common clustering technique due to its simplicity and effectiveness and is frequently used to partition marine environmental data (Ismail et al., 2015; Orhan et al., 2011; Wu et al., 2014).

Upon morphological characterisation of the data, the image objects were exported as a polygon shapefile. Any image object classified as “crest” was selected as an input for the k-means classification, the remaining image objects were excluded (Figure 19). The wavelength for each “crest” derived during the seabed sediment bedform frequency analysis were added to the shapefile attributes. All “crest” image objects were imported into a python coding environment to classify them based on morphology, spatial density, and mean bathymetric derivatives (Table 6). Values 2 to 8 were assessed for values for k by comparing their respective inertial values, which represents the sum of squared distances of the samples to their closest cluster centre (Pedregosa et al., 2011). The value of k found before a significant change in the slope of inertia values will be deemed the most appropriate value for k, as this would indicate the effective clustering of the morphologies displayed by the “crests” while maintaining the minimum number of classes required to describe the data. A separate class density distribution layer was derived for each k-means class. Calculating the density of the features as points for each class over a defined pixel neighbourhood (75 m) with density being displayed as number of class point features per km^2. Geometrical features available in eCognition were derived from the image objects and were the principal components to the classification, all features used in the k-means classification are outlined in Table 6. The features that displayed the greatest degree of inter class variation were used to reconcile the k-means classification to the environment from which they were derived.

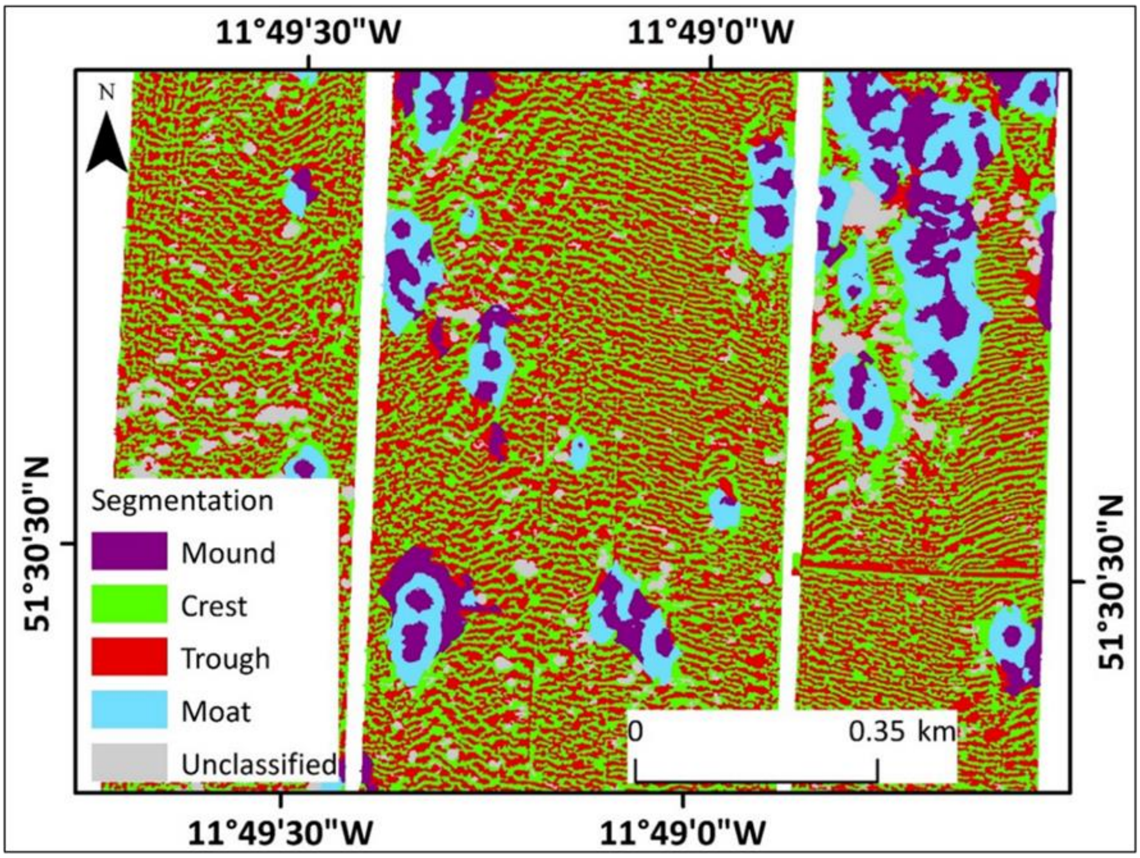

Figure 19: Displaying the multi-scale morphological characterisation output with the larger scale coral mound features—the “mounds” and “moats”—and the lower scale features—the “crests” and “troughs”.

Table 6: Image object features employed in the k-means classification and their respective feature categories.

Feature Category	Image Object Feature
Morphology	Length/Width
	Shape Index
	Length/Area
	Area
	Roundness
	Elliptic Fit
	Asymmetry
	Rectangular Fit
	Curvature/Length
	Wavelength
Spatial Density	Point Density
Bathymetric Derivative	Mean depth difference to neighbouring "troughs"
	Mean Slope

3.2.3. Bedform Velocity Calculation

Current speed calculations were based on the bedform velocity matrix presented by Stow et al. (2009). Stow et al. (2009) delineated transverse bedforms into 6 separate categories including ripples, sinuous dunes, barchanoid dunes, sand waves, gravel waves, and giant sediment waves (mud waves). These categories are defined using the wavelength, wave height, and the sinuosity of the bedform. Furthermore, each category is given a corresponding minimum and maximum current velocity. In our study, we established individual multiple linear regression using the ranges for wavelength, wave height, and current velocity provided by Stow et al. (2009) for each SSB category. With wavelength and wave height as the explanatory variables and current velocity as the response variable. The resultant wavelengths and wave heights obtained from the FFT workflow outlined above were used to identify each "crest" as one of these transverse SSB categories. Once labelled, a predicted velocity was derived for the "crest" using the regression model developed for that category. Median values for current speed were obtained for each k-means class separately at ≤25 m, ≤50 m, ≤100 m, ≤150 m, and ≤200 m distances from the "mounds" to observe any relationships between current speed variation and proximity to "mounds". Median values were also obtained for each class for the 2 dominant SSB orientations. Furthermore, current orientations were derived for each k-means class at ≤25 m and ≤200 m from "mounds" to determine any potential influences the CWC mounds may have on current orientation. Median values for current orientation were also derived at these distances for each k-means class.

3.3. Results

3.3.1. Multibeam Cross Check Analysis

Cross checking revealed that these MBES bathymetry data achieved the IHO special order standard for accuracy of bathymetric data.

3.3.2. Morphological Characterisation

The median area for “crests” was 140 m^2. The median curvature to length value was 7.80 and the median length to width value was 2.31.

3.3.3. Fast Fourier Transform and SSB Frequency Analysis

Three SSB categories were observed within the “crests”: sediment ripples, sinuous dunes, and sand waves. Forty-eight “crests” exceeded the filter parameters and thus were designated a wave height and wavelength of 0 m. The minimum sampling interval observed was 2 m.

3.3.4. Classification

A 5 k-means clustering was chosen as it occurred before a significant local variation in the inertial value slope (Figure 20A&B). Linearity and sinuosity in this classification are depicted by the values for length/width and curvature/length. Higher length/width and lower curvature/length values designate greater SSB linearity. Lower length/width and higher curvature/length values reveal increased SSB sinuosity. Class 0 had the highest median length/width of 3.62 m, and the largest areal extent with a median area of 233 m^2. Moreover, this class exhibits a low sinuosity with the second lowest median curvature/length value of 6.34°. The median wave height for these objects was the second highest observed at 0.315 m. The median wavelength for these image objects was the shortest for any class at 11.29 m. These image objects had a mean slope of 1.47°. Class 1 is the second most linear with a median length/width of 2.79 m and a moderate areal extent with a median value of 155 m^2. This class exhibits a low sinuosity with the lowest median curvature/length value of 6.29°. These image objects had a mean slope of 1.46°. Class 2 had the lowest length to width ratios with a median value of 1.65 m. It also had the lowest median areal extent (90 m^2). This class had the second highest median curvature/length at 9.72° and the second lowest mean slope at 1.39. This class also had a median wave height of 0.293 m. Class 3 had a low median length/width of 1.93. They also had the second lowest median area value at 114 m^2. This class had the highest median curvature/length value length at 10.35°. These image objects a mean slope of 1.31°. Class 4 had the highest median wavelength value recorded at 12.43 m and the lowest median wave height value at 0.128 m. These image objects had moderate median curvature/length and length/width values of 7.15° and 1.93 m, respectively. These image objects had a mean slope of 3.27°. Further median values for each k-means class are provided in Table 7.

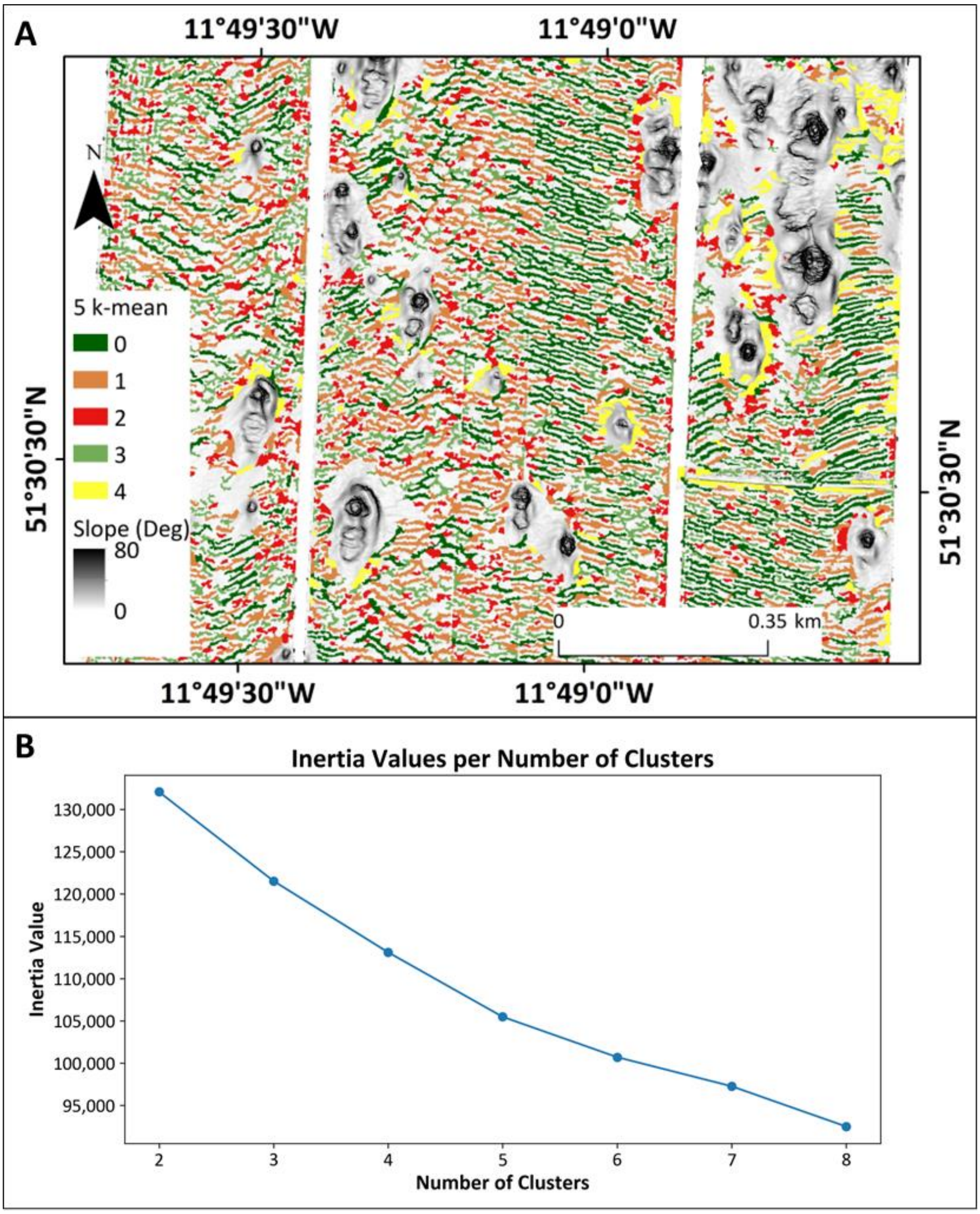

Figure 20: Displaying (**A**) the slope image layer and the product of the 5 k-means classification of morphology, spatial density, and mean bathymetric derivative, (**B**) inertial values for each value of k.

6605 "crests" were orientated from south-west to north-east, 5105 "crests" were orientated from south-east to north-west. Furthermore, 64% of all "crests" that were classified as class 0 and 58% of "crests" that were classified as class 1 are orientated to the north-east.

Table 7: Median area, length/width, curvature/length, mean slope, and wave height for each class.

Class	Area (m^2)	Length/Width	Curvature/Length	Slope (Deg)	Wave Height (m)
0	233	3.62	6.34	1.47	0.315
1	155	2.79	6.29	1.46	0.323
2	90	1.65	9.72	1.39	0.293
3	114	1.93	10.35	1.31	0.293
4	170	1.93	7.15	3.27	0.128

3.3.5. Current Velocity Analysis

A bimodal distribution in current speeds was identified occurring throughout the study site with a mean current speed of 0.37 m s^{-1} (Figure 21A). Therefore, the "crests" were separated into 2 groups: >0.40 m·s^{-1} (the fast group abbreviated to FG), and ≤0.40 m·s^{-1} (the slow group abbreviated to SG) to ensure successful production of summary statistics for each mode. The median current speed for all SG "crests" was 0.28 m·s^{-1} and the median current speed for all FG "crests" was 0.60 m·s^{-1}. When comparing the median current speeds taken at ≤25 m from "mounds" and median current speeds taken at ≤200 m from "mounds", an increase current speed with increasing distance away from the "mounds" was noted. For instance, the SG "crests" displayed a consistent increase in current speed across the 2 chief orientations with increasing distance from the "mounds" (Figure 21B&C). The north-north-west aligned SG "crests" showed an increase in median current speed for all 5 classes when comparing median current speeds acquired at ≤25 m and ≤200 m from the "mounds". Class 0 showed an increase in median current speed of 0.013 m·s^{-1} from 0.266 m·s^{-1} to 0.279 m·s^{-1}. Class 1 exhibited an increase of 0.007 m·s^{-1} from 0.273 m·s^{-1} to 0.280 m·s^{-1}. Class 2 displayed a rise in median current speed of 0.007 m·s^{-1} from 0.269 m·s^{-1} to 0.276 m·s^{-1}. Class 3 showed an increase in median current speed of 0.006 m·s^{-1} from 0.271 m·s^{-1} to 0.277 m·s^{-1}. Class 4 exhibited a rise in median current speed of 0.002 m·s^{-1} from 0.26 m·s^{-1} to 0.262 m·s^{-1}.

The SG image objects orientated to the north-north-east displayed an increase in median current speeds when comparing median current speeds taken at ≤25 m and ≤200 m from the "mounds" in 4 of 5 classes. Class 0 displayed an increase in median current speeds of 0.012 m·s^{-1} from 0.268 m·s^{-1} to 0.280 m·s^{-1}. Class 1 displayed an increase in median current speeds of 0.014 m·s^{-1} from 0.266 m·s^{-1} to 0.280 m·s^{-1}. Class 2 exhibited an increase in median current speeds of 0.001 m·s^{-1} from 0.277 m·s^{-1} to 0.278 m·s^{-1}. Class 3 displayed an increase in median current speeds of 0.014 m·s^{-1} from 0.266 m·s^{-1} to 0.280 m·s^{-1}.

Conversely, class 4 exhibited a decrease in median current speeds of 0.0002 $m{\cdot}s^{-1}$ from 0.264 to 0.263 $m{\cdot}s^{-1}$.

The FG image objects orientated north-north-west have the largest increase in median current speeds between these distance intervals from the “mounds”. Four of the 5 k-means classes contained in the FG “crests” mode exhibit an increase in median current speed between the ≤25 m and ≤200 m distance intervals from the “mounds”. For instance, the FG objects assigned to class 0 and aligned to the north-north-west experienced an increase in median current speed of 0.033 $m{\cdot}s^{-1}$ from 0.542 $m{\cdot}s^{-1}$ m to 0.575 $m{\cdot}s^{-1}$. Class 1 from the same orientation and current regime also experienced an increase in median current speed of 0.034 $m{\cdot}s^{-1}$ from 0.543 $m{\cdot}s^{-1}$ to 0.577 $m{\cdot}s^{-1}$. Class 2 “crests” from this subset exhibited a smaller increase in current speed of 0.006 $m{\cdot}s^{-1}$ from 0.559 $m{\cdot}s^{-1}$ to 0.565 $m{\cdot}s^{-1}$. An increase in current speed of 0.030 $m{\cdot}s^{-1}$ from 0.530 $m{\cdot}s^{-1}$ to 0.560 $m{\cdot}s^{-1}$ was observed for class 3 “crests”. Conversely, class 4 for the same orientation and current regime experienced a decrease in median current speed of 0.023 $m{\cdot}s^{-1}$ from 0.571 $m{\cdot}s^{-1}$ to 0.548$m{\cdot}s^{-1}$.

For the north-north-east aligned FG “crests”, 2 classes exhibited an increase in median current speed. Class 0 had an increase in median current speed of 0.006 $m{\cdot}s^{-1}$ from 0.564 $m{\cdot}s^{-1}$ to 0.570 $m{\cdot}s^{-1}$. Class 1 had an increase in median current speed of 0.021 $m{\cdot}s^{-1}$ from 0.556 $m{\cdot}s^{-1}$ to 0.577 $m{\cdot}s^{-1}$. Three classes aligned north-north-east in the FG current regime have shown a decrease in current speed. Class 2 had a decrease in median current speed of 0.026 $m{\cdot}s^{-1}$ from 0.590 $m{\cdot}s^{-1}$ to 0.564 $m{\cdot}s^{-1}$. Class 3 displayed a decrease in median current speed of 0.002 $m{\cdot}s^{-1}$ from 0.56 $m{\cdot}s^{-1}$ to 0.558 $m{\cdot}s^{-1}$. Class 4 exhibited a decrease in median current speed of 0.001 $m{\cdot}s^{-1}$ from 0.545 $m{\cdot}s^{-1}$ to 0.544 $m{\cdot}s^{-1}$ (Figure 21B–E).

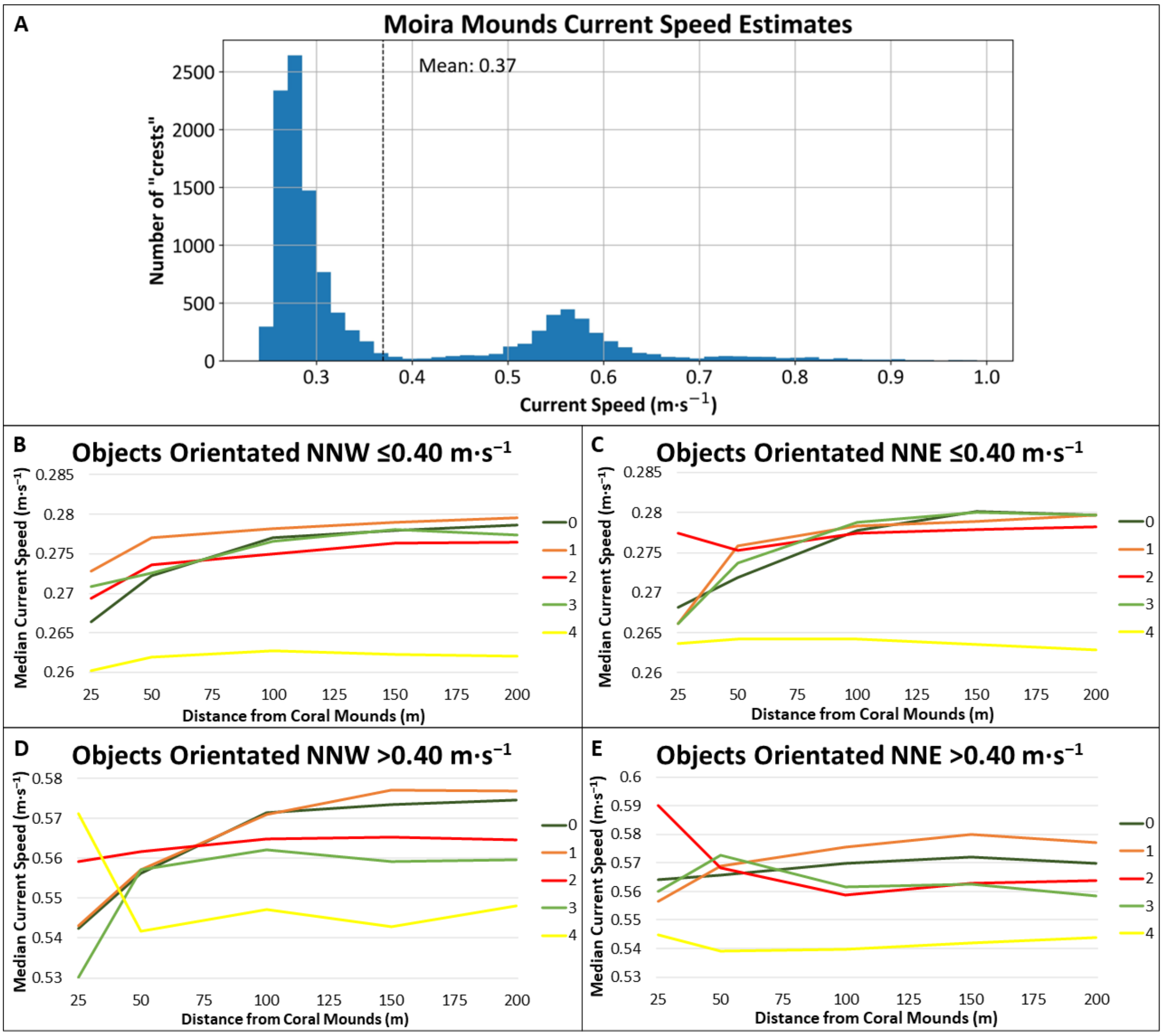

Figure 21: (**A**) Current speed values for all "crests", median current speed values for (**B**) north-north-west aligned slower group (SG) "crests", (**C**) north-north-east aligned SG "crests", (**D**) north-north-west aligned faster group (FG) "crests", (**E**) north-north-east aligned FG "crests".

Moreover, when comparing the relative proportion of FG "crests" versus SG "crests" at the same distance intervals relative to the "mounds", an increase in the proportion of FG "crests" was observed in both orientations. An increase of 11.4 percentage points from 15.6% to 27.0% was noted for "crests" orientated to the north-north-west (Figure 22A). A smaller increase in the proportion of FG "crests" orientated to the north-north-east was noted with an increase of 4.5 percentage points from 23.3% to 27.8% (Figure 22B).

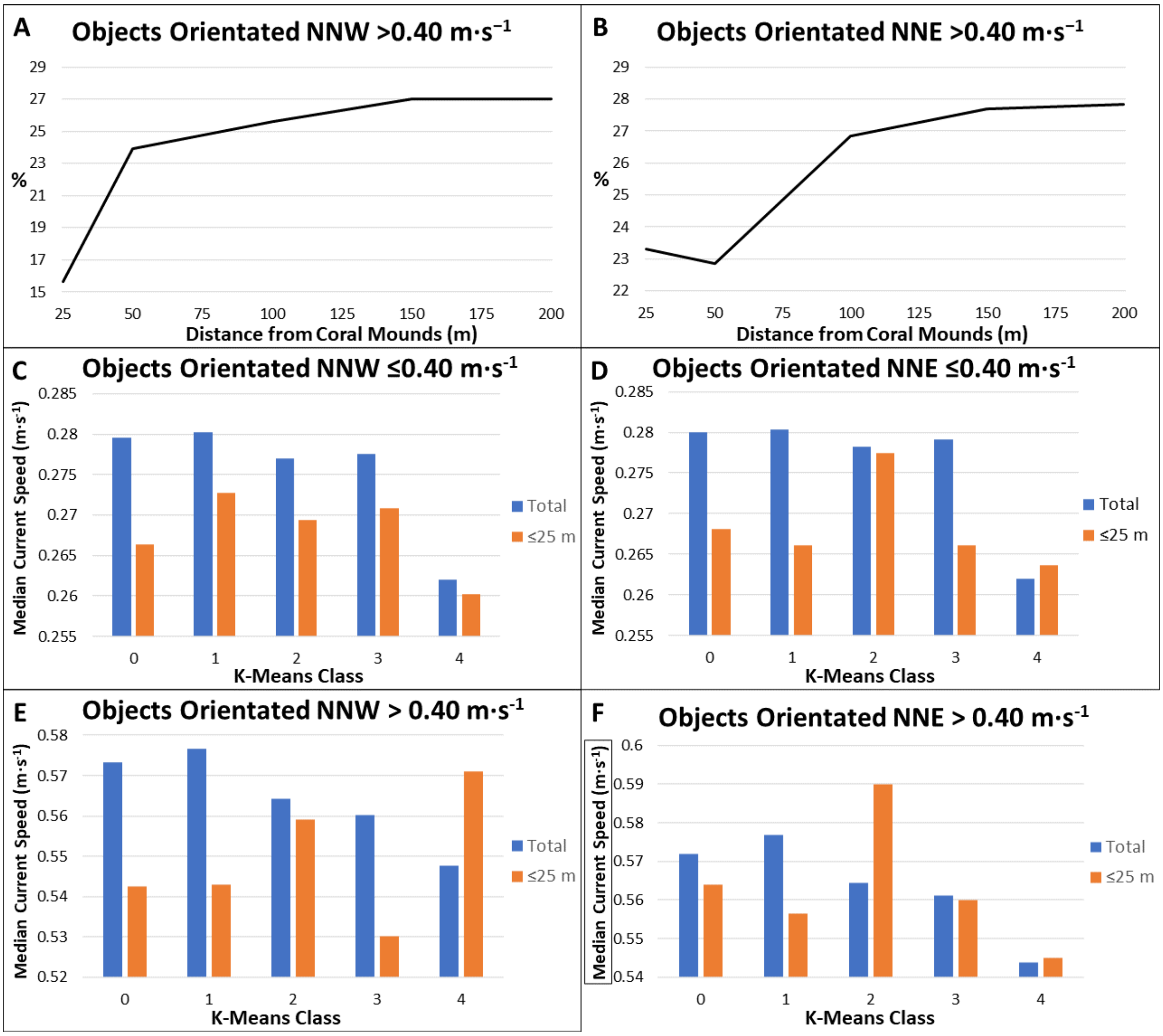

Figure 22: The proportion of FG "crests" over distance from the "mounds" for (**A**) north-north-west aligned "crests", (**B**) north-north-east aligned "crests", and a comparison of median current speeds for each class taken at ≤25 m from the "mounds" and the whole dataset for (**C**) all north-north-west aligned SG "crests" (**D**) north-north-east aligned SG "crests", (**E**) north-north-west aligned FG "crests", (**F**) north-north-east aligned FG "crests".

An increase in median current speeds was observed for all k-means classes when comparing the median current speed per class acquired at ≤25 m away from the "mounds" and the median current speed per class for all SG "crests" aligned to the north-north-west (Figure 22C). The largest increase was observed for class 0 at 0.013 m·s^{-1}. Similarly, an increase in median current speeds per k-means class was observed for 4 of the 5 classes when comparing the median current speed per class acquired at ≤25 m away from the "mounds" and the median current speed per class acquired for all SG "crests" aligned to the north-north-east. The largest increase was observed for class 1 at 0.014 m·s^{-1} (Figure 22D). A decrease of 0.00173 m·s^{-1} was noted for class 4. There was an increase in median current speeds for 4 of the 5 k-means classes when comparing the median current speed per class acquired at ≤25 m away from the "mounds" and the median current speed per class for all FG "crests" aligned to the north-north-west (Figure 22E). The largest increase was observed for class 1 at 0.034 $m \cdot s^{-1}$. A decrease of 0.023 $m \cdot s^{-1}$ was observed for class 4. There was an increase in median current speeds for 3 of the 5 k-means classes noted when comparing the median current speed per class acquired at ≤25 m away from the "mounds" and the median current speed per class for all FG "crest" "class aligned to the north-north-east. The largest increase in median current speed was observed for class 1 at 0.020 $m \cdot s^{-1}$. The largest decrease in median current speed was observed for class 3 at 0.026 $m \cdot s^{-1}$.

Current speed and current direction were extracted for each class image object at ≤25 m and ≤200 m away from the "mounds" (Figure 23A–J). However, as the direction derived from the linear directional mean tool was ambiguous when observed in the full 360° range 180° was subtracted from all direction values above 180°, allowing for separation between the 2 dominant SSB orientations. Thus, any "crest" with orientation values occurring between 0° and 90° represent those SSBs whose crests aligned to the north-north-west. Any "crest" with orientation values occurring between 90° and 180°represent SSBs whose crests were aligned to the north-north-east. The median current orientations acquired at ≤200 m from the "mounds" for classes 0, 1, 2, 3, and 4 aligned to the north-north-west were 340°, 342°, 327°, 332°, and 329°, respectively. The median current orientations acquired at ≤25 m from the "mounds" for classes 0, 1, 2, 3, and 4 with the same alignment were 325°, 341°, 322°, 321°, and 325°, respectively. A bimodal distribution of current flow was noted for class 0 at ≤200 m from the "mounds" however, this was not noted for any of the other k-means classes. The median current orientations acquired at ≤200 m from the "mounds" for classes 0, 1, 2, 3, and 4 aligned to the north-north-east were 20°, 19°, 29°, 29°, and 28°, respectively. The median current orientations acquired at ≤25 m from the "mound" image objects for classes 0, 1, 2, 3, and 4 with the same alignment were 28°, 24°, 37°, 33°, and 20°, respectively.

Density distribution layers reveal that the greatest density of class 0 occurs to the north-east of the study site (Figure 24A). The greatest density of class 1 occurs to the centre and south of the study site (Figure 24B). The greatest density of class 2 and 3 occurs to the east and north-west (Figure 24C, D). Class 4 "crests" occur in greatest density to the north-east directly surrounding the CWC mounds in this area (Figure 24E).

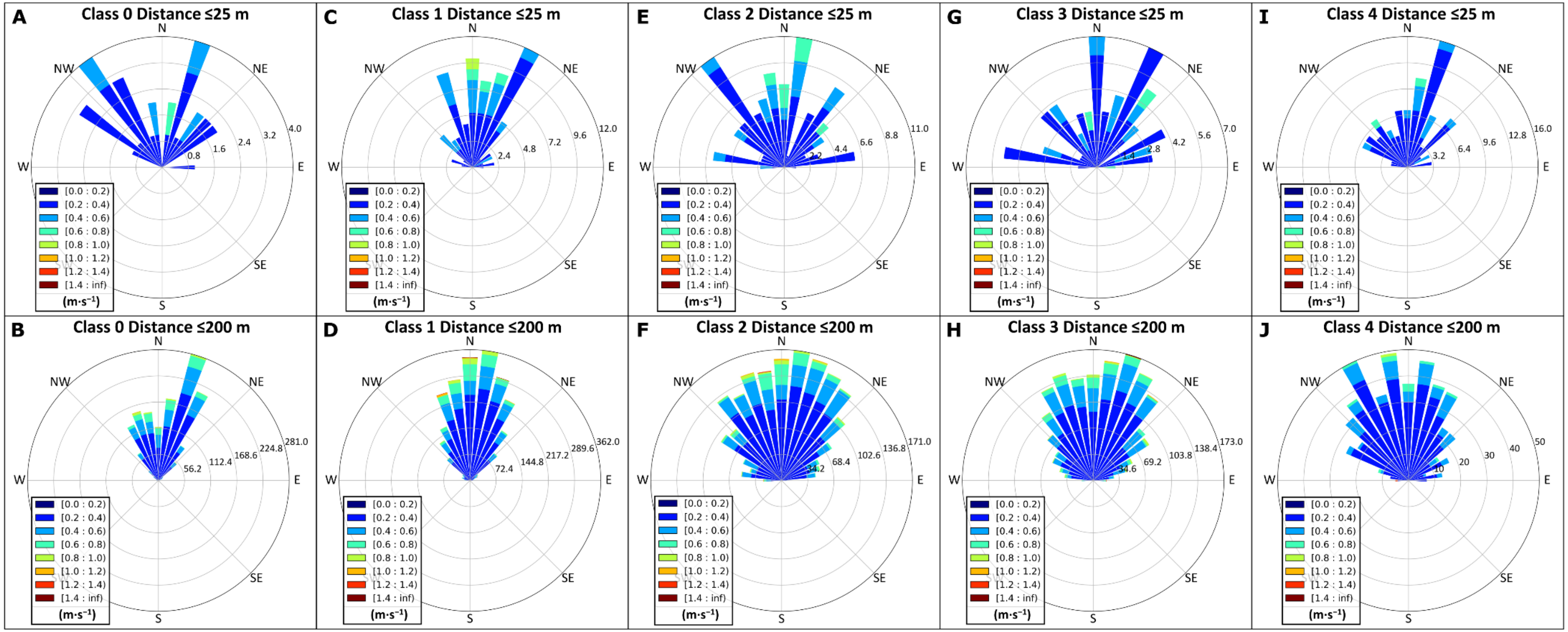

Figure 23: Polar plots indicating current speed and orientation for (**A**) class 0 ≤25 m proximity to the "mounds", (**B**) class 1 ≤200 m proximity to the "mounds", (**C**) class 1 ≤25 m proximity to the "mounds", (**D**) class 1 ≤200 m proximity to the "mounds", (E) class 2 ≤25 m proximity to the "mounds", (**F**) class 2 ≤200 m proximity to the "mounds", (**G**) class 3 ≤25 m proximity to the "mounds", (**H**) class 3 ≤200 m proximity to the "mounds", (**I**) class 4 ≤25 m proximity to the "mounds", (**J**) class 4 ≤200 m proximity to the "mounds".

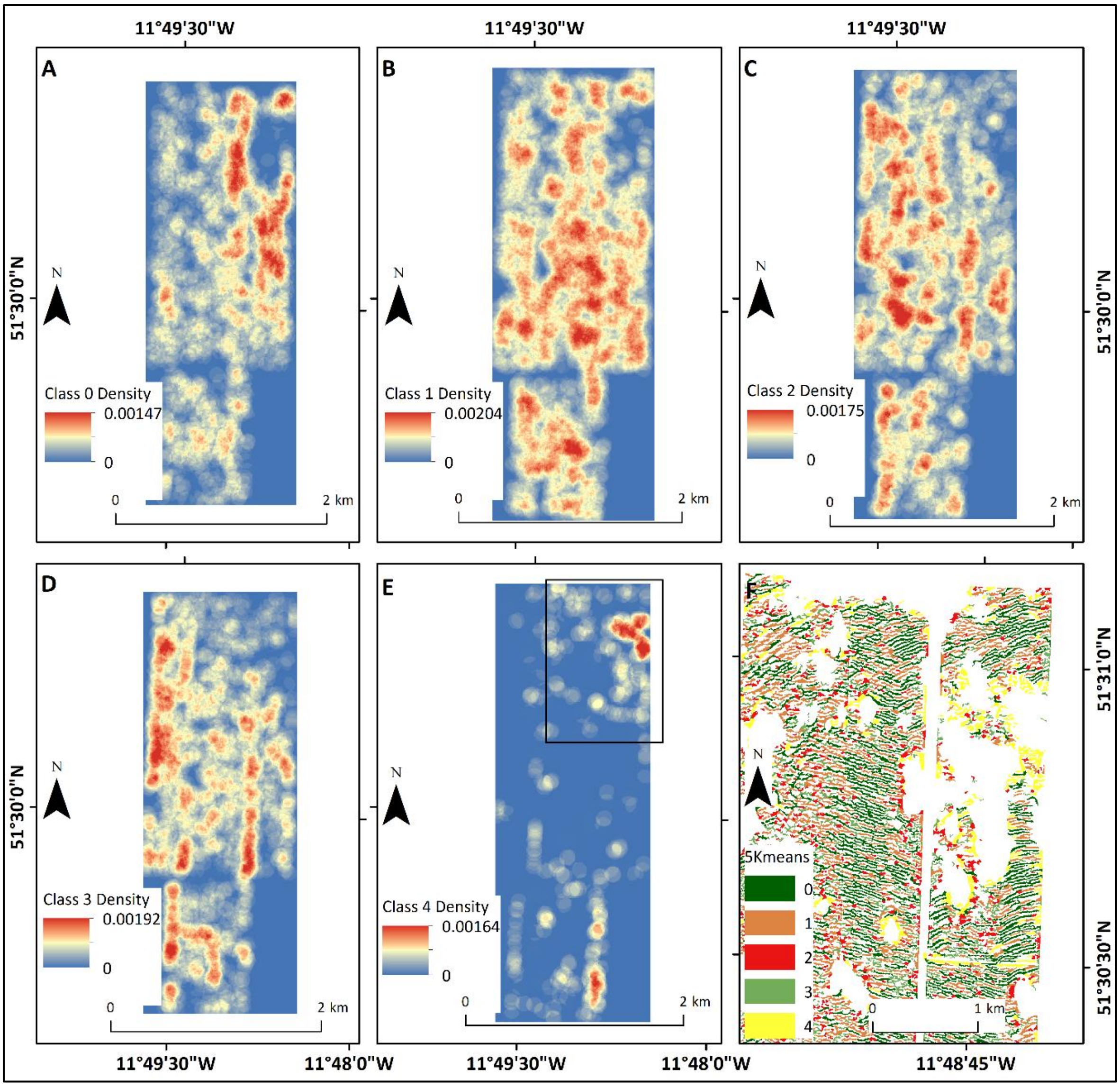

Figure 24: 5 k-mean class density maps for each class: (**A**) class 0, (**B**) class 1, (**C**) class 2, (**D**) class 3, and (**E**) class 4 displaying the extent of (**F**) outlined in black, (**F**) displays the k-means classification for the "crests" in the north-western portion of the study site.

3.4. Discussion

3.4.1. K-Means Classification of Sediment Bedform Type

A five k-means classification produced a robust identification of transverse SSB types separating each class chiefly by linearity, sinuosity, and areal extent (Table 8). Sinuosity gradually increased from class 0 to class 3, with class 0 representing large straight SSBs and class 3 representing medium sinuous SSBs (Table 8). A slight decrease in median current speed was observed for classes 2 and 3—small and medium sinuous SSBs—when comparing them with classes 0 and 1—large and medium straight SSBs (Figure 22C–F). Therefore, the increase in sinuosity observed for the medium and small sinuous SSBs is not due to an increase in current speed, rather this increase in sinuosity is a result of the superimposition of one or more sets of bedforms onto another. Large straight SSBs represent the most linear SSBs that occur in regions of local unidirectional flow. Furthermore, the unidirectional flow denoted by this category is supported by the clear bimodality of the current flow orientations acquired for these SSBs at ≤200 m proximity to the "mounds" (Figure 23B). Few intermediate current flow orientations occur between these two modes, indicating the presence of two dominant current regimes, one flowing to the north-north-east, and the other flowing to the north-north-west. This bimodality is not detected at ≤200 m proximity to the "mounds" for any of the other SSB categories. Hence, this suggests an increase in interference between the two dominant current regimes for each of the remaining categories. Moreover, this interference is most pronounced in the small and medium sinuous SSBs, where SSBs exhibit a greater level of sinuosity and thus, a greater degree of SSB superimposition. Class 4—medium obstructed SSBs—are SSBs adjacent to CWC mounds, whose wave heights are reduced due to the obstruction in current flow created by the CWC mounds. Consequently, these SSBs consistently have the lowest median current speed (Figure 22C–F).

Table 8: Reconciliation of k-means classes to environmental categories complete with a brief interpretation.

K-Means Class	Category	Interpretation
0	Large straight SSBs	Elongate parallel SSBs formed due to consistent unidirectional flow.
1	Medium straight SSBs	Truncated parallel SSBs formed due to consistent unidirectional flow with an increase in bedform superimposition.
2	Small sinuous SSBs	Sinuous crests with the smallest areal extent whose profile formed due to bedform superimposition rather than increased local current speeds.
3	Medium sinuous SSBs	Sinuous crests with a moderate areal extent, this class represents the bedforms with the highest degree of interference between the two dominant current regimes.
4	Medium obstructed SSBs	Profoundly influenced by the obstruction of the current flow induced by the CWC mounds, causing a significant reduction in their wave height relative to the other classes.

3.4.2. Regional, Local and Micro Hydrodynamics

This study site occurs between 941 and 1006 m depth which is within the MOW water mass which generates northerly flowing contour currents that are influenced by tidal rectification processes (White, 2007; Dorschel et al., 2007; Wheeler et al., 2011). Dorschel et al. (2007) observed north-north-west migrating sediment waves to the east of the nearby Galway Mound and postulated that the regional geostrophic contour currents were chiefly responsible for their formation. Given that the north-north-west aligned currents observed here agree with these findings, the associated bedforms are considered to have a similar origin. However, this does not explain the clear presence of a north-north-east current regime within this region. The density of distribution of each of the SSB categories can be used as a surrogate for the consistency of local current flow. An increase in the density of medium and small sinuous SSBs can be found to the east and north-east of the study site, this increase implies an increase in the inconsistency of the current flow within this portion of the site. Moreover, this increase occurs as the site approaches the margin of the blind channel (Figure 16A), suggesting that the topographic effects of the channel margin cause this disruption. Consequently, the north-north-east aligned flow may be due to the local topographical steering of the contour currents by the channel margin. Additionally, the presence of the large linear SSBs to the north-west of the study site coincides with the centre of the channel and may signify a decrease in the disruption of the contour currents, leading to more consistent unidirectional flow (Figure 23F). This is also supported by the larger proportion of north-north-west aligned large linear SSBs to the west of the region. This local increase in unidirectional flow to the north-west of the study site also corresponds with the greatest density of mounds reported by Lim et al. (2018a), suggesting that this type of flow is more favourable to CWC growth. This may explain the decrease in mound density to the east of the site, where greater disruption of currents occurs. Therefore, the interaction of the regional MOW tidally influenced contour currents coupled with the local topographical steering by the blind channel may be the cause of the bimodal distribution of current flow direction.

A change of >7° in median current direction is observed for both dominant current regimes when comparing the orientations of the current flow acquired within ≤25 m of the "mounds" and ≤200 m to the "mounds" for large linear SSBs and small sinuous SSBs (Figure 23A, B, E, F). This suggests that current flow for both current regimes is refracted as it approaches the "mounds" thus, demonstrating topographic steering that is proximal to the "mounds" where topographical steering occurs on a micro scale directly surrounding the "mounds". Nevertheless, this topographic steering is not as apparent when observing the smaller coral mounds, suggesting larger mounds have a more profound influence on the current regime, this is in agreement with the analysis conducted by Lim et al. (2018a).

In addition to the current orientation, a bimodal distribution of the current speed values is also evident (Figure 21A). The >0.40 $m \cdot s^{-1}$ FG mode is significantly lower than the ≤0.40 $m \cdot s^{-1}$ SG mode suggesting that these higher current speeds are locally intensified currents and are not indicative of the prevailing regional current speed. While the mean value for current speed procured for the entire "crest" class may not adequately reflect the overall current speed distribution observed in Figure 21A, it is similar to previous regional current speed estimations for this and nearby areas

(Dorschel et al., 2007; Lim et al., 2018a). Moreover, this mean value may demonstrate how current speed estimations derived from a single or limited sediment samples can be misleading and therefore, not a reflection of the significant spatial variations in local current speeds.

3.4.3. Mound Proximity and SSB Characteristics

The presence of the "moats" surrounding the larger "mounds" illustrates intensive scouring, forming a comet and tail morphology, and is postulated to occur due to high intensity, low frequency north–south cold water cascade events (Lim et al., 2018a). However, when examining the BPI25 bathymetric derivative layer, we can see that the tails alter direction with movement towards the east and north-east of the study site (Figure 25). This change in tail orientation coincides with the increase in density of medium and small sinuous SSBs, indicating an increased disruption of current flow potentially attributable to the local topographic steering imprinted by the approach to the channel margin (Conti et al., 2019). The resulting current flow would become more aligned with the CWCs occurring on slopes orientated to the SW, exposing the CWCs on slopes orientated to the NE to more erosive conditions that are unfavourable to CWC growth. Conversely, a consistent reduction in the median current speed is observed with increasing proximity to the mounds for each of the SSB categories. For instance, the lowest current speeds for each SSB category for the north-north-west aligned "crests" are found within ≤25 m of the "mounds". This is consistent for the SG and the FG "crests" except for the FG medium obstructed SSBs. Additionally, the declining proportion of FG SSBs with increasing proximity to "mounds" for the north-north-west SSB orientation further indicates the deceleration of current speed.

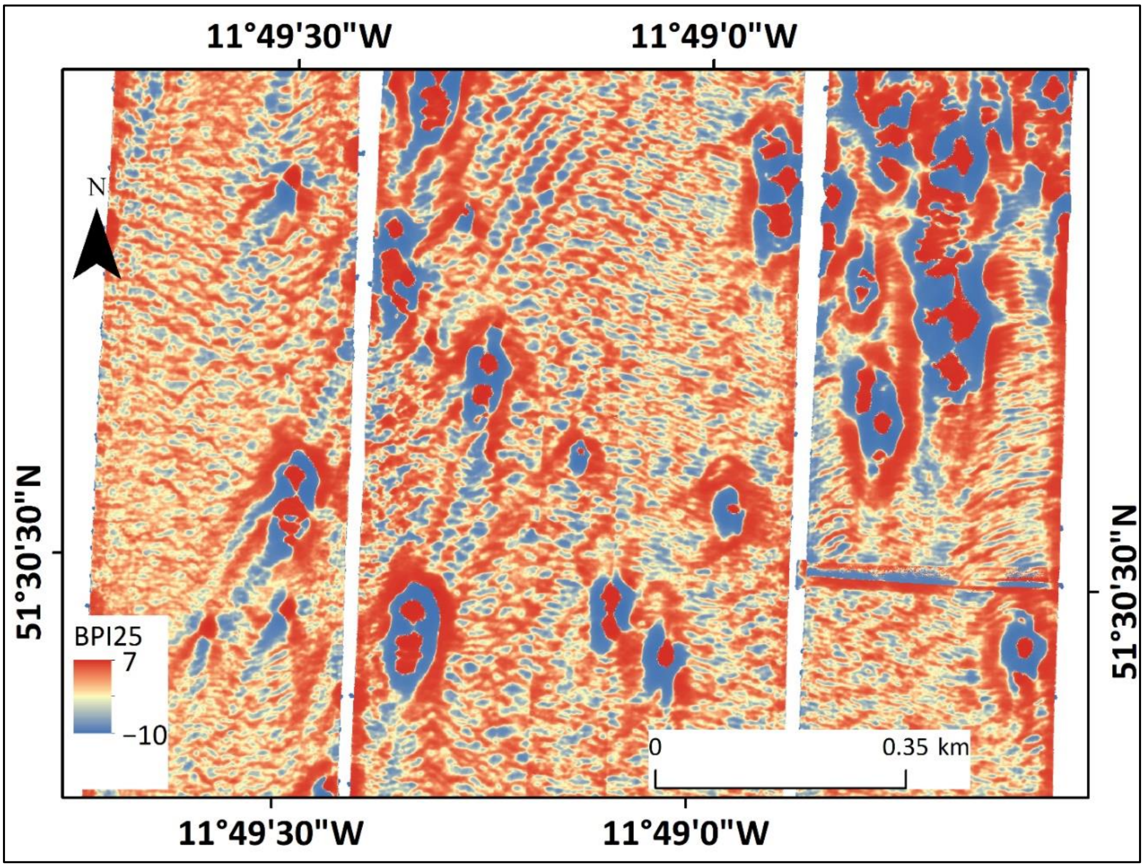

Figure 25: BPI25 bathymetry derivative layer displaying the intense scouring as negative topographic features surrounding the CWC mounds forming a comet and tail morphology.

However, the decline of current speed is not equal across the two dominant current orientations. What is evident is a slight decline in the current speed values for the SG and FG SSBs orientated to the north-north-east, however this decline is not as significant as those orientated to the north-north-west. Moreover, the proportion of FG SSBs orientated to the north-north-east remain relatively consistent with proximity to the "mounds". Suggesting that the currents originating from the south-south-west are not impeded as much as their south-south-eastern counterparts. This direction specific obstruction may be influenced by the intensely scoured moats, causing increased erosion of CWC framework, and removing a portion of the obstruction that they provide on north-east aligned slopes. These findings are reflected by Conti et al. (2019) who note that live coral framework mainly occur on the north of Piddington Mound across two main slope orientations, at 300° and 70°, with most of the live coral framework occurring on slopes with an orientation of 300°. The diminished presence of CWCs on the north-eastern side of the Piddington

Mound may indicate that the conditions imposed by the postulated cold water cascade events may prevent effective growth of CWCs for slopes with this orientation or that regular current speeds are too high for corals to thrive. The reported mean slope value of 300° is shallower than the north-north-west current flow direction derived at ≤200 m from the "mounds" for all SSB categories. However, the slightly shallower median direction of the current flow observed at ≤25 m to the "mounds" suggests that currents slow down and alter direction upon approach to the "mounds". These micro-scale topographic steering forces imprint a better alignment with the live coral framework. Moreover, the slower current speeds proximal to the "mounds" encourage better conditions for food capture (Figure 23A–J).

3.4.4. Implications

Lim et al. (2020) demonstrated the use of acoustic Doppler current profiler (ADCP) derived hydrodynamic data in augmenting the interpretative capabilities of high resolution semi-automated classification of CWC environments. Here, we have provided a means of estimating the current speed from bathymetric data without the use of ADCP instrumentation that is largely congruent with their findings. Furthermore, ADCP deployment offers the opportunity for finer calibration of this technique, enabling the direct extrapolation of knowledge deduced from ADCP current data from individual points to entire bathymetric mosaics. Thus, providing a technique that could reduce *in situ* data acquisition requirements when appraising benthic seabed currents. Future research could focus on implementing this strategy to provide a more robust current speed estimation. The OBIA morphological characterisation employed with this classification scheme has been proven to be robust to significant disparities in spatial resolution, making this technique flexible to a wide range of scales (Summers et al., 2021). Such properties render this technique an essential mechanism to produce multi-scale seabed habitat maps for MPA management and monitoring, logistics for offshore physical infrastructure (Savini et al., 2014).

On a broader scale, the method described can be used to quickly derive objective, allogenic environmental information from bathymetric data. This can subsequently be used in maritime industrial development, environmental impact assessments as well as preliminary desktop studies. With large scale datasets now readily available, such methods can simply be applied by non-experts. Digital elevation models (DEMs) and sedimentary bedforms are not unique to the marine realm and, as such, the workflow presented here could be used to integrate terrestrial DEM data, promoting the potential of a seamless geomorphological habitat map (Prampolini et al., 2020). Furthermore, such workflows could be applied to extra-terrestrial settings, where seafloor bedforms provide an excellent analogue for thick atmosphere environments (Neakrase et al., 2017).

3.5. Conclusions

This research has established the first OBIA workflow that can provide an indication of the consistency, direction, and velocity of the hydrodynamic regime directly above the seafloor solely using MBES bathymetry data. Our findings have wide applications but are used here to report that CWC growth in the downslope Moira Mounds area was shaped by regional north-north-west aligned geostrophic contour currents induced by the MOW that were influenced themselves by local and micro topographic features. Local topographic steering resulted in the disruption of the contour current flow with approach to the channel margin, resulting in the presence of a bimodal distribution of current flow direction throughout the area. This bimodal current direction corresponds with the two predominant CWC slope orientations found within the region (Conti et al., 2019). Moreover, geomorphological characterisation of the SSBs provided a proxy to define regions of consistent unidirectional flow. Previous observations on CWC mound spatial density within this region indicates that the CWC mounds occur in the greatest densities in regions with consistent unidirectional flow (Lim et al., 2018a). While micro topographic steering forces resulted in the decrease of current speeds with increasing proximity to the CWC mounds. Furthermore, these micro topographic steering forces imprinted a current direction that was more aligned with CWC occurring on slopes facing away from the prevailing current direction, congruent with findings acquired in other CWC mound regions. These results underline the capacity of this approach to derive qualitative data on hydrodynamic regimes on the seabed surface with minimal sampling requirements. Additionally, this technique can be reconciled with current measurements taken from *in situ* monitoring equipment such as ADCPs to ensure a more effective hydrodynamic regime appraisal.

Author Contributions: Conceptualisation, G.S. and A.L.; Methodology, G.S. and A.L.; Software, G.S.; Validation, G.S.; Formal Analysis, G.S.; Investigation, G.S.; Resources, G.S. and A.L.; Data Curation, G.S. and A.L.; Writing—Original Draft Preparation—G.S.; Writing—Review and Editing, G.S., A.L. and A.J.W.; Visualisation, G.S.; Supervision, A.L. and A.J.W.; Project Administration, A.J.W.; Funding Acquisition, A.J.W. All authors have read and agreed to the published version of the manuscript.

Funding: This research was developed under the Marine Protected Area Management and Monitoring (MarPAMM) (Project IVA5059) supported by the European Union's INTERREG VA Programme, managed by the Special EU Programmes Body (SEUPB). Holland 1 ROV. RV Celtic Explorer cruises were grant aided by the Marine Institute under the Ship Time Program of the National Development Plan, Ireland. The data processing workflow was developed by Gerard Summers and Aaron Lim is jointly funded by the EU INTERREG V through the Special EU Programmes Body (SEUPB) and the Irish Research Council (Project GOIPG/2015/2700), respectively.

Acknowledgments: Authors would like to thank all cruise crew and scientific parties on RV Celtic Explorer (cruise number CE15009).

Conflicts of Interest: The authors declare no conflict of interest.

Preface to Chapter 4

Chapter 4 adapts the two techniques outlined in Chapter 2 and Chapter 3 and deploys them over multiple resolutions of data from the same region to determine the optimum resolution for the assessment of seabed benthic currents. This workflow will be complemented by MBES backscatter data that will be processed to provide further SSB compositional attributes.

This chapter is in preparation to be published for the Elsevier journal Geomorphology.

Author Contributions

Gerard Summers was responsible for the concept of this study. Gerard Summers and Aaron Lim were responsible for the development of the methodology used within this study. Gerard Summers was responsible for the software used in this paper. Validation techniques for this paper were established by Gerard Summers. Formal Analysis was completed by Gerard Summers. Investigation of the results was conducted by Gerard Summers. The resources were organised by Gerard Summers and Aaron Lim. The data curation was organised by Gerard Summers. Writing and preparation of the original draft of the original manuscript was completed by Gerard Summers. The editing and review of the original manuscript were coordinated by Gerard Summers, Aaron Lim, and Andrew James Wheeler. All data visualisation was completed by Gerard Summers. Supervision of the development of this manuscript was completed by Aaron Lim and Andrew James Wheeler. Administration of the project was conducted by Andrew James Wheeler. The funding for this research was acquired by Andrew James Wheeler. All authors have read and agreed to this version of the manuscript.

Chapter 4. Multi-Resolution Appraisal of Cork Harbour Estuary: An Object-Based Image Analysis Approach

(Status: under review)

Gerard Summers [1,*], Aaron Lim [2,3] and Andrew J. Wheeler [1,4]

1. *School of Biological, Earth and Environmental Sciences, Environmental Research Institute, University College Cork, Distillery Fields, North Mall, T23 TK30 Cork, Ireland*
2. *Environmental Research Institute, University College Cork, Ireland.*
3. *Department of Geography, University College Cork (UCC), T12 K8AF Cork, Ireland*
4. *Irish Centre for Applied Geosciences (ICRAG), Marine & Renewable Energy Institute (MaREI), University College Cork, P43 C573 Cork, Ireland*

* *Corresponding author*

Abstract:

Lithic sedimentary benthic habitats are often organised by the overlying hydrodynamic regime, generating seabed sedimentary bedforms (SSBs) whose morphology and sediment compositions are controlled by the current flow properties including speed, direction, and duration. Furthermore, SSBs can manifest at a variety of spatial scales reflecting different aspects of the hydrodynamic regime that operate at distinct intensities and temporal scales. Acoustic seabed mapping of SSBs permits the quantification of the complex seafloor hydrodynamics without *in situ* measurements. As such, seabed mapping efforts must determine the minimum spatial resolution required to effectively capture the complete seabed hydrodynamic picture. Here, we have provided a semi-automated, object-based image analysis (OBIA) of SSBs occurring over 0.5, 1.0, 1.5, 2.0, and 2.5 m spatial resolutions of multibeam echosounder (MBES) data acquired in Cork Harbour, Ireland, to ascertain the optimum resolution at which to derive current velocity attributes. Estimations of

seabed sediment grain size were completed through the angular range analysis (ARA) of co-located 400 kHz multibeam backscatter data. Results show that current flow estimations derived at 0.5, 1.0 and 1.5 m resolutions of MBES bathymetry agree with previous *in situ* current speed measurements. Moreover, sediment grain size estimations produced during the ARA of the 400 kHz backscatter data displayed a clear pattern of sediment disturbance at each section of the harbour, and this was effectively depicted at 0.5, 1.0, and 1.5 m resolution of MBES bathymetry data. However, current flow estimates derived from 2.0 and 2.5 m resolution failed to portray the short-term current variation induced by the ebb phase of the tide. Therefore, it is recommended that MBES data with a pixel size of >50% of the wavelength of the SSB observed is insufficient for inclusion in an OBIA workflow.

4.1. Introduction

Seabed benthic habitats defined by unconsolidated sediments are often moulded by the nature of the overlying hydrodynamic environment (Barnard et al., 2013; Lebrec et al., 2022). The properties of the currents comprising this hydrodynamic environment, such as direction, velocity, and consistency, are imposed upon this habitat, interacting with the seabed topography and the sediment grain size to produce a variety of seabed sedimentary bedforms (SSBs) (Knaapen et al., 2005; Duţu et al., 2018). Therefore, the orientation, size, and shape of these current-induced SSBs can be diametrically related to the direction, velocity, and consistency of the dominant current flow regime (Kostylev et al., 2001; Stow et al., 2009). The orientation of these SSBs is indicated by the sloping direction of the steeper or lee side (Cheng et al., 2020). Furthermore, SSBs are dynamic seafloor features and when active they migrate with the dominant current direction thus, are used as a representation of the net bedload transport direction (Barnard et al., 2013; Durán et al., 2017; Cheng et al., 2020). In tidally dominated current regimes, the current flow reverses with each phase of the tidal cycle; thus, smaller SSBs are rearranged to align with the latest tidal phase, providing information on the short-term variability of local current flow (Lefebvre et al., 2022). However, tidal influence is not always equally balanced, as nearshore processes such as topographic steering can cause magnitude asymmetry between the ebb and flood tides, producing seabed currents with reduced velocities during the weaker phase of the tide (Piano et al., 2017). These reduced current velocities may not be sufficient to cause migration in larger SSBs; hence, larger SSBs reflect longer term tidal asymmetry and migrate during periods of inequality between the ebb and flood tides (Knaapen et al., 2005). Additionally, due to their transient nature, these features represent regions of seafloor instability and present a significant challenge for underwater infrastructure including navigation channels, cables and pipelines, and wind farms (Greene et al., 2021; Zhou et al., 2018; Wang et al., 2020). Therefore, the exact location, composition, and extent of these SSBs needs to be determined and mapped to ascertain the risks to offshore development (Zhou et al., 2018; Yan et al., 2020). Moreover, small scale and large scale SSBs must be adequately represented to effectively ascertain the long and short-term influences on near-seabed hydrodynamics.

Consequently, fine resolution seabed mapping has been recognised as an essential prerequisite for marine spatial planning (Janowski et al., 2018b). Acoustic remote sensing techniques have significantly reduced the time and resources necessary to map seafloor benthic environments (Gaida et al., 2019). Multibeam echosounder (MBES) systems are the latest incarnation of underwater acoustic remote sensing technology and are designed to measure the position, the impedance contrast, and the angular backscatter intensity of the seafloor across a wide swath (Lamarche et al., 2011; Fakiris et al., 2019). Furthermore, the relationship between the substrate characteristics and the acoustic response of the seabed is reliant on the acoustic angle of incidence and the frequency emitted by the MBES (Masetti et al., 2011), both of which can be exploited to provide information on the attributes of the substrate (Janowski et al., 2018b; Misiuk and Brown, 2022). Quantitative sediment characteristics can be determined by analysing the variation of the backscatter strength from each individual beam and its angle of incidence in a technique known as angular range analysis (ARA) (Fonseca and Mayer, 2007). Here, a mathematical model is used link seabed acoustic and physical attributes to the observed acoustic response, hence estimates for characteristics such as acoustic impedance, surface roughness, and grain size can be derived (Masetti et al., 2011; Fonseca et al., 2009). In addition, this has been applied to derive sediment characteristics from environments defined by strong hydrodynamic influences, including rivers (Santos et al., 2018). Contemporary studies have focused on the application of multifrequency MBES data and its ability to derive additional characteristics from finer sediments (Janowski et al., 2018b; Brown et al., 2019). Lower frequency sonar penetrates further through finer grained sediment, whereas higher frequency sonar has a higher degree of attenuation with depth in sediment thus, the comparison between the two provides additional information on the sediment subsurface (Gaida et al., 2018). Moreover, MBES sonar frequency is negatively correlated with sediment grain size (Runya et al., 2021; Snellen et al., 2019). Consequently, multifrequency MBES data enhances the discrimination between variations in unconsolidated sedimentary habitat (Costa, 2019).

Thus, the introduction of MBESs to seabed mapping research increased the resolution of finer scale geomorphological details, their associated seabed sediment transport pathways, and subsurface characteristics while reducing the time required to achieve complete survey coverage (Barnard et al., 2011). As of 2018, 18% of the world's oceans were mapped at resolutions that rival terrestrial ecosystems; thus, international mapping initiatives have committed to amend this data deficit and map the entire seafloor by 2030 (Mayer et al., 2018). However, the increased data volumes associated with these high resolution MBES systems, and the quantity of data required to complete this task necessitates repeatable processing techniques that provide objective and significant geomorphological information (Diesing et al., 2014; Ierodiaconou et al., 2018; Zelada Leon et al., 2020). Manual interpretation of these data is not feasible due to the intensive strains on time and resources (Ierodiaconou et al., 2018). Additionally, such classifications are reliant on the proficiency and experience of the individual completing the task, increasing the susceptibility for user bias and thus, increasing the inconsistency within the seabed maps (Brown et al., 2012). Furthermore, seabed mapping approaches that are robust to variations in the scale of geomorphological features that are depicted through multiple spatial resolutions of MBES data are prudent to preserve the representation of the environmental processes responsible for their formation (Summers et al., 2021). Object-based image analysis (OBIA) is a classification technique that is compatible with these prerequisites (Goodchild, 2011). This approach exploits the high resolution capacity of MBES data, where seafloor features are represented across multiple pixels, by separating pixels into distinct regions of uniform pixel values, aggregation of these values provides the input for the classification (Koop et al., 2021). This amalgamation removes the noise from the data within the image objects, thereby reducing the intra object heterogeneity (Conti et al., 2019). Fast Fourier transformations (FFTs) can provide information on the frequency, wavelength and wave heights of SSBs depicted in MBES bathymetry data and these attributes can be incorporated as part of an OBIA (Cazenave et al., 2013; Spagnolo et al., 2017; Trzcinska et al., 2020). Summers et al. (2021) created a scale robust OBIA approach to classify SSBs in MBES data. This approach was adapted by Summers et al. (2022) to provide a framework to derive the frequency information from the classified SSBs. The resultant wavelength and wave heights derived for each classified SSB was used as an input for a current velocity estimation developed from the bedform velocity matrix outlined by Stow et al. (2009).

Here, we apply this OBIA approach to investigate the effects of spatial resolution on the hydrodynamic patterns evident within estimations of current velocity derived from SSBs depicted in 0.5, 1.0, 1.5, 2.0, and 2.5 m spatial resolutions of MBES data. An OBIA was executed separately on each resolution deriving image objects that correspond to SSB crests within the data, a fast Fourier transform was applied to the bathymetric profiles derived from these image objects. The wavelength and wave height were used as explanatory variables within a multiple linear regression that generated an estimate for current speed. An estimation of sediment grain size was established through ARA analysis of backscatter intensity evident within 400 kHz MBES backscatter and was used to determine the sedimentary disturbance evident within the harbour. This the first study to appraise the appropriate resolution for the provision of representative current velocities derived from an OBIA of MBES data acquired from current induced SSBs.

4.1.1. Study Site

The shape of Cork Harbour is strongly influenced by the structural and compositional properties of the underlying bedrock, which comprise a series of E–W anticlines and synclines formed due the Late Carboniferous Variscan Orogeny (Allen and Milenic, 2007). A series of N–S river valleys eroded through the Mesozoic cover from the

Jurassic to Late Cenozoic, becoming entrained in N–S faults (Allen and Milenic, 2007). Erosion of the Mesozoic cover proceeded and the river valleys became captured and realigned E–W along synclines (Allen and Milenic, 2007). Glaciers that formed during the Pleistocene advanced eastward, this eastward flow eroded weak shales and limestones producing a series of u-shaped valleys that trend either E–W or ENE–WSW (Davis et al., 2006; Allen and Milenic, 2003).

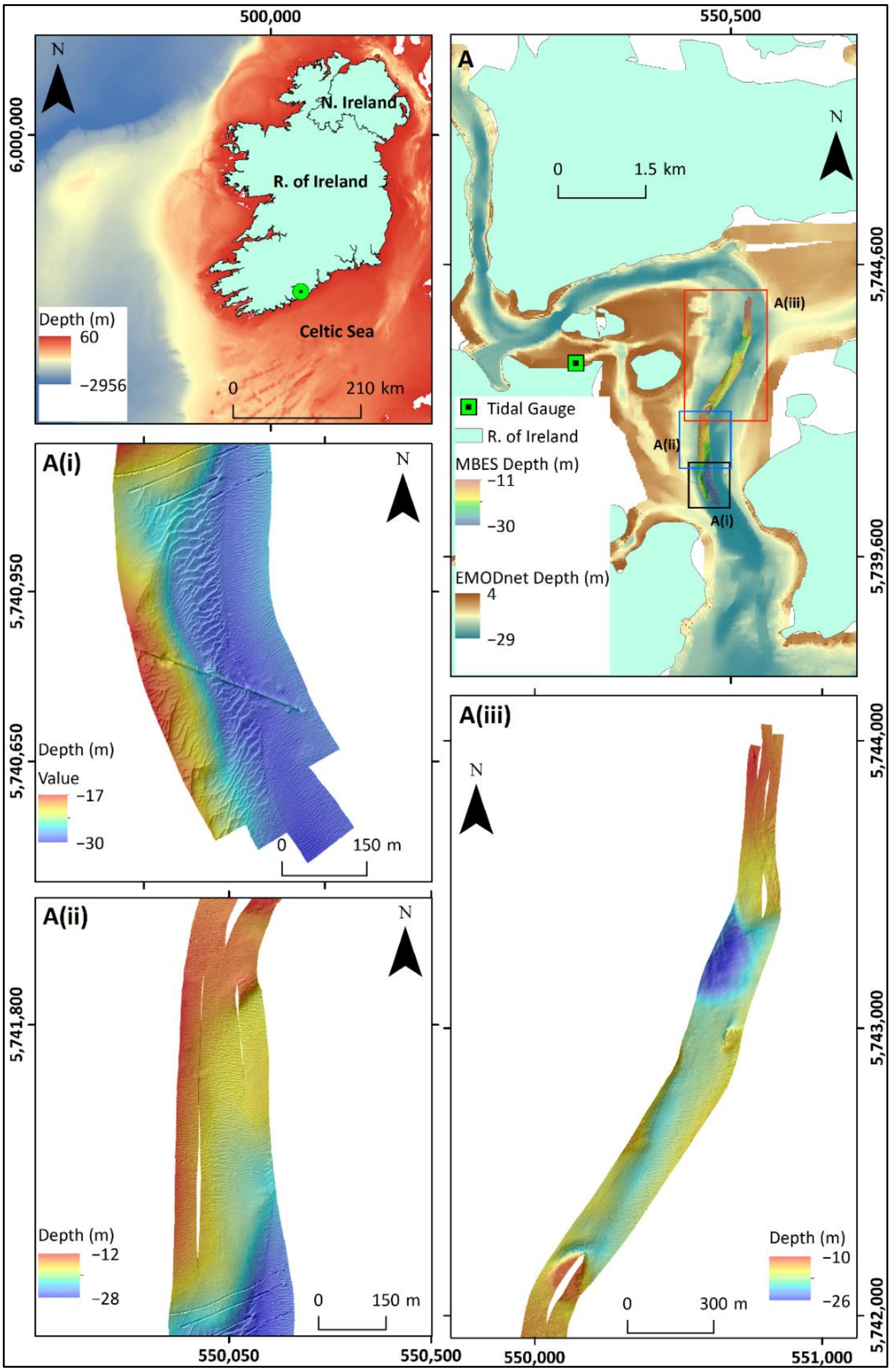

Figure 26: Map showing the location of the study site. (**A**) Cork Harbour multibeam (MBES) bathymetry data superimposed onto the EMODnet 25 m resolution bathymetry dataset (EMODnet Bathymetry Consortium, 2020), the Ringaskiddy tide gauge location, and the extents of (**A(i)**) in black, (**A(ii)**) in blue, and (**A(iii)**) in red, (**A(i)**) displaying the MBES data from the harbour mouth, (**A(ii)**) displaying the MBES data from the middle of the harbour, and (**A(iii)**) displaying the MBES data from the north of the study site.

Cork Harbour is a semi-diurnal macrotidal harbour with a maximum tidal range of 4.2 m during spring tide and a minimum tidal range of 2.1 m during neap tide (Figure 26A) (Kelly and Downes, 2014). Furthermore, current speed estimates derived using acoustic Doppler current profilers (ADCPs) show rectilinear current flow with speeds reaching a maximum of ~0.60 m·s^{-1} and orientated to the north at Cobh Spit Bank near the top of the harbour during flood tide (Office of Public Works, 2017). Peak current speed noted for the ebb portion of the tide was ~0.45 m·s^{-1} and orientated to the south. The geomorphology of the harbour is relatively stable with localised regions of erosion and deposition (Office of Public Works, 2017). Sinuous bifurcating sediment waves are evident at the north (hereafter referred to as the top), middle, and mouth of the harbour. Sediment waves are visible at the mouth of the harbour with most of the lee sides orientated to the north−west and are aligned with the flood tide entering the harbour (Figure 26A(i)). To the west, adjacent to these larger sediment waves are smaller sediment waves, these display a greater variation in lee side alignment, indicating increased influence of the ebb portion of the tide (Durán et al., 2017). Furthermore, these smaller sediment waves are found within middle and the top of the harbour, suggesting a greater variation of the current flow within these sections of the harbour (Figure 26(A)(ii) & (iii)). The SSBs within the harbour form a thin veneer of sandy sediment over hard bedrock as a result of long term sediment scouring; this scouring is evident surround the outflow pipeline in the mouth of the harbour (O'Toole et al., 2012).

4.2. Materials and Methods

4.2.1. Multibeam Echosounder Data Acquisition and Processing

The multibeam echosounder (MBES) data were collected using a Kongsberg EM2040 operating at 400 kHz aboard the RV Celtic Voyager. The acquisition settings for this data are found within Summers et al. (2021). All MBES data were imported into as *.all files into QPS's bathymetric processing suite Qimera (QPS, 2019b). Tidal observations were acquired from the Ringaskiddy tide gauge, and these were imported into Qimera to apply tidal corrections to the MBES data. Erroneous MBES data points were manually removed via the swath editing tool (QPS, 2019b). These processed data were then gridded at 0.5 m resolution and exported in an ArcGRID *.asc file format. All processed data were then imported into ArcGIS 10.6 where the resample tool from the raster toolset of the data management toolbox was increase the spatial resolution of the bathymetric data through bilinear weighted average to 1.0, 1.5, 2.0, and 2.5 m. Bathymetric derivatives were then generated separately for each resolution of data (Table 9). The slope, sinaspect, and cosaspect were produced using the Benthic Terrain Modeler 3.0 toolbox in ArcGIS (Walbridge et al., 2018). The bathymetric position index (BPI) was calculated using the equation detailed below:

$$BPI = Zgrid - focalmean(Zgrid, circle, r)$$

where *Zgrid* is the gridded bathymetric data, the *focalmean* calculates the mean of the bathymetric within a circular kernel of radius *r* (Wilson et al., 2007). This *focalmean* was completed in the focal statistics tool in the neighbourhood toolset of ArcGIS 10.6. The scale of the *BPI* is then controlled by the radius of the kernel. The *BPI* layer is completed by subtracting the mean bathymetric layer from the *Zgrid*. This process was executed in the raster calculator tool in the map algebra toolset of ArcGIS 10.6.

Table 9: Image features used in the geomorphological characterisation in eCognition Developer.

Image Layers	Scale (pixel)
Bathymetric Position Index (BPI)	5
Cosaspect (Northness)	3
Sinaspect (Eastness)	3
Slope	3

The *.all files of the MBES data were imported into QPS's backscatter processing suite FMGT (QPS, 2019a). Here, the radiometric and geometric corrections are applied to the backscatter data and acquisition gains are removed during the initial backscatter processing to ensure a standardised angular range analysis (ARA) is calculated for each line. Furthermore, a beam pattern correction was applied to this data over a flat region in the middle of the harbour to ensure consistent results. An ARA of the backscatter was then completed to provide an estimate of the grain size indicated by phi score. With this technique, thirty consecutive pulses were inspected together along the width of half a swath of MBES data (Rzhanov et al., 2012; Dufek, 2013). Consequently, the noise present in the backscatter signal was reduced; however, the resolution of the ARA derived data is much coarser than the original backscatter intensity mosaic (Fonseca et al., 2009). The phi value estimation was exported in ArcGRID *.asc file format.

4.2.2. Object-Based Image Analysis

4.2.2.1. Morphological Characterisation

Object-based image analysis (OBIA) is a remote sensing data processing technique that occurs over two stages: segmentation and classification (Blaschke, 2010). Segmentation generates image objects by creating boundaries between discrete regions of homogeneous image values and it is vital in the successful application of OBIA (Lang, 2008; Belgiu and Drăguţ, 2014). The most utilised segmentation algorithm is the multiresolution segmentation algorithm provided by Trimble's image processing suite eCognition Developer (Hossain and Chen, 2019). This algorithm initially amalgamates similar adjacent pixels into image objects and then merges homogeneous neighbouring image objects until a user-defined threshold for intra-object heterogeneity, defined as the scale parameter, has been achieved (Eisank et al., 2014). Efficient segmentations produce image objects whose borders directly relate to the features of interest (Kavzoglu and Tonbul, 2018). However, determining the appropriate scale parameter is a heuristic process that is susceptible to over-segmentation or under-segmentation (Gaetano et al., 2015). Over-segmentation occurs when a feature of interest is encompassed by multiple smaller image objects, under-segmentation occurs when multiple features of interest occur within one object (Troya-Galvis et al., 2015; El-naggar, 2018). Furthermore, the spectral difference algorithm within eCognition Developer can refine the representation provided by these image objects through combination of adjacent image objects whose mean layer intensities are below a user defined threshold (Trimble, 2014). Further enhancement can be achieved using the pixel-based object resizing algorithm, where the boundaries of image objects can be adjusted to achieve a desired geometrical parameter or until the boundaries meet a predefined image layer value (Johansen et al., 2011).

In this paper, the morphological characterisation was deployed across three separate phases, as outlined by Summers et al. (2021) and Summers et al. (2022) for each resolution of bathymetry data. The first phase defines the preliminary "seabed sediment bedform" (SSB) image objects, hereafter referred to as SSBs. Here, the multiresolution segmentation, the spectral difference, and the assign class algorithms were used to segment and characterise the SSBs as topographical features occurring in slope, sinaspect and cosaspect data. The second phase of morphological characterisation refined the boundaries of the preliminary SSBs to ensure that they incorporated the entire lee and stoss side of each SSB. Summers et al. (2021) established that BPI5 provided the most accurate depiction of SSB extent; therefore, this image layer was used to first define the boundaries of the crests (positive topographic features) and then the troughs (negative topographic features) of the SSBs. Furthermore, any remaining unclassified image objects that formed partial enclaves to the SSBs were shrunk to create an "intermediate" image object, hereafter referred to as "intermediate". If the shared border between the "intermediate" and the "SSB" was ≥65%, the "intermediate" was then reclassified as an SSB. Phase three of the morphological characterisation followed phase four outlined in Summers et al. (2022). This resulted in "ridge" image objects, hereafter referred to as "crests", and "valley" image objects, hereafter referred to as "troughs". This geomorphological characterisation process was completed separately for each resolution of bathymetry data, resulting in five segmentations of the Cork Harbour region. Mean phi score was derived for each segmentation output.

4.2.2.2. Seabed Sediment Bedform (SSB) Frequency Analysis

The morphological characterisation was exported in two formats, a polygon shapefile, and a line shapefile. The line shapefile was used to derive frequency information from the "crests". Any line that was derived from a "crest" was selected for this processing. The mean trend for each "crest" line object was determined using the linear directional mean tool from the spatial statistics toolbox in ArcGIS 10.6. Trend direction is imparted to the "crest" line objects as part of this process, this trend direction was used to create a perpendicular line extending 25 m from either side each individual "crest". The bathymetric profile was extracted at a 0.5 interval along each perpendicular line. Once the bathymetric profile for each line was obtained, they were imported into a pythonic coding environment to derive their corresponding wavelengths and wave heights through a fast Fourier transform (FFT) workflow outlined in detail Summers et al. (2022). Here, any superimposed regional slope was removed from the bathymetric profile using a moving window polynomial filter called the Savitzky Golay filter to help the profile achieve stationarity (Savitzky and Golay, 1964). Window size values at ten step intervals from 21 to 101 were evaluated for each bathymetric profile, the window size that produced the lowest amalgamated standard deviation and root mean square values was deemed the appropriate window size. Windowing was applied to the profiles to ensure an integral number of "crests" were present to prevent spectral leakage (Perron et al., 2008; Spagnolo et al., 2017). FFTs have been utilised as a means of extracting spatial series information from bathymetric data depicting to SSBs (Trzcinska et al., 2020; Cazenave et al., 2013; Tegowski et al., 2016; Tęgowski et al., 2018). Statistics such as the wave number, the wavelength, and wave height can be generated through FFT (Levey et al., 1980).

4.2.2.3. SSB Asymmetry and Current Flow Direction

In addition to this workflow, an automated mean of deriving the dominant current flow direction through SSB asymmetry was also developed. Here, the direction of the asymmetry is defined as the direction that the slope of the shorter flank, or lee side, of the SSB is orientated towards (Lebrec et al., 2022). A peak detection algorithm was deployed to identify all positive bathymetric features (peaks) and negative topographic features (valleys) within the bathymetric profile (Figure 27A) (Billauer, 2009). The peak occurring closest to the centre of the bathymetric profile was identified as the target "crest" feature from which the direction of asymmetry was to be determined. Once the location of this "crest" ascertained the closest valleys at either side of this peak were chosen as the corresponding "troughs" of the bedform. The trough with the shortest distance away from the "crest" along the x axis was defined as the lee side of the profile (Figure 27B). Any profile with two "troughs" that were equal distance away from the "crest" was deemed to be symmetric and were thus excluded from the analysis.

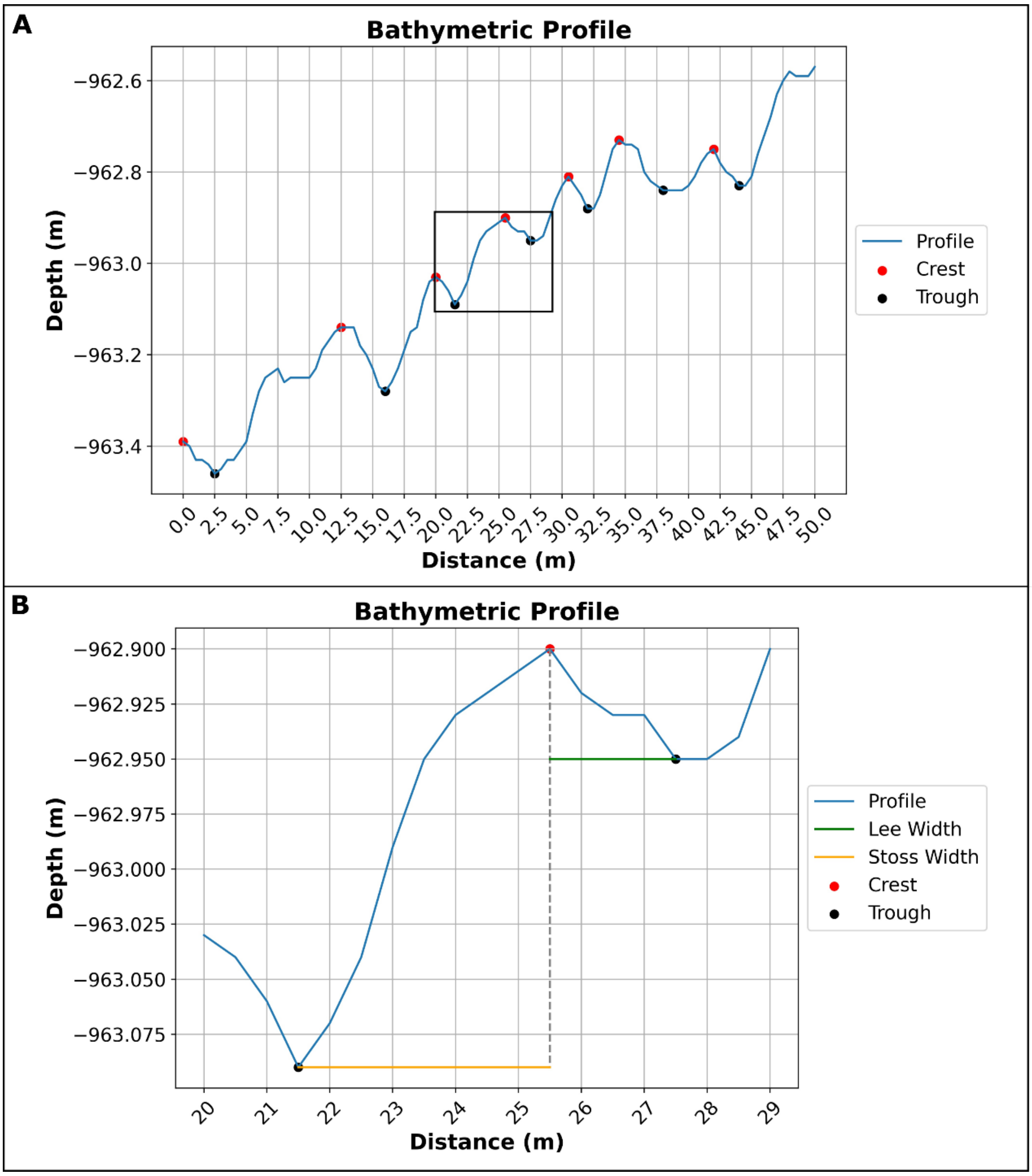

Figure 27. A) The bathymetric profile for a SSB and the outline of **B**) illustrating the shorter lee side and longer stoss side of the target "crest".

4.2.3. SSB-Derived Current Velocity Estimation

Current velocity estimates were derived based on the bedform velocity matrix detailed by Stow et al. (2009). Stow et al. (2009) defined 6 groups of transverse SSBs using wavelength, wave height, and sinuosity of the bedform. Additionally, a minimum and maximum current velocity is denoted for each category inferring a range of associated current velocities for each SSB class. Summers et al. (2022) developed a multiple linear regression using the ranges for wavelength, wave height and current velocity for each SSB class as specified by Stow et al. (2009). The wavelength and wave height were used as explanatory variables and current velocity was defined as the response variable (Summers et al., 2022). This multiple linear regression for current velocity was replicated in this paper. The wavelength and wave height for each asymmetric line object (determined in Section 4.2.2.3) were used to categorise each SSB into one of the transverse SSB categories. Furthermore, once the calculation was completed the median of the *phi* value for each seabed category was derived from the ARA of the 400 kHz backscatter data.

4.2.4. Tidal Measurements

Water level data was acquired from the 01/11/2018 to the 29/11/2018 to determine the long-term tidal cycle preceding the acquisition of the MBES data. These data were collected using the National Maritime College of Ireland (NMCI) tide gauge in Ringaskiddy, Co. Cork, Ireland (Figure 26A). This tide gauge is part of the Irish National Tide Gauge Network and is owned by the Office of Public Works (OPW). The peak and low tides were determined through the peak detection algorithm (Billauer, 2009). Furthermore, tidal range was determined by subtracting the low tide from the peak tide. The pytides2 package in python 3.7 was used to determine the principal tidal constituents within the water level data (Cox, 2020).

4.3. Results

4.3.1. Morphological Characterisation

The mouth of the harbour had 1343, 406, 169, 70, and 57 “crests” derived at 0.5, 1.0, 1.5, 2.0, and 2.5 m resolutions of bathymetry data respectively (Table 10, Figure 28A–F). The entire harbour had 5521, 1272, 427, 187, and 110 “crests” derived at 0.5, 1.0, 1.5, 2.0, and 2.5 m resolutions of bathymetry data respectively.

Table 10. The number of "crests" displayed for each subsection of the study site for each resolution of MBES bathymetry data.

Location	0.5 m	1.0 m	1.5 m	2.0 m	2.5 m
Harbour Mouth	1343	406	169	70	57
Middle of the Harbour	1683	322	92	30	19
Top of the Harbour	2495	544	166	87	34
Entire Study Site	5521	1272	427	187	110

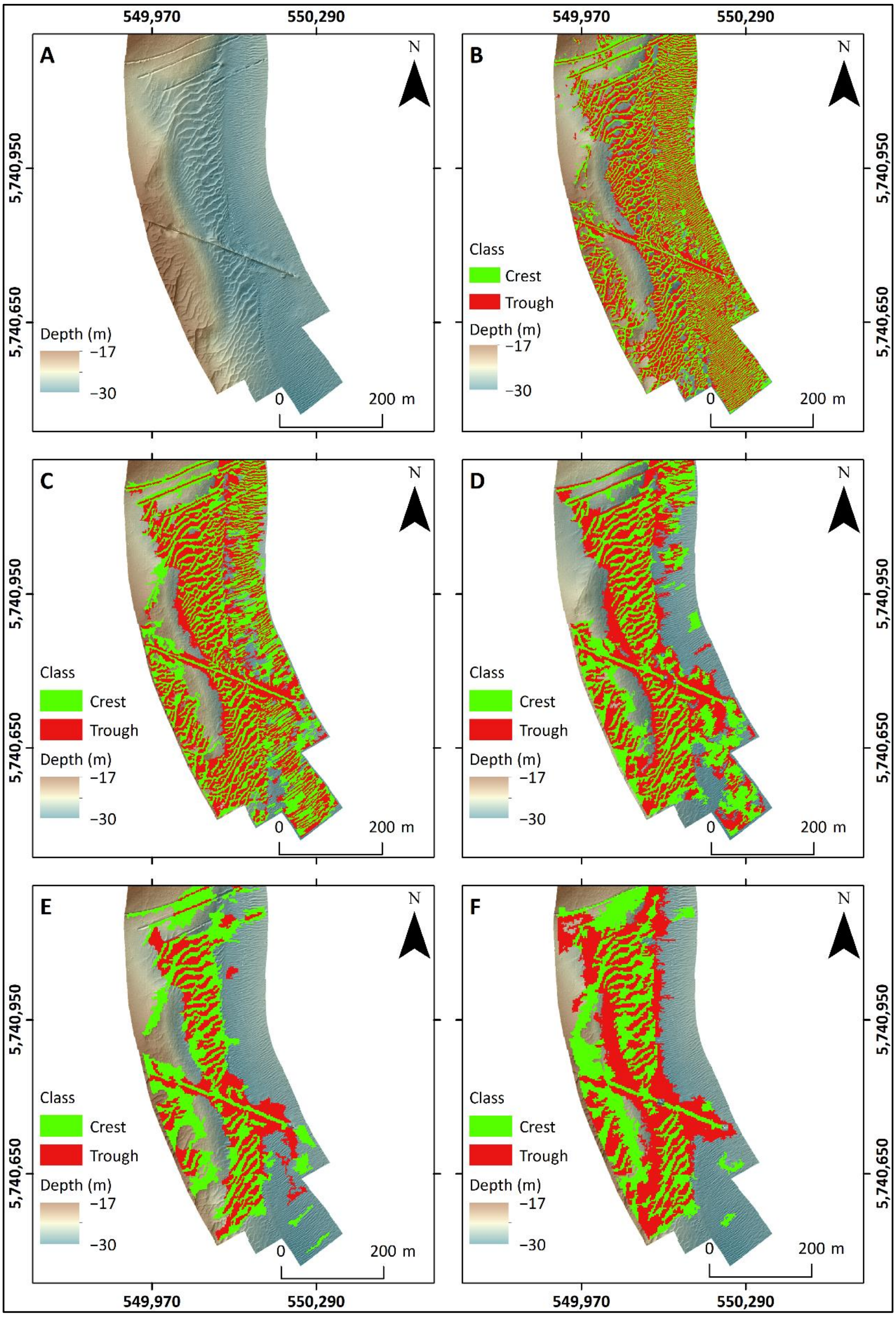

Figure 28. The mouth of the harbour displaying (**A**) the 0.5 m resolution MBES bathymetry, the morphological characterisation output for the bathymetry data gridded at (**B**) 0.5, (**C**) 1.0, (**D**) 1.5, (**E**) 2.0, and (**F**) 2.5 m resolutions.

The middle of the harbour had 1683, 322, 92, 30, and 19 "crests" derived at 0.5, 1.0, 1.5, 2.0, and 2.5 m resolution of bathymetry data respectively (Figure 29A–F).

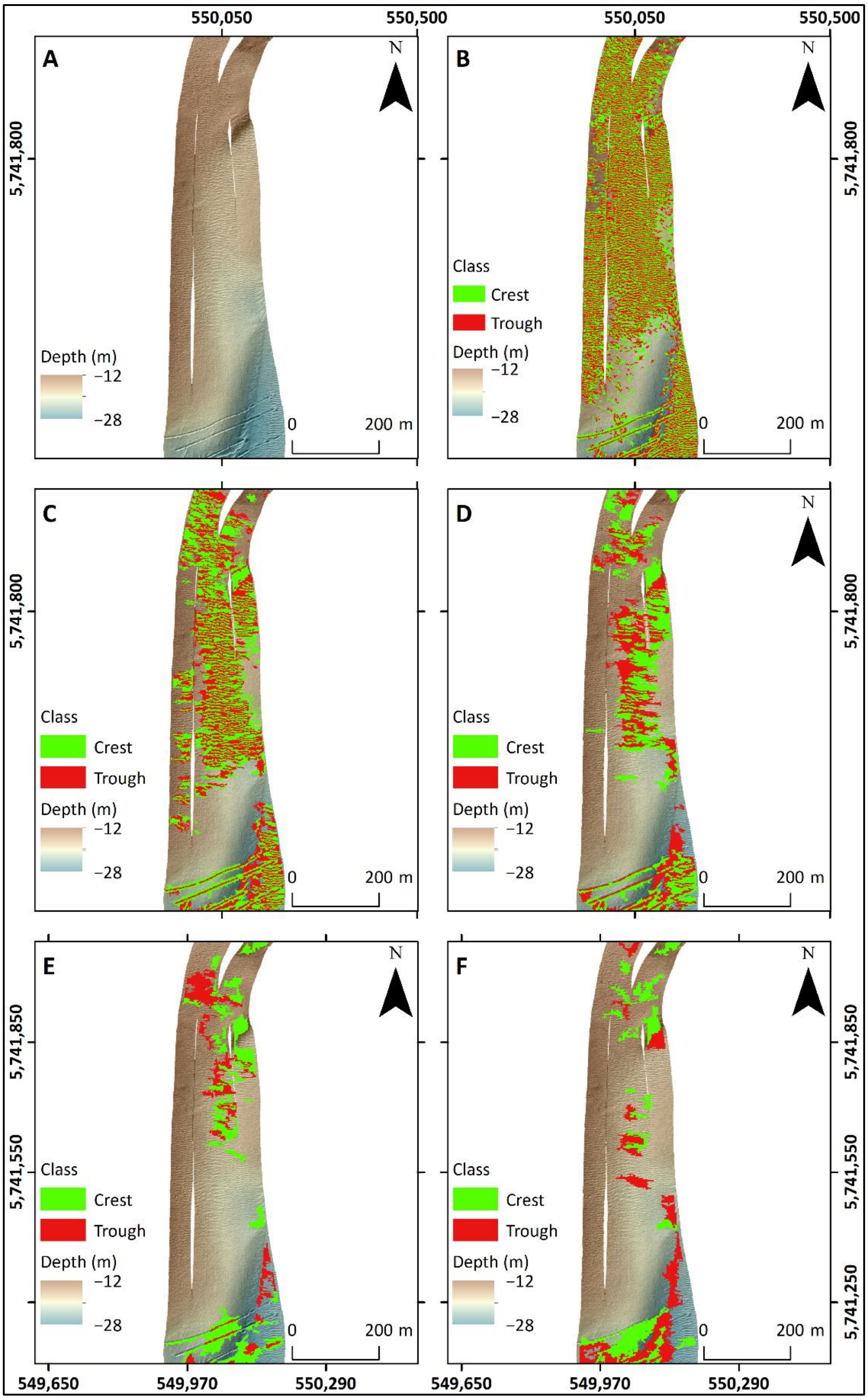

Figure 29. The middle of the harbour displaying (**A**) the 0.5 m resolution MBES bathymetry, the morphological characterisation output for the bathymetry data gridded at (**B**) 0.5, (**C**) 1.0, (**D**) 1.5, (**E**) 2.0, and (**F**) 2.5 m resolutions.

The top of the harbour had 2495, 544, 166, 87, and 34 “crests” derived at 0.5, 1.0, 1.5, 2.0, and 2.5 m resolution of bathymetry data respectively (Figure 30A–F).

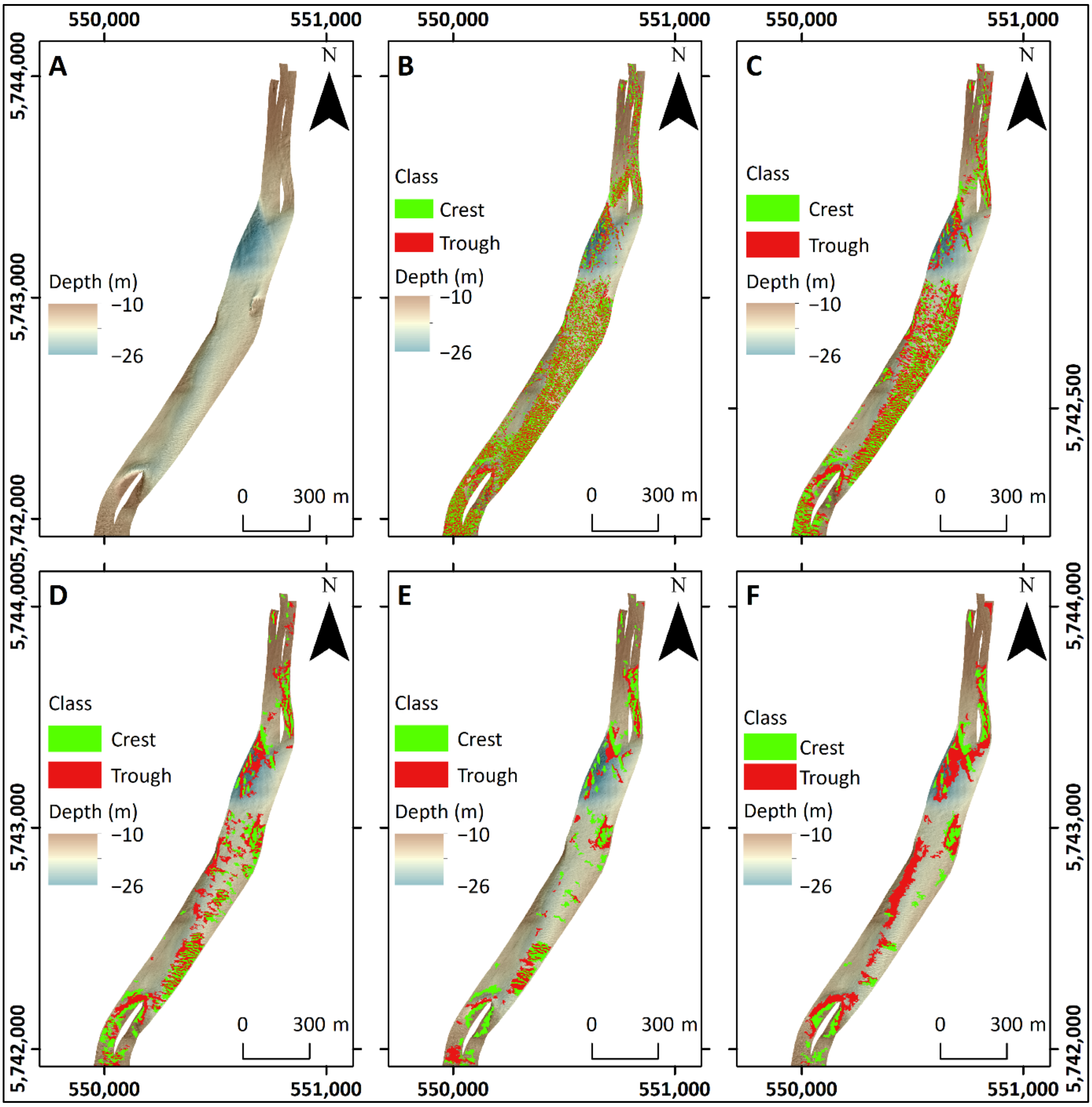

Figure 30. The top of the harbour displaying (**A**) the 0.5 m resolution MBES bathymetry, the morphological characterisation output for the bathymetry data gridded at (**B**) 0.5, (**C**) 1.0, (**D**) 1.5, (**E**) 2.0, and (**F**) 2.5 m resolutions.

4.3.2. Estimated Current Flow Direction and Velocity

Current flow estimates derived from 0.5, 1.0, 1.5, 2.0, and 2.5 m resolution bathymetry acquired within the harbour mouth show that 65%, 68%, 66%, 75%, and 77% respectively were orientated northwards (Figure 31A–E). Inversely, 35%, 32%, 34%, 25%, and 23% of current flow estimates derived from 0.5, 1.0, 1.5, 2.0, and 2.5 m resolution bathymetry respectively acquired within the harbour mouth were orientated southwards. The median current directions for the current flow estimates derived from 0.5, 1.0, 1.5, 2.0, and 2.5 m resolution bathymetry acquired within the harbour mouth orientated to the north were 331°, 328°, 328°, 322°, and 323° respectively (Table 11).

Table 11. The median direction and standard deviation of direction for current flow estimates aligned to the north, and south for all "crests" derived from the 0.5, 1.0, 1.5, 2.0, and 2.5 m resolution bathymetry data for the mouth, middle and top of the harbour respectively.

Section	Resolution (m)	Median North Direction (°)	Standard Deviation North (°)	Median South Direction (°)	Standard Deviation South (°)
Mouth	0.5	331	31	162	41
	1.0	328	27	149	39
	1.5	328	35	165	44
	2.0	322	28	161	43
	2.5	323	28	213	36
Middle	0.5	359	24	194	29
	1.0	1	26	194	29
	1.5	4	31	195	34
	2.0	351	36	206	57
	2.5	336	37	151	52
Top	0.5	21	41	196	40
	1.0	25	41	193	43
	1.5	17	51	186	48
	2.0	353	61	184	57
	2.5	43	53	216	55

The standard deviations of current direction for the current flow estimates derived from 0.5, 1.0, 1.5, 2.0, and 2.5 m resolution bathymetry acquired within the harbour mouth orientated to the north were 31°, 27°, 35°, 28°, and 28° respectively. The median directions for the current flow estimates derived from 0.5, 1.0, 1.5, 2.0, and 2.5 m resolution bathymetry acquired within the harbour mouth orientated to the south were 162°, 149°, 165°, 161°, and 213° respectively. The standard deviations of current direction for the current flow estimates derived from 0.5, 1.0, 1.5, 2.0, and 2.5 m resolution bathymetry acquired within the harbour mouth orientated to the south were 41°, 39°, 44°, 43°, and 36° respectively. Moreover, in the mouth of the harbour 371, 106, 67, 33, and 20 of the "crests" derived from the bathymetry data of 0.5, 1.0, 1.5, 2.0, and 2.5 m resolutions respectively were classified as "sediment waves" (SW) (Table 12). The number of these SWs that were orientated northwards were 264, 84, 49, 26, and 17 for the bathymetry data of 0.5, 1.0, 1.5, 2.0, and 2.5 m resolutions respectively.

Table 12. The total and the number of SWs and SSDs aligned northward, and the median wavelength, and median wave height for the SWs and SSDs derived from the 0.5, 1.0, 1.5, 2.0, and 2.5 m resolution bathymetry data for the mouth, middle and top of the harbour respectively.

Section	Class	Resolution (m)	Count	Aligned Northward	Wavelength (m)	Wave Height (m)
Mouth	SW	0.5	371	264	12.53	0.32
		1.0	106	84	11.93	0.34
		1.5	68	49	12.45	0.39
		2	33	26	13.92	0.42
		2.5	20	17	13.18	0.42
	SSD	0.5	968	612	3.43	0.08
		1.0	300	194	3.41	0.07
		1.5	101	62	2.98	0.10
		2.0	37	27	3.25	0.16
		2.5	37	27	4.01	0.20
Middle	SW	0.5	167	101	10.44	0.13
		1.0	37	22	11.39	0.18
		1.5	6	3	12.27	0.32
		2.0	3	2	13.18	0.19
		2.5	3	1	9.03	0.06
	SSD	0.5	1515	1062	3.25	0.06
		1.0	285	181	3.08	0.06
		1.5	86	60	2.59	0.08
		2.0	27	11	2.99	0.07
		2.5	15	6	2.87	0.06
Top	SW	0.5	403	209	11.39	0.14
		1.0	114	64	12.53	0.16
		1.5	38	22	11.73	0.19
		2.0	21	12	12.53	0.28
		2.5	5	2	13.92	0.35
	SSD	0.5	2085	1104	3.02	0.04
		1.0	415	204	2.38	0.04
		1.5	128	64	2.50	0.05
		2.0	66	38	2.62	0.06
		2.5	29	17	2.82	0.08

Additionally, 968, 300, 101, 37, and 37 of the “crests” derived from the bathymetry data of 0.5, 1.0, 1.5, 2.0, and 2.5 m resolutions respectively were classified as “sinuous sedimentary dunes” (SSDs) (Table 12). The number of SSDs orientated northwards were 612, 194, 62, 27, and 27 for the bathymetry data of 0.5, 1.0, 1.5, 2.0, and 2.5 m resolutions respectively.

Current flow estimates derived from 0.5, 1.0, 1.5, 2.0, and 2.5 m resolution bathymetry acquired within the middle of the harbour show that 69%, 63%, 68%, 43%, and 39% respectively were orientated northwards (Figure 31F–J). Inversely, 31%, 37%, 32%, 57%, and 61% of current flow estimates were derived from 0.5, 1.0, 1.5, 2.0, and 2.5 m resolution bathymetry respectively acquired within the middle of the harbour were orientated southwards (Table 12). The median directions for the current flow estimates derived from 0.5, 1.0, 1.5, 2.0, and 2.5 m resolution bathymetry acquired within the middle of the harbour orientated to the north were 359°, 1°, 4°, 351°, and 336° respectively (Table 11). The standard deviations of current direction for the current flow estimates derived from 0.5, 1.0, 1.5, 2.0, and 2.5 m resolution bathymetry acquired within the middle of the harbour orientated to the north were 24°, 26°, 31°, 36°, and 37° respectively. The median directions for the current flow estimates derived from 0.5, 1.0, 1.5, 2.0, and 2.5 m resolution bathymetry acquired within the middle of the harbour orientated to the south were 194°, 194°, 195°, 206°, and 151° respectively. The standard deviations of current direction for the current flow estimates derived from 0.5, 1.0, 1.5, 2.0, and 2.5 m resolution bathymetry acquired within the middle of the harbour orientated to the south were 29°, 29°, 34°, 57°, and 52° respectively. Moreover, in the middle of the harbour 167, 37, 6, 3, and 3 of the “crests” derived from the bathymetry data of 0.5, 1.0, 1.5, 2.0, and 2.5 m resolutions respectively were classified as SW. The number of these SW that were orientated northwards were 101, 22, 3, 2, and 1 for the bathymetry data of 0.5, 1.0, 1.5, 2.0, and 2.5 m resolutions respectively. Additionally, 1515, 285, 86, 27, and 15 of the “crests” derived from the bathymetry data of 0.5, 1.0, 1.5, 2.0, and 2.5 m resolution respectively were classified as SSDs in the middle of the harbour. The number of these SSD orientated northwards were 1062, 181, 60, 11, and 6 for the bathymetry data of 0.5, 1.0, 1.5, 2.0, and 2.5 m resolutions respectively.

Current flow estimates derived from 0.5, 1.0, 1.5, 2.0, and 2.5 m resolution bathymetry acquired within the top of the harbour show that 53%, 51%, 52%, 57%, and 56% respectively were orientated northwards (Figure 31K–O). Inversely, 47%, 49%, 48%, 43%, and 44% of current flow estimates derived from 0.5, 1.0, 1.5, 2.0, and 2.5 m resolution bathymetry respectively acquired within the middle of the harbour were orientated southwards. The median directions for the current flow estimates derived from 0.5, 1.0, 1.5, 2.0, and 2.5 m resolution bathymetry acquired within the top of the harbour orientated to the north were 21°, 25°, 17°, 353°, and 43° respectively. The standard deviations of current direction for the current flow estimates derived from 0.5, 1.0, 1.5, 2.0, and 2.5 m resolution bathymetry acquired within the top of the harbour orientated to the north were 41°, 41°, 51°, 61°, and 53° respectively. The median directions for the current flow estimates derived from 0.5, 1.0, 1.5, 2.0, and 2.5 m resolution bathymetry acquired within the top of the harbour orientated to the south were 196°, 193°, 186°, 184°, and 216° respectively. The standard deviations of current direction for the current flow estimates derived from 0.5, 1.0, 1.5, 2.0, and 2.5 m resolution bathymetry acquired within the top of the harbour orientated to the south were 40°, 43°, 48°, 57°, and 55° respectively. Moreover, in the top of the harbour 403, 121, 37, 21, and 5 “crests” derived from the bathymetry data of 0.5, 1.0, 1.5, 2.0, and 2.5 m resolutions respectively were classified as SW. The number of these SWs that were orientated northwards were 209, 64, 22, 12, and 2 for the bathymetry data of 0.5, 1.0, 1.5, 2.0, and 2.5 m resolutions respectively. Additionally, 2085, 416, 132, 66, and 29 “crests” derived from the bathymetry data of 0.5, 1.0, 1.5, 2.0, and 2.5 m resolution respectively were classified as SSDs. The number of these SSDs orientated northwards were 1104, 204, 64, 38, and 17 for the bathymetry data of 0.5, 1.0, 1.5, 2.0, and 2.5 m resolutions respectively.

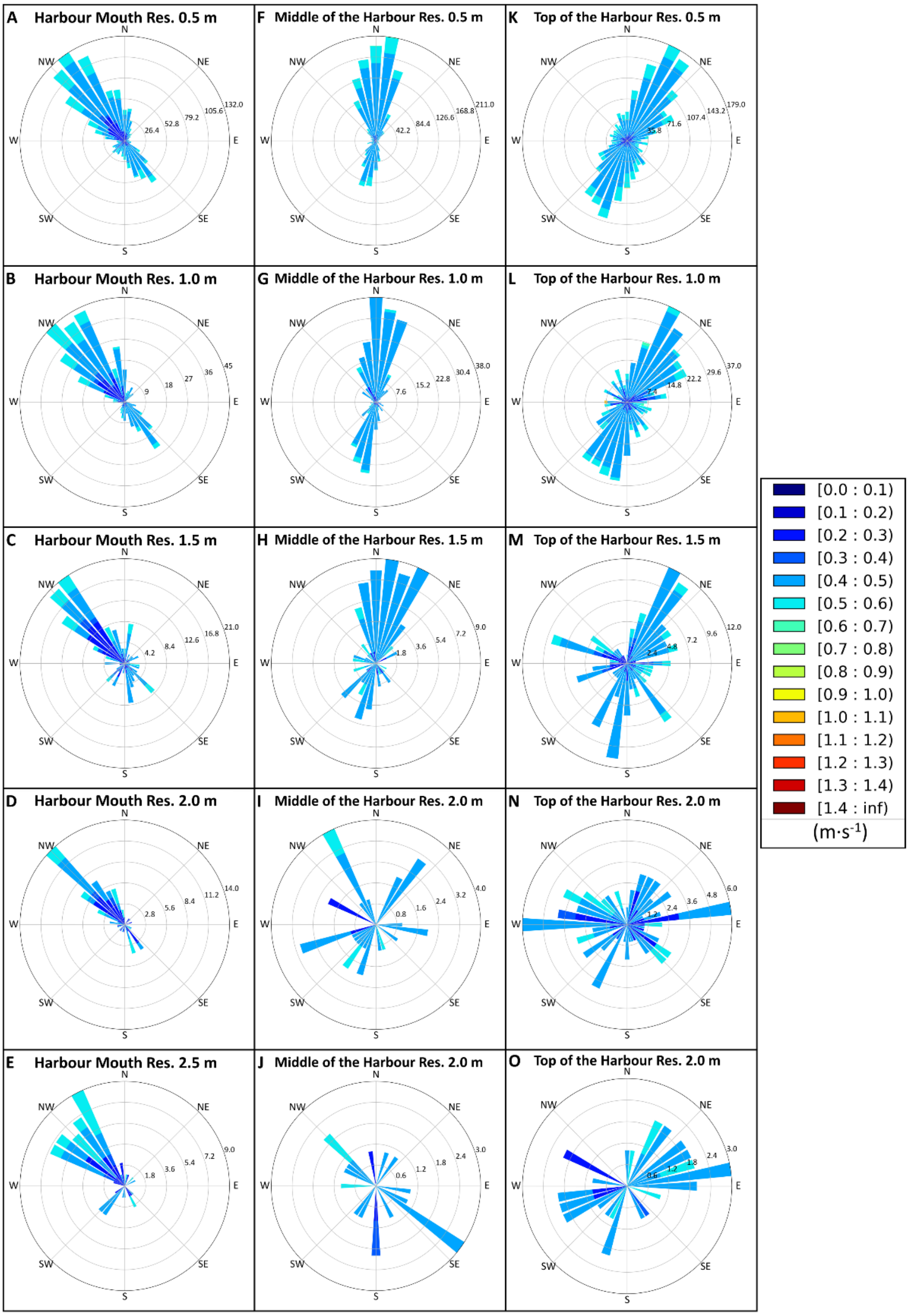

Figure 31. Current velocity profiles for the mouth of the harbour for bathymetry gridded at (**A**) 0.5, (**B**) 1.0, (**C**) 1.5, (**D**) 2.0, and (**E**) 2.5 m resolutions, for the middle of the harbour for bathymetry gridded at (**F**) 0.5, (**G**) 1.0, (**H**) 1.5, (**I**) 2.0, and (**J**) 2.5 m resolutions, and for the top of the harbour for bathymetry gridded at (**K**) 0.5, (**L**) 1.0, (**M**) 1.5, (**N**) 2.0, and (**O**) 2.5 m resolutions.

4.3.3. Tidal Information

Seven tidal constituents presented with an amplitude of greater than 0.05 m (Table 13). The M2 constituent, or principal lunar semidiurnal constituent, was the largest tidal constituent, with an amplitude of 1.45 m and a phase of 148°. The S2 constituent, or principal solar diurnal constituent, was the second largest tidal constituent, with an amplitude of 0.45 m and a phase of 193°. The N2 constituent, or the larger lunar elliptic semidiurnal constituent, was the third largest tidal constituent, with an amplitude of 0.26 m and a phase of 126°. The K2 constituent, or the lunisolar semidiurnal constituent, was the fourth largest tidal constituent with an amplitude of 0.13 m and a phase of 191°. The M4 constituent, or the shallow water overtides of the principal lunar constituent, was the fifth largest tidal constituent and had an amplitude of 0.07 and a phase of 232°. The L2 tidal constituent, or the smaller lunar elliptic semidiurnal constituent, has an amplitude of 0.07 m and a phase of 161°. The nu2 constituent, or the Larger lunar evectional constituent, has an amplitude of 0.07 and a phase of 124°. The largest diurnal constituent is the O1 constituent, or the Lunar diurnal constituent, this is the 10th largest constituent and has an amplitude of 0.38 and a phase of 40°.

Table 13. The seven largest tidal constituents calculated during the harmonic analysis of the water level acquired from the Ringaskiddy tide gauge.

Constituents	Amplitude (m)	Phase (°)	Period (hrs)
M2	1.45	148	12.42
S2	0.45	193	12
N2	0.26	126	12.66
K2	0.13	191	11.97
M4	0.07	232	6.21
L2	0.07	161	12.19
nu2	0.07	124	12.63

The maximum observed tidal range for the month was 3.97 m and occurred on the 7th of November (Figure 32A). During the week prior to the acquisition of the MBES data, the water level data shows that the tide cycle was in a spring tide with the descent into the neap portion beginning 48 hrs prior to the 26th of November (Figure 32B). Furthermore, low tide been reached, and the tides were beginning to ascend into peak tide as the MBES data were being collected (between 10:55 to 15:46), (Figure 32C).

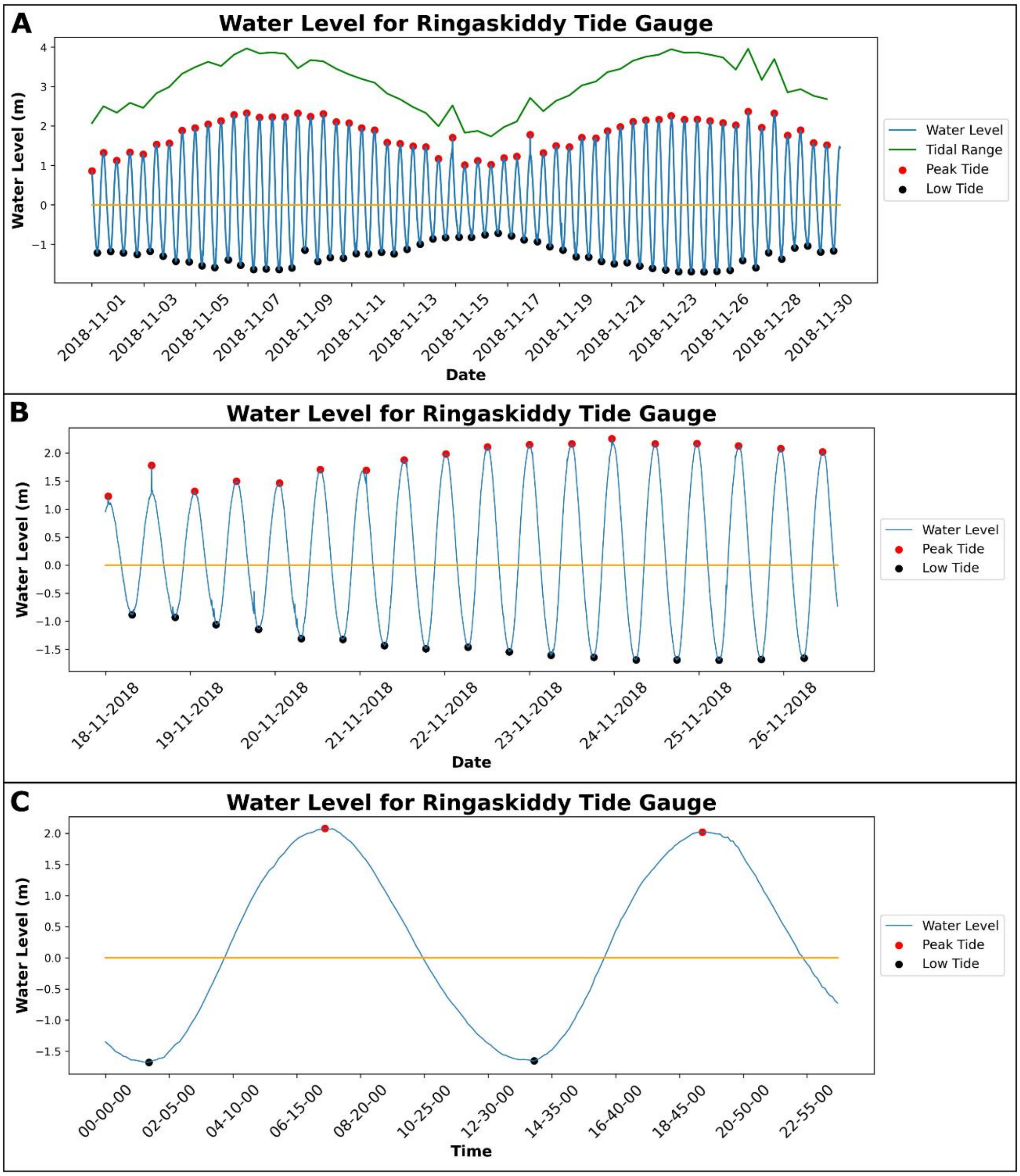

Figure 32. The recorded water level acquired by the Ringaskiddy tide gauge, the peak and low tide points, and tidal range for (**A**) the month of November 2018, and (**B**) the week from the 19th to the 26th of November 2018, and (**C**) the recorded water level and peak and low tide points for the entire day of the 26th of November 2018.

4.3.4. Angular Range Analysis

Median *phi* values derived from the 400 kHz backscatter data for the SWs occurring within bathymetry gridded at 0.5, 1.0, 1.5, 2.0, and 2.5 m resolutions acquired within the mouth of the harbour were 2.91, 2.99, 3.02, 2.87, and 2.98 respectively (Table 14).

Table 14. The median *phi* value for the SWs and SSDs derived from the 0.5, 1.0, 1.5, 2.0, and 2.5 m resolution bathymetry data for the mouth, middle and top of the harbour respectively.

Section	Class	Resolution (m)	***Median Phi* Value**
Mouth	SW	0.5	2.91
		1.0	2.99
		1.5	3.02
		2.0	2.87
		2.5	2.98
	SSD	0.5	1.93
		1.0	1.66
		1.5	2.33
		2.0	2.97
		2.5	2.96
Middle	SW	0.5	2.53
		1.0	2.84
		1.5	2.10
		2.0	2.60
		2.5	2.50
	SSD	0.5	2.38
		1.0	2.27
		1.5	2.33
		2.0	2.38
		2.5	2.53
Top	SW	0.5	2.90
		1.0	2.97
		1.5	2.89
		2.0	3.03
		2.5	3.10
	SSD	0.5	2.80
		1.0	2.84
		1.5	2.86
		2.0	2.87
		2.5	3.08

Median *phi* values derived from the 400 kHz backscatter data for the SSDs occurring within bathymetry gridded at 0.5, 1.0, 1.5, 2.0, and 2.5 m resolutions acquired within the mouth of the harbour were 1.93, 1.66, 2.33, 2.97, and 2.96 respectively(Figure 33A–E).

Median *phi* values derived from the 400 kHz backscatter data for the SWs occurring within bathymetry gridded at 0.5, 1.0, 1.5, 2.0, and 2.5 m resolutions acquired within the middle of the harbour were 2.53, 2.84, 2.10, 2.60, and 2.50 respectively (Figure 33F–J). Median *phi* values derived from the 400 kHz backscatter data for the SSDs occurring within bathymetry gridded at 0.5, 1.0, 1.5, 2.0, and 2.5 m resolutions acquired within the middle of the harbour were 2.38, 2.27, 2.33, 2.38, and 2.53 respectively.

Median *phi* values derived from the 400 kHz backscatter data for the SWs occurring within bathymetry gridded at 0.5, 1.0, 1.5, 2.0, and 2.5 m resolutions acquired within the top of the harbour were 2.90, 2.97, 2.89, 3.03, and 3.10 respectively (Figure 33K–O). Median *phi* values derived from the 400 kHz backscatter data for the SSDs occurring within bathymetry gridded at 0.5, 1.0, 1.5, 2.0, and 2.5 m resolutions acquired within the top of the harbour were 2.80, 2.84, 2.86, 2.87, and 3.08 respectively.

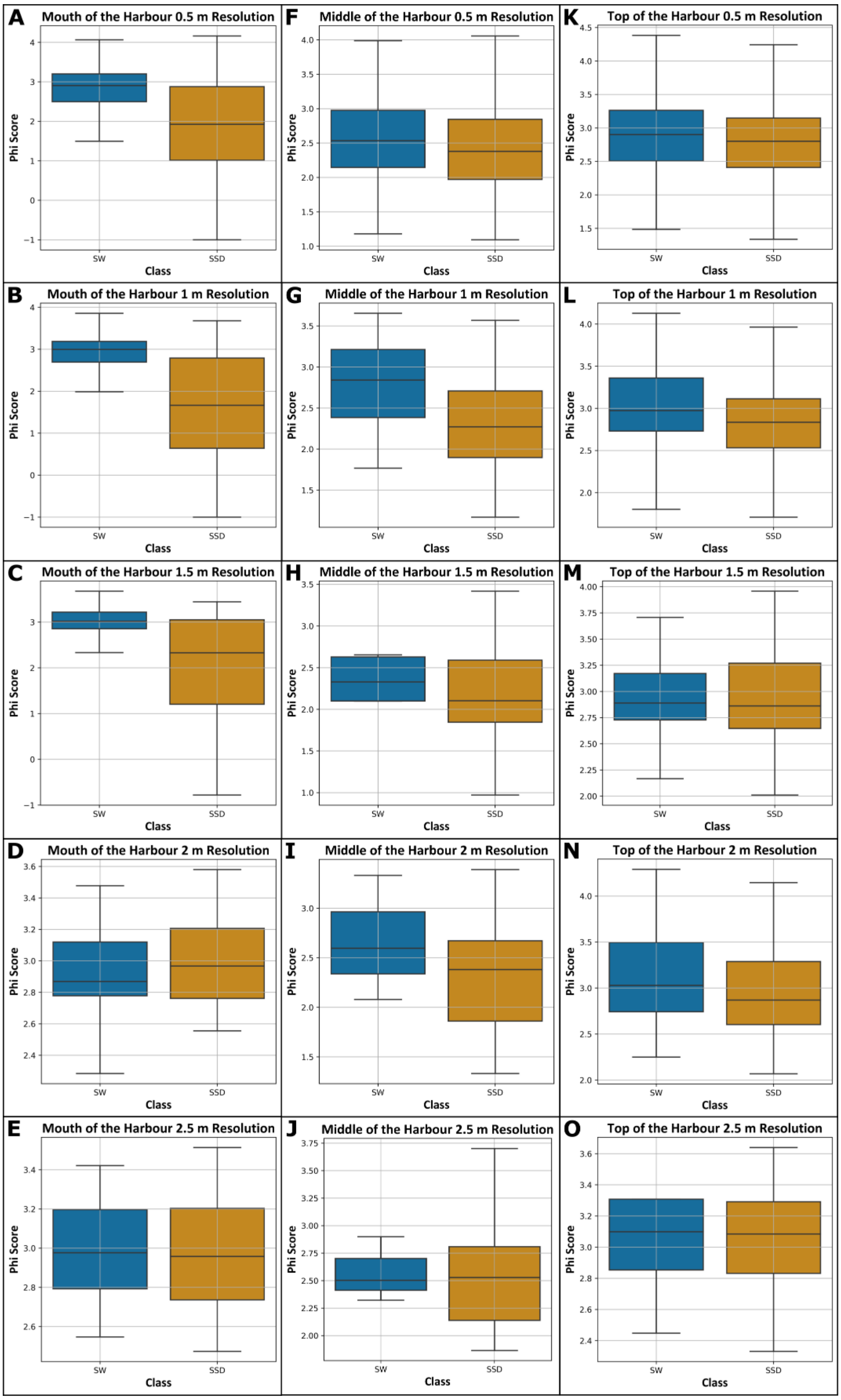

Figure 33. *Phi* scores derived by ARA of 400 kHz MBES backscatter for sediment waves (SW) and sinuous sedimentary dunes (SSD) from the bottom of the harbour for bathymetry gridded at (**A**) 0.5, (**B**) 1.0, (**C**) 1.5, (**D**) 2.0, and (**E**) 2.5 m resolutions, for the middle of the harbour for bathymetry gridded at (**F**) 0.5, (**G**) 1.0, (**H**) 1.5, (**I**) 2.0, and (**J**) 2.5 m resolutions, and for the top of the harbour for bathymetry gridded at (**K**) 0.5, (**L**) 1.0, (**M**) 1.5, (**N**) 2.0, and (**O**) 2.5 m resolutions.

4.4. Discussion

4.4.1. The Tidal Regime in Cork Harbour

Current flow in Cork Harbour is controlled by the dominant semidiurnal tidal cycle as evidenced through the harmonic analysis of the tidal data, where 6 of the major tidal constituents are semi diurnal (Table 13). Moreover, the O1 constituent is the largest diurnal tidal constituent, although it has an amplitude that is 38 times smaller than the M1 constituent. Furthermore, this semidiurnal tidal series has a superimposed spring and neap cycle that amplifies the tidal range every fortnight (Figure 32A–C). The MBES data were acquired two days after the spring tide maximum, as the water level approached low tide. Previous acoustic doppler current profiler (ADCP) measurements conducted at Spit Bank within the harbour show that current velocities are greatest during the peak or flood tide with a second smaller peak in current velocity occurring at low or ebb tide (Office of Public Works, 2017). This asymmetry is further corroborated by the results from the current velocity estimates derived at 0.5 m resolution data, where a larger proportion of the current velocities are aligned with the flood tide throughout the harbour. Moreover, this flood tide asymmetry is maintained even though the current velocity estimates were derived from MBES data acquired during the ebb phase of the tide (Figure 32C). However, topographic is steering evident throughout the Cork Harbour region and has led to local variations in the influence and direction of the flood and ebb tides as seen in the SSB orientations (Figure 31A, F, K). For example, 63 % of current velocity estimates derived from the analysis of SSBs in the mouth of the harbour are aligned with the flood tide and are orientated to the north-west. The middle of the harbour displays the greatest asymmetry with 69% of current velocity estimates aligned to the north with the flood tide. Conversely, the lowest influence imposed by the flood tide can be found at the top of the harbour, where 53% of current velocity estimates are aligned to the north-east with the flood tide. This change in direction for each section of the harbour tracks the change in orientation of the main channel within the harbour at these locations (Figure 26A). The current flow in these regions is rectilinear with the ebb tide occurring at ~180° to the flood tide.

Two classes of "crests" were observed in the harbour: sediment waves (SWs) and SSDs. The largest proportion of SWs to SSDs is found in the mouth of the harbour at 28%, these SWs have a larger wavelength and wave height than the corresponding SSDs within this section of the harbour. According to Stow et al. (2009), these SWs have formed over longer timespans than the SSDs. Furthermore, 72% of these SWs are orientated with the flood tide. Therefore, these SWs are formed due to long term flood tidal forces reworking the sediment in this section of the harbour. In addition, these SWs occur to the west of this section of the harbour. Hence, the more consistent long-term influence of the flood tide is due to increased distance from the main channel of the harbour and greater proximity to the sea (Figure 26A(i)). The SSDs found within this section of the harbour mainly occur to the east and south-east. Moreover, the smaller size of these SSDs are symptomatic of short term variations in the current flow direction (Stow et al., 2009). This is further evidenced by the greater variation in current velocity orientations for the SSDs within this portion of the site, where a lower proportion (63%) of these SSDs are orientated northwards when compared with the SWs. Therefore, the increased presence of the SSDs signifies increased proximity to the main channel of the harbour, where the currents induced from the ebb tide impose a greater influence over the formation of the bedforms within this region.

The greatest proportion of SSDs are observed within the middle of the harbour at 90%. Moreover, as seen with the mouth of the harbour, the SSDs have a lower wavelength and wave height than the corresponding SWs. Therefore, this section of the harbour is defined by shorter term variations in the current flow orientation, despite having the largest proportion of flood tide-aligned current flow estimates (69%). Additionally, fewer SWs are aligned with the flood tide in this section of the harbour than what was observed in the mouth of the harbour (60%). Consequently, the flood tide asymmetry is not maintained over the same timespan as is seen in the mouth of the harbour. Therefore, despite the clear influence of the flood tide within the middle of the harbour, the SSD and SWs and are subject to more short-term variation in the current flow. This may be due to the increased distance from the harbour mouth reducing the effects of the tides entering the harbour. A marginal flood tide asymmetry is observed in the top of the harbour as 53% of the current flow estimation are aligned with the flood tide. This decrease in flood tide alignment is a result of the increased distance away from the mouth of the harbour relative to the other two sections. Thus, the impact of the flood tide induced currents are dampened in this region with ebb tides have an increased influence on SSB formation.

4.4.2. The Influence of MBES Data Spatial Resolution on the Temporal Resolution of Benthic Currents Derived from SSBs

When considering the OBIA outputs for each resolution of MBES bathymetry data, the number of "crests" generated was significantly lower with increase in resolution of MBES bathymetry. The largest decrease was observed between the results for the 0.5 and 1.0 m resolution for each section of the harbour. Despite this decrease, the median flood tide and ebb tide current directions, and the relative proportion of flood tide versus ebb tide estimates remains similar between these two resolutions (Figure 31A, B, F, G, K, L). However, the current velocity estimates begin to vary significantly when appraising the results acquired at 2.0 m for each section of the harbour against those acquired for the 0.5 m resolution bathymetry data. For example, a drop in the proportion of SSDs relative to the SWs is noted for the current velocity estimates derived at 2.0 m for the top and mouth of the harbour (Table 12). Underlining the loss of more diminutive bedforms during the geomorphological characterisation of the coarser resolution data for these locations. Therefore, at 2.0 m resolution of bathymetry data these smaller bedforms no longer present as high-resolution objects that occur across multiple pixels of MBES bathymetry data and hence, are excluded during an OBIA workflow. This is evident when considering that the median wavelength for SSDs at each resolution is ~3 m, which creates a pixel size to SSD wavelength ratio of 2:3. Hence, indicating that any MBES data with a pixel size of >50% of the wavelength of the SSD is insufficient and should not be considered in an OBIA workflow.

For example, despite the mouth of the harbour achieving the least "crests" during the geomorphological characterisation of the 0.5 m resolution data, it maintained the highest number of "crests" during the geomorphological characterisation of the 2.5 m resolution data. The "crests" produced at this resolution have a greater proportion of SWs than for any other section of the harbour at any other resolution. Furthermore, the persistence of these SWs with coarsening resolution is due to the greater presence of larger bedforms within the region. Conversely, the smaller SSDs that represent shorter-term hydrodynamic processes are under-represented in the profile. The larger bedforms persisting with the coarser resolution MBES data indicate that the temporal resolution of the hydrodynamic processes expressed through seabed bedforms decreases with decreasing spatial resolution of MBES bathymetry data. Consequently, coarser resolution MBES bathymetry data prevents the analysis of shorter-term variations in seabed benthic habitats. Additionally, this is reflected in the lower standard deviation in current direction for the flood tide aligned current estimates and the higher standard deviation in current direction for the ebb tide aligned current velocity estimates at 2.5 m resolution in the mouth of the harbour. Where the integrity of orientation of the flood tide induced currents is maintained as they persist as larger bedforms, whereas the orientation of the ebb tide induced currents is inconsistent as they are expressed as smaller bedforms that are not perceived within the coarser resolution data. Moreover, the difference in median current direction between the 0.5 and the 2.5 m resolution data is lowest for the flood tide aligned currents in the mouth of the harbour. However, the median current direction determined for the ebb tide at 2.5 m resolution data at this location shows the largest deviation from the median current direction determined from the 0.5 m resolution data. This illustrates the loss of information relating to the ebb portion of the tide at this location with coarser resolutions of analysis.

Throughout the rest of the harbour, the median current directions for the flood tide and the ebb tide provided by the current flow estimates are influenced by the diminished presence of SSDs within the coarser resolution bathymetry data. As the largest divergence from the median flood and ebb tide current direction provided by the 0.5 m resolution data is found for either the 2.0 or 2.5 m resolution dataset for each section of the harbour. Moreover, the standard deviation of current flow direction for the ebb and flood tide-aligned currents derived from the top and middle of the harbour increases with decreasing resolution. These two locations have the highest proportion of SSDs and therefore would be more susceptible to the loss of information presented by the loss of the SSDs with decreased resolution of MBES bathymetry data. Additionally, the median orientation provided for both the flood tide and ebb tide currents at the 2.5 m resolution data for these sites varied significantly from the median current directions determined from the 0.5 m resolution bathymetry data. The standard deviation of current orientation increased when comparing the estimates derived from coarser resolution data to those derived from the finer resolutions for these sites. Furthermore, the tidal dominance inferred from the greater alignment of current velocity estimates for the middle of the harbour inverted indicating ebb tide dominance when examining the results from the 2.0 and 2.5 m resolution bathymetry data. Thus, the inversion of the tidal asymmetry underlines the poor representation of the tidal regime at these resolutions.

Despite significant decreases in the number of current velocity estimates produced for the 1.5 m resolution dataset, the proportion of these estimates that were orientated with the flood and ebb tide were within ~1% of the proportions derived from the 0.5 m resolution data throughout the harbour. Furthermore, the median current directions for the flood and ebb portions of the tide remain within 10° of the original current flow orientations presented by the 0.5 m resolution data for the mouth, middle, and top of the harbour. Additionally, the pixel size to wavelength ratio for SSDs would be 1:2. Therefore, this would achieve the minimum resolution required to characterise these features (<50%). Moreover, the lower number of "crests" reduces the overall computation time required for the data, while still producing similar results to the higher resolution dataset. While computation time is not a vital prerequisite for this study, these findings have significant implications for acquisition, storage, and processing requirements for global mapping initiatives such as seabed 2030 (Mayer et al., 2018). Where minor improvements on survey and processing efficiency could scale up to provide substantial benefits for such projects.

4.4.3. Angular Range Analysis and Sediment Disturbance

The *phi* values inferred from the ARA of the 400 kHz backscatter show that there is a disparity in grain size between the SWs and SSDs derived from 0.5, 1.0, and 1.5 m of bathymetry in the mouth of the harbour. Here, the smaller SSDs have a low *phi* value and thus, a coarser grain size than the SWs. As discussed above, the smaller SSDs in this location are representative of short-term variations in the current direction due to the change between flood and ebb tide. Whereas the SWs in the mouth of the harbour represent a region with very little ebb tide influence. Therefore, as these data were collected during the ebb portion of the tide, the smaller SSDs likely experienced resuspension of finer sediments more recently than the SWs, resulting in finer sedimentation for these SSDs. Moreover, the median *phi* values acquired for the SWs and SSDs derived from 2.0 and 2.5 m resolution bathymetry are more congruent with each other. This increase in *phi* value for the SSDs corresponds with the loss of the SSDs from the main channel where the ebb tide exerts the greatest influence within this section of the harbour (Figure 28E&F).

Moreover, higher *phi* values for SSDs derived from the 0.5 m resolution bathymetry in the middle and top of the harbour indicate that the grain size becomes finer with progression into the harbour (Figure 33A, F, K). Baseline tidal modelling of the harbour conducted by Office of Public Works (2017) provided the maximum velocities achievable over a single tidal cycle with the largest values were achieved in the mouth of the harbour (Figure 34). Additionally, this velocity decreases with progression into the harbour thus, this corresponds with the decrease in sediment grain size.

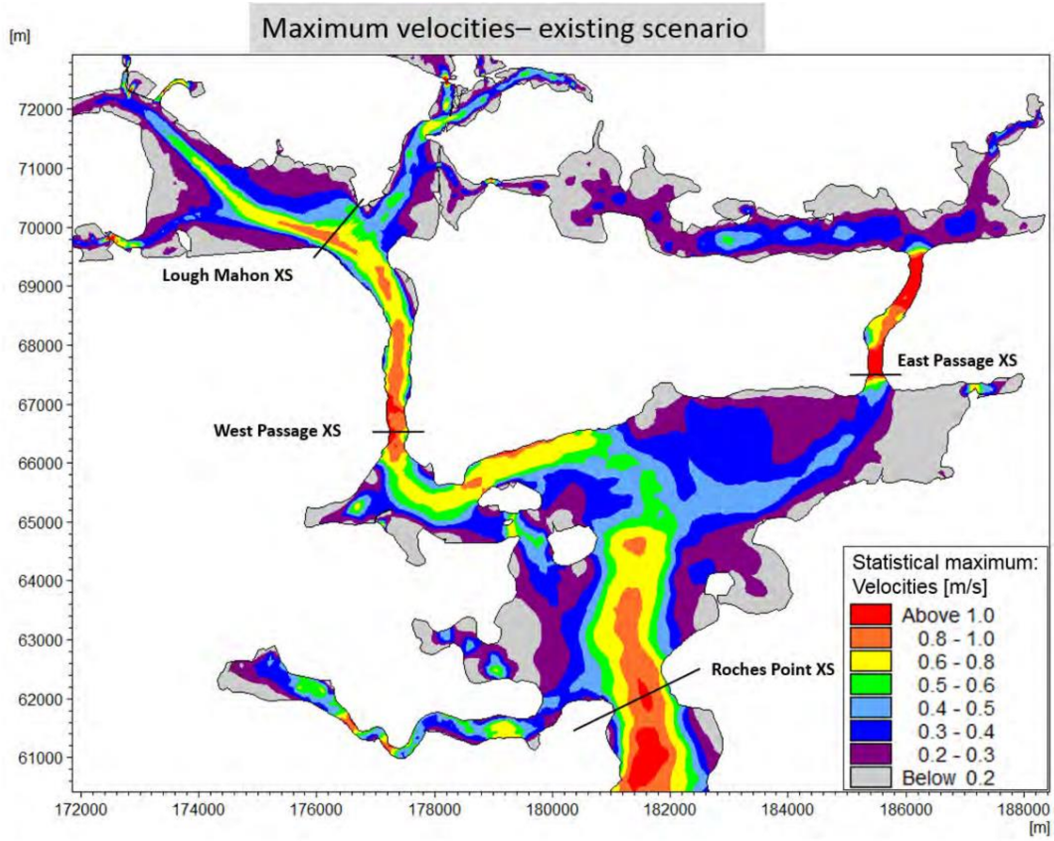

Figure 34: Map of the maximum velocity over a full tidal cycle adapted from Office of Public Works (2017).

Therefore, the grain size decrease from the mouth of the harbour to the top of the harbour is a direct result of the decrease in current velocity. Hence, while the finer grain size of the SW relative to the SSDs in the mouth of the harbour indicates a reduction in the short-term variation of the current flow, the finer grain size of depicted for SSDs at the top and middle of the harbour indicate a reduction in current flow velocity.

4.5. Conclusions

This research outlines the first OBIA workflow to integrate current velocity estimates derived from multiple resolutions of MBES bathymetry data and an ARA of concurrent backscatter to appraise the hydrodynamics within an estuarine environment. Our findings show that the representation of the hydrodynamics expressed through the SSBs evident throughout the harbour was well preserved at 0.5, 1.0 and 1.5 m spatial resolutions of MBES bathymetry. Furthermore, this representation persisted in the 1.5 m resolution bathymetry output despite a substantial drop in the number of current velocity estimates when compared with the 0.5 m dataset. However, a significant decline in the integrity of the representation of the current flow regime is observed in the 2.0 and 2.5 m resolution data, indicating that smaller SSBs were no longer evident at these resolutions and thus, impacted the veracity of the representation of the hydrodynamic regime. Moreover, these smaller SSBs represent the short-term variation in current direction with the change in the phases of the tide; therefore, coarser resolution MBES data prevents the analysis of finer temporal resolution hydrodynamic phenomena. Therefore, MBES data with a pixel size of >50% of the wavelength of the SSB being appraised is insufficient for inclusion in an OBIA workflow. Furthermore, the sediment characteristics estimated through an ARA of the corresponding backscatter illustrated regions of consistent sediment re-suspension in the mouth of the harbour, and a reduction of current velocity with increased progression into the harbour. Previous OBIA research has failed to consider the impact that these alterations in spatial resolution of MBES bathymetry data would have on the temporal resolution of seabed environmental processes conveyed through SSB geomorphology. Consequently, these results underline the significance of the framing of the hydrodynamic processes depicted by SSBs within separate spatial resolutions of MBES bathymetry data and affords valuable insight on the resolution appropriate for large scale seabed habitat mapping programmes (Mayer et al., 2018). Moreover, these findings can be integrated with *in situ* current velocity measurements to provide more robust appraisals of the current velocity regime while reducing the spatial density requirements for this sampling.

Author Contributions: Conceptualisation, G.S.; Methodology, G.S. and A.L.; Software, G.S.; Validation, G.S.; Formal Analysis, G.S.; Investigation, G.S.; Resources, G.S. and A.L.; Data Curation, G.S.; Writing—Original Draft Preparation—G.S.; Writing—Review and Editing, G.S., A.L. and A.J.W.; Visualisation, G.S.; Supervision, A.L. and A.J.W.; Project Administration, G.S and A.J.W.; Funding Acquisition, A.J.W. All authors have read and agreed to the published version of the manuscript.

Funding: This research was developed under the Marine Protected Area Management and Monitoring (MarPAMM) (Project IVA5059) supported by the European Union's INTERREG VA Pro-gramme, managed by the Special EU Programmes Body (SEUPB). Bathymetric data were supplied by the Geological Survey Ireland and Marine Institute INFOMAR programme. The data processing workflow was developed by Gerard Summers and Aaron Lim is funded by the EU INTERREG V through the Special EU Programmes Body (SEUPB) and the Irish Research Council (Project GOIPG/2015/2700), respectively.

Acknowledgments: Authors would like to thank all cruise crew and scientific parties on RV Celtic Voyager (cruise number CV18027).

Chapter 5. Conclusions

Object based image analysis is widely recognised as the most effective method for automated classification of high spatial resolution features depicted in MBES data and is quickly being adopted to map a wide variety of seafloor features (Diesing et al., 2014; Zelada Leon et al., 2020; Janowski et al., 2020). Furthermore, the ability of this technique to map features as part of a hierarchal workflow allows for the separation of image features by different magnitudes of scale (Tiede, 2014). This study presents the first appraisal of the capacity of OBIA to classify seabed features that occur across multiple spatial scales whose physical properties can provide insight into seabed benthic currents.

To understand the influence of spatial scale on the classification of SSBs in MBES bathymetry data, an OBIA was deployed to assess the ability of 4 machine learning classifiers to characterise SSBs that were observed in two resolutions of MBES bathymetry, answering the following research question: **Which classifier provided the most stable classification results for high resolution MBES bathymetry?** A k-fold cross validation was performed on the high-resolution samples derived from Cork Harbour showed that the voting classifier achieved the highest training and test accuracy scores. The samples from the low-resolution MBES data derived from the Hempton's Turbot Bank SAC and Offshore South Wexford were used to answer the following research questions: **Which classifier provided the highest accuracy score for the low resolution MBES bathymetry?** and **What implications do these findings have for the suitability of each classifier for a scale standardised object-based technique?** Metrics such as accuracy and Cohen's kappa coefficient showed that the voting classifier achieved the most accurate classification, demonstrating that the most complex classifier provided the most accurate results. However, the relative difference in classification accuracy between the classifications was low. Moreover, a significant spatial clustering of the erroneously classified samples for each classifier was found where the SSB orientation was highly variable and the extent of the SSBs was greatly reduced. Therefore, these results indicate that OBIA is robust to variations in spatial scale however, the SSB image features must be represented over several pixels to ensure an accurate classification is achieved. Consequently, this research displayed an OBIA workflow that attained a high fidelity of accuracy while maintaining consistent segmentation and classification parameters.

This OBIA workflow was adapted for Chapter 3, permitting the first two research question to be answered: **Can a semi-automated methodology be developed to identify SSBs and separate them based on their inherent morphological features?** and **Can this method be further developed to estimate current speed from bathymetric profiles extracted from MBES data?** The separation of SSB morphology offered by the k-means classification also allowed for the separation of unidirectional current flow represented by long straight crested SSBs and more disrupted current flow represented by small sinuous crested SSBs. Density maps of the classes derived from the k-means classification were used to show that consistency of unidirectional current flow was greatest where the greatest density of CWC mounds were previously reported by Lim et al. (2018a). Successful estimation of current speeds from the SSBs exhibited a bimodal distribution of current speed and current orientation. Moreover, the average current velocity of 0.37 $m \cdot s^{-1}$ produced was congruent with the current velocities derived from grain-size analysis of box-cores acquired within the region (Lim et al., 2018a). Indicating a successful replication of the general current conditions within the area.

The current speeds derived from this bedform velocity estimation enabled the last two research questions to be answered: **What do the classified SSB morphologies in combination with the current speed estimates infer about the regional, local, and, micro hydrodynamics?** and **Does CWC mound proximity influence the velocity of the currents?** The estimated current flow velocity and the consistency depicted in the k-means classification displayed the influence of topographic steering on the current flow orientation and consistency at regional, local, and micro scales. For instance, currents derived at the eastern portion of the study site were found orientated to the NNW. This alignment matches the orientation of sediment waves observed by Dorschel et al. (2007). These sediment waves were postulated to be generated by geostrophic contour currents induced by the MOW. Thus, the common alignment between these sediment waves and the SSBs at this site indicate a common origin. However, current flow becomes aligned to the NNE upon approach to the western edge of the NNE aligned channel, with a decrease in current flow consistency, suggesting a local topographic steering influence imposed by the channel. The micro scale steering effects are seen around the CWC mounds. Where the median current direction alters by >7° upon approach to the CWC mounds. Conti et al. (2019) classified orthomosaics derived from ROV video of CWC mounds within this region and noted that live coral framework occurred on slopes with two prevailing orientations, at 300° and 7°. These slope orientations face obliquely away from the median current directions depicted for the NNW and the NNE orientated estimates at 200 m away from the mounds. However, the current flow alters with greater proximity to the mounds, imprinting a better alignment with the slopes that the live coral framework occurs on. Moreover, mound obstruction effects results in decreased current flow velocities with increasing proximity to the mounds, with a greater decline noted for the NNW aligned currents, encouraging better conditions for food capture. The increased success of CWC growth on slopes facing away from established current flow regimes has been reported by Lim et al. (2020). Here, ADCP data were integrated with a semi-automated classification of CWC environments, where higher proportions live coral framework were observed on slopes orientated away from high current speeds.

The OBIA characterisation from Chapter 2 and the current speed estimation from Chapter 3 were further adapted for Chapter 4 and were used to answer: **Can the tidal regime at each sub site of Cork Harbour be determined?** The current speeds derived from the 0.5 m resolution data were used as the baseline dataset to ascertain the current flow properties throughout Cork Harbour. Current speed estimations for Cork Harbour exhibited a rectilinear current flow throughout the site. Moreover, tidal asymmetry was observed throughout the harbour, with the flood tide imposing the greatest influence the orientation of SSBs within each section of the harbour. This flood tide asymmetric rectilinear flow matches current speeds measurements previously acquired by ADCP with the harbour. The OBIA derived current velocity estimates were repeated across 1.0, 1.5, 2.0, and 2.5 m resolutions of MBES data acquired in Cork Harbour to answer: **What is the optimum resolution to reconstruct**

the tidal regime? Preservation of the rectilinear current pattern was evident in the current velocity estimates derived from the 1.0 and 1.5 m resolution across each section of Cork Harbour. However, this pattern was not evident in the current velocity estimates derived from the 2.0 and 2.5 m resolution MBES data. Considering the intense computational requirements implied by the acquisition of and processing of data from the entire seafloor by 2030 the current speeds derived from the 1.5 m resolution MBES data provide the optimum depiction of benthic current regimes. As far fewer objects are produced when compared with the current velocity estimates derived from the 0.5 and 1.0 m resolution MBES data, yet these objects preserve the patterns exhibited at the finer resolutions.

ARA of the corresponding backscatter was used to answer the question: **Do the ARA derived grain size measurements help to evaluate the consistency of sediment disturbance due to the influence of the change in tide?** *Phi* values provided by the ARA showed that the median grain size for the SW classified SSDs in the mouth of the harbour were finer than the SSDs in the same section of the harbour. Here, the SWs are larger in extent and therefore, their morphologies are more stable over time. However, the SSDs are smaller in extent thus, they would be symptomatic of short-term variations in the current flow. These short-term variations would indicate more frequent re-mobilisation of sediment, preventing the settling of finer grained sediments relative to the SWs within this region. Moreover, the SSDs in the middle and top of the harbour exhibit higher median *phi* values with indicating decreased grain size, the finest median grain size depicted for SSDs was found at the top of the harbour Consequently, the median grain size decreases with increasing distance away from the harbour mouth. This may indicate a local decrease in the imposition of the flood tide within the top and middle of the harbour, resulting in less resuspension of sediment over the semi diurnal tidal cycle.

5.1. Recommendations for Future Studies

It is clear from the wider literature that classification of geomorphological features through supervised techniques is the most effective approach to replicating human interpretation of MBES bathymetry data (Zelada Leon et al., 2020; Janowski et al., 2020). Chapter 2 focused on appraising the ability of supervised classifications to accurately characterise SSBs in two different resolutions of MBES data. However, the SSBs within this chapter represent a very narrow selection of the geomorphological features and their relative scales of occurrence within the marine realm. Therefore, the inclusion of a greater variety of geomorphological features within a supervised classification scheme would offer a greater implement to effectively map the seabed. Furthermore, the classification presented in this study exhibited an inability to identify bedrock from SSBs when applied to areas of more complex sediment wave fields. Consequently, small amounts of bedrock were erroneously classified as SSBs. This distinction is obvious to the human interpreter and these examples were not included in the publishable data presented here. Moreover, these bedrock features have a pronounced response in MBES backscatter intensity data signature, one that provides a clear dissimilarity to unconsolidated SSBs. However, the ambiguity that currently remains in MBES backscatter intensity data between regions and between seabed cover classes precludes their inclusion in supervised classification schemes. Thus, once rigorous and ubiquitous acquisition, calibration, and processing parameters can be developed for these data, this will provide the information required by supervised classifiers to distinguish between SSBs and bedrock. Additionally, the creation of a full inventory of geomorphological features within a supervised classification would dramatically increase the number of classes required to adequately describe the seafloor. Deep learning algorithms have been shown to exceed human interpreters when characterising data with a significant number of classes (Diegues et al., 2018). Therefore, the supervised classification offered by deep learning algorithms would be most adequately suited in the provision of an automated classification of seabed mapping data.

SSBs depicted in MBES bathymetry data offer an avenue for the investigation of the nature of seabed hydrodynamics across a wide area of seafloor. Chapter 3 investigated the adaptation of the workflow from Chapter 2 to derive seabed current velocity estimates from SSBs depicted in MBES bathymetry data. While the current velocity estimates were derived from SSBs occurring adjacent to CWC habitats, these features occur across a wide range of spatial scales and seabed habitats and thus raise the question of large-scale application across the marine realm. Contemporary *in situ* seabed current measurement apparatuses provide current data for a single point above the seabed. Such data are useful to characterise the current conditions over time for that point in space. However, it does not achieve the spatial resolution necessary to depict the interaction of seabed current with complicated topography or heterogeneous geomorphological environments. Therefore, to effectively depict the intricate seabed current hydrodynamics over larger scale environments the information from these single point measurements will need to be extended to entire seabed habitats. The density of *in situ* monitoring devices required to provide this information would alter the very current flow that they are attempting to measure and thus, render such a task unfeasible. Consequently, the information offered by these devices needs to be reconciled the complex geomorphology inherent to the seabed. The seabed benthic current velocity estimate methodology outlined in Chapter 3 offer the means to complete this task. Reducing the number of *in situ* devices required to determine seafloor hydrodynamics and hence, reducing the cost of environmental monitoring. Moreover, integrating these two datasets would help challenge the assumptions made in the bedform velocity matrix outlined by Stow et al. (2009). Calibrating these estimates using corresponding groundtruthing data and allowing for more accurate estimates of the seabed hydrodynamics to be derived within this workflow. Furthermore, this workflow has applications in many economic and ecological sectors within the marine realm. For instance, many sessile underwater species require enhanced benthic currents for the delivery of nutrients, provision of hard ground for settlement on the seafloor, and for the dispersal of larvae. Thus, the current velocity estimate workflow could be used as an input for species distribution modelling. Additionally, offshore infrastructural projects are heavily dependent on the seabed current environment and the nature of the sediment transport, as unstable seafloor surfaces present issues for the long-term viability of offshore developments. The current velocity analysis provided by Chapter 3 would provide vital information for the assessment of offshore development candidate sites.

Definition of the appropriate resolution of observation is fundamental to the evaluation of marine environmental processes. Chapter 4 defined an iterative approach to analysing and defining the suitable spatial resolution to adequately depict the seafloor hydrodynamics that are expressed through a wide variation of scales of SSBs. However, this resolution is adequate for the examination of seabed induced currents within a semi diurnal tidal cycle within an enclosed estuary. This does not present a representation of the full range of temporal scales that these seafloor currents operate over. Nor does it provide the full picture of the intricate interaction of the diverse array of seafloor hydrodynamics with each seafloor cover category. Therefore, for a full assessment of each of these processes, a larger scale study must be executed, one that derives current velocities from a wide range of SSB morphologies evident in open water and confined flow conditions.

Appendices

Appendix I. Courses Completed During the Ph. D.

2020

- 5 credits of Programming in Python with Data Science Applications (CS6507) — University College Cork — Grade: pass (pass or fail grading system)
- Autonomous Underwater Vehicle (AUV) — Workshop Scottish Association for Marine Science — No grade
- Research Integrity Training — Epigeum — Grade: pass (pass or fail grading system).
- Offshore Security Awareness Training — Secure West Training Online — Grade: pass (pass or fail grading system)

2019

- 10 credits of Quantitative Skills for Biologists using R (BL6024) — University College Cork — Grade: pass (pass or fail grading system)

2018

- R Studio Clinic — University College Cork — No grade

Appendix II. Publications Completed During the Ph. D.

2022

- Summers, G., Lim, A., & Wheeler, A.J. (2022). A characterization of benthic currents from seabed bathymetry: an object-based image analysis of cold-water coral mounds, Remote Sensing, 14, 4731. https://doi.org/10.3390/rs14194731

2021

- Summers, G., Lim, A., & Wheeler, A.J. A scalable, supervised classification of seabed sediment waves using an object-based image analysis approach. Remote Sensing (2021), 13, 2317. https://doi.org/10.3390/rs13122317

Appendix III. Research Cruises Undertaken as Part of, and During the Ph. D.

2022

- CE 22013 — Sediment Plume Sampling, Bedrock Drilling and Coral Surveying (Geoscientist).

2021

- CE 21011 (Leg 2) — Systematic Monitoring Survey of the Moira Mound Chain I (Day shift leader).
- RV Corystes — MarPAMM cruise to the Foyle, North Channel, and Sound of Jura (Geoscientist).

2020

- CE20011 (Leg 1) — Systematic Monitoring Survey of the Moira Mound Chain I (Day shift leader).
- CE20007 — INFOMAR (Night Shift Leader).

2019

- CE19023 (Leg 1) — De-risking Offshore Wind Energy Development Potential in Irish Waters I (Night shift leader).
- CE19014 (Leg 2) — Monitoring Changes in Submarine Canyon Coral Habitats II (Day shift leader).
- CE19001 (Leg 1) — Monitoring Changes in Submarine Canyon Coral Habitats I (Day shift leader).

2018

- CE18011 (Leg 2) — Controls of Cold-Water Coral Habitats in Submarine Canyons II (Geoscientist).

2017

- RH17002 (Leg 1) — Controls of Cold-Water Coral Habitats in Submarine Canyons I (Geoscientist).

Appendix IV. Awards and Grants Received During the Ph. D.

Awards

2022

- Best oral presentation (including post-doctoral researchers) — Irish Earth Observation Symposium.

2020

- Honourable Mention (Poster Presentation) — Irish Geological Research Meeting.

Grants

2022

- Ron McDowell Student Award, GeoHab — €855.
- Marine Institute Network and Travel Award — €750 — Provisionally Accepted.
- Marine Institute Network and Travel Award — €750 — Provisionally accepted.

2020

- Marine Institute Ship Time Grant — €136,000 — I was lead applicant for the Developing Efficient and Effective Habitat Mapping Tools for Marine Protected Areas ship time grant, this survey was proposed to provide baseline data for mapping and monitoring approaches for several key Irish Marine Protected Areas — cancelled due to COVID 19 restrictions.

Appendix V. Conference Presentations Completed During the Ph. D.

2022

- Irish Earth Observation Symposium — Dublin, Ireland — Oral Presentation (A Characterisation of Benthic Currents from Seabed Bathymetry: An Object-Based Image Analysis of Cold-Water Coral Mounds).
- Marine Protected Areas Management and Monitoring Closure Event — Dublin, Ireland — Poster Presentation (Investigating the use of Novel Technology for the Management and Monitoring of Benthic Ecosystem).
- Irish Geosciences Early Career Symposium — Cork, Ireland — Flash Oral Presentation (A Characterisation of Benthic Currents from Seabed Bathymetry: An Object-Based Image Analysis of Cold-Water Coral Mounds).
- GeoHab — Venice, Italy — Oral Presentation (A geomorphological object-based image analysis approach to investigate the hydrodynamics surrounding cold-water coral mounds).

2021

- GeoHab — Online — Oral Presentation (A Scalable, Supervised Classification of Seabed Sediment Waves Using an Object-Based Image Analysis Approach).

2020

- Irish Geological Research Meeting — Athlone, Ireland — Poster Presentation (Assessment of semi-automated classification techniques in characterising seabed sediment wave fields).
- Irish Geosciences Early Career Symposium — Cork, Ireland — Flash Oral Presentation (Monitoring of suspended material through multibeam echosounder water column data).

2019

- Irish Geological Research Meeting — Dublin, Ireland — In attendance.

Appendix VI. Outreach During the Ph. D.

I was an invited guest on the Tommy Outdoors podcast on the 13/04/2022, where I talked about the newest trends in automated benthic habitat mapping and the challenges faced by conservationists around the world. This is accessible through YouTube online (https://www.youtube.com/watch?v=R-IwdGc5hz4&t=3s).

Appendix VII. Publicly Available Data Repositories Generated

- A scale robust classifier – Python code available at GitHub.

Thesis References

ALEVIZOS, E. & GREINERT, J. 2018. The hyper-angular cube concept for improving the spatial and acoustic resolution of MBES backscatter angular response analysis. *Geosciences* [Online], 8.

ALLEN, A. & MILENIC, D. 2003. Drainage problems during construction operations within a burried valley gravel aquifer. *MATERIALS AND GEOENVIRONMENT,* 50**,** 1-4.

ALLEN, A. & MILENIC, D. 2007. Groundwater vulnerability assessment of the Cork Harbour area, SW Ireland. *Environmental geology,* 53**,** 485-492.

ALLEN, J. 1984. Development in sedimentology 30: Sedimentary structures their character and physical basis. Elsevier Science, Inc.

AMIRI-SIMKOOEI, A. R., SNELLEN, M. & SIMONS, D. G. 2011. Principal component analysis of single-beam echo-sounder signal features for seafloor classification. *IEEE Journal of Oceanic Engineering,* 36**,** 259-272.

ANDERS, N. S., SEIJMONSBERGEN, A. C. & BOUTEN, W. 2011. Segmentation optimization and stratified object-based analysis for semi-automated geomorphological mapping. *Remote Sensing of Environment,* 115**,** 2976-2985.

ANDERSON, J. T., VAN HOLLIDAY, D., KLOSER, R., REID, D. G. & SIMARD, Y. 2008. Acoustic seabed classification: current practice and future directions. *ICES Journal of Marine Science,* 65**,** 1004-1011.

ARSENI, M., VOICULESCU, M., GEORGESCU, L. P., ITICESCU, C. & ROSU, A. 2019. Testing Different Interpolation Methods Based on Single Beam Echosounder River Surveying. Case Study: Siret River. *ISPRS International Journal of Geo-Information* [Online], 8.

ASHLEY, G. M. 1990. Classification of large-scale subaqueous bedforms; a new look at an old problem. *Journal of Sedimentary Research,* 60**,** 160-172.

ATALAH, J., FITCH, J., COUGHLAN, J., CHOPELET, J., COSCIA, I. & FARRELL, E. 2013. Diversity of demersal and megafaunal assemblages inhabiting sandbanks of the Irish Sea. *Marine Biodiversity,* 43**,** 121-132.

AZAMI, H., MOHAMMADI, K. & BOZORGTABAR, B. 2012. An improved signal segmentation using moving average and Savitzky-Golay filter. *Journal of Signal and Information Processing,* Vol.03No.01**,** 6.

BAILLON, S., HAMEL, J.-F., WAREHAM, V. E. & MERCIER, A. 2012. Deep cold-water corals as nurseries for fish larvae. *Frontiers in Ecology and the Environment,* 10**,** 351-356.

BARGAIN, A., MARCHESE, F., SAVINI, A., TAVIANI, M. & FABRI, M.-C. 2017. Santa Maria di Leuca Province (Mediterranean Sea): Identification of suitable mounds for cold-water coral settlement using geomorphometric proxies and maxent methods. *Frontiers in Marine Science,* 4.

BARNARD, P. L., ERIKSON, L. H., ELIAS, E. P. L. & DARTNELL, P. 2013. Sediment transport patterns in the San Francisco Bay Coastal System from cross-validation of bedform asymmetry and modeled residual flux. *Marine Geology,* 345**,** 72-95.

BARNARD, P. L., ERIKSON, L. H. & KVITEK, R. G. 2011. Small-scale sediment transport patterns and bedform morphodynamics: new insights from high-resolution multibeam bathymetry. *Geo-Marine Letters,* 31**,** 227-236.

BARTLETT, D. & CELLIERS, L. 2016. Geoinformatics for applied coastal and marine management. *Geoinformatics for Marine and Coastal Management.* CRC Press.

BEISIEGEL, K., DARR, A., GOGINA, M. & ZETTLER, M. L. 2017. Benefits and shortcomings of non-destructive benthic imagery for monitoring hard-bottom habitats. *Marine Pollution Bulletin,* 121**,** 5-15.

BELDERSON, R. H., JOHNSON, M. A. & KENYON, N. H. 1982. Offshore tidal sands. *In:* STRIDE, A. H. (ed.) *Offshore tidal sands processes and deposit.* London: Chapman Hall.

BELGIU, M. & DRĂGUŢ, L. 2014. Comparing supervised and unsupervised multiresolution segmentation approaches for extracting buildings from very high resolution imagery. *ISPRS Journal of Photogrammetry and Remote Sensing,* 96**,** 67-75.

BEYER, A., SCHENKE, H. W., KLENKE, M. & NIEDERJASPER, F. 2003. High resolution bathymetry of the eastern slope of the Porcupine Seabight. *Marine Geology,* 198**,** 27-54.

BILLAUER, E. 2009. Peak detection in python. GitHub.

BLASCHKE, T. 2010. Object based image analysis for remote sensing. *ISPRS journal of photogrammetry and remote sensing,* 65**,** 2-16.

BLASCHKE, T., HAY, G. J., KELLY, M., LANG, S., HOFMANN, P., ADDINK, E., QUEIROZ FEITOSA, R., VAN DER MEER, F., VAN DER WERFF, H., VAN COILLIE, F. & TIEDE, D. 2014. Geographic object-based image analysis – towards a new paradigm. *ISPRS Journal of Photogrammetry and Remote Sensing,* 87**,** 180-191.

BOOLUKOS, C. M., LIM, A., O'RIORDAN, R. M. & WHEELER, A. J. 2019. Cold-water corals in decline – A temporal (4 year) species abundance and biodiversity appraisal of complete photomosaiced cold-water coral reef on the Irish Margin. *Deep Sea Research Part I: Oceanographic Research Papers,* 146**,** 44-54.

BOSWARVA, K., BUTTERS, A., FOX, C. J., HOWE, J. A. & NARAYANASWAMY, B. 2018. Improving marine habitat mapping using high-resolution acoustic data; a predictive habitat map for the Firth of Lorn, Scotland. *Continental Shelf Research,* 168**,** 39-47.

BRANDT, A., GUTT, J., HILDEBRANDT, M., PAWLOWSKI, J., SCHWENDNER, J., SOLTWEDEL, T. & THOMSEN, L. 2016. Cutting the umbilical: new technological perspectives in benthic deep-sea research. *Journal of Marine Science and Engineering,* 4**,** 36.

BROWN, C. J., BEAUDOIN, J., BRISSETTE, M. & GAZZOLA, V. 2019. Multispectral multibeam echo sounder backscatter as a tool for improved seafloor characterization. *Geosciences,* 9**,** 126.

BROWN, C. J. & BLONDEL, P. 2009. Developments in the application of multibeam sonar backscatter for seafloor habitat mapping. *Applied Acoustics,* 70**,** 1242-1247.

BROWN, C. J. & COLLIER, J. S. 2008. Mapping benthic habitat in regions of gradational substrata: an automated approach utilising geophysical, geological, and biological relationships. *Estuarine, Coastal and Shelf Science,* 78**,** 203-214.

BROWN, C. J., SAMEOTO, J. A. & SMITH, S. J. 2012. Multiple methods, maps, and management applications: Purpose made seafloor maps in support of ocean management. *Journal of Sea Research,* 72**,** 1-13.

BROWN, C. J., SMITH, S. J., LAWTON, P. & ANDERSON, J. T. 2011. Benthic habitat mapping: A review of progress towards improved understanding of the spatial ecology of the seafloor using acoustic techniques. *Estuarine Coastal and Shelf Science,* 92**,** 502-520.

BUHL-MORTENSEN, L., BUHL-MORTENSEN, P., DOLAN, M. J. F. & GONZALEZ-MIRELIS, G. 2015. Habitat mapping as a tool for conservation and sustainable use of marine resources: Some perspectives from the MAREANO Programme, Norway. *Journal of Sea Research,* 100**,** 46-61.

BUHL-MORTENSEN, P., HOVLAND, T., FOSSÅ, J. H. & FUREVIK, D. M. 2001. Distribution, abundance and size of *Lophelia pertusa* coral reefs in mid-Norway in relation to seabed characteristics. *Journal of the Marine Biological Association of the United Kingdom,* 81**,** 581-597.

BURGOS, J. M., BUHL-MORTENSEN, L., BUHL-MORTENSEN, P., ÓLAFSDÓTTIR, S. H., STEINGRUND, P., RAGNARSSON, S. Á. & SKAGSETH, Ø. 2020. Predicting the distribution of indicator taxa of vulnerable marine ecosystems in the arctic and sub-arctic waters of the nordic seas. *Frontiers in Marine Science,* 7.

BUSCOMBE, D. 2017. Shallow water benthic imaging and substrate characterization using recreational-grade sidescan-sonar. *Environmental Modelling & Software,* 89**,** 1-18.

CALVERT, J., STRONG, J. A., SERVICE, M., MCGONIGLE, C. & QUINN, R. 2014. An evaluation of supervised and unsupervised classification techniques for marine benthic habitat mapping using multibeam echosounder data. *ICES Journal of Marine Science,* 72**,** 1498-1513.

CARTER, L., GAVEY, R., TALLING, P. J. & LIU, J. T. 2014. Insights into submarine geohazards from breaks in subsea telecommunication cables. *Oceanography,* 27**,** 58-67.

CASAL, G., CORDEIRO, C. & MCCARTHY, T. 2022. Using satellite-based data to facilitate consistent monitoring of the marine environment around Ireland. *Remote Sensing,* 14**,** 1749.

CASSOL, W. N., DANIEL, S. & GUILBERT, É. 2021. A segmentation approach to identify underwater dunes from digital bathymetric models. *Geosciences* [Online], 11.

CAZENAVE, P. W., DIX, J. K., LAMBKIN, D. O. & MCNEILL, L. C. 2013. A method for semi-automated objective quantification of linear bedforms from multi-scale digital elevation models. *Earth Surface Processes and Landforms,* 38**,** 221-236.

CBD, S. The strategic plan for biodiversity 2011–2020 and the Aichi biodiversity targets. Secretariat of the Convention on Biological Diversity: Nagoya, Japan, 2010.

CHAPRON, L., PERU, E., ENGLER, A., GHIGLIONE, J. F., MEISTERTZHEIM, A. L., PRUSKI, A. M., PURSER, A., VÉTION, G., GALAND, P. E. & LARTAUD, F. 2018. Macro- and microplastics affect cold-water corals growth, feeding and behaviour. *Scientific Reports,* 8**,** 15299.

CHEN, G., WENG, Q., HAY, G. J. & HE, Y. 2018. Geographic object-based image analysis (GEOBIA): emerging trends and future opportunities. *GIScience & Remote Sensing,* 55**,** 159-182.

CHEN, J., JÖNSSON, P., TAMURA, M., GU, Z., MATSUSHITA, B. & EKLUNDH, L. 2004. A simple method for reconstructing a high-quality NDVI time-series data set based on the Savitzky–Golay filter. *Remote Sensing of Environment,* 91**,** 332-344.

CHENG, C. H., SOETAERT, K. & BORSJE, B. W. 2020. Sediment characteristics over asymmetrical tidal sand waves in the dutch North Sea. *Journal of Marine Science and Engineering* [Online], 8.

COIRAS, E., IACONO, C. L., GRACIA, E., DANOBEITIA, J. & SANZ, J. L. 2011. Automatic segmentation of multi-beam data for predictive mapping of benthic habitats on the Chella Seamount (North-Eastern Alboran Sea, Western Mediterranean). *IEEE Journal of Selected Topics in Applied Earth Observations and Remote Sensing,* 4**,** 809-813.

COLLIER, J. S. & BROWN, C. J. 2005. Correlation of sidescan backscatter with grain size distribution of surficial seabed sediments. *Marine Geology,* 214**,** 431-449.

CONTI, L. A., LIM, A. & WHEELER, A. J. 2019. High resolution mapping of a cold water coral mound. *Scientific Reports,* 9**,** 1016.

COOPER, K. M., BOLAM, S. G., DOWNIE, A.-L. & BARRY, J. 2019. Biological-based habitat classification approaches promote cost-efficient monitoring: An example using seabed assemblages. *Journal of Applied Ecology,* 56**,** 1085-1098.

COPELAND, A., EDINGER, E., DEVILLERS, R., BELL, T., LEBLANC, P. & WROBLEWSKI, J. 2013. Marine habitat mapping in support of Marine Protected Area management in a subarctic fjord: Gilbert Bay, Labrador, Canada. *Journal of Coastal Conservation,* 17**,** 225-237.

CORBANE, C., LANG, S., PIPKINS, K., ALLEAUME, S., DESHAYES, M., GARCÍA MILLÁN, V. E., STRASSER, T., VANDEN BORRE, J., TOON, S. & MICHAEL, F. 2015. Remote sensing for mapping natural habitats and their conservation status – New opportunities and challenges. *International Journal of Applied Earth Observation and Geoinformation,* 37**,** 7-16.

CORTES, C. & VAPNIK, V. 1995. Support-vector networks. *Machine Learning,* 20**,** 273-297.

COSTA, B. 2019. Multispectral acoustic backscatter: How useful is it for marine habitat mapping and management? *Journal of Coastal Research,* 35**,** 1062-1079.

COSTA, B.M., BATTISTA, T.A., PITTMAN, S.J., 2009. Comparative evaluation of airborne LiDAR and ship-based multibeam SoNAR bathymetry and intensity for mapping coral reef ecosystems. Remote Sens. Environ. 113, 1082–1100. https://doi.org/10.1016/j.rse.2009.01.015

COSTA, B. M. & BATTISTA, T. A. 2013. The semi-automated classification of acoustic imagery for characterizing coral reef ecosystems. *International Journal of Remote Sensing,* 34**,** 6389-6422.

COSTA, H., FOODY, G. M. & BOYD, D. S. 2017. Using mixed objects in the training of object-based image classifications. *Remote Sensing of Environment,* 190**,** 188-197.

COSTELLO, M. J. 2009. Distinguishing marine habitat classification concepts for ecological data management. *Marine Ecology Progress Series,* 397**,** 253-268.

COULDREY, A. J., BENSON, T., KNAAPEN, M. A. F., MARTEN, K. V. & WHITEHOUSE, R. J. S. 2020. Morphological evolution of a barchan dune migrating past an offshore wind farm foundation. *Earth Surface Processes and Landforms,* 45**,** 2884-2896.

COX, S. 2020. pytides2 0.0.5,. *Python community for the Python community.*

CREANE, S., COUGHLAN, M., O'SHEA, M. & MURPHY, J. 2022. Development and dynamics of sediment waves in a complex morphological and tidal dominant system: Southern Irish Sea. *Geosciences* [Online], 12.

CUI, X., LIU, H., FAN, M., AI, B., MA, D. & YANG, F. 2021. Seafloor habitat mapping using multibeam bathymetric and backscatter intensity multi-features SVM classification framework. *Applied Acoustics,* 174**,** 107728.

CZECHOWSKA, K., FELDENS, P., TUYA, F., COSME DE ESTEBAN, M., ESPINO, F., HAROUN, R., SCHÖNKE, M. & OTERO-FERRER, F. 2020. Testing side-scan sonar and multibeam echosounder to study black coral gardens: A case study from Macaronesia. *Remote Sensing,* 12**,** 3244.

DA SILVA PEREIRA, D. L. & CLARKE, J. E. H. Improving shallow water multibeam target detection at low grazing angles. Proc. US Hydrographic Conf., 2015. 1-21.

DA SILVEIRA, C. B., STRENZEL, G. M., MAIDA, M., GASPAR, A. L. & FERREIRA, B. P. 2021. Coral reef mapping with remote sensing and machine learning: A nurture and nature analysis in Marine Protected Areas. *Remote Sensing* [Online], 13.

DAMVELD, J. H., ROOS, P. C., BORSJE, B. W. & HULSCHER, S. J. M. H. 2019. Modelling the two-way coupling of tidal sand waves and benthic organisms: a linear stability approach. *Environmental Fluid Mechanics,* 19**,** 1073-1103.

DAMVELD, J. H., VAN DER REIJDEN, K. J., CHENG, C., KOOP, L., HAAKSMA, L. R., WALSH, C. A. J., SOETAERT, K., BORSJE, B. W., GOVERS, L. L., ROOS, P. C., OLFF, H. & HULSCHER, S. J. M. H. 2018. Video transects reveal that tidal sand waves affect the spatial distribution of benthic organisms and sand ripples. *Geophysical Research Letters,* 45**,** 11,837-11,846.

DAVIS, T., MACCARTHY, I. A., ALLEN, A. R. & HIGGS, B. 2006. Late Pleistocene-Holocene buried valleys in the Cork Syncline, Ireland. *Journal of Maps,* 2**,** 79-93.

DE CLIPPELE, L. H., GAFEIRA, J., ROBERT, K., HENNIGE, S., LAVALEYE, M. S., DUINEVELD, G. C. A., HUVENNE, V. A. I. & ROBERTS, J. M. 2017. Using novel acoustic and visual mapping tools to predict the small-scale spatial distribution of live biogenic reef framework in cold-water coral habitats. *Coral Reefs,* 36**,** 255-268.

DE CLIPPELE, L. H., VAN DER KAADEN, A.-S., MAIER, S. R., DE FROE, E. & ROBERTS, J. M. 2021. Biomass mapping for an improved understanding of the contribution of cold-water coral carbonate mounds to C and N Cycling. *Frontiers in Marine Science,* 8.

DE KNEGT, H. J., VAN LANGEVELDE, F., COUGHENOUR, M. B., SKIDMORE, A. K., DE BOER, W. F., HEITKÖNIG, I. M. A., KNOX, N. M., SLOTOW, R., VAN DER WAAL, C. & PRINS, H. H. T. 2010. Spatial autocorrelation and the scaling of species–environment relationships. *Ecology,* 91**,** 2455-2465.

DE OLIVEIRA, L. M. C., LIM, A., CONTI, L. A. & WHEELER, A. J. 2021. 3D classification of cold-water coral reefs: A comparison of classification techniques for 3D reconstructions of cold-water coral reefs and seabed. *Frontiers in Marine Science,* 8.

DEGRAER, S., MOERKERKE, G., RABAUT, M., VAN HOEY, G., DU FOUR, I., VINCX, M., HENRIET, J.-P. & VAN LANCKER, V. 2008. Very-high resolution side-scan sonar mapping of biogenic reefs of the tube-worm *Lanice conchilega*. *Remote Sensing of Environment,* 112**,** 3323-3328.

DEGRENDELE, K., ROCHE, M., SCHOTTE, P., VAN LANCKER, V. R. M., BELLEC, V. K. & BONNE, W. M. I. 2010. Morphological evolution of the Kwinte Bank Central Depression before and after the cessation of aggregate extraction. *Journal of Coastal Research***,** 77-86.

DESANTO, J., SANDWELL, D. & CHADWELL, C. 2016. Seafloor geodesy from repeated sidescan sonar surveys: Seafloor geodesy with sidescan sonar. *Journal of Geophysical Research: Solid Earth,* 121**,** 4800-4813.

DIEGUES, A., PINTO, J., RIBEIRO, P., FRIAS, R. & D, C. A. Automatic Habitat Mapping using Convolutional Neural Networks. 2018 IEEE/OES Autonomous Underwater Vehicle Workshop (AUV), 6-9 Nov. 2018 2018. 1-6.

DIESING, M., GREEN, S. L., STEPHENS, D., LARK, R. M., STEWART, H. A. & DOVE, D. 2014. Mapping seabed sediments: Comparison of manual, geostatistical, object-based image analysis and machine learning approaches. *Continental Shelf Research,* 84**,** 107-119.

DIESING, M., MITCHELL, P. & STEPHENS, D. 2016. Image-based seabed classification: what can we learn from terrestrial remote sensing? *ICES Journal of Marine Science,* 73**,** 2425-2441.

DIESING, M. & STEPHENS, D. 2015. A multi-model ensemble approach to seabed mapping. *Journal of Sea Research,* 100**,** 62-69.

DIESING, M. & THORSNES, T. 2018. Mapping of cold-water coral carbonate mounds based on geomorphometric features: An object-based approach. *Geosciences,* 8**,** 34.

DIXON, B. & CANDADE, N. 2008. Multispectral landuse classification using neural networks and support vector machines: one or the other, or both? *International Journal of Remote Sensing,* 29**,** 1185-1206.

DORSCHEL, B., HEBBELN, D., FOUBERT, A., WHITE, M. & WHEELER, A. J. 2007. Hydrodynamics and cold-water coral facies distribution related to recent sedimentary processes at Galway Mound west of Ireland. *Marine Geology,* 244**,** 184-195.

DORSCHEL, B., WHEELER, A. J., HUVENNE, V. A. I. & DE HAAS, H. 2009. Cold-water coral mounds in an erosive environmental setting: TOBI side-scan sonar data and ROV video footage from the northwest Porcupine Bank, NE Atlantic. *Marine Geology,* 264**,** 218-229.

DORSCHEL, B., WHEELER, A.J., MONTEYS, X., VERBRUGGEN, K., 2010. Mound Features and Coral Carbonate Mounds, in: Dorschel, Boris, Wheeler, Andrew J., Monteys, Xavier, Verbruggen, Koen (Eds.), Atlas of the Deep-Water Seabed: Ireland. Springer Netherlands, Dordrecht, pp. 97–116. https://doi.org/10.1007/978-90-481-9376-1_10

DOVE, D., NANSON, R., BJARNADÓTTIR, L., GUINAN, J., GAFEIRA, J., POST, A., DOLAN, M., STEWART, H., AROSIO, R. & G.A, S. 2020. *A two-part seabed geomorphology classification scheme (v.2); Part 1: morphology features glossary*.

DRĂGUŢ, L. & BLASCHKE, T. 2006. Automated classification of landform elements using object-based image analysis. *Geomorphology,* 81**,** 330-344.

DRĂGUŢ, L., TIEDE, D. & LEVICK, S. R. 2010. ESP: a tool to estimate scale parameter for multiresolution image segmentation of remotely sensed data. *International Journal of Geographical Information Science,* 24**,** 859-871.

DUFEK, T. 2013. Backscatter analysis of multi-beam sonar data in the area of the Valdivia fracture zone. *Hydraulic Engineering Repository***,** 6.

DURÁN, R., GUILLÉN, J., RIVERA, J., MUÑOZ, A., LOBO, F. J., FERNÁNDEZ-SALAS, L. M. & ACOSTA, J. 2017. Subaqueous dunes over sand ridges on the Murcia outer shelf. *In:* GUILLÉN, J., ACOSTA, J., CHIOCCI, F. L. & PALANQUES, A. (eds.) *Atlas of Bedforms in the Western Mediterranean.* Cham: Springer International Publishing.

DURDEN, J., BETT, B., SCHOENING, T., MORRIS, K., NATTKEMPER, T. & RUHL, H. 2016. Comparison of image annotation data generated by multiple investigators for benthic ecology. *Marine Ecology Progress Series,* 552**,** 61-70.

DUŢU, F., PANIN, N., ION, G. & TIRON DUŢU, L. 2018. Multibeam bathymetric investigations of the morphology and associated bedforms, Sulina Channel, Danube Delta. *Geosciences* [Online], 8.

EASTERDAY, K., KISLIK, C., DAWSON, T. E., HOGAN, S. & KELLY, M. 2019. Remotely sensed water limitation in vegetation: Insights from an experiment with unmanned aerial vehicles (UAVs). *Remote Sensing,* 11**,** 1853.

EISANK, C., SMITH, M. & HILLIER, J. 2014. Assessment of multiresolution segmentation for delimiting drumlins in digital elevation models. *Geomorphology,* 214**,** 452-464.

EL-NAGGAR, A. M. 2018. Determination of optimum segmentation parameter values for extracting building from remote sensing images. *Alexandria Engineering Journal,* 57**,** 3089-3097.

ELEFTHERAKIS, D., BERGER, L., LE BOUFFANT, N., PACAULT, A., AUGUSTIN, J.-M. & LURTON, X. 2018. Backscatter calibration of high-frequency multibeam echosounder using a reference single-beam system, on natural seafloor. *Marine Geophysical Research,* 39**,** 55-73.

EMODNET BATHYMETRY CONSORTIUM 2020. EMODnet digital bathymetry (DTM). *In:* EMODNET (ed.).

FABRI, M. C., PEDEL, L., BEUCK, L., GALGANI, F., HEBBELN, D. & FREIWALD, A. 2014. Megafauna of vulnerable marine ecosystems in French mediterranean submarine canyons: Spatial distribution and anthropogenic impacts. *Deep Sea Research Part II: Topical Studies in Oceanography,* 104**,** 184-207.

FAKIRIS, E., BLONDEL, P., PAPATHEODOROU, G., CHRISTODOULOU, D., DIMAS, X., GEORGIOU, N., KORDELLA, S., DIMITRIADIS, C., RZHANOV, Y., GERAGA, M. & FERENTINOS, G. 2019. Multi-frequency, multi-sonar mapping of shallow habitats—Efficacy and management implications in the national marine park of Zakynthos, Greece. *Remote Sensing,* 11**,** 461.

FAKIRIS, E., RZHANOV, Y. & ZOURA, D. 2012. *On importance of acoustic backscatter corrections for texture-based seafloor characterization*.

FELDENS, P., SCHULZE, I., PAPENMEIER, S., SCHÖNKE, M. & SCHNEIDER VON DEIMLING, J. 2018. Improved interpretation of marine sedimentary environments using multi-frequency multibeam backscatter data. *Geosciences,* 8**,** 214.

FENTIMEN, R., RÜGGEBERG, A., LIM, A., KATEB, A. E., FOUBERT, A., WHEELER, A. J. & SPEZZAFERRI, S. 2018. Benthic foraminifera in a deep-sea high-energy environment: the Moira Mounds (Porcupine Seabight, SW of Ireland). *Swiss Journal of Geosciences,* 111**,** 561-572.

FERN, R. R., FOXLEY, E. A., BRUNO, A. & MORRISON, M. L. 2018. Suitability of NDVI and OSAVI as estimators of green biomass and coverage in a semi-arid rangeland. *Ecological Indicators,* 94**,** 16-21.

FEZZANI, R., BERGER, L., LE BOUFFANT, N., FONSECA, L. & LURTON, X. 2021. Multispectral and multiangle measurements of acoustic seabed backscatter acquired with a tilted calibrated echosounder. *The Journal of the Acoustical Society of America,* 149**,** 4503-4515.

FEZZANI, R., ZERR, B., MANSOUR, A., LEGRIS, M. & VRIGNAUD, C. 2019. Fusion of swath bathymetric data: Application to AUV rapid environment assessment. *IEEE Journal of Oceanic Engineering,* 44**,** 111-120.

FONSECA, L., BROWN, C., CALDER, B., MAYER, L. & RZHANOV, Y. 2009. Angular range analysis of acoustic themes from Stanton Banks Ireland: A link between visual interpretation and multibeam echosounder angular signatures. *Applied Acoustics,* 70**,** 1298-1304.

FONSECA, L. & MAYER, L. 2007. Remote estimation of surficial seafloor properties through the application Angular Range Analysis to multibeam sonar data. *Marine Geophysical Researches,* 28**,** 119-126.

FOUBERT, A., BECK, T., WHEELER, A. J., OPDERBECKE, J., GREHAN, A., KLAGES, M., THIEDE, J., HENRIET, J.-P. & POLARSTERN, A.-X. 2005. New view of the Belgica Mounds, Porcupine Seabight, NE Atlantic: preliminary results from the Polarstern ARK-XIX/3a ROV cruise. *Cold-water corals and ecosystems.* Springer.

FOUBERT, A., HUVENNE, V. A. I., WHEELER, A., KOZACHENKO, M., OPDERBECKE, J. & HENRIET, J. P. 2011. The Moira Mounds, small cold-water coral mounds in the Porcupine Seabight, NE Atlantic: Part B—Evaluating the impact of sediment dynamics through high-resolution ROV-borne bathymetric mapping. *Marine Geology,* 282**,** 65-78.

FREEMAN, S. M. & ROGERS, S. I. 2003. A new analytical approach to the characterisation of macro-epibenthic habitats: linking species to the environment. *Estuarine, Coastal and Shelf Science,* 56**,** 749-764.

GAETANO, R., MASI, G., POGGI, G., VERDOLIVA, L. & SCARPA, G. 2015. Marker-controlled watershed-based segmentation of multiresolution remote sensing images. *IEEE Transactions on Geoscience and Remote Sensing,* 53**,** 2987-3004.

GAIDA, C. T., TENGKU ALI, A. T., SNELLEN, M., AMIRI-SIMKOOEI, A., VAN DIJK, A. T. & SIMONS, G. D. 2018. A multispectral bayesian classification method for increased acoustic discrimination of seabed sediments using multi-frequency multibeam backscatter data. *Geosciences,* 8.

GAIDA, T. C., SNELLEN, M., VAN DIJK, T. A. G. P. & SIMONS, D. G. 2019. Geostatistical modelling of multibeam backscatter for full-coverage seabed sediment maps. *Hydrobiologia,* 845**,** 55-79.

GAO, Y. & MAS, J. F. 2008. A comparison of the performance of pixel based and object based classifications over images with various spatial resolutions.

GAO, Y., MAS, J. F., KERLE, N. & NAVARRETE PACHECO, J. A. 2011. Optimal region growing segmentation and its effect on classification accuracy. *International journal of remote sensing,* 32**,** 3747-3763.

GAZIS, I.-Z. & GREINERT, J. 2021. Importance of spatial autocorrelation in machine learning modeling of polymetallic nodules, model uncertainty and transferability at local scale. *Minerals,* 11.

GAZIS, I. Z., SCHOENING, T., ALEVIZOS, E. & GREINERT, J. 2018. Quantitative mapping and predictive modeling of Mn nodules' distribution from hydroacoustic and optical AUV data linked by random forests machine learning. *Biogeosciences,* 15**,** 7347-7377.

GOODCHILD, M. F. 2011. Scale in GIS: An overview. *Geomorphology,* 130**,** 5-9.

GREENE, H. G., BAKER, M. & ASCHOFF, J. 2020. Chapter 14 - A dynamic bedforms habitat for the forage fish Pacific sand lance, San Juan Islands, WA, United States. *In:* HARRIS, P. T. & BAKER, E. (eds.) *Seafloor Geomorphology as Benthic Habitat (Second Edition).* Elsevier.

GREENE, H. G., BAKER, M. R., ASCHOFF, J. & PACUNSKI, R. 2021. Hazards evaluation of a valuable vulnerable sand-wave field forage fish habitat in the marginal Central Salish Sea using a submersible. *Oceanologia*.

GREENE, H. G., BIZZARRO, J. J., O'CONNELL, V. M. & BRYLINSKY, C. K. 2007. Construction of digital potential marine benthic habitat maps using a coded classification scheme and its application. *Mapping the seafloor for habitat characterization: Geological Association of Canada Special Paper,* 47**,** 141-155.

GREENE, H. G., CACCHIONE, D. A. & HAMPTON, M. A. 2017. Characteristics and dynamics of a large sub-tidal sand wave field—habitat for Pacific sand lance (*Ammodytes personatus*), Salish Sea, Washington, USA. *Geosciences,* 7**,** 107.

GREENE, H. G., YOKLAVICH, M. M., STARR, R. M., O'CONNELL, V. M., WAKEFIELD, W. W., SULLIVAN, D. E., MCREA JR, J. E. & CAILLIET, G. M. 1999. A classification scheme for deep seafloor habitats. *Oceanologica acta,* 22**,** 663-678.

GRIPPA, T., LENNERT, M., BEAUMONT, B., VANHUYSSE, S., STEPHENNE, N. & WOLFF, E. 2017. An open-source semi-automated processing chain for urban object-based classification. *Remote Sensing,* 9.

GUINAN, J., MCKEON, C., KEEFFE, E., MONTEYS, X., SACCHETTI, F., COUGHLAN, M. & NIC AONGHUSA, C. 2021. INFOMAR data supports offshore energy development and marine spatial planning in the Irish offshore via the EMODnet Geology portal. *Quarterly Journal of Engineering Geology and Hydrogeology,* 54**,** qjegh2020-033.

GUO, Z., HONG, Y. & JENG, D.-S. 2021. Structure–seabed interactions in marine environments. *Journal of Marine Science and Engineering,* 9**,** 972.

HAMILTON, L. J. & PARNUM, I. 2011. Acoustic seabed segmentation from direct statistical clustering of entire multibeam sonar backscatter curves. *Continental Shelf Research,* 31**,** 138-148.

HARPER, S. J. M., BATES, C. R., GUZMAN, H. M. & MAIR, J. M. 2010. Acoustic mapping of fish aggregation areas to improve fisheries management in Las Perlas Archipelago, Pacific Panama. *Ocean & Coastal Management,* 53**,** 615-623.

HARRIS, C. R., MILLMAN, K. J., VAN DER WALT, S. J., GOMMERS, R., VIRTANEN, P., COURNAPEAU, D., WIESER, E., TAYLOR, J., BERG, S., SMITH, N. J., KERN, R., PICUS, M., HOYER, S., VAN KERKWIJK, M. H., BRETT, M., HALDANE, A., DEL RÍO, J. F., WIEBE, M., PETERSON, P., GÉRARD-MARCHANT, P., SHEPPARD, K., REDDY, T., WECKESSER, W., ABBASI, H., GOHLKE, C. & OLIPHANT, T. E. 2020. Array programming with NumPy. *Nature,* 585**,** 357-362.

HARRIS, P. T. & BAKER, E. K. 2020. Chapter 60 - GeoHab Atlas of seafloor geomorphic features and benthic habitats–synthesis and lessons learned. *In:* HARRIS, P. T. & BAKER, E. (eds.) *Seafloor Geomorphology as Benthic Habitat (Second Edition).* Elsevier.

HARRIS, R. I. D. 1992. Testing for unit roots using the augmented Dickey-Fuller test: Some issues relating to the size, power and the lag structure of the test. *Economics Letters,* 38**,** 381-386.

HASAN, R. C., IERODIACONOU, D. & LAURENSON, L. 2012a. Combining angular response classification and backscatter imagery segmentation for benthic biological habitat mapping. *Estuarine, Coastal and Shelf Science,* 97**,** 1-9.

HASAN, R. C., IERODIACONOU, D., LAURENSON, L. & SCHIMEL, A. 2014. Integrating multibeam backscatter angular response, mosaic and bathymetry data for benthic habitat mapping. *Plos one,* 9**,** e97339.

HASAN, R. C., IERODIACONOU, D. & MONK, J. 2012b. Evaluation of four supervised learning methods for benthic habitat mapping using backscatter from multi-beam sonar. *Remote Sensing,* 4**,** 3427-3443.

HAY, G. & CASTILLA, G. Object-based image analysis: strengths, weaknesses, opportunities and threats (SWOT). Proc. 1st Int. Conf. OBIA, 2006. 4-5.

HEIL, J., HÄRING, V., MARSCHNER, B. & STUMPE, B. 2019. Advantages of fuzzy k-means over k-means clustering in the classification of diffuse reflectance soil spectra: A case study with West African soils. *Geoderma,* 337**,** 11-21.

HELD, P. & SCHNEIDER VON DEIMLING, J. 2019. New feature classes for acoustic habitat mapping—A multibeam echosounder point cloud analysis for mapping submerged aquatic vegetation (SAV). *Geosciences,* 9**,** 235.

HERKÜL, K., PETERSON, A. & PAEKIVI, S. 2017. Applying multibeam sonar and mathematical modeling for mapping seabed substrate and biota of offshore shallows. *Estuarine, Coastal and Shelf Science,* 192**,** 57-71.

HILLMAN, J. I. T., LAMARCHE, G., PALLENTIN, A., PECHER, I. A., GORMAN, A. R. & SCHNEIDER VON DEIMLING, J. 2018. Validation of automated supervised segmentation of multibeam backscatter data from the Chatham Rise, New Zealand. *Marine Geophysical Research,* 39**,** 205-227.

HOGG, O. T., HUVENNE, V. A. I., GRIFFITHS, H. J., DORSCHEL, B. & LINSE, K. 2016. Landscape mapping at sub-Antarctic South Georgia provides a protocol for underpinning large-scale marine protected areas. *Scientific Reports,* 6**,** 33163.

HOPKINSON, B. M., KING, A. C., OWEN, D. P., JOHNSON-ROBERSON, M., LONG, M. H. & BHANDARKAR, S. M. 2020. Automated classification of three-dimensional reconstructions of coral reefs using convolutional neural networks. *PLOS ONE,* 15**,** e0230671.

HOSSAIN, M. D. & CHEN, D. 2019. Segmentation for object-based image analysis (OBIA): A review of algorithms and challenges from remote sensing perspective. *ISPRS Journal of Photogrammetry and Remote Sensing,* 150**,** 115-134.

HOWELL, K. L., HOLT, R., ENDRINO, I. P. & STEWART, H. 2011. When the species is also a habitat: Comparing the predictively modelled distributions of *Lophelia pertusa* and the reef habitat it forms. *Biological Conservation,* 144**,** 2656-2665.

HUANG, Z., SIWABESSY, J., HEQIN, C. & NICHOL, S. 2018. Using multibeam backscatter data to investigate sediment-acoustic relationships. *Journal of Geophysical Research: Oceans*.

HUGHES CLARKE, J., LAMPLUGH, M. & CZOTTER, K. Multibeam water column imaging: improved wreck least-depth determination. Canadian hydrographic Conference, 2006.

HUGHES CLARKE, J. E. Multispectral acoustic backscatter from multibeam, improved classification potential. Proceedings of the United States Hydrographic Conference, San Diego, CA, USA, 2015. 15-19.

HUSSAIN, M., CHEN, D., CHENG, A., WEI, H. & STANLEY, D. 2013. Change detection from remotely sensed images: From pixel-based to object-based approaches. *ISPRS Journal of Photogrammetry and Remote Sensing,* 80**,** 91-106.

HUTIN, E., SIMARD, Y. & ARCHAMBAULT, P. 2005. Acoustic detection of a scallop bed from a single-beam echosounder in the St. Lawrence. *ICES Journal of Marine Science,* 62**,** 966-983.

HUVENNE, V. A., TYLER, P. A., MASSON, D. G., FISHER, E. H., HAUTON, C., HUHNERBACH, V., LE BAS, T. P. & WOLFF, G. A. 2011. A picture on the wall: innovative mapping reveals cold-water coral refuge in submarine canyon. *PLoS One,* 6**,** e28755.

HUVENNE, V. A. I., BETT, B. J., MASSON, D. G., LE BAS, T. P. & WHEELER, A. J. 2016. Effectiveness of a deep-sea cold-water coral Marine Protected Area, following eight years of fisheries closure. *Biological Conservation,* 200**,** 60-69.

HUVENNE, V. A. I., BLONDEL, P. & HENRIET, J. P. 2002. Textural analyses of sidescan sonar imagery from two mound provinces in the Porcupine Seabight. *Marine Geology,* 189**,** 323-341.

IERODIACONOU, D., MONK, J., RATTRAY, A., LAURENSON, L. & VERSACE, V. L. 2011. Comparison of automated classification techniques for predicting benthic biological communities using hydroacoustics and video observations. *Continental Shelf Research,* 31**,** S28-S38.

IERODIACONOU, D., SCHIMEL, A. C. G., KENNEDY, D., MONK, J., GAYLARD, G., YOUNG, M., DIESING, M. & RATTRAY, A. 2018. Combining pixel and object based image analysis of ultra-high resolution multibeam bathymetry and backscatter for habitat mapping in shallow marine waters. *Marine Geophysical Research,* 39**,** 271-288.

INTERNATIONAL HYDROGRAPHIC ORGANISATION 2020. IHO standards for hydrographic surveys. *Special Publication.*

ISACHENKO, A., GUBANOVA, Y., TZETLIN, A. & MOKIEVSKY, V. 2014. High-resolution habitat mapping on mud fields: New approach to quantitative mapping of Ocean quahog. *Marine Environmental Research,* 102**,** 36-42.

ISMAIL, K., HUVENNE, V. A. I. & MASSON, D. G. 2015. Objective automated classification technique for marine landscape mapping in submarine canyons. *Marine Geology,* 362**,** 17-32.

JACKSON, E. L., DAVIES, A. J., HOWELL, K. L., KERSHAW, P. J. & HALL-SPENCER, J. M. 2014. Future-proofing marine protected area networks for cold water coral reefs. *ICES Journal of Marine Science,* 71**,** 2621-2629.

JANOWSKI, L., MADRICARDO, F., FOGARIN, S., KRUSS, A., MOLINAROLI, E., KUBOWICZ-GRAJEWSKA, A. & TEGOWSKI, J. 2020. Spatial and temporal changes of tidal inlet using object-based image analysis of multibeam echosounder measurements: A case from the Lagoon of Venice, Italy. *Remote Sensing,* 12**,** 2117.

JANOWSKI, L., TEGOWSKI, J. & NOWAK, J. 2018a. Seafloor mapping based on multibeam echosounder bathymetry and backscatter data using object-based image analysis: a case study from the Rewal site, the Southern Baltic. *Oceanological and Hydrobiological Studies,* 47**,** 248-259.

JANOWSKI, L., TRZCINSKA, K., TEGOWSKI, J., KRUSS, A., RUCINSKA-ZJADACZ, M. & POCWIARDOWSKI, P. 2018b. Nearshore benthic habitat mapping based on multi-frequency, multibeam echosounder data using a combined object-based approach: A case study from the Rowy Site in the Southern Baltic Sea. *Remote Sensing,* 10**,** 1983.

JANOWSKI, L., WROBLEWSKI, R., DWORNICZAK, J., KOLAKOWSKI, M., ROGOWSKA, K., WOJCIK, M. & GAJEWSKI, J. 2021. Offshore benthic habitat mapping based on object-based image analysis and geomorphometric approach. A case study from the Slupsk Bank, Southern Baltic Sea. *Science of The Total Environment,* 801**,** 149712.

JAVADI, S., HASHEMY, S. M., MOHAMMADI, K., HOWARD, K. W. F. & NESHAT, A. 2017. Classification of aquifer vulnerability using k-means cluster analysis. *Journal of Hydrology,* 549**,** 27-37.

JENSEN, J. R. 2005. *Introductory digital image processing: a remote sensing perspective,* Upper Saddle River, NJ, Prentice-Hall Inc.

JEROSCH, K., KUHN, G., KRAJNIK, I., SCHARF, F. K. & DORSCHEL, B. 2016. A geomorphological seabed classification for the Weddell Sea, Antarctica. *Marine Geophysical Research,* 37**,** 127-141.

JOHANSEN, K., TIEDE, D., BLASCHKE, T., ARROYO, L. A. & PHINN, S. 2011. Automatic geographic object based mapping of streambed and riparian zone extent from LiDAR data in a temperate rural urban environment, Australia. *Remote Sensing,* 3**,** 1139-1156.

JOHNSON, B. & XIE, Z. 2011. Unsupervised image segmentation evaluation and refinement using a multi-scale approach. *ISPRS Journal of Photogrammetry and Remote Sensing,* 66**,** 473-483.

JONY, R. I., WOODLEY, A., RAJ, A. & PERRIN, D. Ensemble classification technique for water detection in satellite images. 2018 Digital Image Computing: Techniques and Applications (DICTA), 10-13 Dec. 2018 2018. 1-8.

JORDAHL, K. 2014. GeoPandas: Python tools for geographic data. *URL: [https://github.](https://github.com/geopandas/geopandas) com/geopandas/geopandas*.

JOZDANI, S. E., JOHNSON, B. A. & CHEN, D. 2019. Comparing deep neural networks, ensemble classifiers, and support vector machine algorithms for object-based urban land use/land cover classification. *Remote Sensing,* 11**,** 1713.

KACHELRIESS, D., WEGMANN, M., GOLLOCK, M. & PETTORELLI, N. 2014. The application of remote sensing for marine protected area management. *Ecological Indicators,* 36**,** 169-177.

KAESER, A. J., LITTS, T. L. & TRACY, T. W. 2013. Using low-cost side-scan sonar for benthic mapping throughout the lower Flint River, Georgia, USA. *River Research and Applications,* 29**,** 634-644.

KAVZOGLU, T. & TONBUL, H. 2018. An experimental comparison of multi-resolution segmentation, SLIC and k-means clustering for object-based classification of VHR imagery. *International Journal of Remote Sensing,* 39**,** 6020-6036.

KELLY, E. & DOWNES, S. 2014. Port of Cork maintenance dredging habitats directive assessment, screening statement. *In:* RPS; (ed.). Port of Cork;.

KENNY, A., CATO, I., DESPREZ, M., FADER, G., SCHÜTTENHELM, R. & SIDE, J. 2003. An overview of seabed-mapping technologies in the context of marine habitat classification. *ICES Journal of Marine Science,* 60**,** 411-418.

KENYON, N. H., AKHMETZHANOV, A. M., WHEELER, A. J., VAN WEERING, T. C. E., DE HAAS, H. & IVANOV, M. K. 2003. Giant carbonate mud mounds in the southern Rockall Trough. *Marine Geology,* 195**,** 5-30.

KHOSRONEJAD, A. & SOTIROPOULOS, F. 2017. On the genesis and evolution of barchan dunes: morphodynamics. *Journal of Fluid Mechanics,* 815**,** 117-148.

KIRIAKOULAKIS, K., FREIWALD, A., FISHER, E. & WOLFF, G. A. 2007. Organic matter quality and supply to deep-water coral/mound systems of the NW European Continental Margin. *International Journal of Earth Sciences,* 96**,** 159-170.

KLIMETZEK, D., STĂNCIOIU, P. T., PARASCHIV, M. & NIȚĂ, M. D. 2021. Ecological monitoring with spy satellite images—The case of red wood ants in romania. *Remote Sensing,* 13**,** 520.

KNAAPEN, M. A. F., VAN BERGEN HENEGOUW, C. N. & HU, Y. Y. 2005. Quantifying bedform migration using multi-beam sonar. *Geo-Marine Letters,* 25**,** 306-314.

KOOP, L., AMIRI-SIMKOOEI, A., J. VAN DER REIJDEN, K., O'FLYNN, S., SNELLEN, M. & G. SIMONS, D. 2019. Seafloor classification in a sand wave environment on the Dutch Continental Shelf using multibeam echosounder backscatter data. *Geosciences* [Online], 9.

KOOP, L., SNELLEN, M. & SIMONS, D. G. 2021. An object-based image analysis approach using bathymetry and bathymetric derivatives to classify the seafloor. *Geosciences,* 11**,** 45.

KOSTYLEV, V. E. 2012. Benthic habitat mapping from seabed acoustic surveys: do implicit assumptions hold? *Int. Assoc. Sedimentol. Spec. Publ,* 44**,** 405-416.

KOSTYLEV, V. E. & HANNAH, C. G. 2007. Process-driven characterization and mapping of seabed habitats. *Mapping the Seafloor for Habitat Characterization: Geological Association of Canada, Special Paper,* 47**,** 171-184.

KOSTYLEV, V. E., TODD, B. J., FADER, G. B., COURTNEY, R., CAMERON, G. D. & PICKRILL, R. A. 2001. Benthic habitat mapping on the Scotian Shelf based on multibeam bathymetry, surficial geology and sea floor photographs. *Marine Ecology Progress Series,* 219**,** 121-137.

KUAI, K. Z. & TSAI, C. W. 2012. Identification of varying time scales in sediment transport using the Hilbert–Huang Transform method. *Journal of Hydrology,* 420-421**,** 245-254.

KUCHARCZYK, M., HAY, G. J., GHAFFARIAN, S. & HUGENHOLTZ, C. H. 2020. Geographic object-based image analysis: A primer and future directions. *Remote Sensing,* 12**,** 2012.

LACHARITÉ, M., BROWN, C. J. & GAZZOLA, V. 2018. Multisource multibeam backscatter data: developing a strategy for the production of benthic habitat maps using semi-automated seafloor classification methods. *Marine Geophysical Research,* 39**,** 307-322.

LACHARITÉ, M., METAXAS, A. & LAWTON, P. 2015. Using object-based image analysis to determine seafloor fine-scale features and complexity. *Limnology and Oceanography: Methods,* 13**,** 553-567.

LAMARCHE, G. & LURTON, X. 2018. Recommendations for improved and coherent acquisition and processing of backscatter data from seafloor-mapping sonars. *Marine Geophysical Research,* 39**,** 5-22.

LAMARCHE, G., LURTON, X., VERDIER, A.-L. & AUGUSTIN, J.-M. 2011. Quantitative characterisation of seafloor substrate and bedforms using advanced processing of multibeam backscatter—Application to Cook Strait, New Zealand. *Continental Shelf Research,* 31**,** S93-S109.

LAMARCHE, G., ORPIN, A. R., MITCHELL, J. S. & PALLENTIN, A. 2016. Benthic habitat mapping. *Biological Sampling in the Deep Sea*.

LANDERO FIGUEROA, M. M., PARSONS, M. J. G., SAUNDERS, B. J., RADFORD, B., SALGADO-KENT, C. & PARNUM, I. M. 2021. The use of singlebeam echo-sounder depth data to produce demersal fish distribution models that are comparable to models produced using multibeam echo-sounder depth. *Ecology and Evolution,* 11**,** 17873-17884.

LANG, S. 2008. Object-based image analysis for remote sensing applications: modeling reality – dealing with complexity. *In:* BLASCHKE, T., LANG, S. & HAY, G. J. (eds.) *Object-Based Image Analysis: Spatial Concepts for Knowledge-Driven Remote Sensing Applications.* Berlin, Heidelberg: Springer Berlin Heidelberg.

LANGTON, R., STIRLING, D. A., BOULCOTT, P. & WRIGHT, P. J. 2020. Are MPAs effective in removing fishing pressure from benthic species and habitats? *Biological Conservation,* 247**,** 108511.

LATHROP, R. G., COLE, M., SENYK, N. & BUTMAN, B. 2006. Seafloor habitat mapping of the New York Bight incorporating sidescan sonar data. *Estuarine, Coastal and Shelf Science,* 68**,** 221-230.

LE BAS, T. & HUVENNE, V. 2009. Acquisition and processing of backscatter data for habitat mapping–comparison of multibeam and sidescan systems. *Applied Acoustics,* 70**,** 1248-1257.

LEBREC, U., RIERA, R., PAUMARD, V., LEARY, M. J. & LANG, S. C. 2022. Automatic mapping and characterisation of linear depositional bedforms: Theory and application using bathymetry from the north west shelf of Australia. *Remote Sensing,* 14.

LECOURS, V., DEVILLERS, R., SCHNEIDER, D. C., LUCIEER, V. L., BROWN, C. J. & EDINGER, E. N. 2015. Spatial scale and geographic context in benthic habitat

mapping: review and future directions. *Marine Ecology Progress Series,* 535**,** 259-284.
LEFEBVRE, A., HERRLING, G., BECKER, M., ZORNDT, A., KRÄMER, K. & WINTER, C. 2022. Morphology of estuarine bedforms, Weser Estuary, Germany. *Earth Surface Processes and Landforms,* 47**,** 242-256.
LEVEY, R. A., KJERFVE, B. & GETZEN, R. T. 1980. Comparison of bed form variance spectra within a meander bend during flood and average discharge. *Journal of Sedimentary Research,* 50**,** 149-155.
LI, D., TANG, C., XIA, C. & ZHANG, H. 2017. Acoustic mapping and classification of benthic habitat using unsupervised learning in artificial reef water. *Estuarine, Coastal and Shelf Science,* 185**,** 11-21.
LI, M. Z. & KING, E. L. 2007. Multibeam bathymetric investigations of the morphology of sand ridges and associated bedforms and their relation to storm processes, Sable Island Bank, Scotian Shelf. *Marine Geology,* 243**,** 200-228.
LIM, A., HUVENNE, V. A. I., VERTINO, A., SPEZZAFERRI, S. & WHEELER, A. J. 2018a. New insights on coral mound development from groundtruthed high-resolution ROV-mounted multibeam imaging. *Marine Geology,* 403**,** 225-237.
LIM, A., KANE, A., ARNAUBEC, A. & WHEELER, A. J. 2018b. Seabed image acquisition and survey design for cold water coral mound characterisation. *Marine Geology,* 395**,** 22-32.
LIM, A., WHEELER, A. J. & ARNAUBEC, A. 2017. High-resolution facies zonation within a cold-water coral mound: The case of the Piddington Mound, Porcupine Seabight, NE Atlantic. *Marine Geology,* 390**,** 120-130.
LIM, A., WHEELER, A. J. & CONTI, L. 2021. Cold-water coral habitat mapping: Trends and developments in acquisition and processing methods. *Geosciences,* 11**,** 9.
LIM, A., WHEELER, A. J., PRICE, D. M., O'REILLY, L., HARRIS, K. & CONTI, L. 2020. Influence of benthic currents on cold-water coral habitats: a combined benthic monitoring and 3D photogrammetric investigation. *Scientific Reports,* 10**,** 19433.
LINKLATER, M., INGLETON, T. C., KINSELA, M. A., MORRIS, B. D., ALLEN, K. M., SUTHERLAND, M. D. & HANSLOW, D. J. 2019. Techniques for classifying seabed morphology and composition on a subtropical-temperate continental shelf. *Geosciences,* 9**,** 141.
LIU, H., XU, K., LI, B., HAN, Y. & LI, G. 2019a. Sediment identification using machine learning classifiers in a mixed-texture dredge pit of Louisiana Shelf for coastal restoration. *Water,* 11**,** 1257.
LIU, M., YU, T., GU, X., SUN, Z., YANG, J., ZHANG, Z., MI, X., CAO, W. & LI, J. 2020. The impact of spatial resolution on the classification of vegetation types in highly fragmented planting areas based on unmanned aerial vehicle hyperspectral images. *Remote Sensing,* 12**,** 146.
LIU, S., QI, Z., LI, X. & YEH, A. G.-O. 2019b. Integration of convolutional neural networks and object-based post-classification refinement for land use and land cover mapping with optical and SAR data. *Remote Sensing,* 11**,** 690.
LOBO, F. J., MALDONADO, A. & NOORMETS, R. 2010. Large-scale sediment bodies and superimposed bedforms on the continental shelf close to the Strait of Gibraltar: Interplay of complex oceanographic conditions and physiographic constraints. *Earth Surface Processes and Landforms,* 35**,** 663-679.

LUCATELLI, D., GOES, E. R., BROWN, C. J., SOUZA-FILHO, J. F., GUEDES-SILVA, E. & ARAÚJO, T. C. M. 2020. Geodiversity as an indicator to benthic habitat distribution: An integrative approach in a tropical continental shelf. *Geo-Marine Letters,* 40**,** 911-923.

LUCIEER, V. & LAMARCHE, G. 2011. Unsupervised fuzzy classification and object-based image analysis of multibeam data to map deep water substrates, Cook Strait, New Zealand. *Continental Shelf Research,* 31**,** 1236-1247.

LUCIEER, V. L. 2008. Object-oriented classification of sidescan sonar data for mapping benthic marine habitats. *International Journal of Remote Sensing,* 29**,** 905-921.

LURTON, X. 2002. *An introduction to underwater acoustics: principles and applications*, Springer Science & Business Media.

LURTON, X., LAMARCHE, G., BROWN, C., LUCIEER, V., RICE, G., SCHIMEL, A. & WEBER, T. 2015. *Backscatter measurements by seafloor-mapping sonars: Guidelines and recommendations,* Eastsound, WA, USA, GeoHab Backscatter Working Group.

MA, L., LI, M., MA, X., CHENG, L., DU, P. & LIU, Y. 2017. A review of supervised object-based land-cover image classification. *ISPRS Journal of Photogrammetry and Remote Sensing,* 130**,** 277-293.

MALEIKA, W. 2013. The influence of track configuration and multibeam echosounder parameters on the accuracy of seabed DTMs obtained in shallow water. *Earth Science Informatics,* 6**,** 47-69.

MALIK, M., LURTON, X. & MAYER, L. 2018. A framework to quantify uncertainties of seafloor backscatter from swath mapping echosounders. *Marine Geophysical Research,* 39**,** 151-168.

MARKS, K. M. & SMITH, W. H. F. 2008. An uncertainty model for deep ocean single beam and multibeam echo sounder data. *Marine Geophysical Researches,* 29**,** 239-250.

MARPU, P. R., NEUBERT, M., HEROLD, H. & NIEMEYER, I. 2010. Enhanced evaluation of image segmentation results. *Journal of Spatial Science,* 55**,** 55-68.

MARSH, I. & BROWN, C. 2009. Neural network classification of multibeam backscatter and bathymetry data from Stanton Bank (Area IV). *Applied Acoustics,* 70**,** 1269-1276.

MAS, J. F. & FLORES, J. J. 2008. The application of artificial neural networks to the analysis of remotely sensed data. *International Journal of Remote Sensing,* 29**,** 617-663.

MASETTI, G., SACILE, R. & TRUCCO, A. 2011. Remote characterization of seafloor adjacent to shipwrecks using mosaicking and analysis of backscatter response. *Italian Journal of Remote Sensing,* 43**,** 77-92.

MATOS, L., WIENBERG, C., TITSCHACK, J., SCHMIEDL, G., FRANK, N., ABRANTES, F., CUNHA, M. R. & HEBBELN, D. 2017. Coral mound development at the Campeche cold-water coral province, southern Gulf of Mexico: Implications of Antarctic Intermediate Water increased influence during interglacials. *Marine Geology,* 392**,** 53-65.

MAYER, L., JAKOBSSON, M., ALLEN, G., DORSCHEL, B., FALCONER, R., FERRINI, V., LAMARCHE, G., SNAITH, H. & WEATHERALL, P. 2018. The Nippon

Foundation—GEBCO seabed 2030 project: The quest to see the world's oceans completely mapped by 2030. *Geosciences,* 8**,** 63.
MAYER, L. A. 2006. Frontiers in seafloor mapping and visualization. *Marine Geophysical Researches,* 27**,** 7-17.
MCGONIGLE, C., BROWN, C. J. & QUINN, R. 2010a. Insonification orientation and its relevance for image-based classification of multibeam backscatter. *ICES Journal of Marine Science,* 67**,** 1010-1023.
MCGONIGLE, C., BROWN, C. J. & QUINN, R. 2010b. Operational parameters, data density and benthic ecology: Considerations for image-based classification of multibeam backscatter. *Marine Geodesy,* 33**,** 16-38.
MCGONIGLE, C. & COLLIER, J. S. 2014. Interlinking backscatter, grain size and benthic community structure. *Estuarine, Coastal and Shelf Science,* 147**,** 123-136.
MEIJER, K. J., FRANKEN, O., VAN DER HEIDE, T., HOLTHUIJSEN, S. J., VISSER, W., GOVERS, L. L. & OLFF, H. 2022. Characterizing bedforms in shallow seas as an integrative predictor of seafloor stability and the occurrence of macrozoobenthic species. *Remote Sensing in Ecology and Conservation,* n/a.
MENANDRO, P. S., BASTOS, A. C., BONI, G., FERREIRA, L. C., VIEIRA, F. V., LAVAGNINO, A. C., MOURA, R. L. & DIESING, M. 2020. Reef mapping using different seabed automatic classification tools. *Geosciences* [Online], 10.
MENANDRO, P. S., BASTOS, A. C., MISIUK, B. & BROWN, C. J. 2022. Applying a multi-method framework to analyze the multispectral acoustic response of the seafloor. *Frontiers in Remote Sensing,* 3.
MESTDAGH, S., AMIRI-SIMKOOEI, A., VAN DER REIJDEN, K. J., KOOP, L., O'FLYNN, S., SNELLEN, M., VAN SLUIS, C., GOVERS, L. L., SIMONS, D. G., HERMAN, P. M. J., OLFF, H. & YSEBAERT, T. 2020. Linking the morphology and ecology of subtidal soft-bottom marine benthic habitats: A novel multiscale approach. *Estuarine, Coastal and Shelf Science,* 238**,** 106687.
MICALLEF, A., LE BAS, T. P., HUVENNE, V. A. I., BLONDEL, P., HÜHNERBACH, V. & DEIDUN, A. 2012. A multi-method approach for benthic habitat mapping of shallow coastal areas with high-resolution multibeam data. *Continental Shelf Research,* 39-40**,** 14-26.
MICHAUD, J.-S., COOPS, N. C., ANDREW, M. E. & WULDER, M. A. 2012. Characterising spatiotemporal environmental and natural variation using a dynamic habitat index throughout the province of Ontario. *Ecological Indicators,* 18**,** 303-311.
MIENIS, F., DE STIGTER, H. C., WHITE, M., DUINEVELD, G., DE HAAS, H. & VAN WEERING, T. C. E. 2007. Hydrodynamic controls on cold-water coral growth and carbonate-mound development at the SW and SE Rockall Trough Margin, NE Atlantic Ocean. *Deep Sea Research Part I: Oceanographic Research Papers,* 54**,** 1655-1674.
MING, D., ZHOU, W., XU, L., WANG, M. & MA, Y. 2018. Coupling relationship among scale parameter, segmentation accuracy, and classification accuracy in GEOBIA. *Photogrammetric Engineering & Remote Sensing,* 84**,** 681-693.
MIRAMONTES, E., GARREAU, P., CAILLAUD, M., JOUET, G., PELLEN, R., HERNÁNDEZ-MOLINA, F. J., CLARE, M. A. & CATTANEO, A. 2019. Contourite distribution and bottom currents in the NW Mediterranean Sea: Coupling seafloor geomorphology and hydrodynamic modelling. *Geomorphology,* 333**,** 43-60.

MISHRA, N. B. & CREWS, K. A. 2014. Mapping vegetation morphology types in a dry savanna ecosystem: integrating hierarchical object-based image analysis with Random Forest. *International Journal of Remote Sensing,* 35**,** 1175-1198.

MISIUK, B. & BROWN, C. J. 2022. Multiple imputation of multibeam angular response data for high resolution full coverage seabed mapping. *Marine Geophysical Research,* 43**,** 7.

MISIUK, B., BROWN, C. J., ROBERT, K. & LACHARITÉ, M. 2020. Harmonizing multi-source sonar backscatter datasets for seabed mapping using bulk shift approaches. *Remote Sensing,* 12**,** 601.

MISIUK, B., DIESING, M., AITKEN, A., BROWN, C. J., EDINGER, E. N. & BELL, T. 2019. A spatially explicit comparison of quantitative and categorical modelling approaches for mapping seabed sediments using random forest. *Geosciences,* 9**,** 254.

MITCHELL, P. J., DOWNIE, A.-L. & DIESING, M. 2018. How good is my map? A tool for semi-automated thematic mapping and spatially explicit confidence assessment. *Environmental Modelling & Software,* 108**,** 111-122.

MOHAMED, H., NADAOKA, K. & NAKAMURA, T. 2020. Towards benthic habitat 3D mapping using machine learning algorithms and structures from motion photogrammetry. *Remote Sensing,* 12.

MOMENI, R., APLIN, P. & BOYD, D. S. 2016. Mapping complex urban land cover from spaceborne imagery: The influence of spatial resolution, spectral band set and classification approach. *Remote Sensing,* 8**,** 88.

MONTEREALE GAVAZZI, G., MADRICARDO, F., JANOWSKI, L., KRUSS, A., BLONDEL, P., SIGOVINI, M. & FOGLINI, F. 2016. Evaluation of seabed mapping methods for fine-scale classification of extremely shallow benthic habitats – Application to the Venice Lagoon, Italy. *Estuarine, Coastal and Shelf Science,* 170**,** 45-60.

MONTSENY, M., LINARES, C., CARREIRO-SILVA, M., HENRY, L.-A., BILLETT, D., CORDES, E. E., SMITH, C. J., PAPADOPOULOU, N., BILAN, M., GIRARD, F., BURDETT, H. L., LARSSON, A., STRÖMBERG, S., VILADRICH, N., BARRY, J. P., BAENA, P., GODINHO, A., GRINYÓ, J., SANTÍN, A., MORATO, T., SWEETMAN, A. K., GILI, J.-M. & GORI, A. 2021. Active ecological restoration of cold-water corals: Techniques, challenges, costs and future directions. *Frontiers in Marine Science,* 8.

MORITZ, P., NISHIHARA, R., WANG, S., TUMANOV, A., LIAW, R., LIANG, E., ELIBOL, M., YANG, Z., PAUL, W. & JORDAN, M. I. Ray: A distributed framework for emerging {AI} applications. 13th {USENIX} Symposium on Operating Systems Design and Implementation ({OSDI} 18), 2018. 561-577.

MOUNTRAKIS, G., IM, J., OGOLE, C., 2011. Support vector machines in remote sensing: A review. ISPRS Journal of Photogrammetry and Remote Sensing 66, 247–259. https://doi.org/10.1016/j.isprsjprs.2010.11.001

MPATLAS. 2022. *Atlas of marine protection* [Online]. Available: https://mpatlas.org/zones/ [Accessed].

NASH, S., HARTNETT, M. & DABROWSKI, T. 2011. Modelling phytoplankton dynamics in a complex estuarine system. *Proceedings of the Institution of Civil Engineers - Water Management,* 164**,** 35-54.

NATIONAL PARKS & WILDLIFE SERVICE 2015. Hempton's Turbot Bank SAC (002999) Conservation objectives supporting document - Marine habitats. *In:* ARTS, H. A. T. G. (ed.). Dublin, Ireland: NPWS.

NATIONAL PARKS & WILDLIFE SERVICE 2014. Hempton's Turbot Bank SAC Site Synopsis. *In:* GAELTACHT, D. O. A. H. A. T. (ed.). Dublin Ireland: NPWS.

NEAKRASE, L. D. V., KLOSE, M. & TITUS, T. N. 2017. Terrestrial subaqueous seafloor dunes: Possible analogs for Venus. *Aeolian Research,* 26**,** 47-56.

NEMANI, S., COTE, D., MISIUK, B., EDINGER, E., MACKIN-MCLAUGHLIN, J., TEMPLETON, A., SHAW, J. & ROBERT, K. 2022. A multi-scale feature selection approach for predicting benthic assemblages. *Estuarine, Coastal and Shelf Science,* 277**,** 108053.

O'LEARY, B. C., WINTHER-JANSON, M., BAINBRIDGE, J. M., AITKEN, J., HAWKINS, J. P. & ROBERTS, C. M. 2016. Effective coverage targets for ocean protection. *Conservation Letters,* 9**,** 398-404.

O'TOOLE, R., MACCRAITH, E. & FINN, N. 2012. KRY12_05 Cork Harbour and Approaches. Dublin: Geological Survey of Ireland, Marine Institute.

OFFICE OF PUBLIC WORKS 2017. Lower Lee (Cork city) flood relief scheme: Supplementary report.: Office of Public Works.

OMO-IRABOR, O. O. 2016. A comparative study of image classification algorithms for landscape assessment of the Niger Delta Region. *Journal of Geographic Information System,* 8**,** 163-170.

ORHAN, U., HEKIM, M. & OZER, M. 2011. EEG signals classification using the k-means clustering and a multilayer perceptron neural network model. *Expert Systems with Applications,* 38**,** 13475-13481.

PARNUM, I., SIWABESSY, J., GAVRILOV, A. & PARSONS, M. A comparison of single beam and multibeam sonar systems in seafloor habitat mapping. Proc. 3rd Int. Conf. and Exhibition of Underwater Acoustic Measurements: Technologies & Results, Nafplion, Greece, 2009. 155-162.

PATINO, J. E. & DUQUE, J. C. 2013. A review of regional science applications of satellite remote sensing in urban settings. *Computers, Environment and Urban Systems,* 37**,** 1-17.

PEARCE, S. K. & BIRD, J. S. 2013. Sharpening sidescan sonar images for shallow-water target and habitat classification with a vertically stacked array. *IEEE Journal of Oceanic Engineering,* 38**,** 455-469.

PEDREGOSA, F., VAROQUAUX, G., GRAMFORT, A., MICHEL, V., THIRION, B., GRISEL, O., BLONDEL, M., PRETTENHOFER, P., WEISS, R. & DUBOURG, V. 2011. Scikit-learn: Machine learning in Python. *the Journal of machine Learning research,* 12**,** 2825-2830.

PERGENT, G., MONNIER, B., CLABAUT, P., GASCON, G., PERGENT-MARTINI, C. & VALETTE-SANSEVIN, A. 2017. Innovative method for optimizing side-scan sonar mapping: The blind band unveiled. *Estuarine, Coastal and Shelf Science,* 194**,** 77-83.

PERRON, J. T., KIRCHNER, J. W. & DIETRICH, W. E. 2008. Spectral signatures of characteristic spatial scales and nonfractal structure in landscapes. *Journal of Geophysical Research: Earth Surface,* 113.

PHINN, S., ROELFSEMA, C. & MUMBY, P. 2012. Multi-scale, object-based image analysis for mapping geomorphic and ecological zones on coral reefs. *International Journal of Remote Sensing,* 33**,** 3768-3797.

PHIRI, D. & MORGENROTH, J. 2017. Developments in Landsat land cover classification methods: A review. *Remote Sensing,* 9**,** 967.

PIANO, M., NEILL, S. P., LEWIS, M. J., ROBINS, P. E., HASHEMI, M. R., DAVIES, A. G., WARD, S. L. & ROBERTS, M. J. 2017. Tidal stream resource assessment uncertainty due to flow asymmetry and turbine yaw misalignment. *Renewable Energy,* 114**,** 1363-1375.

PIERDOMENICO, M., GUIDA, V. G., MACELLONI, L., CHIOCCI, F. L., RONA, P. A., SCRANTON, M. I., ASPER, V. & DIERCKS, A. 2015. Sedimentary facies, geomorphic features and habitat distribution at the Hudson Canyon head from AUV multibeam data. *Deep Sea Research Part II: Topical Studies in Oceanography,* 121**,** 112-125.

PILLAY, T., CAWTHRA, H. C., LOMBARD, A. T. & SINK, K. 2021. Benthic habitat mapping from a machine learning perspective on the Cape St Francis inner shelf, Eastern Cape, South Africa. *Marine Geology,* 440**,** 106595.

PORSKAMP, P., RATTRAY, A., YOUNG, M. & IERODIACONOU, D. 2018. Multiscale and hierarchical classification for benthic habitat mapping. *Geosciences* [Online], 8.

POWERS, R. P., HAY, G. J. & CHEN, G. 2012. How wetland type and area differ through scale: A GEOBIA case study in Alberta's Boreal Plains. *Remote Sensing of Environment,* 117**,** 135-145.

PRADA, M. C., APPELDOORN, R. S. & RIVERA, J. A. 2008. The effects of minimum map unit in coral reefs maps generated from high resolution side scan sonar mosaics. *Coral Reefs,* 27**,** 297-310.

PRAMPOLINI, M., ANGELETTI, L., CASTELLAN, G., GRANDE, V., LE BAS, T., TAVIANI, M. & FOGLINI, F. 2021. Benthic habitat map of the Southern Adriatic Sea (Mediterranean Sea) from object-based image analysis of multi-source acoustic backscatter data. *Remote Sensing,* 13**,** 2913.

PRAMPOLINI, M., SAVINI, A., FOGLINI, F. & SOLDATI, M. 2020. Seven good reasons for integrating terrestrial and marine spatial datasets in changing environments. *Water,* 12**,** 2221.

PRASAD, D. H. & KUMAR, N. D. 2014. Coastal Erosion Studies: A Review. *International Journal of Geosciences,* Vol.05No.03**,** 5.

PROUDFOOT, B., DEVILLERS, R., BROWN, C. J., EDINGER, E. & COPELAND, A. 2020. Seafloor mapping to support conservation planning in an ecologically unique fjord in Newfoundland and Labrador, Canada. *Journal of Coastal Conservation,* 24**,** 36.

QPS 2019a. Fledermaus geocoding toolbox (FMGT). 7.8 ed.

QPS 2019b. Qimera. 1.7.6 ed.

RENDE, S. F., BOSMAN, A., DI MENTO, R., BRUNO, F., LAGUDI, A., IRVING, A. D., DATTOLA, L., GIAMBATTISTA, L. D., LANERA, P., PROIETTI, R., PARLAGRECO, L., STROOBANT, M. & CELLINI, E. 2020. Ultra-high-resolution mapping of *Posidonia oceanica* (L.) Delile Meadows through acoustic, optical data and object-based image classification. *Journal of Marine Science and Engineering* [Online], 8.

RESHITNYK, L., COSTA, M., ROBINSON, C. & DEARDEN, P. 2014. Evaluation of WorldView-2 and acoustic remote sensing for mapping benthic habitats in temperate coastal Pacific waters. *Remote Sensing of Environment,* 153**,** 7-23.

REY-AREA, M., GUIRADO, E., TABIK, S. & RUIZ-HIDALGO, J. 2020. FuCiTNet: Improving the generalization of deep learning networks by the fusion of learned class-inherent transformations. *Information Fusion,* 63**,** 188-195.

ROBERT, K., HUVENNE, V. A. I., GEORGIOPOULOU, A., JONES, D. O. B., MARSH, L., G, D. O. C. & CHAUMILLON, L. 2017. New approaches to high-resolution mapping of marine vertical structures. *Sci Rep,* 7**,** 9005.

ROBERTS, J. M. & CAIRNS, S. D. 2014. Cold-water corals in a changing ocean. *Current Opinion in Environmental Sustainability,* 7**,** 118-126.

ROBERTS, J. M., WHEELER, A. J. & FREIWALD, A. 2006. Reefs of the deep: The biology and geology of cold-water coral ecosystems. *Science,* 312**,** 543.

RUDDICK, K., NEUKERMANS, G., VANHELLEMONT, Q. & JOLIVET, D. 2014. Challenges and opportunities for geostationary ocean colour remote sensing of regional seas: A review of recent results. *Remote Sensing of Environment,* 146**,** 63-76.

RUNYA, R. M., MCGONIGLE, C., QUINN, R., HOWE, J., COLLIER, J., FOX, C., DOOLEY, J., O'LOUGHLIN, R., CALVERT, J., SCOTT, L., ABERNETHY, C. & EVANS, W. 2021. Examining the links between multi-frequency multibeam backscatter data and sediment grain size. *Remote Sensing,* 13**,** 1539.

RYAN, D. A., BROOKE, B. P., COLLINS, L. B., KENDRICK, G. A., BAXTER, K. J., BICKERS, A. N., SIWABESSY, P. J. W. & PATTIARATCHI, C. B. 2007. The influence of geomorphology and sedimentary processes on shallow-water benthic habitat distribution: Esperance Bay, Western Australia. *Estuarine, Coastal and Shelf Science,* 72**,** 379-386.

RZHANOV, Y., FONSECA, L. & MAYER, L. 2012. Construction of seafloor thematic maps from multibeam acoustic backscatter angular response data. *Computers & Geosciences,* 41**,** 181-187.

SANTOS, R., RODRIGUES, A. & QUARTAU, R. 2018. Acoustic remote characterization of seabed sediments using the angular range analysis technique: The inlet channel of Tagus River estuary (Portugal). *Marine Geology,* 400**,** 60-75.

SAQLAIN, M., JARGALSAIKHAN, B. & LEE, J. Y. 2019. A voting ensemble classifier for wafer map defect patterns identification in semiconductor manufacturing. *IEEE Transactions on Semiconductor Manufacturing,* 32**,** 171-182.

SAVINI, A., VERTINO, A., MARCHESE, F., BEUCK, L. & FREIWALD, A. 2014. Mapping cold-water coral habitats at different scales within the Northern Ionian Sea (Central Mediterranean): An assessment of coral coverage and associated vulnerability. *PLOS ONE,* 9**,** e87108.

SAVITZKY, A. & GOLAY, M. J. E. 1964. Smoothing and Differentiation of Data by Simplified Least Squares Procedures. *Analytical Chemistry,* 36**,** 1627-1639.

SCHÉRÉ, C. M., DAWSON, T. P. & SCHRECKENBERG, K. 2020. Multiple conservation designations: what impact on the effectiveness of marine protected areas in the Irish Sea? *International Journal of Sustainable Development & World Ecology,* 27**,** 596-610.

SCHIMEL, A. C. G., BEAUDOIN, J., PARNUM, I. M., LE BAS, T., SCHMIDT, V., KEITH, G. & IERODIACONOU, D. 2018. Multibeam sonar backscatter data processing. *Marine Geophysical Research,* 39**,** 121-137.

SCHIMEL, A. C. G., HEALY, T. R., JOHNSON, D. & IMMENGA, D. 2010. Quantitative experimental comparison of single-beam, sidescan, and multibeam benthic habitat maps. *ICES Journal of Marine Science,* 67**,** 1766-1779.

SCHOENING, T., KUHN, T. & NATTKEMPER, T. W. Seabed classification using a bag-of-prototypes feature representation. 2014 ICPR Workshop on Computer Vision for Analysis of Underwater Imagery, 24-24 Aug. 2014 2014. 17-24.

SECOMANDIA, M., OWENB, M. J., JONESA, E., TERENTEA, V. & COMRIEA, R. Application of the bathymetric position index method (BPI) for the purpose of defining a reference seabed level for cable burial. Offshore Site Investigation Geotechnics 8th International Conference Proceeding, 2017. Society for Underwater Technology, 904-913.

SERPETTI, N., HEATH, M., ARMSTRONG, E. & WITTE, U. 2011. Blending single beam RoxAnn and multi-beam swathe QTC hydro-acoustic discrimination techniques for the Stonehaven area, Scotland, UK. *Journal of Sea Research,* 65**,** 442-455.

SHANG, X., ROBERT, K., MISIUK, B., MACKIN-MCLAUGHLIN, J. & ZHAO, J. 2021. Self-adaptive analysis scale determination for terrain features in seafloor substrate classification. *Estuarine, Coastal and Shelf Science,* 254**,** 107359.

SHANG, X., ZHAO, J. & ZHANG, H. 2019. Obtaining high-resolution seabed topography and surface details by co-registration of side-scan sonar and multibeam echo sounder images. *Remote Sensing,* 11**,** 1496.

SHEELA, K. G. & DEEPA, S. N. 2013. Review on methods to fix number of hidden neurons in neural networks. *Mathematical Problems in Engineering,* 2013**,** 425740.

SHORTEN, C. & KHOSHGOFTAAR, T. M. 2019. A survey on image data augmentation for deep learning. *Journal of Big Data,* 6**,** 60.

SHUMCHENIA, E. J. & KING, J. W. 2010. Comparison of methods for integrating biological and physical data for marine habitat mapping and classification. *Continental Shelf Research,* 30**,** 1717-1729.

SIMARRO, G., GUILLÉN, J., PUIG, P., RIBÓ, M., LO IACONO, C., PALANQUES, A., MUÑOZ, A., DURÁN, R. & ACOSTA, J. 2015. Sediment dynamics over sand ridges on a tideless mid-outer continental shelf. *Marine Geology,* 361**,** 25-40.

SNELLEN, M., GAIDA, T. C., KOOP, L., ALEVIZOS, E. & SIMONS, D. G. 2019. Performance of multibeam echosounder backscatter-based classification for monitoring sediment distributions using multitemporal large-scale ocean data sets. *IEEE Journal of Oceanic Engineering,* 44**,** 142-155.

SNELLEN, M., SIEMES, K. & SIMONS, D. G. 2011. Model-based sediment classification using single-beam echosounder signals. *The Journal of the Acoustical Society of America,* 129**,** 2878-2888.

SPAGNOLO, M., BARTHOLOMAUS, T. C., CLARK, C. D., STOKES, C. R., ATKINSON, N., DOWDESWELL, J. A., ELY, J. C., GRAHAM, A. G. C., HOGAN, K. A., KING, E. C., LARTER, R. D., LIVINGSTONE, S. J. & PRITCHARD, H. D. 2017. The periodic topography of ice stream beds: Insights from the Fourier spectra of mega-scale glacial lineations. *Journal of Geophysical Research: Earth Surface,* 122**,** 1355-1373.

STOW, D. A., HERNÁNDEZ-MOLINA, F. J., LLAVE, E., SAYAGO-GIL, M., DÍAZ DEL RÍO, V. & BRANSON, A. 2009. Bedform-velocity matrix: the estimation of bottom current velocity from bedform observations. *Geology,* 37**,** 327-330.

STRONG, J. A. & ELLIOTT, M. 2017. The value of remote sensing techniques in supporting effective extrapolation across multiple marine spatial scales. *Marine Pollution Bulletin,* 116**,** 405-419.

SUMMERS, G., LIM, A. & WHEELER, A. J. 2021. A scalable, supervised classification of seabed sediment waves using an object-based image analysis approach. *Remote Sensing,* 13.

SUMMERS, G., LIM, A. & WHEELER, A. J. 2022. A characterisation of benthic currents from seabed bathymetry: An object-based image analysis of cold-water coral mounds. *Remote Sensing,* 14.

SYMONS, W. O., SUMNER, E. J., TALLING, P. J., CARTIGNY, M. J. B. & CLARE, M. A. 2016. Large-scale sediment waves and scours on the modern seafloor and their implications for the prevalence of supercritical flows. *Marine Geology,* 371**,** 130-148.

TAMSETT, D., MCILVENNY, J. & WATTS, A. 2016. Colour sonar: Multi-frequency sidescan sonar images of the seabed in the Inner Sound of the Pentland Firth, Scotland. *Journal of Marine Science and Engineering,* 4**,** 26.

TECCHIATO, S., COLLINS, L., PARNUM, I. & STEVENS, A. 2015. The influence of geomorphology and sedimentary processes on benthic habitat distribution and littoral sediment dynamics: Geraldton, Western Australia. *Marine Geology,* 359**,** 148-162.

TEGOWSKI, J., TRZCINSKA, K., KASPRZAK, M. & NOWAK, J. 2016. Statistical and spectral features of corrugated seafloor shaped by the Hans Glacier in Svalbard. *Remote Sensing,* 8.

TĘGOWSKI, J., TRZCIŃSKA, K., Ł, J., KRUSS, A., KUSEK, K. & NOWAK, J. Comparison of backscatter and seabed topographic characteristics recorded by multibeam echosounder at Rewal Area - Southern Baltic Sea. 2018 Joint Conference - Acoustics, 11-14 Sept. 2018 2018. 1-4.

THIERENS, M., BROWNING, E., PIRLET, H., LOUTRE, M. F., DORSCHEL, B., HUVENNE, V. A. I., TITSCHACK, J., COLIN, C., FOUBERT, A. & WHEELER, A. J. 2013. Cold-water coral carbonate mounds as unique palaeo-archives: the Plio-Pleistocene Challenger Mound record (NE Atlantic). *Quaternary Science Reviews,* 73**,** 14-30.

THORSNES, T. 2009. MAREANO–an introduction. *Norwegian Journal of Geology,* 89**,** 3.

TIEDE, D. 2014. A new geospatial overlay method for the analysis and visualization of spatial change patterns using object-oriented data modeling concepts. *Cartography and Geographic Information Science,* 41**,** 227-234.

TONG, C., WU, J., YONG, S., YANG, J. & YONG, W. 2004. A landscape-scale assessment of steppe degradation in the Xilin River Basin, Inner Mongolia, China. *Journal of Arid Environments,* 59**,** 133-149.

TRIMBLE 2014. eCognition Developer 9.0 user guide. *Trimble Germany GmbH: Munich, Germany*.

TRIMBLE 2020. Ecognition Developer reference book 10.0.1. *Trimble Documentation München, Germany.*

TROYA-GALVIS, A., GANCARSKI, P., PASSAT, N. & BERTI-EQUILLE, L. 2015. Unsupervised quantification of under- and over-segmentation for object-based remote sensing image analysis. *IEEE Journal of Selected Topics in Applied Earth Observations and Remote Sensing,* 8**,** 1-10.

TRZCINSKA, K., JANOWSKI, L., NOWAK, J., RUCINSKA-ZJADACZ, M., KRUSS, A., VON DEIMLING, J. S., POCWIARDOWSKI, P. & TEGOWSKI, J. 2020. Spectral features of dual-frequency multibeam echosounder data for benthic habitat mapping. *Marine Geology,* 427**,** 106239.

VAN DER KAADEN, A.-S., VAN OEVELEN, D., RIETKERK, M., SOETAERT, K. & VAN DE KOPPEL, J. 2020. Spatial self-organization as a new perspective on cold-water coral mound development. *Frontiers in Marine Science,* 7.

VAN LANDEGHEM, K. J., WHEELER, A. J., MITCHELL, N. C. & SUTTON, G. 2009a. Variations in sediment wave dimensions across the tidally dominated Irish Sea, NW Europe. *Marine Geology,* 263**,** 108-119.

VAN LANDEGHEM, K. J. J., BAAS, J. H., MITCHELL, N. C., WILCOCKSON, D. & WHEELER, A. J. 2012. Reversed sediment wave migration in the Irish Sea, NW Europe: A reappraisal of the validity of geometry-based predictive modelling and assumptions. *Marine Geology,* 295-298**,** 95-112.

VAN LANDEGHEM, K. J. J., UEHARA, K., WHEELER, A. J., MITCHELL, N. C. & SCOURSE, J. D. 2009b. Post-glacial sediment dynamics in the Irish Sea and sediment wave morphology: Data–model comparisons. *Continental Shelf Research,* 29**,** 1723-1736.

VAN WEERING, T. C. E., DE HAAS, H., DE STIGTER, H. C., LYKKE-ANDERSEN, H. & KOUVAEV, I. 2003. Structure and development of giant carbonate mounds at the SW and SE Rockall Trough margins, NE Atlantic Ocean. *Marine Geology,* 198**,** 67-81.

VERFAILLIE, E., DOORNENBAL, P., MITCHELL, A. J., WHITE, J. & VAN-LANCKER, V. 2007. The bathymetric position index (BPI) as a support tool for habitat mapping. *Worked example for the MESH Final Guidance***,** 1-14.

VIALA, C., LAMOURET, M. & ABADIE, A. 2021. Seafloor classification using a multibeam echo sounder: A new rugosity index coupled with a pixel-based process to map Mediterranean marine habitats. *Applied Acoustics,* 179**,** 108067.

UNITED NATIONS CONVENTION ON THE LAW OF THE SEA, 2023. Draft agreement under the United Nations Convention on the Law of the Sea on the conservation and sustainable use of marine biological diversity of areas beyond national jurisdiction.

WAGNER, H., PURSER, A., THOMSEN, L., JESUS, C. C. & LUNDÄLV, T. 2011. Particulate organic matter fluxes and hydrodynamics at the Tisler cold-water coral reef. *Journal of Marine Systems,* 85**,** 19-29.

WALBRIDGE, S., SLOCUM, N., POBUDA, M. & WRIGHT, D. J. 2018. Unified geomorphological analysis workflows with benthic terrain modeler. *Geosciences,* 8**,** 94.

WALLIS, D. 2005. Rockall-North Channel MESH geophysical survey, RRS Charles Darwin Cruise CD174, BGS Project 05/05 Operations Report. *In:* HOLMES, R., LONG, D., WAKEFIELD, E. & BRIDGER, M. (eds.). British Geological Survey.

WAN, J., QIN, Z., CUI, X., YANG, F., YASIR, M., MA, B. & LIU, X. 2022. MBES seabed sediment classification based on a decision fusion method using deep learning model. *Remote Sensing,* 14.

WANG, L., YU, Q., ZHANG, Y., FLEMMING, B. W., WANG, Y. & GAO, S. 2020. An automated procedure to calculate the morphological parameters of superimposed rhythmic bedforms. *Earth Surface Processes and Landforms,* 45**,** 3496-3509.

WARD, S. L., NEILL, S. P., VAN LANDEGHEM, K. J. & SCOURSE, J. D. 2015. Classifying seabed sediment type using simulated tidal-induced bed shear stress. *Marine Geology,* 367**,** 94-104.

WHEELER, A., CAPOCCI, R., CRIPPA, L., CONNOLLY, N., HOGAN, R., LIM, A., MCCARTHY, E., MCGONIGLE, C., O'DONNELL, E. & O'SULLIVAN, K. 2015. Cruise report: Quantifying environmental controls on cold-water coral reef growth (QuERCi). *Report No. CE15009,(University College Cork, Ireland, 2015)*.

WHEELER, A. J., KOZACHENKO, M., BEYER, A., FOUBERT, A., HUVENNE, V. A. I., KLAGES, M., MASSON, D. G., OLU-LE ROY, K. & THIEDE, J. 2005. Sedimentary processes and carbonate mounds in the Belgica Mound province, Porcupine Seabight, NE Atlantic. *In:* FREIWALD, A. & ROBERTS, J. M. (eds.) *Cold-Water Corals and Ecosystems.* Berlin, Heidelberg: Springer Berlin Heidelberg.

WHEELER, A. J., KOZACHENKO, M., HENRY, L. A., FOUBERT, A., DE HAAS, H., HUVENNE, V. A. I., MASSON, D. G. & OLU, K. 2011. The Moira Mounds, small cold-water coral banks in the Porcupine Seabight, NE Atlantic: Part A—an early stage growth phase for future coral carbonate mounds? *Marine Geology,* 282**,** 53-64.

WHEELER, A. J., KOZACHENKO, M., MASSON, D. G. & HUVENNE, V. A. I. 2008. Influence of benthic sediment transport on cold-water coral bank morphology and growth: the example of the Darwin Mounds, north-east Atlantic. *Sedimentology,* 55**,** 1875-1887.

WHITE, D. J. BO'SUN, a multi-beam sonar for search and survey. Offshore Technology Conference, 1971. Offshore Technology Conference.

WHITE, M. 2007. Benthic dynamics at the carbonate mound regions of the Porcupine Sea Bight continental margin. *International Journal of Earth Sciences,* 96**,** 1.

WICAKSONO, P., ARYAGUNA, P. A. & LAZUARDI, W. 2019. Benthic habitat mapping model and cross validation using machine-learning classification algorithms. *Remote Sensing,* 11**,** 1279.

WIENBERG, C., TITSCHACK, J., FRANK, N., DE POL-HOLZ, R., FIETZKE, J., EISELE, M., KREMER, A. & HEBBELN, D. 2020. Deglacial upslope shift of NE Atlantic intermediate waters controlled slope erosion and cold-water coral mound formation (Porcupine Seabight, Irish margin). *Quaternary Science Reviews,* 237**,** 106310.

WILSON, M. F., O'CONNELL, B., BROWN, C., GUINAN, J. C. & GREHAN, A. J. 2007. Multiscale terrain analysis of multibeam bathymetry data for habitat mapping on the continental slope. *Marine Geodesy,* 30**,** 3-35.

WITHARANA, C. & LYNCH, H. J. 2016. An object-based image analysis approach for detecting penguin guano in very high spatial resolution satellite images. *Remote Sensing,* 8**,** 375.

WOLF, J., WALKINGTON, I. A., HOLT, J. & BURROWS, R. 2009. Environmental impacts of tidal power schemes. *Proceedings of the Institution of Civil Engineers - Maritime Engineering,* 162**,** 165-177.

WU, H., CHENG, Z., SHI, W., MIAO, Z. & XU, C. 2014. An object-based image analysis for building seismic vulnerability assessment using high-resolution remote sensing imagery. *Natural Hazards,* 71**,** 151-174.

WYNN, R. B. & MASSON, D. G. 2008. Chapter 15 sediment waves and bedforms. *In:* REBESCO, M. & CAMERLENGHI, A. (eds.) *Developments in Sedimentology.* Elsevier.

YAN, G., CHENG, H., TENG, L., XU, W., JIANG, Y., YANG, G. & ZHOU, Q. 2020. Analysis of the use of geomorphic elements mapping to characterize subaqueous bedforms using multibeam bathymetric data in river system. *Applied Sciences* [Online], 10.

YANG, W., CAI, L. & WU, F. 2020. Image segmentation based on gray level and local relative entropy two dimensional histogram. *PLOS ONE,* 15**,** e0229651.

YASIR, M., RAHMAN, A. U. & GOHAR, M. 2021. Habitat mapping using deep neural networks. *Multimedia Systems,* 27**,** 679-690.

YUBA, N., KAWAMURA, K., YASUDA, T., LIM, J., YOSHITOSHI, R., WATANABE, N., KUROKAWA, Y. & MAEDA, T. 2021. Discriminating Pennisetum alopecuoides plants in a grazed pasture from unmanned aerial vehicles using object-based image analysis and random forest classifier. *Grassland Science,* 67**,** 73-82.

ZACHARIAS, M. A. & GREGR, E. J. 2005. Sensitivity and vulnerability in marine environments: An approach to identifying vulnerable marine areas. *Conservation Biology,* 19**,** 86-97.

ZAJAC, R. N. 2008. Challenges in marine, soft-sediment benthoscape ecology. *Landscape Ecology,* 23**,** 7-18.

ZELADA LEON, A., HUVENNE, V. A. I., BENOIST, N. M. A., FERGUSON, M., BETT, B. J. & WYNN, R. B. 2020. Assessing the repeatability of automated seafloor classification algorithms, with application in Marine Protected Area monitoring. *Remote Sensing,* 12**,** 1572.

ZHANG, C. 2019. Combining Ikonos and Bathymetric LiDAR Data to Improve Reef Habitat Mapping in the Florida Keys. *Papers in Applied Geography,* 5**,** 256-271.

ZHANG, X., XIAO, P. & FENG, X. 2020. Object-specific optimization of hierarchical multiscale segmentations for high-spatial resolution remote sensing images. *ISPRS Journal of Photogrammetry and Remote Sensing,* 159**,** 308-321.

ZHAO, T., MONTEREALE GAVAZZI, G., LAZENDIĆ, S., ZHAO, Y. & PIŽURICA, A. 2021. Acoustic seafloor classification using the Weyl transform of multibeam echosounder backscatter mosaic. *Remote Sensing,* 13**,** 1760.

ZHI, H., SIWABESSY, J., NICHOL, S. L. & BROOKE, B. P. 2014. Predictive mapping of seabed substrata using high-resolution multibeam sonar data: A case study from a shelf with complex geomorphology. *Marine Geology,* 357**,** 37-52.

ZHONG, L., HU, L. & ZHOU, H. 2019. Deep learning based multi-temporal crop classification. *Remote Sensing of Environment,* 221**,** 430.

ZHOU, J., WU, Z., JIN, X., ZHAO, D., CAO, Z. & GUAN, W. 2018. Observations and analysis of giant sand wave fields on the Taiwan Banks, northern South China Sea. *Marine Geology,* 406**,** 132-141.

ZHU, Z., CUI, X., ZHANG, K., AI, B., SHI, B. & YANG, F. 2021. DNN-based seabed classification using differently weighted MBES multifeatures. *Marine Geology,* 438**,** 106519.

ZLINSZKY, A., HEILMEIER, H., BALZTER, H., CZÚCZ, B. & PFEIFER, N. 2015. Remote sensing and GIS for habitat quality monitoring: New approaches and future research. *Remote Sensing,* 7**,** 7987-7994.